

UNIVERSITÀ DI ROMA “SAPIENZA”
FACOLTÀ DI SCIENZE MATEMATICHE, FISICHE E NATURALI
DIPARTIMENTO DI FISICA



TESI DI DOTTORATO
IN
ASTRONOMIA
XXVI CICLO

The role of dynamical friction in the formation of Compact Massive Objects

Author:

Manuel ARCA SEDDA

Supervisor:

Pr. Roberto
CAPUZZO-DOLCETTA

*A thesis submitted in fulfilment of the requirements
for the degree of Doctor of Philosophy*

in

ASTRONOMIA

December 2013

University of Rome “Sapienza”

Abstract

Facoltà di Scienze Matematiche, Fisiche e Naturali

Dipartimento di Fisica

Doctor of Philosophy

The role of dynamical friction in the formation of Compact Massive Objects

by Manuel ARCA SEDDA

In this thesis it has been treated the physical process called dynamical friction, which is responsible for the decay of massive objects traveling in systems composed by lighter particles, such as a Globular Cluster traveling in a Galaxy or massive stars moving in stellar systems. After a careful validation, the treatment it has been applied to real astrophysical objects on different scales. On small scales, it has been provided a study on the possible formation of Intermediate Mass Black Holes in Globular Clusters, as results of the decaying and merging of massive stars within the center of the clusters. Considering larger scales, it has been studied the evolution of the Globular Cluster System belonging to the dwarf spheroidal galaxy known as Fornax, giving a possible solution to the so-called "Fornax timing problem" and providing a wide set of initial condition for the clusters which allows to predict with good approximation their observed positions. Moreover, it has been studied the formation in the center of galaxies of dense, massive clusters, commonly referred as Nuclear Star Clusters. In particular, the work made here is based on the so-called "dry merger scenario", in which this central super-cluster has been formed by the merging of decaying Globular Clusters. Using statistical and analytical arguments, it has been possible to provide scaling laws, which connects the Nuclear Star Cluster mass with the host global properties, in excellent agreement with observed scaling laws. In the last part of the thesis, it has been studied the problem of the lacking of Nuclear Star Clusters in galaxies whose masses are above ten billion of solar masses. Using a wide set of direct N-body simulations, it has been demonstrated that the tidal effects induced by a central Super Massive Black Holes could leads to the total disruption of the building blocks of the central super clusters, i.e. the Globular Clusters, suppressing, or even preventing at all, the formation of a Nuclear Star Clusters.

Abstract	i
1 Introduction	1
2 Dynamical friction	6
2.1 A new method for the evaluation of the dynamical friction term	6
2.2 Calibration by means of N -body simulation	11
2.2.1 Sampling effects	13
2.2.2 Determination of the free parameters in the one-body scheme . . .	15
2.3 An estimation of the dynamical friction timescale	17
2.3.1 Dynamical friction dependence on the test mass	22
2.3.2 A fitting formula for dynamical friction decay time	24
2.3.3 A straightforward application to a galactic satellite population sinking	25
2.3.4 Massive object stalling in core galaxies	26
2.4 The role of a central black hole in dynamical friction	29
2.5 Summary	32
3 Dynamical friction applications in astrophysical context	34
3.1 Intermediate Mass Black Holes in Globular Clusters	34
3.1.1 Sampling method and stars mass loss	35
3.1.2 Results	38
3.1.3 Testing IMBH formation through N -body simulations.	41
3.1.4 The Spitzer instability	45
3.1.5 Spitzer instability with a mass spectrum	47
3.1.6 Summary	51
3.2 A possible solution to the Fornax dwarf spheroidal timing problem	53
3.2.1 The Fornax dSph model	54
3.2.2 Initial conditions for the Fornax Globular Cluster System	56
3.2.3 Semi analytical simulations	58
3.2.4 Nbody simulations	61

3.2.5	Self interaction effects	62
3.2.6	Summary	63
4	The formation of Nuclear Star Clusters	65
4.1	NSC formation hypothesis: Globular Clusters infall scenario	68
4.1.1	Data sample	69
4.1.2	Modeling the host galaxy	69
4.2	Testing the dry merger scenario	73
4.2.1	Analytical approach	73
4.2.2	Statistical approach	77
4.2.3	Results	79
4.3	Scaling laws	81
4.3.1	$M_{NSC} - M_G$ relation	83
4.3.2	$M_{NSC} - M_B$ relation	86
4.3.3	$M_{NSC} - \sigma_G$ relation	86
4.4	Tidal disruption effects	88
4.5	Summary	95
5	The lack of high mass NSCs	98
5.1	Modeling the host galaxies and the cluster	99
5.2	Runs analysis	101
5.2.1	Cluster analysis	105
5.3	Caveats	111
5.4	Analytical considerations about the tidal radius evolution.	112
5.5	Summary	114
6	Discussion and conclusions	116
A	Dynamical friction integral convergence	120
B	Dynamical friction mass dependences	125
C	Sampling self consistent models for N-body simulations	128
C.1	Introduction	128
C.2	N -body system: global properties	129
C.3	Sampling strategy	131
C.4	Well-known density profiles	134
C.5	User utilities	135
C.5.1	Input parameters	135
C.5.2	Compiling and running the code	137
C.6	Tests and comparison	138
C.6.1	Plummer profile	139
C.6.2	Dehnen profiles	140
C.6.3	NFW profile	145
C.6.4	King profile	145

D The formation of the Milky Way Nuclear Star Cluster	148
D.1 The Milky Way galaxy	148
D.2 The formation of the Milky Way Nuclear Star Cluster	151
D.3 Previous works	151
D.4 A new, improved simulation of the Milky Way NSC	152
D.5 Summary	160
Bibliography	174

Alla mia famiglia, con me in ogni momento

CHAPTER 1

INTRODUCTION

Gravitational encounters between a massive body and a sea of light particles, such as a globular cluster moving in a galaxy, lead to a braking of the motion of the satellite widely known as dynamical friction (df).

This effect was firstly studied by Chandrasekhar and Von Neumann and a classical treatment exist to deal with this physical problem [27, 28].

In the astrophysical context, dynamical friction plays a crucial role in several fields: from large scales, since it drives the motion of galaxies in galaxy clusters, to smaller scales, due to the consequences of this mechanism on the motion of Black Holes (BHs) and star clusters in galaxies.

The satellite mass and its orbits, together with the geometry of the system in which it moves, are relevant in the determination of the braking effect. As an example, the geometry of the galaxy plays a crucial role leading to significantly different efficiency in spherical, axisymmetric and triaxial galaxies [16, 26, 92]. Moreover, the presence of a cusp in the background matter distribution could affect it [81, 92].

Actually, the existence of ‘cuspy’ density profiles of matter in galaxies has been argued since the last 20 years as a result of high resolution observations by the Hubble Space Telescope.

Many galaxies exhibit, indeed, a luminosity profile steeply increasing in the inner region toward their geometrical center, at least within the telescope resolution. In general, these luminosity profiles are well described by the so called Sérsic profiles [104]:

$$\ln I(R) = \ln I(0) - kR^{1/n}, \quad (1.1)$$

where R is the projected radial coordinate and $n > 0$, called the ‘Sérsic index’, determines the steepness of the profile. Brighter galaxies have larger best fit values of n ($n = 4$ corresponds to the γ -models [34] often used to fit giant ellipticals profiles); dwarf galaxies are characterized by smaller values of n .

Defining Γ as the logarithmic derivative of the luminosity profile:

$$\Gamma(R) = \frac{d \ln I}{d \ln R}, \quad (1.2)$$

the brightness profile slope of Sersic’s model is

$$\frac{dI}{dR} = \frac{I(R)}{R} \Gamma(R) = -I(R) \frac{k}{n} R^{(1-n)/n}, \quad (1.3)$$

so that $n > 1$ correspond to a ‘true’ cuspidal central brightness profile ($dI/dR \xrightarrow{R \rightarrow 0} -\infty$).

In the innermost (3 – 10 arcsec) regions of early type galaxies, the luminosity profile is well approximated by the Nuker law [121]:

$$I(R) = 2^{(\beta-\delta)/\alpha} I_b \left(\frac{R_b}{R} \right)^\delta \left[1 + \left(\frac{R}{R_b} \right)^\alpha \right]^{(\delta-\beta)/\alpha}, \quad (1.4)$$

where α , β , δ , R_b , and I_b are parameters to be calibrated with the observations.

The value of Γ around $R = 0$ allows the distinction of galaxies into two main classes [72, 81]:

- “*core galaxies*” ($\Gamma < 0.3$), showing a shallow cusp, which are mainly bright ellipticals in slow rotation, weakly triaxial and anisotropic in the phase space;
- “*power-law galaxies*” ($\Gamma > 0.5$), fainter than the core galaxies, almost isotropic and without a clear nucleus.

As shown by [72], the distribution is not exactly bimodal, since there is also a small population of galaxies with $0.3 < \Gamma < 0.5$.

Considering a reasonable mass-to-light ratio, a suitable family of spatial density profiles exists which well reproduce observed luminosity profiles, the so called γ -models [35]. We will discuss this kind of density profile deeply in Appendix A.

Of course, the real existence of cuspy (infinite density) innermost profiles for galaxies is just an extrapolation within the resolution limit of the behaviour of the observed distribution. As a matter of fact, also finite central density profiles as the Einasto models [39] well fit the observations down to the resolution limit. Actually, steeply decreasing profiles cannot be distinguished from real cuspy profiles out of the resolution limit.

On a theoretical point of view, numerical simulations of standard Cold Dark Matter (CDM) halo dynamics predict density profiles with $\rho \propto r^{-1}$ at small radii [85]; this prediction does not depend on particular cosmogonies or choice of initial conditions [63, 64], or on the specific form of the dark matter power spectrum [41]. Adding a dissipative baryon component makes mass distributions even more concentrated [18, 37]. Anyway, there is not a general consensus about the real existence of a cusp in the dark matter distribution, because it could be an artefact of the finite resolution of the N -body simulations.

An important additional point is that many (if not all) galaxies host at their center a Compact Massive Object, identified with a Super Massive Black Hole (SMBH) in massive galaxies (well above $10^{11}M_{\odot}$), or a Nuclear Star Cluster (NSC) in lower mass galaxies (around or below 10^9M_{\odot}). There are quite a few cases of galaxies where an SMBH coexists with a NSC.

The presence of such objects in the galactic center could be important in the determination of the braking effect.

Despite the importance to develop a theory of dynamical friction which deals well with cuspy density profiles, its correct treatment is important also in the study of astrophysical problems on very different scales.

In fact, df determines the decay of Super Massive Black Holes (SMBHs) in remnants of merged galaxies [83] that leads to the formation of SMBH binaries. As a consequence of gravitational wave emission, the binary shrinks until the merging of the two components [102]. In a non spherical merging, the final SMBH gain a kick that pull the object out of its original position [13], and the kicked BH could escape from the galaxy [21]. However, for small kick velocity, the recoiled objects tends to decay again into the galactic centre because of dynamical friction [58, 118]. Also the commonly observed presence of a giant elliptical galaxy at the center of galaxy clusters is due to df which action is stronger on more massive galaxies.

The effect of df in a galaxy depends both on the orbit of the test object and on the local phase space density along its orbital path. Regarding the overall matter distribution of the host galaxy, the lack of symmetry in the potential favours df braking because of the loss of angular momentum conservation and the consequent closer approach of the massive objects to the central denser region of the galaxy [92]. Moreover, it is known that the central galactic regions are those of highest phase space density (as measured by the proxy ρ/σ^3) so to make low eccentricity orbits as the ones suffering most of df deceleration. Consequently, central regions of cuspy galaxies with a triaxial shape over the large spatial scale are candidates to be sites of strongly enhanced df decay, so that its correct evaluation turns out to be of paramount importance.

Since there is growing evidence for cusps in the matter distribution of real galaxies, our aim is to give more reliable, quantitative estimates of the dynamical friction effect on massive objects moving in the vicinity of such cusps. This work could be seen as an extension of the work made so far by Chandrasekhar, which instead gives only poorly accurated estimations of the braking effects in such problems.

To reach our aims we use a semi-analytical approach, deeply described in Chap.2, based on the numerical evaluation of the equation of motion for the massive satellite, and direct N-body simulations in which the massive body moves in a background system sampled with an optimal number of particles.

The first goal of this Ph.D. research has been to develop a new treatment for df from a theoretical and numerical point of view to partially extend the Chandrasekhar treatment and make it usable in many astrophysical context.

After a careful validation of our approach, the natural continuation of this work has been to investigate how it works in dealing with astrophysical situations.

Firstly, the dynamical decay of massive stars in globular clusters, as a consequence of gravitational encounters, has been studied. The basic idea was to model the interactions between stars with different masses with the dynamical friction treatment I developed; in this framework, the mass segregation process is a direct consequence of the action of dynamical friction mechanism.

Using statistical and analytical arguments, and taking advantage of very precise N -body simulations, estimations of accumulated masses in the clusters centers have been compared with mass excesses found by observations.

In Sec.3.1 it will be shown the excellent agreement found between our predictions and results given in literature.

The packaging of massive stars in a fairly small, central region of globular clusters has also an interesting consequence, the possible formation of Intermediate Mass Black Holes.

I investigated this framework also from a theoretical point of view, trying to extend the so-called “Spitzer instability” to a mass distribution which predicts the formation of a sub-cluster of massive stars, gravitationally decoupled from the lighter particles placed at the center of the cluster.

Moreover, considering larger length and mass scales, I studied the Fornax globular cluster system problem. Fornax dwarf spheroidal, in fact, hosts 5 globular clusters (GCs) which, considering the classical dynamical friction treatment, should be completely decayed into the Fornax center.

In Sec.3.2, using N -body and semi-analytical simulations it will be shown that this “puzzle” could be solved considering detailed and reliable treatment of the dynamical friction process developed in this work.

Later, the work moved toward the study of the formation of very dense and massive star clusters placed at the center of many galaxies, called Nuclear Star Clusters (NSCs). As it will be shown in Chap.4, my work would give a theoretical effort to the so called “dry merger scenario”, in which NSCs were formed by subsequent merging of decaying clusters.

Using analytical and statistical arguments, I developed scaling laws connecting NSCs masses with the hosts properties which are in excellent agreement with observations.

The results presented here would highlight how a careful treatment of the dynamical friction process has interesting consequences on many astrophysical frameworks and on very different scales.

The last part of this thesis is devoted to the study of the lacking of NSCs in galaxies with masses above $\sim 10^{11}M_{\odot}$. Using analytical arguments and a wide set of N -body simulations, I studied the effects of tidal forces exerted by a central, pre-existing SMBH on the building blocks of the NSC, i.e. globular clusters. As it will be shown in Chap.5, the results obtained indicate that when the SMBH mass exceeds 10^8M_{\odot} , corresponding to galaxies with masses above $10^{11}M_{\odot}$, tidal forces are strong enough to disrupt the infalling cluster well before it could reach the galaxy center.

2.1 A new method for the evaluation of the dynamical friction term

In order to explain the df process we recall here the two body problem, showing that if one body is massive than the other, it suffers a braking called dynamical friction.

Letting M and m the mass of the test particle and of the generic field star, respectively, and identifying with \mathbf{v}_M and \mathbf{v}_m their velocities, given also the impact parameter vector \mathbf{b} (see Fig.2.1), the 2-body hyperbolic interaction between the test mass and the field star induces the velocity variation for the test mass:

$$\Delta \mathbf{v}_M = - \left(\frac{m}{m+M} \right) 2V \left[1 + \frac{b^2 V^4}{G^2 (m+M)^2} \right]^{-1} \frac{\mathbf{V}}{V}, \quad (2.1)$$

where G is the Newton's gravitational constant and $\mathbf{V} = \mathbf{v}_M - \mathbf{v}_m$ is the 2-body relative velocity.

The effective time duration of such a 2-body interaction is the *fly-by* time, assumed to be $\Delta t \sim 2b/V$, so that the mean deceleration due to the single encounter in the direction of the initial motion is well approximated by $\Delta \mathbf{v}_M / \Delta t$. Consequently, the global deceleration effect is simply given by an integral over the whole distribution of scatterers:

$$\left(\frac{d\mathbf{v}_M}{dt} \right)_{df} = \int \frac{\Delta \mathbf{v}_M}{\Delta t} dN, \quad (2.2)$$

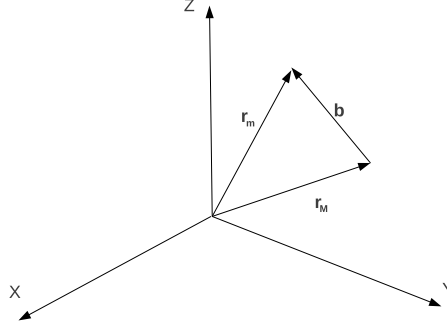


Figure 2.1: The symbol \mathbf{r}_M indicates the position vector of the test particle of mass M , while \mathbf{r}_m is the position of the field particle of mass m ; \mathbf{b} indicates the impact vector pointing to the field particle.

where dN is the (infinitesimal) number of field stars in the elementary space volume centered in $\mathbf{r}_m = \mathbf{r}_M + \mathbf{b}$ having velocities in the (infinitesimal) velocity volume centered in \mathbf{v}_m . Once that the field stars' steady state distribution function (hereafter DF) is known as $f(\mathbf{r}_m, \mathbf{v}_m)$, dN is written as:

$$dN = f(\mathbf{r}_m, \mathbf{v}_m) d^3\mathbf{v}_m d^3\mathbf{r}_m. \quad (2.3)$$

As a consequence, we can express the mean cumulative deceleration in Eq. 2.2 as:

$$\left(\frac{d\mathbf{v}_M}{dt} \right)_{\text{df}} = -\frac{m}{m+M} \iint f(\mathbf{r}_M + \mathbf{b}, \mathbf{v}_m) \frac{V}{b} \frac{\mathbf{V}}{1 + b^2 V^4 G^{-2} (M+m)^{-2}} d^3\mathbf{v}_m d^3\mathbf{b}, \quad (2.4)$$

where the integral is over the whole range of values of \mathbf{b} and \mathbf{v}_m allowed by self-consistency.

The integral in Eq. 2.4 is, in general, quite complicated; it can be simplified adopting the so called *local* approximation, that is the assumption of weighing encounters at any distance from the test object with the local density $\rho(\mathbf{r}_M)$ instead of the density of scatterers where they actually are. This, together with the further assumption of isotropy in phase space, leads to the much simpler expression:

$$\left(\frac{d\mathbf{v}_M}{dt} \right)_{\text{loc}} = -4\pi^2 G^2 (m+M) \ln \Lambda \rho(r_M, v_m \leq v_M) \frac{\mathbf{v}_M}{v_M^3}, \quad (2.5)$$

where $\ln \Lambda$ is the usual Coulomb's logarithm and $\rho(r_M, v_m \leq v_M)$ is the, local, mass density of field stars slower than the test particle, i.e.

$$\rho(r_M, v_m \leq v_M) = 4\pi \int_0^{v_M} v_m^2 f[v_m^2/2 + \phi(r_M)] dv_m, \quad (2.6)$$

where the DF is in the form $f(\mathbf{r}_m, \mathbf{v}_m) \equiv f(r_m, v_m) = f(E)$, where $E = v_m^2/2 + \Phi(r_m)$ is the field stars mechanical energy per unit mass.

Several authors (e.g. [113]) suggested that allowing a variation of the Coulomb logarithm, $\ln \Lambda$, may be important for a good determination of its orbital evolution. [67] derived an expression for $\ln \Lambda$ allowing the variation of the maximum impact parameter, b_{max} , and the $a_{90 \text{ deg}}$ parameter (the typical impact parameter for a 90 deg degrees deflection in a two body encounter). The effect of this variations on the orbits of massive body traveling in cuspy galaxies are deeply discuss in Just et al. [66].

Now, whenever the test particle is significantly off center with respect to the stellar system (star cluster, galaxy, etc.) where it moves, the local expression (Eq. 2.5) gives an acceptable approximation; on the contrary, it loses its validity in the neighbourhood of the host system center. In this case the local approximation is clearly an overestimate of the actual dynamical friction, because it corresponds to weighing the contribution of the gravitational encounters at any distance from the test particle not with the, correct, density of target stars at that distance but, rather, with the density of targets evaluated at the location of the test particle itself, that is maximum at the origin of any self-gravitating system. This overestimate is a particularly serious problem when dealing with cuspy galaxies, where the spatial density of stars *diverges* at the galactic center. This divergence may be partially cured by introducing an artificial spatial cut-off in the density distribution but this, of course, implies a relevant dependence of df on the choice of this radial cut-off.

We can illustrate better all this with the example of a DF as obtained using a γ model [35] around the central spatial cusp of a spherical galaxy, where the stellar density may indeed be represented as $\rho(r) \propto r^{-\gamma}$. As it is easily seen (see Appendix A), when $\gamma = 1$ the following expression for $\rho(r, v_m \leq v_M)$ in the high binding energy regime, i.e. around the galactic center, is obtained:

$$\rho(r, v_m \leq v_M) = \frac{4\pi}{3} A \frac{v_M^3}{(r/a) [(v_M^2/2)/(GM/a) + r/a]^{3/2}} \quad (2.7)$$

where A is the multiplicative constant in the expression of the DF (see Appendix A). The resulting local approximation (Eq. 2.5) for the df deceleration yields

$$\left(\frac{d\mathbf{v}_M}{dt}\right)_{loc} = -\frac{16\pi^3}{3}AG^2(m+M)\ln\Lambda\frac{\mathbf{v}_M}{(r/a)\left[(v_M^2/2)/(GM/a)+r/a\right]^{3/2}}. \quad (2.8)$$

If, in the denominator of Eq. 2.8, r/a and $(v_M^2/2)/(GM/a)$ go (contemporarily) to zero with same order of infinitesimal, the local df deceleration diverges as $(r/a)^{-2}$ (or, equivalently, $[v_M^2/(GM/a)]^{-2}$). This divergence is due to the local approximation, while the correct (Eq. 2.4) expression for the df deceleration *does not* diverge; on the contrary, df deceleration goes to zero for particles of very high binding energy (see Appendix A). Therefore the local approximation formula cannot be used to get astrophysically significant results when treating the motion of massive objects passing through (or close to) the center of a cuspy galaxy.

In Appendix A we show that the fully isotropic DFs of the Dehnen's gamma model lead to a df deceleration which is finite around the galactic central density cusps, while its local approximation is not. This convinces us of the need to use, instead of the wrong local approximation, the complete (Eq. 2.4) expression for the df.

Unfortunately, the integral in Eq. 2.4 is of overwhelming complexity, unless some simplifications are adopted. An intuitive, immediate, approximation comes from letting both $\mathbf{r}_M = 0$ and spatial isotropy (i.e. spherical symmetry) for the DF ($f(\mathbf{r}_m, \mathbf{v}_m) = f(r_m, \mathbf{v}_m)$) to get the simpler expression for the df deceleration:

$$\left(\frac{d\mathbf{v}_M}{dt}\right)_{cen} = -\frac{4\pi m}{m+M} \int_{b_{min}}^{b_{max}} \int f(b, \mathbf{v}_m) \frac{V}{1+b^2V^4G^{-2}(m+M)^{-2}} \mathbf{V} d^3\mathbf{v}_m b db, \quad (2.9)$$

where b_{min} and b_{max} are, respectively, the minimum and maximum impact parameters allowed. The lower minimum cannot be zero, because this would correspond to a front collision, i.e. to a radial relative motion which does not fulfil the basic condition of positive mechanical energy for the idealized 2-body encounter. On the other side, the upper limit, b_{max} , is, usually, chosen large enough to guarantee that the stellar density at distance b_{max} from the center is much smaller than in the neighbourhood of the test object.

For a huge set of DFs, the vector integral in Eq. 2.9 is both convergent (see Appendix A) and suited to a proper numerical integration.

The integration over field stars' velocities in Eq. 2.9 has done over the all interval allowed, i.e. limited to the central escape velocity.

Of course, the df evaluated this way gives a good result along the motion of the test mass in the neighbourhood of the galactic center but cannot be used on a larger spatial

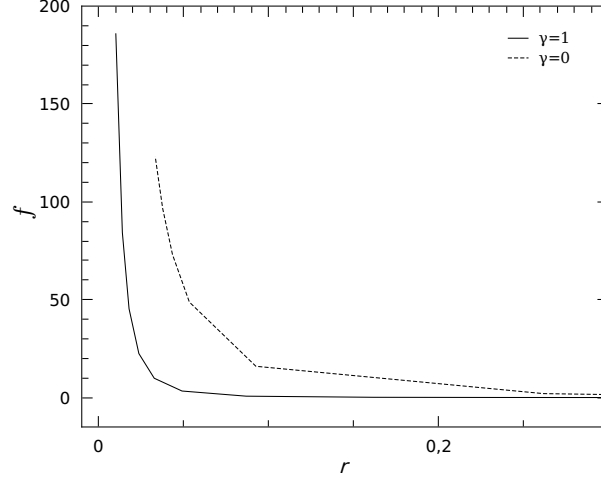


Figure 2.2: The ratio, f , of the dynamical friction acceleration evaluated with the local approximation formula in Eq. 2.5 to the central given by Eq. 2.9, in the cases $\gamma = 0$ (dashed line) and $\gamma = 1$ (solid line).

scale. Consequently, our choice was that of an interpolation between the ‘central’ df evaluation and the ‘local’ approximation, by mean of a proper interpolation formula of the type:

$$\left(\frac{d\mathbf{v}_M}{dt}\right)_{df} = p(r) \left(\frac{d\mathbf{v}_M}{dt}\right)_{cen} + [1 - p(r)] \left(\frac{d\mathbf{v}_M}{dt}\right)_{loc}, \quad (2.10)$$

where the interpolation function, $0 \leq p(r) \leq 1$, is assumed monotonically decreasing from $p(0) = 1$ outward. Within these constraints, the interpolation function is a priori arbitrary; the only way to tune it is through a careful comparison with N -body simulation of the df decay of massive objects under different initial conditions. Thanks to this comparison, we found that a good interpolation expression is $p(r) = e^{-r/r_{cr}}$ where r_{cr} is the size of the region of dominance, in the contribution to the df deceleration, of the central cusp. The actual r_{cr} values are determined in Sect. 2.2. It is relevant noting that although the exponential choice is not unique, the, simpler, linear interpolation can be excluded because our results shows that a linear function weights too much the central contribution, giving an unrealistically high deceleration.

The computation of the scattering integral in Eq. 2.9 presents numerical difficulties due to the singularity in the integrand. These difficulties can be overcome by using a proper cubature algorithm; in particular, we used DECUHR, an algorithm which combines an adaptive subdivision strategy with extrapolation [43].

In Fig. 2.2 it is evident the departure of the local df evaluated via Eq 2.5 respect to the central estimate given by Eq. 2.9.

We can note that, in the regime of very low or very high speed for the test particle and/or when its mass, M , is small, the above integration algorithm requires an exceedingly large number of iterations to reach convergence. In such cases, to speed up computations we looked for an appropriate approximation formula.

We actually found that the linear dependence of df on v_M is recovered, while at high velocities the dependence is a power law with a spectral index, α , that depends both on γ and on b_{min}

$$\alpha = \begin{cases} 2(\gamma - 1) & \text{if } b_{min} = 0, \\ -2 & \text{if } b_{min} > 0, \end{cases}$$

in the range $0 \leq \gamma \leq 2$.

2.2 Calibration by means of N -body simulation

A fully self consistent study of the dynamical friction caused by environment stars on the motion of a (massive) object (a star cluster or a galaxy as satellite of another galaxy) of mass M requires the numerical integration of an N -body problem where N_f particles sample the galactic field and N_M particles represent the massive star system ($N_f + N_M = N$). Of course, to have results of real astrophysical interest high resolution simulations are needed, which require both a large value of N_f and of N_M over a huge set of initial conditions.

The usage of realistic number of particles ($N > 10^{10}$) to simulate realistic astrophysical environments is something unfeasible at present, since the duration of each simulation would exceed years of computation. Using lower number of particles ($N \sim 10^6$), instead, it is possible to reach a good balance between precision and a reasonable computational time.

At the same time, moreover, it is possible to reduce significantly the computational time searching for a suitable method to solve the equations of motion of a single, massive object in a given external potential $\Phi(\mathbf{r})$ with the inclusion of a drag term given by Eq. 2.10. This is a dragged one-body problem.

In this work, we made a large set of N -body simulations, to compare with the numerical solution of the equation of motion of the massive object, in order to give an extensive analysis which allows to deduce results which are general enough.

The equations of motion to solve are, written as:

$$\ddot{\mathbf{r}}_M = \nabla\Phi(\mathbf{r}_M) + \left(\frac{d\mathbf{v}_M}{dt}\right)_{\text{df}}, \quad (2.11)$$

with the proper initial conditions. To solve this set of differential equations, we use a high precision 6th(7th) order Runge-Kutta-Nyström method with variable time step [44]. The time step size, Δt , was varied according to

$$\Delta t = \eta \min \left(\frac{|\mathbf{r}_M|}{|\dot{\mathbf{r}}_M|}, \frac{|\dot{\mathbf{r}}_M|}{|\ddot{\mathbf{r}}_M|} \right),$$

that, with the choice of $\eta = 0.01$, allows both a fast integration and an energy and angular momentum conservation at a fractionary 10^{-11} level (per time step).

We choose as units of mass and length the galactic mass and scale length of its density distribution, denoted by M_G and a . The further choice of setting the gravitational constant $G = 1$ leads to

$$T = \frac{a^{3/2}}{\sqrt{GM_G}} \quad (2.12)$$

as unit of time.

Once that the expression for the interpolation function, $p(r) = e^{-r/r_{cr}}$ cited in Sect. 2.1, is given, the free parameters in the semi-analytical evaluation of df are the scale length r_{cr} in $p(r)$, and the values for b_{min} and b_{max} in the local (Eq.2.5) and central (Eq.2.9) expressions of df deceleration.

We made several simulations using both constant and variable b_{max} , to conclude that the advantages in accuracy given by a somewhat arbitrary variation in b_{max} are not such to overcome the simplicity of the choice of b_{max} set at the constant value R , the assumed radius of the spherical galaxy. On the other side, due to its undoubted relevance in a cuspy galaxy, we let b_{min} to vary. Also the length scale r_{cr} , which determines the size of the region of dominance of the central to the local df term, is allowed to vary.

An unambiguous way to select their optimal values is through a comparison of results got via the integration of Eq. 2.11 at varying the pair (r_{cr}, b_{min}) and the, supposedly ‘exact’, results coming from the integration of motion of a single, point-like, massive object of mass M interacting with N bodies of mass m representing the galactic field. At this scope we used our direct summation, high precision, 6th order Hermite’s integrator with individual block time steps called HiGPUs [25]. HiGPUs runs on composite platforms where the host governs the activity of Graphic Processing Units (GPUs) as computing accelerators. The code exploits all the potential of such architectures, since it uses at

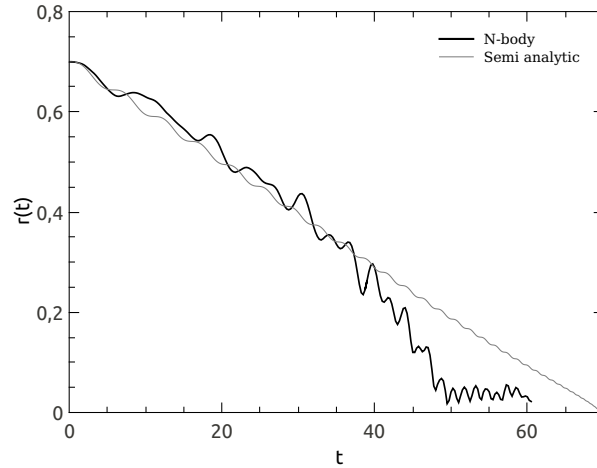


Figure 2.3: Time evolution of the galactocentric distance of an $M = 10^{-3}$ test mass on initially circular orbit in the $\gamma = 1$ model.

the same time Message Passing (MPI), Open Multiprocessing (Open MP) on the host CPUs and Compute Unified Device Architecture (CUDA) or Open Computing Language (OpenCL) on the GPUs.

2.2.1 Sampling effects

In order to make an optimal selection of the two free parameters needed to set the df drag term in the one-body scheme, we perform an adequate set of direct N -body integrations, as explained above. To calibrate these parameters it is, of course, important to be sure of the reliability of such N -body simulations. The main problem, at this regard, is the sampling. Actually the N -body sampling acts on both small (‘granularity’) and large (deviation from spherical symmetry) scale. This makes initially circular orbits evolve into precessing ellipses of moderate eccentricity (see Fig. 2.3). This is one of the, unavoidable, causes of departure of the decay times in the N case from the semi analytical case. To reduce spurious sampling effects we tried to determine an acceptable threshold value of N above which fluctuations are kept small enough. To do this, we followed the orbital evolution of a particle of the same mass of the generic particle of the N -body representation of the galaxy, starting from initial conditions corresponding to the extreme (in eccentricity) cases of circular and radial orbits.

As it can be seen from Figs. 2.4 and 2.5, in both of these extreme cases the quadratic deviation of the actual trajectory computed in a finite N -body representation of a Dehnen’s $\gamma = 1$ galactic density law respect to the ideal (infinite N) circular and radial trajectories decreases significantly when N is in the range $10^5 < N < 10^6$. Actually, the reduction of fluctuations passing from $N = 131,072$ to $N = 524,288$ suggested us to choose this

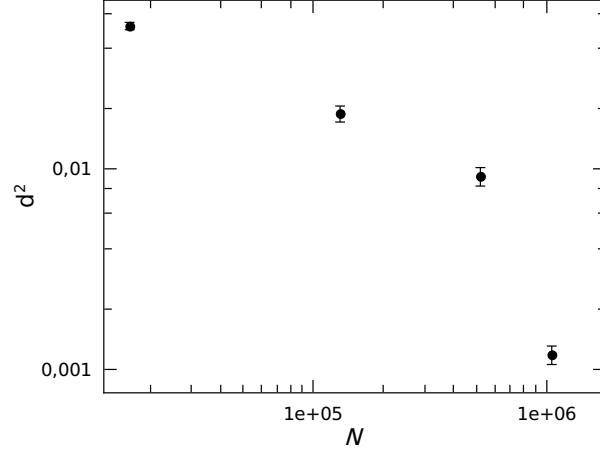


Figure 2.4: *The squared, fractional departure of the distance to the center of a test particle of same mass of the field particles along its motion as integrated in an N -body sampled $\gamma = 1$ model respect to the ideal radial orbit.*

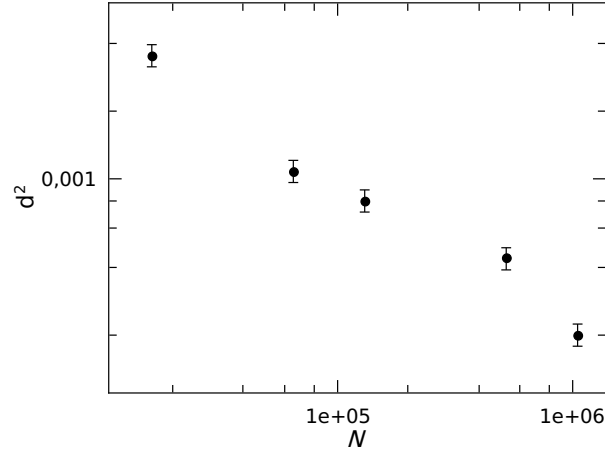


Figure 2.5: *The squared, fractional departure of the distance to the center of a test particle of same mass of the field particles along its motion as integrated in an N -body sampled $\gamma = 1$ model respect to the ideal circular orbit.*

latter value as a good compromise in giving an acceptable smoothness at a reasonable computational cost.

Once the optimal number of particles has been set, we perform several simulations to check the accuracy of the N -body code. In particular, we verified that over the typical timescales of our simulations, the code preserve the total energy of the system with a relative error down to 10^{-8} ; moreover, it has been checked that the simulated systems do not expand or contract significantly during their evolution, as a guaranty of both correct choice of initial conditions and quality of time integration.

System stability has been verified also looking at the lagrangian radii and density profiles, which remain substantially constant during the whole orbital evolution of the satellite.

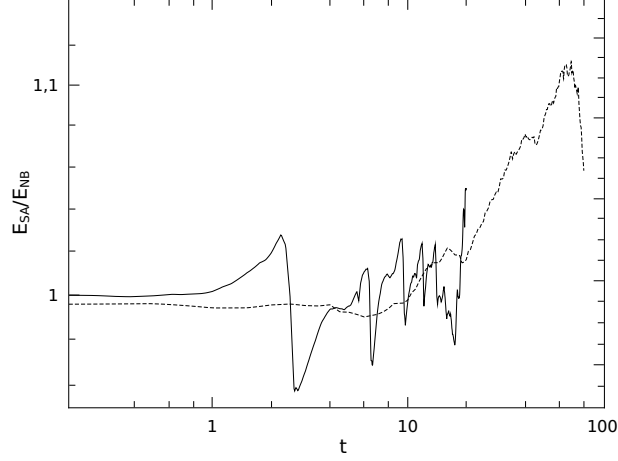


Figure 2.6: *Time evolution of the ratio between the test particle energy evaluated in the one-body, semi-analytical case and that computed in the N -body sampled galaxy for a radial (solid line) and a circular orbit (dotted line).*

2.2.2 Determination of the free parameters in the one-body scheme

Once determined the threshold in N over which an acceptable fit between the N -body test object integration and that obtained by the solution of the single body motion in the external smooth galactic field, the following step is that of getting reliable pairs of values (r_{cr}, b_{min}) in dependence on γ . We proceeded this way: i) perform N -body integrations of the motion of a massive point mass, starting from an initial distance r_{cr} from the galactic center with the local circular velocity; ii) perform a similar time evolution in the simplified one-body scheme of Eq. 2.11 where the df dissipation term is given in the standard local approximation form; iii) reduce r_{cr} until the difference between the orbit self-consistently evaluated in i) and that obtained as explained in ii) changes significantly; iv) take this latter value of r_{cr} as optimal value for the $p(r)$ function in the interpolation formula (Eq.2.10). To do this we set $M = 10^{-3}$ as value of the test particle mass.

An idea of the quality of this fitting procedure to determine the pair (r_{cr}, b_{min}) in getting the results of interest here is given by Fig. 2.6. It reports the ratio between the test particle orbital energy evaluated in the one-body approximation with the df term written in the complete (Eq. 2.10) form to that computed in the full N -body simulation. As it is seen, the variations are within 4% over 20 time units in the radial case and within 2% in the circular case over the same time interval. In the circular case we extended the comparison up to 80 time units, finding a relative maximum of the fractional difference of about 12 %.

We found that the greater the γ the smaller the r_{cr} , as expected. Actually, higher values of γ represent steeper profiles toward the center, with a large part of the total mass

Table 2.1

The critical radius and the radius that encloses 10% of the total mass. The last column reports the relative variation between the two.

γ	r_{cr}	$r(0.1)$	$\Delta r/r$ %
0.5	0.7	0.661	0.059
1.0	0.5	0.463	0.080
1.5	0.3	0.275	0.091

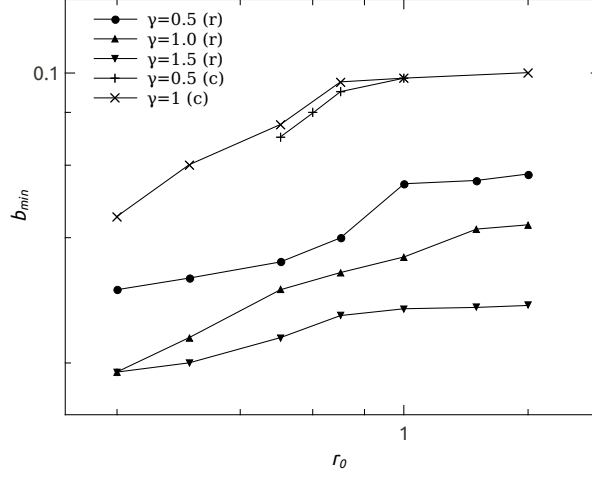


Figure 2.7: *Minimum impact parameter as a function of the initial galactocentric distance, for initially radial (r) and circular (c) orbits at various values of γ .*

enclosed within a relatively small radius. On the other side, less intuitive is the result of r_{cr} as very similar to the radius enclosing 10% of the mass of the system. A simple inversion of the mass-radius profile for Dehnen's models gives:

$$r(x_M) = \frac{x_M^{1/(3-\gamma)}}{1 - x_M^{1/(3-\gamma)}} \quad (2.13)$$

with $x_M = M(r)/M_G$. The value of $r(0.1)$ is found (see Tab.2.1) in good agreement with those of r_{cr} obtained in the way indicated above.

Once that the r_{cr} values are obtained for different γ , to get the best minimum impact parameter b_{min} we vary it in a set of one-body integrations covering circular and radial cases to find those best fitting results of direct N -body computations. In Fig. 2.7 we show the b_{min} selected this way, as a function of γ .

Table 2.2*Parameters defining the N -body $\gamma = 1/2$ simulations.*

r_0	$e = 0$	$e = 0.50$		$e = 1$	
	$M = 10^{-3}$	$M = 10^{-3}$	$M = 5 \times 10^{-4}$	$M = 10^{-3}$	$M = 5 \times 10^{-3}$
0.2	✓	—	—	✓	—
0.3	—	—	—	✓	—
0.31	—	—	—	—	—
0.5	—	—	—	✓	—
0.7	—	—	—	✓	—
0.8	—	—	—	—	—
1.0	—	—	—	✓	—
1.44	—	—	—	—	—
1.5	—	—	—	✓	—
1.67	—	—	—	—	—
2.0	—	—	—	✓	—

In this Table the ✓ symbol indicates the actually exploited values for the initial galactocentric distance (r_0), eccentricity (e), and satellite mass (M) in the N -body simulations performed.

2.3 An estimation of the dynamical friction timescale

The main scope of this part of my work was to obtain reliable estimates of the role of dynamical friction in cuspy density profiles, as explained before.

This aim has been reached by means of both direct numerical integrations of the motion of a massive test particle in an N -body representation of the host cuspy profiles and of the simpler, and much faster, one-body representation given by Eq. 2.11 together with Eqs. 2.5, 2.9, and 2.10.

In Tables 2.2, 2.3, and 2.4 the fundamental data of the whole set of N -body simulations performed are given.

Using these N -body simulations as reference, the quality of the one-body treatment is given in Figs. 2.8, 2.9, 2.10, and 2.11, where the time evolution of the test mass galactocentric distance is reported.

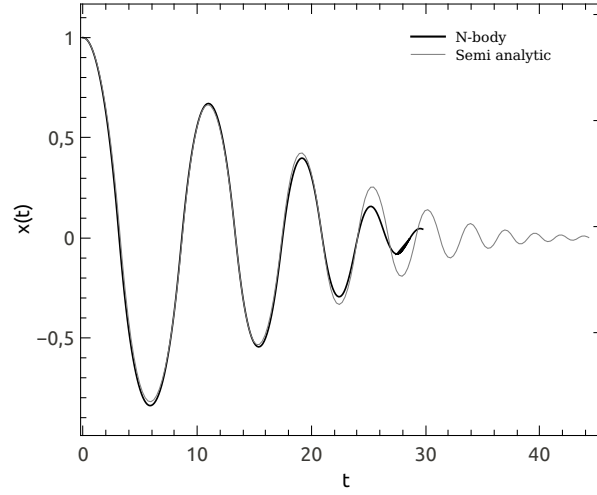


Figure 2.8: *Damped oscillations along the x axis for the test object with mass $M = 10^{-3}$ in the $\gamma = 1$ model. The darker line refers to the N -body simulation, while the grey line to the semi analytical.*

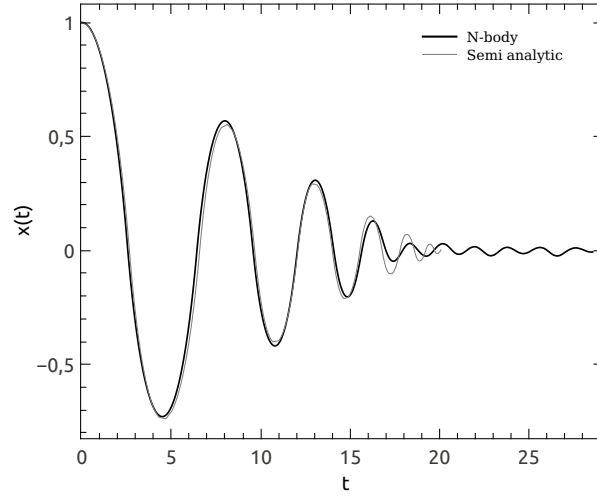


Figure 2.9: *As in Fig.2.8, but for the model with $\gamma = 1/2$.*

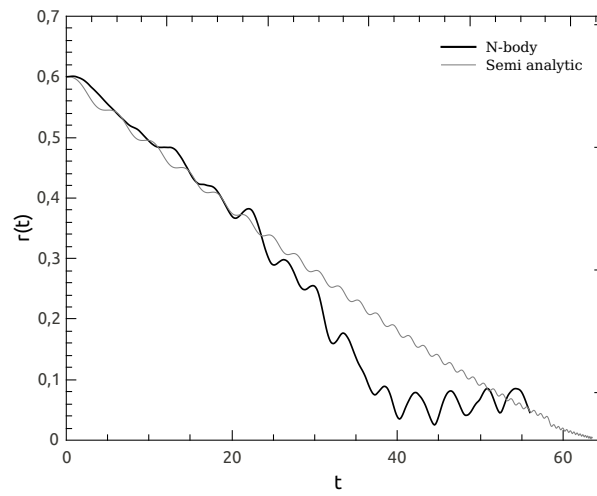


Figure 2.10: *Time evolution of the galactocentric distance of an $M = 10^{-3}$ test mass on initially circular orbit in the $\gamma = 1/2$ model.*

Table 2.3*Parameters defining the N -body $\gamma = 1$ simulations.*

r_0	$e = 0$	$e = 0.50$		$e = 1$	
	$M = 10^{-3}$	$M = 10^{-3}$	$M = 5 \times 10^{-4}$	$M = 10^{-3}$	$M = 5 \times 10^{-3}$
0.2	✓	✓	✓	✓	✓
0.3	✓	—	—	✓	✓
0.31	—	—	—	✓	—
0.5	✓	✓	✓	✓	✓
0.7	✓	—	✓	✓	✓
0.8	—	—	—	✓	—
1.0	✓	✓	✓	✓	✓
1.44	—	✓	—	✓	—
1.5	—	—	—	✓	✓
1.67	—	—	—	✓	—
2.0	—	—	—	✓	—

*All symbols as in Table 2.2.***Table 2.4***Parameters defining the N -body $\gamma = 3/2$ simulations.*

r_0	$e = 0$	$e = 0.50$		$e = 1$	
	$M = 10^{-3}$	$M = 10^{-3}$	$M = 5 \times 10^{-4}$	$M = 10^{-3}$	$M = 5 \times 10^{-3}$
0.2	✓	—	—	✓	—
0.3	✓	—	—	✓	—
0.31	—	—	—	—	—
0.5	✓	—	✓	✓	—
0.7	—	—	—	✓	—
0.8	—	—	—	—	—
1.0	—	—	—	✓	—
1.44	—	—	—	—	—
1.5	—	—	—	—	—
1.67	—	—	—	—	—
2.0	—	—	—	✓	—

All symbols as in Table 2.2.

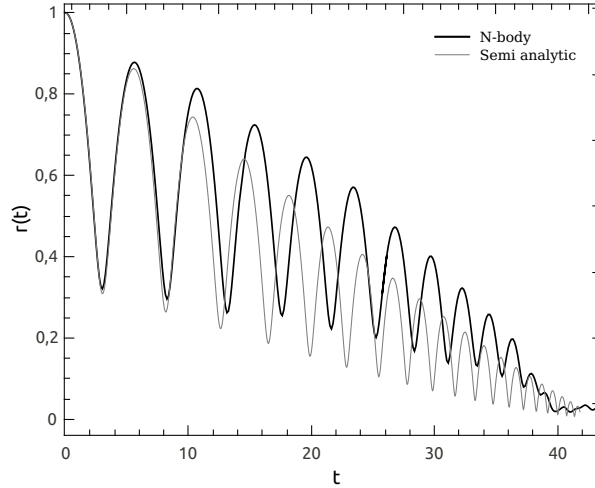


Figure 2.11: Same as in Fig. 2.10, but for an eccentric orbit with $e = 0.5$.

The role of the geometrical shape of the orbit is evident in Fig. 2.12, which shows the energy decay of the test mass for different initial eccentricities at fixed initial orbital energy. As expected, circular ($e = 0$) orbits decay slower than radial ($e = 1$), while orbits with $e = 0.5$ have decay time between these two extreme cases. We also note that, for higher initial orbital energies, the decay time of the $e = 0.5$ orbit approaches that of the circular orbits, indicating a clear non-linearity of the decay time with e in this high energy regime.

Actually, the most important astrophysical parameter that can be inferred in this framework is the dynamical friction decay time, τ_{df} , which we define as the time needed to reduce the test particle orbital energy to $E(\tau_{\text{df}}) = \Phi(5 \times 10^{-3}a)$. A correct evaluation of this time, which depends on both small and large scale characteristics of the galaxy where the test mass moves, as well on the test particle mass, is crucial in determining the actual role of dynamical friction in carrying matter toward the center of galaxies with the consequent, relevant, astrophysical implications.

Fig. 2.13 shows the τ_{df} dependence on the initial radial distance of circular and radial orbits in the $\gamma = 1$ model. The relations are two power laws with a slightly different slope. This is evident again in Fig. 2.14 where we compare τ_{df} for circular and radial orbits with same initial energy.

Consider both circular and radial trajectories of same apocenter allow us to obtain an upper and lower limit, respectively, for decay time of any orbit at fixed position but different velocity. Simulating orbits with same initial energy, instead, we can study the efficiency of df mechanism with respect to the shape of the orbit.

The dynamical friction time depends, obviously, on the model considered: the steeper the density profile (large γ) the shorter the decay time. This is clear in Fig. 2.15, which

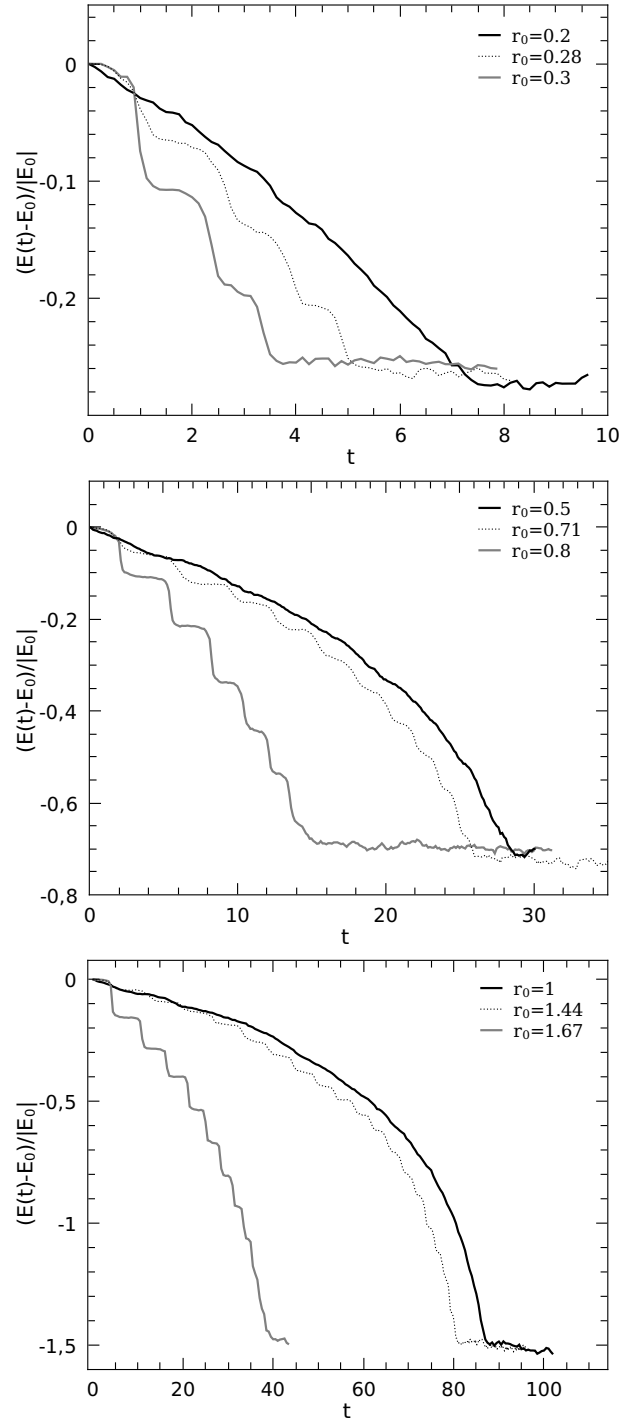


Figure 2.12: Time evolution of the fractional variation of the test particle energy in the circular ($e = 0$, solid black line), radial ($e = 1$, dashed line) and an eccentric ($e = 0.5$, grey line) cases of same initial energy, $E(0)$, in the N -body sampled, $\gamma = 1$, galaxy. The r_0 values refer to the initial distances of the test particle from the galactic center.

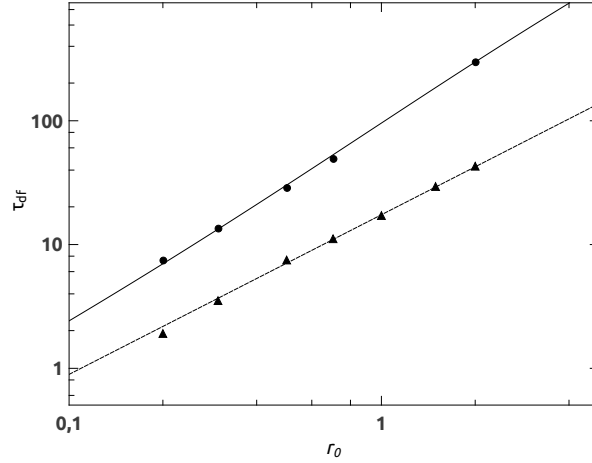


Figure 2.13: *Dynamical friction decay time vs. initial galactocentric distance for circular (filled circles) and radial (triangles) orbits in the $\gamma = 1$ model.*

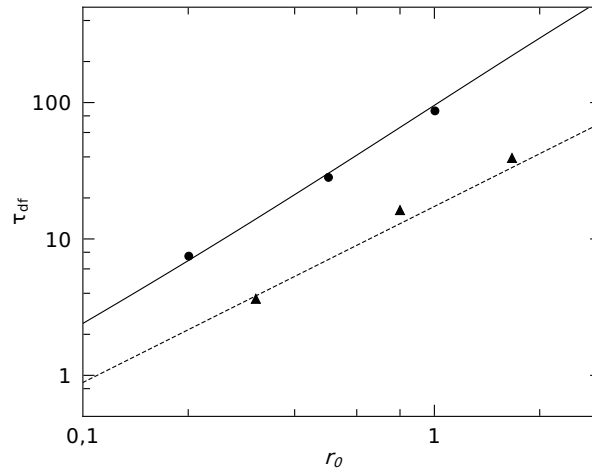


Figure 2.14: *As in Fig. 2.13, limiting the comparison to pair of orbits of same initial energy, $E(0)$.*

shows how increasing γ of a factor 3 (from $\gamma = 1/2$ to $\gamma = 3/2$), the decay time decreases by almost the same factor.

2.3.1 Dynamical friction dependence on the test mass

Beside the dependence from initial position, eccentricity and model, another important parameter that affect the dynamical friction effect is the mass of the satellite. This dependence deserves some considerations. Actually, it is generally assumed a *direct*, linear, proportionality of the dynamical friction braking deceleration to the test mass, M . This comes, in Eq. 2.4, by the contemporary assumption $m \ll M$ and $(b^2 V^4)/(G^2(m + M)^2) \gg 1$. The opposite limit $(b^2 V^4)/(G^2(m + M)^2) \ll 1$ would lead to an *inverse* linear proportionality. So it is logically inferred that performing the integrals in Eq. 2.4

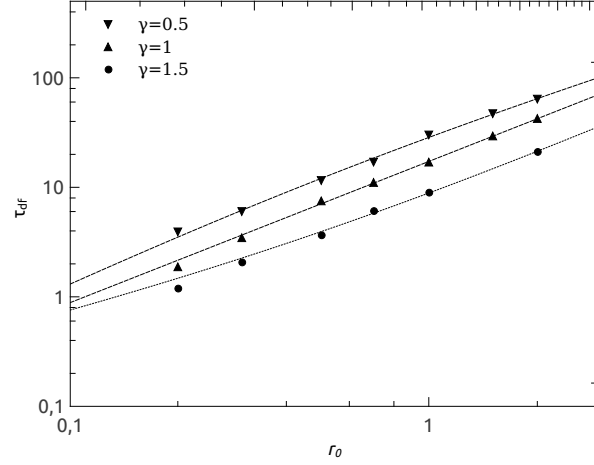


Figure 2.15: *Dynamical friction decay time vs initial galactocentric distance for radial orbits in three different γ models.*

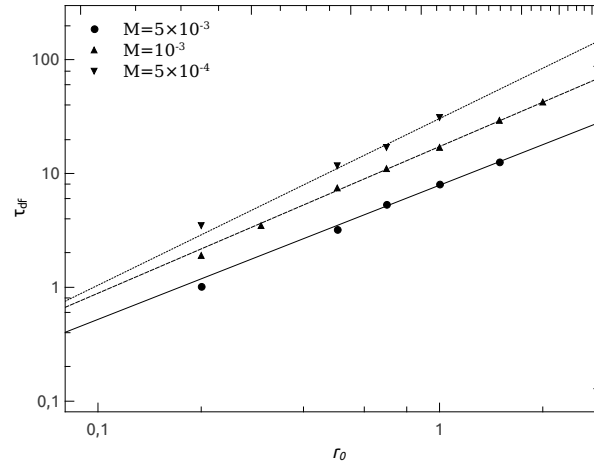


Figure 2.16: *Dynamical friction decay time vs initial galactocentric distance for radial orbits given three different values of the test particle mass, as labeled.*

over the whole integration ranges lead to a dependence on M^α with $-1 < \alpha < 1$, even taking also into account a possible dependence of the integration limits on m and M .

We refer to Appendix B for details.

While it is confirmed that a higher mass of the test object leads to a shorter decay time (see Fig. 2.16) we see that, by varying the satellite mass in the range $[5 \times 10^{-5}, 5 \times 10^{-3}]$, the relation between τ_{df} and M is shallower:

$$\tau_{df} \propto M^{-0.67 \pm 0.1}, \quad (2.14)$$

as obtained by a least square fit to data of Fig. 2.17, coming from direct N -body integrations and confirmed by the simplified one-body scheme.

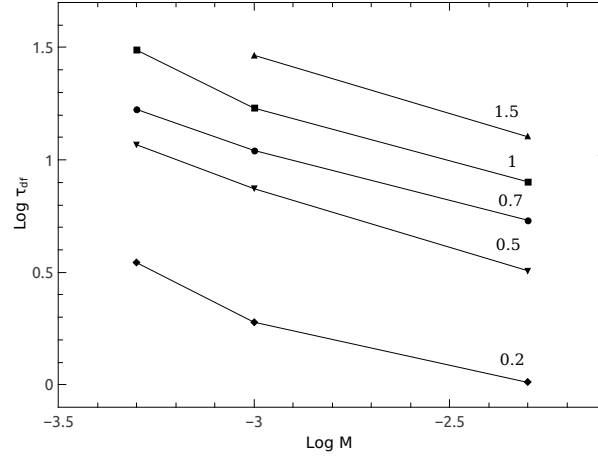


Figure 2.17: Decay time as function of the test particle mass ($M = 5 \times 10^{-4}, 10^{-3}, 5 \times 10^{-3}$) for initially radial orbits at different initial distances, as labeled.

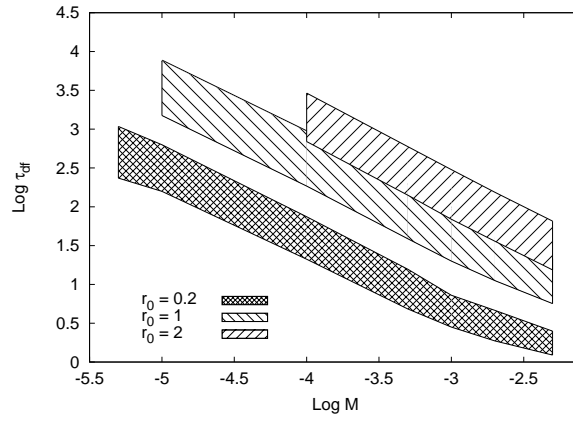


Figure 2.18: Decay time in function of the test mass starting its motion from three different initial galactocentric distances in a $\gamma = 1$ model. Each region is delimited by an upper line which refers to circular and a lower boundary defined by radial orbits. The decay times for all the other values of orbital eccentricity fall within these two boundaries.

Assuming the minimum impact parameter independent of the test mass, we performed semi analytical simulations in a wide range of masses $[10^{-5}, 5 \times 10^{-3}]$ setting the initial position r_0 to the values 0.2, 1 and 2 for initially circular and radial orbits, finding that the decay time-mass relation depends strongly on the starting position of the satellite (see Fig.2.18), as expected.

2.3.2 A fitting formula for dynamical friction decay time

A deep analysis of all the simulations done allowed us to obtain a useful analytical approximation to τ_{df} in dependence on the relevant parameters, as

$$\tau_{df} = \tau_0(1 + g(e))(2 - \gamma)M^{-0.67}r_0^{1.76}, \quad (2.15)$$

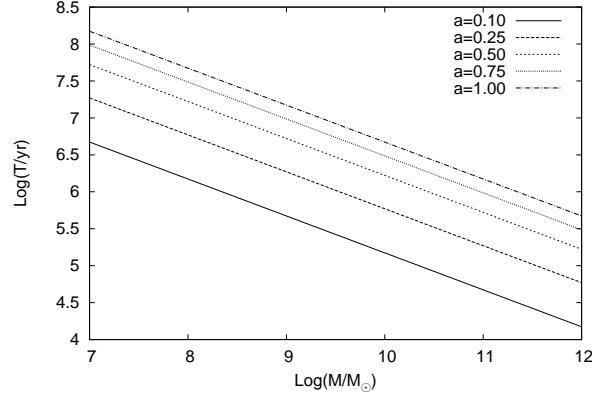


Figure 2.19: The unit of time (Eq. 2.12) transformed into years, assuming galaxy masses ranging from $10^8 M_\odot$ to $10^{12} M_\odot$ and for the length scale a ranging from 0.1 kpc to 1 kpc. This allows an easy rescaling of the decay time of Fig. 2.18 into a physical time for arbitrary choices of the pair (M_G, a) .

where $\tau_0 = 0.2$ is an adimensional time constant and $g(e)$ is an adimensional function of the eccentricity:

$$g(e) = 3.93(1 - e). \quad (2.16)$$

Eq. 2.15 is suited to give some useful astrophysical constraints. For example, for any given set of \bar{e} , $\bar{\gamma}$, \bar{M} values, it gives the radius of the sphere containing all the test objects that, in a galaxy with a cusp $\gamma \geq \bar{\gamma}$, and having $e \leq \bar{e}$ and $M \geq \bar{M}$, have sunk to the galactic center within time t , as

$$r_{max} = 2.5 \left[\frac{t}{(1 + g(\bar{e}))(2 - \bar{\gamma})} \right]^{0.57} \bar{M}^{0.375}. \quad (2.17)$$

2.3.3 A straightforward application to a galactic satellite population sinking

By mean of this formula and assuming a population of galaxy satellites (that may represent globular clusters in a galaxy) initially distributed following either the same γ density law of the background stars or accordingly to a Plummer profile, we estimated the fraction to the total of satellites sunk to the center of the galaxy at different physical times (500 Myr, 1 Gyr and 13.7 Gyr), and synthesized some results in Tab.2.5. It is clearly seen the fundamental role of the steepness of the galaxy density profile into the depletion of the satellite population, as well as that the satellite mass. The cuspy, $\gamma = 3/2$, galactic profile is able to erode around 40% of the initial satellite population of masses larger than $M = 10^5 M_\odot$ within 1 Gyr, assuming satellite moving on circular orbits, and up to 63%–83% of the initial population (the larger erosion for an initial

Table 2.5*Fraction to the total of satellites sunk to the galactic center.*

$M = 10^{-6}$									
	$t = 500 \text{ Myr}$			$t = 1 \text{ Gyr}$			$t = 13.7 \text{ Gyr}$		
e	r_{max}	$f_{3/2}$	f_{Pl}	r_{max}	$f_{3/2}$	f_{Pl}	r_{max}	$f_{3/2}$	f_{Pl}
0	0.754	0.275	0.216	1.12	0.385	0.417	5.05	0.763	0.944
1/2	1.01	0.357	0.354	1.49	0.463	0.570	6.77	0.812	0.968
1	1.87	0.525	0.390	2.77	0.631	0.832	12.55	0.891	0.999
$M = 10^{-4}$									
0	4.24	0.726	0.921	6.28	0.801	0.963	28.42	0.949	0.998
1/2	5.66	0.783	0.944	8.39	0.844	0.979	38.10	0.962	0.999
1	10.52	0.872	0.987	15.60	0.911	0.994	70.55	0.979	0.999

The galaxy mass is $M_G = 10^{11} M_\odot$ and its length scale $a = 250 \text{ pc}$. The galaxy density profile has $\gamma = 3/2$. The fractions to the total satellite population decayed is $f_{3/2}$, assuming initial satellite distribution as a $\gamma = 3/2$ profile, or f_{Pl} , assuming a Plummer profile.

satellite profile following the Plummer’s law) in the case of radial ($e = 1$) orbits. This erosion reduces to a 4%–9% of the initial satellite circular orbits and to 18%–49% of the initial satellite radial orbits, when the galaxy profile follows the, innermost flat, $\gamma = 0$ profile (also here the percentages intervals refer to the satellites distributed as a $\gamma = 0$ profile or as a Plummer’s model). As a general conclusion, dynamical friction effect is maximized for massive satellites ($M/M_G \geq 10^{-6}$) of cuspy, massive and compact galaxies ($M_G \geq 10^{11} M_\odot$, $a \leq 500 \text{ pc}$) whose satellites systems evolve faster in a given physical time due to the $\propto a^{3/2} M_G^{-1/2}$ scaling of the time unit. In few Gyrs, such galaxies remain with a low abundant satellite population, having packed most of their mass (up to 90%, or more) into the galactic nuclear region.

2.3.4 Massive object stalling in core galaxies

The approximation formula given by Eq. 2.15 was obtained by fitting results of N -body integrations in cuspy density profiles. To check its application to cored models we performed two N -body simulations of the evolution of a radial and a circular orbit in a Dehnen model with $\gamma = 0$. The orbits have same initial energy with the circular orbit starting at $r_0 = 0.5$. Fig. 2.21 reports the evolution of the test mass orbital energy in the two case studied.

We see that the extrapolation of Eq. 2.15 to the $\gamma = 0$ case gives a decay time correct within 10% for the radial orbit. On the other side, the N -body evolution of the circular orbit shows that the decay stops when the test particle galactocentric distance reduces to $r \lesssim 0.1$; then, the orbit ‘stalls’, in the sense that the test particle oscillates without appreciable further decay as indicated by Fig. 2.22. This orbit stalling in cored profiles

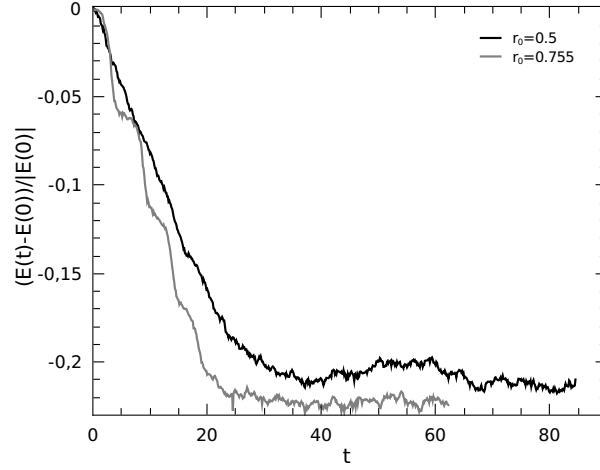


Figure 2.20: Test mass energy loss for radial (dotted line) and circular (straight line) orbits in the case $\gamma = 0$.

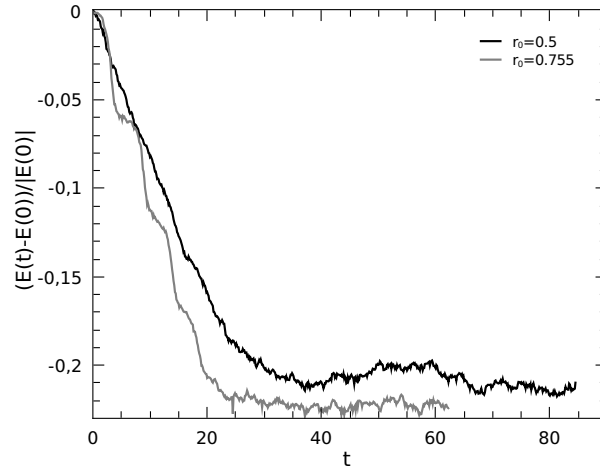


Figure 2.21: Test mass energy loss for radial (dotted line) and circular (straight line) orbits in the case $\gamma = 0$.

was already found by previous authors [68, 95]; in particular, Antonini and Merrit put on evidence that the stall is due to a lack of slow stars within the orbit size [4]. Although it is not exactly true that dynamical friction is contributed by field stars slower than the decaying object, this interpretation is substantially correct as shown by Fig. 2.23 where the fraction (to the total) of stars slower than the decaying object and enclosed within its actual position is reported as function of time.

While in the radial case, the fraction of ‘slow’ increases when the test mass crosses the center of the system resulting into an enhancement of the dynamical friction effect which induces a progressive decay until the particle reaches the center of the system, in the circular case the fraction decrease continuously until $t \sim 30$, that is roughly the time at which the decay ends and the test mass reaches an almost steady eccentric orbit.

Since the spatial distribution of background stars is not significantly altered on all scales

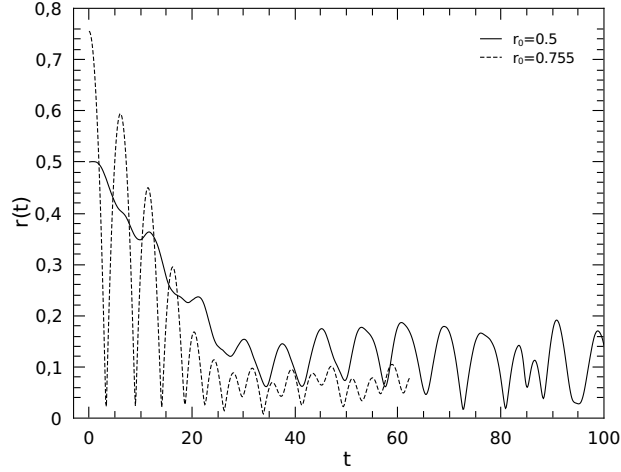


Figure 2.22: Time evolution of the galactocentric distance of the radial (dotted line) and the circular (solid line) orbits with the labeled initial distances from the center, in the $\gamma = 0$ model. In the circular orbit, it is evident that at $t \sim 35$ the orbits becomes eccentric and the test particle almost stalls.

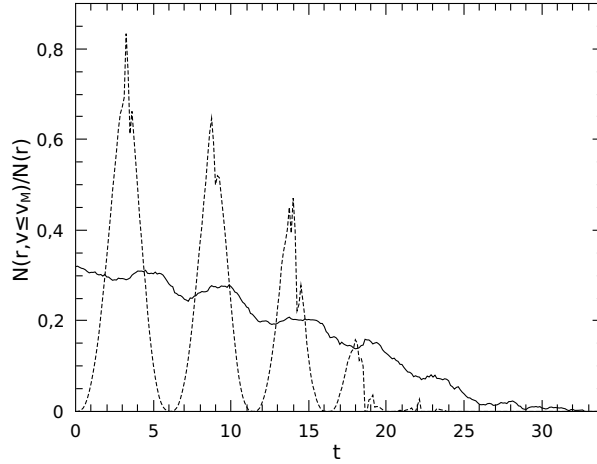


Figure 2.23: The local fraction of field stars slower than the test mass as a function of time for a circular (straight line) and a radial (dotted line) orbit.

by the satellite motion, it is argued that the key parameter in the modes of braking is actually the variation in the number fraction of slow stars.

Looking at the position at which stall begins, we found that the radius at which the dynamical friction action becomes negligible encloses a mass roughly equal to the test mass M , in agreement with the conclusion in Gualandris and Merritt [58]. Obviously, in flattened density core, this “critical mass” is reached at a greater radius with respect to cuspy profiles, enlarging the region of motion stalling. Of course, the stalling radius is smaller for centrally peaked profiles; for example, if $\gamma = 1$ it shrinks to $r \simeq 0.035$, as seen in Fig. 2.3.

2.4 The role of a central black hole in dynamical friction

It is well known that galaxies in a wide range of luminosities and Hubble types host at their center massive or even super massive black holes (SMBHs), whose masses range in the $10^6 - 10^{10} M_\odot$ interval [6, 116], influencing strongly the environment.

As an example of such an influence, Antonini and Merritt noted that a hypothetical stellar-mass BH population would see enlarged significantly the time to reach the center of the Milky Way by the presence of the central SMBH [4].

Actually, the presence of an SMBH affects also larger space and time scale through, for instance, its indirect role on the dynamical friction efficiency.

To check this role, we performed some specific N -body simulations of the motion of a point-like object which starts on an initially radial orbit in a $\gamma = 1$ sphere sampled with $N = 524,288$ particles and in presence of a central SMBH with mass M_{BH} .

In this framework, each background star has a mass $m_* \simeq 2 \times 10^{-6}$.

We chose three different values for M_{BH} , namely $M_{BH} = M, 4M, 10M$, where the mass of the test object is set to $M = 10^{-3} \gg m_*$.

Initial conditions for the test object are those of null initial velocity and of an initial position $\mathbf{r}_0 = (x_0 > 0, 0, 0)$ such that the initial orbital energy of the test object is the same in the three cases, $E_0 = -5 \times 10^{-4}$. This choice leads to about the same speed at the closest approach of the test particle to the center, condition needed to appreciate differences in the decay as mainly due to the presence of the black hole.

The time evolution of the test object distance to the galactic center, shown in Fig. 2.24, indicates that the presence of a SMBH does affect the dynamical friction decay time.

More massive BH determines a longer decay time of the infalling object. It should not surprise that the behaviour of $r(t)$ in the case of absence of SMBH is more similar to the behaviour in the case of the most massive SMBH considered. This is due to that the apocentric distance reached after the first crossing through the center is much more similar in these two extreme cases than in the others because the very massive BH after the close encounter with the test particle gains just a small velocity. Less massive SMBHs, on the other hand, move more and the test mass apocenter reduces consequently, making it moving in an innermost region where the galactic dynamical friction effect is larger. This is made clear by Figs. 2.25, 2.26 and 2.27.

This effect dominates on the other, opposite, effect of deviation from the unperturbed radial trajectory as quantified in Fig. 2.28. This figure shows a very similar time for

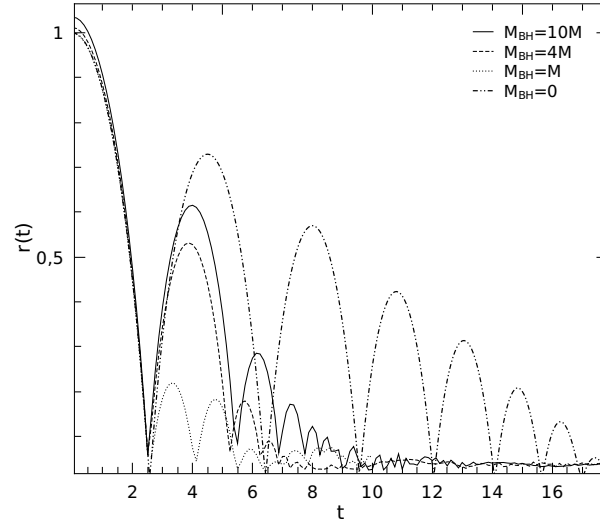


Figure 2.24: Test mass, M , orbital decay in presence of a central black hole, whose mass, M_{BH} , is labelled. The galaxy is modelled as a Hernquist sphere.

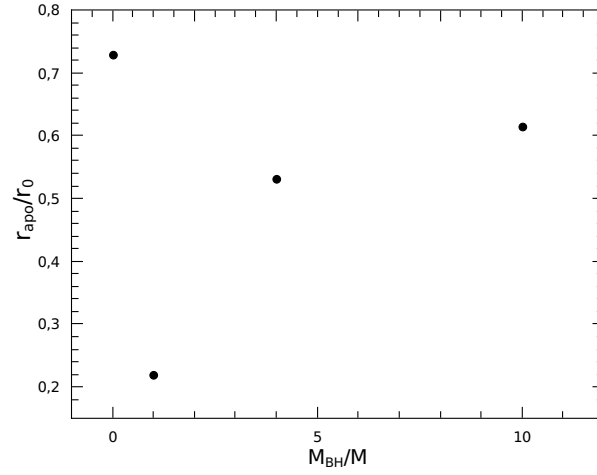


Figure 2.25: The apocenter distance after the first oscillation through the galactic center of the test mass in presence of a central massive black hole of mass M_{BH} .

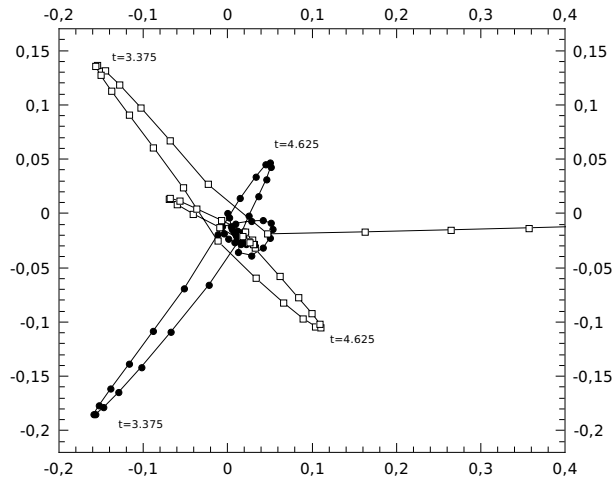


Figure 2.26: The trajectories of the radially falling test mass (empty squares) and of the perturbed central BH (filled squares). Some of the apocenter positions are labeled with their times.

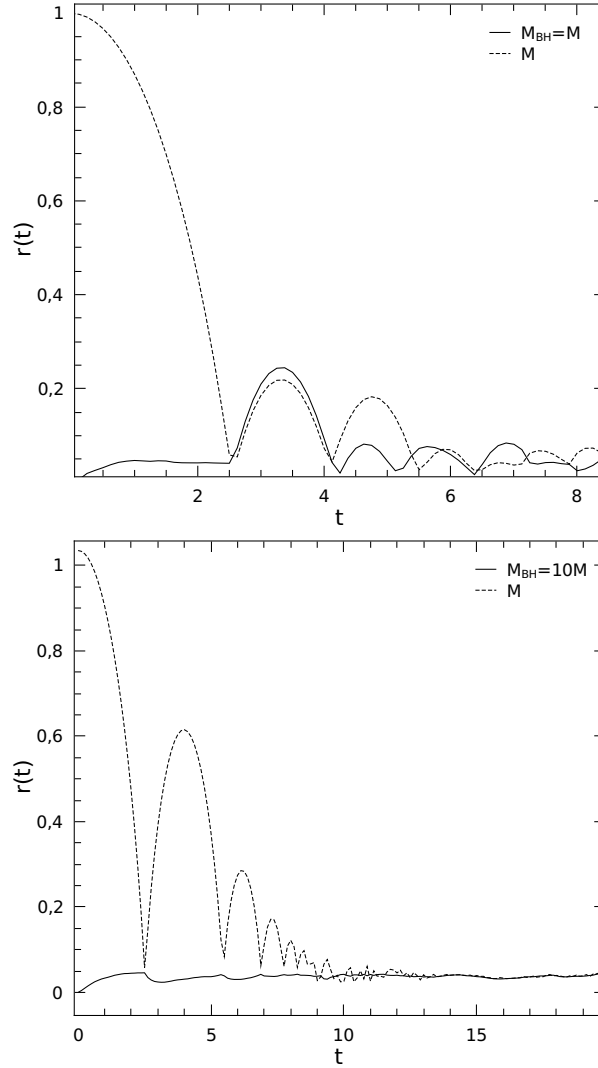


Figure 2.27: Test mass (dotted line) and BH (straight line) galactocentric distances vs. time in the case $M_{BH} = M$ (upper panel) and $M_{BH} = 10M$ (lower panel).

the closest approach to the galactic center (and so to the SMBH therein) in all the cases studied ($t \simeq 2.5$), consequence of the same value of initial orbital energy. After this closest approach, the time evolution of the distance to the center is quite different and differences cumulate over the following closest approaches.

The effect of the interaction BH-test mass is clearly shown in Fig. 2.26, which draws the trajectories (labelled with times) of the test mass and of the SMBHs in the case $M_{BH}/M = 1$ with the clear departure of the central BH from its initial central position.

One important consequence of this part of our work is that the contribution given by the central BH to the braking effect is significant only when its mass is comparable with that of the satellite. However, in realistic situations, the central BH exceeds several times the typical star cluster masses.

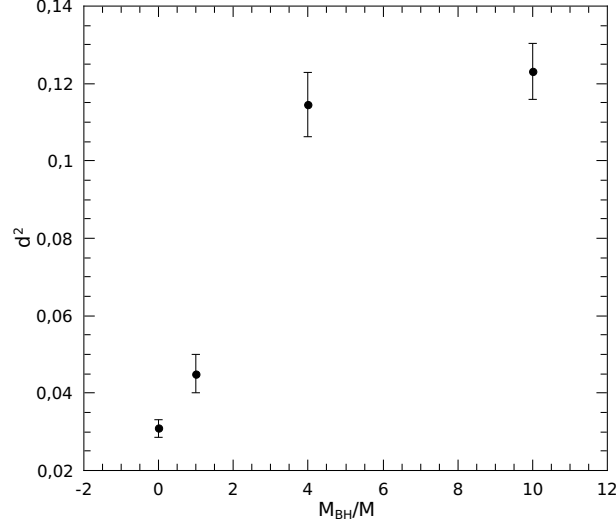


Figure 2.28: *Cumulative standard deviation from the unperturbed radial motion of the test mass M as a function of the BH mass; which shows the standard deviation of the distance of the test mass from the direction of unperturbed radial motion evaluated over the whole orbital evolution of the test mass until its total decay, as function of M_{BH} .*

2.5 Summary

I studied the mechanism of dynamical friction in cuspy density profiles, both on a theoretical and a numerical point of view.

The main results are here summarized:

- the classic [26] formula in its local approximation does not work in the central region of a cuspy distribution, because it diverges at the center and overestimates the actual dynamical friction in the vicinity of the density singularity;
- an alternative, semianalytic expression for the dynamical friction formula (Eq. 2.10) which is finite at center of density diverging galaxies (as mathematically shown in Appendix A in the case of the family of Dehnen [35] γ models) and smoothly connected to the usual local approximation is given and discussed;
- the free parameters in the semianalytic formula are tuned via comparison with high precision N -body simulations of massive object decay in a self consistent particle representation of the cuspy host galaxy (Sect. 3); the best values of the minimum impact parameter is systematically larger for circular ($e = 0$) orbits than for radial ($e = 1$);
- an extensive set of orbits of different initial eccentricities for a massive test object in the N -body representation of the parent galaxy has been computed, showing both a good agreement with the semyanalytic formula as shown by Figs. 2.6–2.11;

- for any given initial orbital energy, the decay times of orbits of different eccentricities range within the interval defined by radial (shortest) and circular (longest) case;
- the ratio of the radial to circular decay times in the case of the $\gamma = 1$ density slope is about $1/2$;
- global approximation formulas for the dynamical friction decay time in function of the relevant structural parameters are obtained, which show clearly how dynamical friction is maximized in massive host galaxies with a steeper central density profile, for higher eccentricity orbits of massive satellites, moreover it is unchanged if the galaxy host a BH heavier than the satellite;
- as an example, our Milky Way, if represented in its central region as a moderate cuspy density ($\gamma = 1/2$) should have lost, in a Hubble time, about 75% of the initial population of massive ($\geq 10^5 M_\odot$) globular clusters, decayed into the innermost region;
- the dynamical friction decay of test objects is altered significantly by the presence of a central massive black hole *if it has a mass comparable to the satellite mass*; the decay time of initially radial orbits is an increasing function of M_{BH} ;
- on the other hand, when the central BH has a mass significantly greater than the satellite mass, the decay time is well estimated by our general formulas;
- the dynamical friction time, τ_{df} , depends on the test object mass in a non-trivial manner, which is different from the usually adopted inverse linearity, $\tau_{df} \propto M^{-1}$, resulting $\tau_{df} \propto M^{-0.67}$, instead.

CHAPTER 3

DYNAMICAL FRICTION APPLICATIONS IN ASTROPHYSICAL CONTEXT

The treatment developed to describe the dynamical friction process does not require any assumption about the scales of the background.

To prove its general validity, in this section, it will be shown how it is possible to apply the treatment on different astrophysical situations and on very different scales.

In Sec. 3.1 I show that df could be used in order to explain a mass excess found in the center of many globular clusters, often interpreted as an Intermediate Mass Black Hole. In Sec. 3.2, instead, we try to give an explanation to the so called *Fornax dSph timing problem*.

3.1 Intermediate Mass Black Holes in Globular Clusters

Recently, it has been argued that some globular clusters (GCs) host a central BH . As an example, observations and modeling of the cluster M15 seems to be consistent with the presence of a compact central object [50]; the same result has been found for the cluster G1 in M31 ([47],[48]). Moreover, Noyola et al. have found that also ω Centauri could host a BH with mass $M = 4.0^{+0.75}_{-1.0} M_{\odot}$ [89].

They had been usually referred as intermediate mass black holes (IMBHs), to distinguish them from stellar BHs ($M \sim 10 - 100 M_{\odot}$) and SMBHs reside in the galactic centers ($M \sim 10^8 - 10^{10} M_{\odot}$).



Figure 3.1: *The globular cluster ω centauri.*

Moreover, many recent studies have been shown that observational data can be interpreted as the presence of a group of compact objects near the center [11].

The formation of an IMBH can be attributed to merger events [94], or to a stellar black hole that has grown through slow accretion [82].

However, another possibility is that two body encounters could carry toward the center of the cluster a significant amount of mass in form of massive stars in a reasonable time.

In this framework, we apply our results on dynamical friction process to several globular cluster models, in order to quantify the amount of mass decayed in form of evolving star in a Hubble time, and give some estimation of the total mass enclosed in a small volume, with a scale length roughly equal to the stall radius, to compare it with the observative and theoretical estimations of IMBH masses.

3.1.1 Sampling method and stars mass loss

To compare our results with observative data, we used the set of 14 GCs given in Lützgendorf et al. (hereafter LU13) [75]. Masses of the GCs and the BHs, or their upper limits, are shown in Tab.3.1.

First, we model the globular cluster with a Dehnen sphere with slope γ and total mass M_{GC} .

Star masses are sampled following as initial mass function (IMF) the Salpeter function $dN/dM \propto M^{-s}$ ranging from $0.1M_{\odot}$ to $100M_{\odot}$ [107].

Table 3.1

Parameters of the observed GCs collected in LU13.

ID	NAME	$\log(M_{GC}/M_{\odot})$	$\log(M_{BH}/M_{\odot})$
G1		6.76	4.25
NGC104	47Tuc	6.04	< 3.17
NGC1851		5.57	< 3.3
NGC1904	M79	5.15	3.47
NGC2808		5.91	< 4
NGC5139	ω Cen	6.40	4.6
NGC5286		5.45	3.17
NGC5694		5.41	< 3.9
NGC5824		5.65	< 3.78
NGC6093	M80	5.53	< 2.9
NGC6266	M62	5.97	3.3
NGC6388		6.04	4.23
NGC6715	M54	6.28	3.97
NGC7078	M15	5.79	< 3.64

For any given star, the initial position, r , and eccentricity of the orbit, e , are selected randomly, considering as maximum initial position the typical radius of the cluster ($\sim 10pc$), while the df timescale is evaluated using Eq. 2.15.

Due to the fact that stars experience mass loss phases during their evolution [29], we considered them as follows.

In the range $0.1 < M/M_{\odot} < 0.8$ there is no mass loss.

In the range $0.8 \leq M/M_{\odot} < 8$ the star experience mass loss during the red giant phase (RG) and the mass loss rate is given by:

$$\dot{M}_{RG} = \eta \frac{LR}{M} \left(\frac{T_{eff}}{4000K} \right)^{3.5} \left(1 + \frac{g_{\odot}}{4300g} \right) M_{\odot} yr^{-1}; \quad (3.1)$$

where L, R, M are luminosity, radius and mass in solar units, T_{eff} is the effective temperature and $g = GM/R^2$ is the surface gravity of the star [101].

The duration of this phase is given by:

$$t_{RG} \simeq 0.07 t_{MS}, \quad (3.2)$$

where:

$$t_{MS} = 10^{10} yr \frac{M}{L}, \quad (3.3)$$

is the timescale of the Main Sequence. In this range of masses, stars lose mass also during the asymptotic giant branch phase (AGB), which timescale is roughly $t_{AGB} \sim 0.15t_{RG}$. During the evolution in AGB, the mass loss rate is evaluated as a constant:

$$\dot{M}_{AGB} \simeq 10^{-4} M_{\odot} yr^{-1}. \quad (3.4)$$

In the range $8 \leq M/M_{\odot} < 20$ stars exiting from the Main Sequence evolve in red supergiant (RSG) remaining in this stage for $t_{RSG} \sim 10^4 - 10^6 yr$. The mass loss rate in this case has been computed firstly by de Jager et al. [33]:

$$\log(\dot{M}/(M_{\odot} yr^{-1})) = 1.769 \log(L) - 1.676 \log(T_{eff}) - 8.158. \quad (3.5)$$

Finally, for stars massive than $20M_{\odot}$, the mass loss rate is evaluated using results given in Nugis and Lamers [90]:

$$\dot{M}_{WR} = 10^{-11} (L)^{1.29} Y^{1.7} Z^{0.5} M_{\odot} yr^{-1}, \quad (3.6)$$

with L the luminosity in solar units, Y the helium mass fraction and Z the metallicity. Since at this stage the star experience the He core burning and subsequently the CNO-cycle, it seems to be appropriate to use $Y = 0.983$ and $Z = 0.0172$ [90].

The duration of this phase is roughly $10^4 - 10^5 yr$.

For each star, we compute the final mass M_f by dividing the “mass loss duration” in steps, evaluating for each step the stellar parameters (M, L, R, T_{eff}) and subtracting the mass lost in that step to the initial mass of the star.

Moreover, we evaluate in each step the df time corresponding to the star mass at the step, keeping as final t_{df} the average of all of them. This take in account the fact that the lighter the star the longer the decay time.

The df process is really enhanced when the test mass is much more massive then the background particle, in fact we found that when the test mass is ~ 20 times the average mass of the stars, the df effect is suppressed by the granularity of the system, that in a GC model surely cannot be negligible (see also Fig. 3.10). Because of this, we consider as affected significantly by the df process only stars which mass is 30 times the mean mass $\langle m \rangle$ of the stars:

Table 3.2

Main parameters of our simulations.

s	γ	M_{GC} [M_{\odot}]	N_{GC}	N_{RG}	N_{RSG}	N_{WR}	N_{dec}	M_{cen} [M_{\odot}]
2.35	0	7×10^6	20937099	1206800	38562	7820	890	12913.1
2.35	0	5×10^6	14960384	862350	27600	5555	682	9831.31
2.35	0	3×10^6	8972534	516878	16621	3345	415	5966.36
2.35	0	10^6	2998155	172033	5494	1112	150	2164.78
2.35	0	5×10^5	1498780	86112	2764	524	79	1138.25
2.35	0	10^5	301328	17165	541	98	15	218.891
2.35	0	5×10^4	151014	8586	275	41	8	116.94
2.35	0	10^4	30733	1807	46	4	2	27.7273
2.35	0	5×10^3	15355	897	26	2	2	28.4398

$$\langle m \rangle = \frac{\int_{M_{min}}^{M_{max}} M f(M) dM}{\int_{M_{min}}^{M_{max}} f(M) dM}, \quad (3.7)$$

where $f(M)$ is the IMF. Considering the Salpeter function, with slope 2.35, the mean mass is $\langle m \rangle = 0.35 M_{\odot}$.

Once t_{df} and M_f are evaluated, we considered only stars which lifetime τ_* is longer then t_{df} , in order to ensure that the star reaches the center of the cluster.

Moreover, we consider obviously only star with $t_{df} < t_H$, with t_H the Hubble time.

In this way it is possible to quantify the amount of decayed mass and the region in which it moves; in fact, since df stalls when the mass enclosed within the particle orbits equals its mass, the decayed stars will lie within a radius that should be roughly the maximum of the stalling radii of each star, i.e. the stalling radius of the heaviest star, which in this case is $r_{stall} \sim 0.033 pc$.

3.1.2 Results

In Tab.3.2 are shown the main parameters of the simulations: γ value, Salpeter slope s , GCs masses M_{GC} and the decayed mass M_{cen} . Moreover the total number of stars, the number of Red Giant, Red Supergiant and OB-WR stars are shown, respectively.

We varied the GC mass in the range $10^3 - 10^7 M_{\odot}$, setting $\gamma = 0$ while $s = 2.35$ was kept as IMF slope.

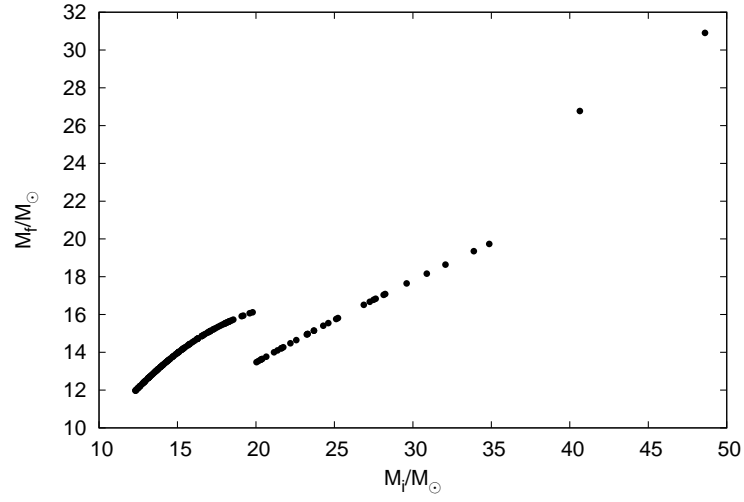


Figure 3.2: *Final masses of the stars at the end of their life with respect the initial mass.*

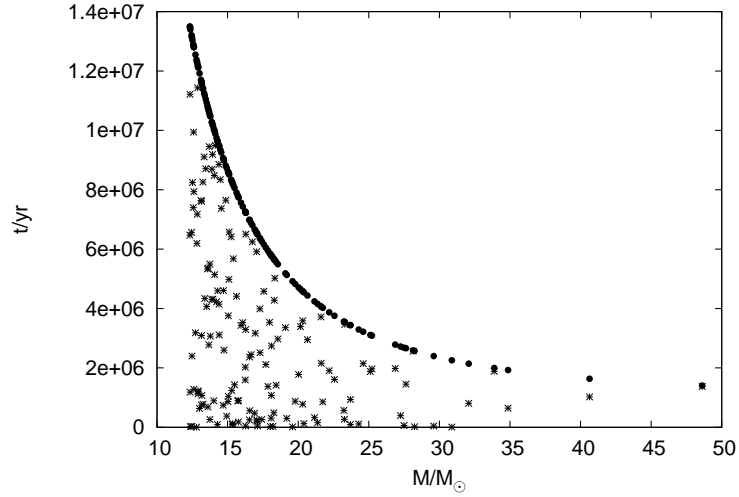


Figure 3.3: *Time life (black points) and decay time (stars) of the decayed stars.*

In Fig. 3.2 are shown the initial and final masses of the decayed stars. Gaps between $M \lesssim 20M_\odot$ and $M \lesssim 40M_\odot$ are related to the different definitions of mass loss rate given in the previous equations.

In Fig. 3.3 is shown the df time and the lifetime of the decayed stars with respect their final masses.

As you can see, only very massive stars have decay time shorter than the lifetime. Since the number of particle is huge ($N \geq 2 \times 10^6$ for $M \sim 10^6 M_\odot$) in the figure are shown only the stars whose decay time is lower than the lifetime.

The formation of an IMBH can occur only if the center of the GC is dense enough to allow strong collisions and merging between the decayed stars.

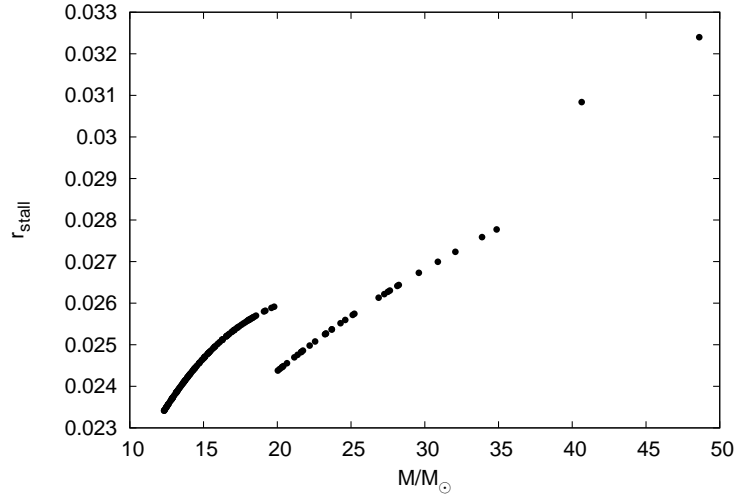


Figure 3.4: Stalling radius r_{stall} of the decayed stars with respect their final masses. The maximum value of r_{stall} can be assumed as an estimation of the region in which all the decayed stars lie.

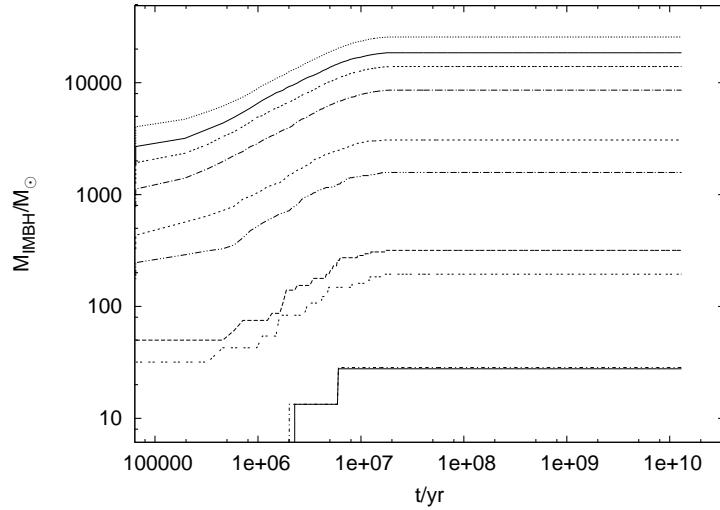


Figure 3.5: Central decayed mass as a function of the time. From top to bottom lines correspond to $M = 7 \times 10^6 - 5 \times 10^6 - 3 \times 10^6 - 10^6 - 5 \times 10^5 - 10^5 - 5 \times 10^4 - 10^4 - 5 \times 10^3 M_{\odot}$. The mass accumulated to the center for each GC is given in Tab.3.2.

To give an estimation of the region in which all the decayed stars lie, we kept the stalling radius of the most massive star. In Fig. 3.4 are shown the stalling radius of the stars with respect their final mass. The region in which the stars move in the brownian regime after the decay is roughly $R \sim 0.033pc$.

The final mass that has reach the center within a Hubble time is shown in Fig. 3.5 with respect the time.

Instead, in Fig.3.6 are shown the central masses compared to the observative values given in LU13 with respect the GCs masses. As you can see, masses predicted using

Table 3.3

The slope, A , of the relation $M_{IMBH} - M_{GC}$ evaluated by LU13

Method	A
FITEXY	0.69 ± 0.28
EM ALGORITHM	1.01 ± 0.34
BUCLEY-JONES	0.96 ± 0.32
BAYESIAN ANALYSIS	0.71 ± 0.59

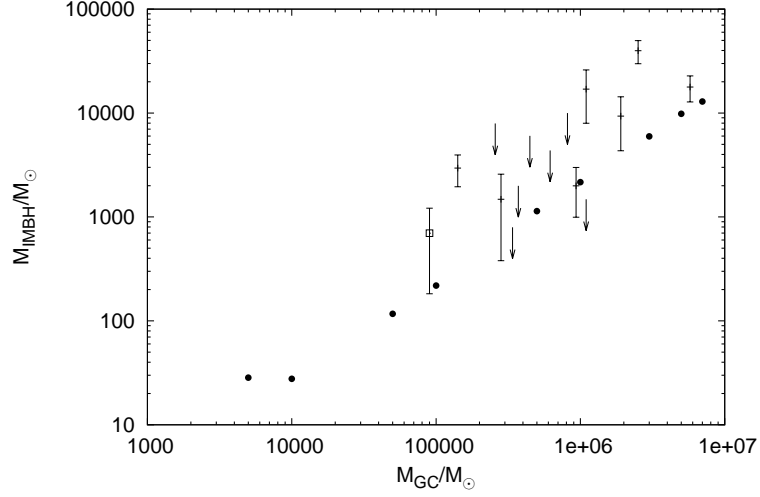


Figure 3.6: Central mass value as a function of the GC mass obtained through our approach (black points), upper limits for IMBH masses (down arrows) and data with relative errors (crosses).

the *df* process as mass transport mechanism are in quite good agreement with the data sample, convincing us that the fitting formula for the decay time given in Fig. 2.15 is a good tool to obtain useful scaling relations also on this relatively small scales.

From a quantitative point of view, correlating the GC mass M_{GC} with the central mass excess M_{IMBH} through the relation:

$$\log(M_{IMBH}/M_{\odot}) = A \log(M_{GC}/M_{\odot}) + B, \quad (3.8)$$

we found that $A = 0.9386 \pm 0.024$ and $B = -2.15 \pm 0.13$, in excellent agreement with results given by LU13, which are shown in Tab. 3.3.

3.1.3 Testing IMBH formation through N -body simulations.

To give an effort to our statistical treatment, we perform also a direct N -body simulation modeling a globular cluster the same global properties already used ($\gamma = 0$, $s = 2.35$).

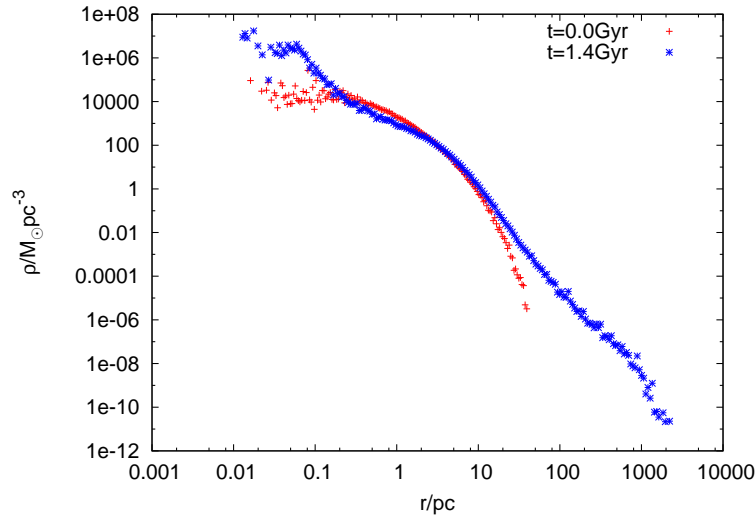


Figure 3.7: *Cluster density profile initially and after $t = 1.4Gyr$. As you can see there is an evident overdensity.*

We used a total number of particle $N = 262,144$ for a total mass of $M_{GC} = 90,000M_{\odot}$, with individual stars masses going from 0.1 to $100M_{\odot}$.

The simulation have been stopped after a time $T = 1.4Gyr$ in order to keep a reasonable energy conservation ($\Delta E/E \sim 10^{-5}$).

In such kind of simulation the only effect that drives the evolution of the system is the two-body relaxation process.

In Fig. 3.7 is shown the cluster density profile at two different times; it is interesting to note the formation of a cored overdensity after $1Gyr$, due to the accumulation of mass in the central region. Moreover, is well evident an expansion of the system beyond $1000pc$ due to low mass stars which tend to move away from the cluster.

The expansion of the structure could be put on evidence by looking at the evolution of the lagrangian radii, that are shown in Fig.3.8.

Moreover, looking separately at the lagrangian radii evaluated considering only stars heavier than $50M_{\odot}$ and lighter than $0.5M_{\odot}$, respectively, it is possible to put in evidence a strong mass segregation occuring in few times 10^8yr as it is shown in Fig.3.9.

As it has been stated in the previous section, only stars massive enough suffer significantly the df effect, since df is suppressed by the brownian motion if the star is too light.

In Fig. 3.10 are shown the trajectories for a relatively light star ($M = 1M_{\odot}$) and a massive star ($M = 25M_{\odot}$). It is well evident that while the small star has a trajectory

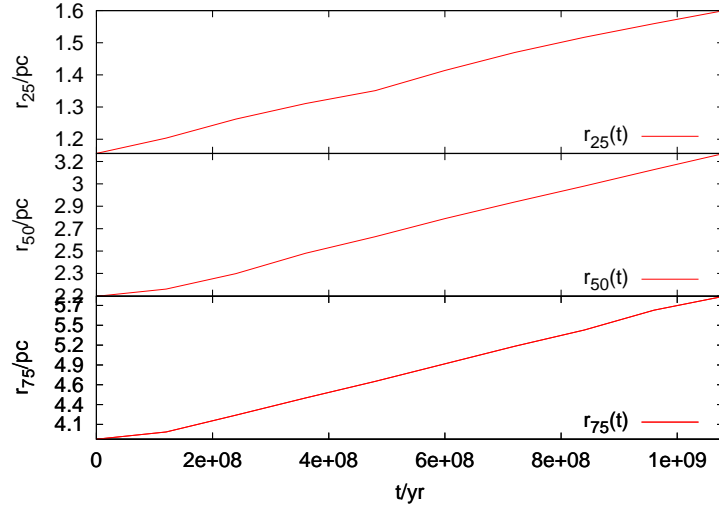


Figure 3.8: *Lagrangian radii evolution in time. From top to bottom, the radii enclose 25 – 50 – 75% of the cluster mass.*

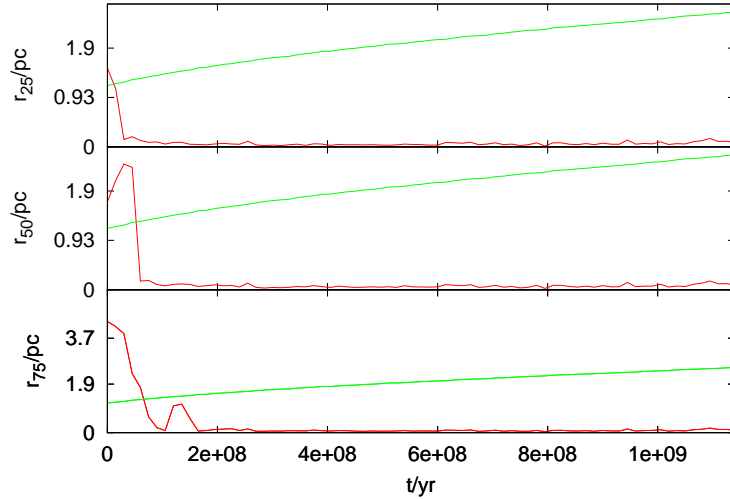


Figure 3.9: *Lagrangian radii evolution in time for high mass stars (red line) and low mass stars (green line). From top to bottom, the radii enclose 25 – 50 – 75% of the cluster mass.*

completely driven by the encounters with other stars, the massive one decay in a time that is in agreement with prediction evaluable by using Eq.2.15.

This give an effort to our statistical calculations presented above.

To put on evidence the amount of matter transported toward the center of the cluster, we show in Fig.3.11 the comparison between the mass profile at the beginning and the end of the simulation. As you can see, there is a significant increase in mass within 0.1pc. This growth of the central mass is well evident in Fig.3.12 which show the mean mass enclosed within this region of the system as a function of time.

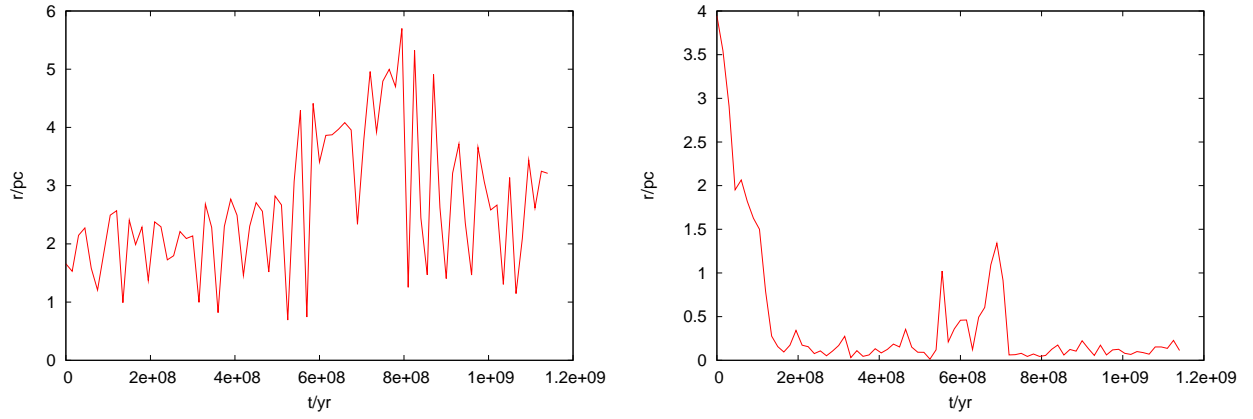


Figure 3.10: Left panel: trajectory for a $1M_{\odot}$ star. Right panel: trajectory for a $25M_{\odot}$ star. As you can see, the massive the star the greater the *df* effect.

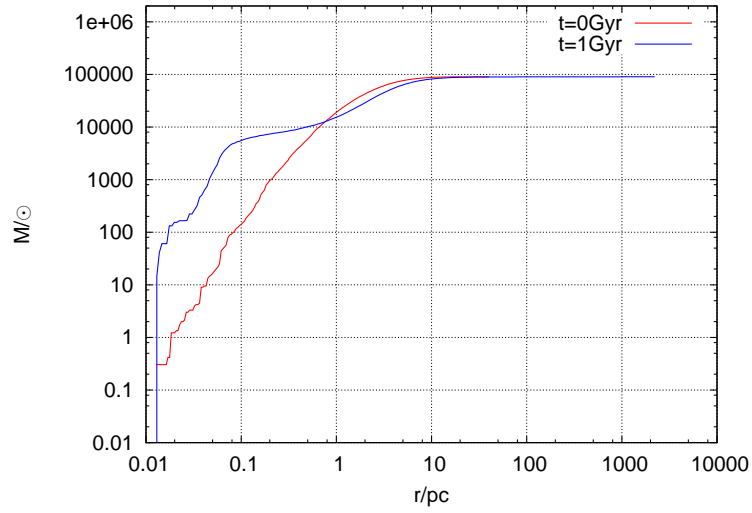


Figure 3.11: Mass profile of the cluster at $t = 0$ and $t = 1.4 \text{ Gyr}$. There is a considerable increase in mass within 1 pc that put on evidence the *df* effect.

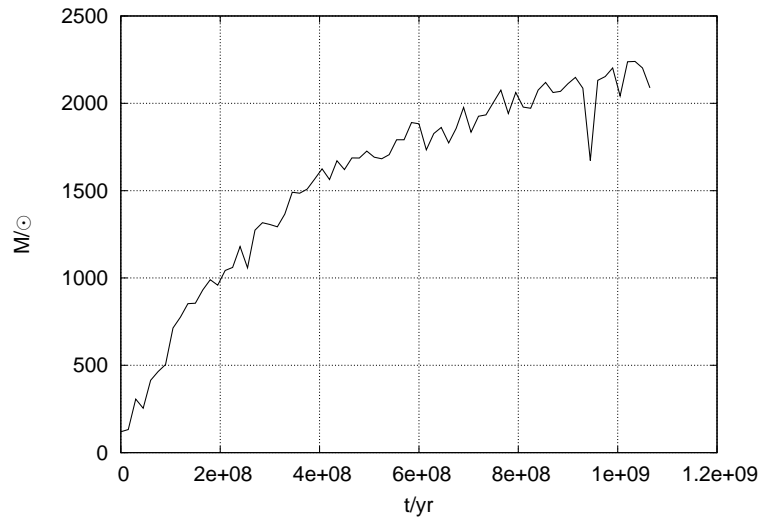


Figure 3.12: Mean mass enclosed within 0.1 pc from the center as a function of time. The final value of the central mass is $2000M_{\odot}$ around.

It is not surprising to see that the enclosed mass within $0.1pc$ after more than $1Gyr$ exceed $2000M_{\odot}$, that is surely greater than what is expected by looking at Fig.3.2 for a $M = 90000M_{\odot}$ cluster. This overestimation is due to the fact that the N -body code we used (HiGPUs), does not take in account the stellar evolution; but actually we are working to include it, and give this way more reliable results.

Actually, however, it is possible to give an estimation of the real central mass by identifying which kind are the decayed stars and subtracting them the mass lost evaluated by meaning of the formulas discussed in the last section. The central mass evaluated this way is $M_{IMBH} = (698 \pm 516)M_{\odot}$ as it is shown in Fig.3.6.

3.1.4 The Spitzer instability

The secular evolution of the cluster is dominated by gravitational encounters, which are responsible for several mechanisms as relaxation, equipartition and evaporation [17]. More precisely, the relaxation process leads to the equipartition, which in turn facilitate the ejection of stars from the system [61, 109].

Moreover, if the system has a mass spectrum, equipartition leads to the mass segregation process, which is a concentration toward the center of the system of the more massive stars, while lighter stars lie in an outer, sometimes expanding, region.

For the sake of simplicity, let's consider for a given system with potential $\Phi(\mathbf{r})$ two populations of particles whose masses are $m_H > m_L$.

The equipartition will be reached when:

$$m_L \langle v_L^2 \rangle = m_H \langle v_H^2 \rangle, \quad (3.9)$$

with $\langle v_i^2 \rangle$ the mean squared velocity of the i -th component.

As a consequence, heavier stars vent energy on lighter stars and sink toward the center, leading the system to the mass segregation.

As heavy stars sink to the center, they reach regions in which orbital speed are likely to be higher, due to the potential well, thus equipartition lead to a growth in kinetic energy of more massive stars.

However, Spitzer has shown that equipartition is possible only if some conditions are satisfied. To derive this result, let's consider the two populations of stars in such a way that the total mass of heavy stars M_H is negligible with respect to the total mass of light stars M_L [110].

It is trivial to show that the mass profile of the generic population i is related with the density through the relation:

$$M_i(r) = \int_0^{r_i} \rho_i(r) d^3r. \quad (3.10)$$

In agreement with the virial theorem, the mean square velocity of the heavy component is given by:

$$\langle v_H^2 \rangle = \frac{GM_H}{r_H} + \frac{G}{M_H} \int_0^{r_H} \frac{\rho_H(r) M_L(r)}{r} d^3r, \quad (3.11)$$

and the same for the light component is obtained just by replacing L with H and viceversa.

Following Spitzer [110], we can introduce a mean density such that:

$$M_i(r) = \frac{4\pi}{3} r_i^3 \langle \rho_i \rangle \quad (3.12)$$

In this way it is possible to solve the integral in Eq.3.11 in an easy way, leading to:

$$\langle v_H^2 \rangle = \frac{\alpha GM_H}{r_H} + \frac{G}{M_H} \frac{16\pi^2}{15} \langle \rho_H \rangle \langle \rho_L^0 \rangle r_H^5, \quad (3.13)$$

where $\langle \rho_L^0 \rangle$ is the mean central density of the light component.

Putting on evidence the term $\alpha GM_H/r_H$ and expressing the radius and the mass as a function of the mean density we obtain:

$$\langle v_H^2 \rangle = \frac{\alpha GM_H}{M_H^{1/3}} \left(\frac{4\pi}{3} \langle \rho_H \rangle \right)^{1/3} \left[1 + \frac{16\pi^2}{15\alpha} \frac{9 \langle \rho_H \rangle \langle \rho_L^0 \rangle r_H^6}{16\pi^2 r_H^6 \langle \rho_H \rangle^2} \right], \quad (3.14)$$

which leads to:

$$\frac{m_H \langle v_H^2 \rangle}{G} = m_H M_H^{2/3} \left(\frac{4\pi}{3} \langle \rho_H \rangle \right)^{1/3} \left[1 + \frac{9}{15\alpha} \frac{\langle \rho_L^0 \rangle}{\langle \rho_H \rangle} \right], \quad (3.15)$$

and in the same way we obtain the equation for the light component.

By using the equipartition, $m_H \langle v_H^2 \rangle = m_L \langle v_L^2 \rangle$ finally we obtain:

$$\frac{m_H}{m_L} \left(\frac{M_H}{M_L} \right)^{2/3} = \left(\frac{\langle \rho_L \rangle}{\langle \rho_H \rangle} \right)^{1/3} \left(\frac{1 + \frac{9}{15\alpha} \frac{\langle \rho_H^0 \rangle}{\langle \rho_L \rangle}}{1 + \frac{9}{15\alpha} \frac{\langle \rho_L^0 \rangle}{\langle \rho_H \rangle}} \right). \quad (3.16)$$

Let's now consider the case in which $M_H \ll M_L$, then the second term in Eq.3.11 related to the light component can be neglected and this leads to the Spitzer equipartition condition [110]:

$$\frac{m_H}{m_L} \left(\frac{M_H}{M_L} \right)^{2/3} = \left(\frac{\langle \rho_L \rangle}{\langle \rho_H \rangle} \right)^{1/3} \frac{1}{\left(1 + \frac{9}{15\alpha} \frac{\langle \rho_L^0 \rangle}{\langle \rho_H \rangle} \right)}, \quad (3.17)$$

which can be rewrite by defining the β parameter:

$$\beta = \frac{9}{15\alpha} \frac{\langle \rho_L^0 \rangle}{\langle \rho_L \rangle}, \quad (3.18)$$

in its final form:

$$\left(\frac{m_H}{m_L} \right)^{3/2} \frac{M_H}{M_L} = \frac{(\langle \rho_L \rangle / \langle \rho_H \rangle)^{1/2}}{(1 + \beta \langle \rho_L \rangle / \langle \rho_H \rangle)^{3/2}}. \quad (3.19)$$

Spitzer has found $\beta = 5.6$, hence the right hand term in the equation has a maximum value corresponding to 0.16; this means that the condition to have equipartition in a bimodal distribution of mass which satisfies the Salpeter hypothesis could reach the equipartition only if:

$$\left(\frac{m_H}{m_L} \right)^{3/2} \frac{M_H}{M_L} \leq 0.16. \quad (3.20)$$

3.1.5 Spitzer instability with a mass spectrum

Various researches had been done in order to investigate the Spitzer instability when a more realistic mass spectrum is considered instead of a bimodal mass distribution (see for example [59, 99, 119]). In general, it seems to be that if the cluster has a mass spectrum, it is very difficult to reach the equipartition.

Here I would show in an easy way, what happens to the Spitzer criterion when an IMF is considered.

Let's consider $f_i(m)dm$ the number of stars which mass is in the range $(m, m + dm)$; and let's $\rho_i(r)$ their spatial distribution; then, the generic population of stars i will have a mass profile given by:

$$M_i(r) = \int_{m_1}^{m_2} m f(m) dm \int_0^r \rho_i(r_*) d^3 r_* = \mathcal{F}_i \zeta_i(r), \quad (3.21)$$

Defining the mean mass $\langle m \rangle$ of the mass distribution as in Eq.3.7, we can divide the population into a heavy population:

$$M_H(r) = \int_{\langle m \rangle}^{m_H} m f(m) dm \int_0^r \rho_H(r_*) d^3 r_* = \mathcal{F}_H \zeta_H(r), \quad (3.22)$$

and a light population:

$$M_L(r) = \int_{m_L}^{\langle m \rangle} m f(m) dm \int_0^r \rho_L(r_*) d^3 r_* = \mathcal{F}_L \zeta_L(r). \quad (3.23)$$

Using exactly the same process followed in the previous section, we can obtain the equipartition condition just multiplying $\langle \rho_i \rangle$ by \mathcal{F}_i in Eq.3.16:

$$\frac{m_H}{m_L} \left(\frac{M_H}{M_L} \right)^{2/3} = \left(\frac{\mathcal{F}_L \langle \rho_L \rangle}{\mathcal{F}_H \langle \rho_H \rangle} \right)^{1/3} \left(\frac{1 + \frac{9}{15\alpha} \frac{\mathcal{F}_H \langle \rho_H^0 \rangle}{\mathcal{F}_L \langle \rho_L \rangle}}{1 + \frac{9}{15\alpha} \frac{\mathcal{F}_L \langle \rho_L^0 \rangle}{\mathcal{F}_H \langle \rho_H \rangle}} \right), \quad (3.24)$$

that can be simplified defining the adimensional quantities:

$$x = \frac{\langle \rho_H \rangle}{\langle \rho_L \rangle}, \quad (3.25)$$

$$F = \frac{\mathcal{F}_H}{\mathcal{F}_L}, \quad (3.26)$$

$$\beta_i = \frac{\rho_i^0}{\rho_i}, \quad (3.27)$$

in the form:

$$\left(\frac{m_H}{m_L} \right)^{3/2} \frac{M_H}{M_L} = \frac{1}{Fx} \left(\frac{\beta_H + Fx}{\beta_L Fx + 1} \right)^{3/2}. \quad (3.28)$$

Let's now consider the Spitzer hypothesis, that here corresponds to the case $\beta_H/(Fx) \ll 1$; the equation reduces to:

$$\left(\frac{m_H}{m_L} \right)^{3/2} \frac{M_H}{M_L} = \frac{(Fx)^{1/2}}{(\beta_L Fx + 1)^{3/2}}, \quad (3.29)$$

in this case it is trivial to show that the maximum value found by Spitzer doesn't change, in fact only the point at which the maximum is reached varies by a factor F^{-1} but the inclusion of an IMF doesn't change the maximum value of the right hand function. In Fig.3.13 is shown the comparison between the case in which the IMF is taken in account and it is not, assuming a Salpeter function with slope $s = 2.35$ and $\beta_L = 5.6$.

Considering again the hypothesis $\beta_H/(Fx) \ll 1$, which corresponds to the condition $M_H \ll M_L$, we would like to investigate what happens if: i) the two components have

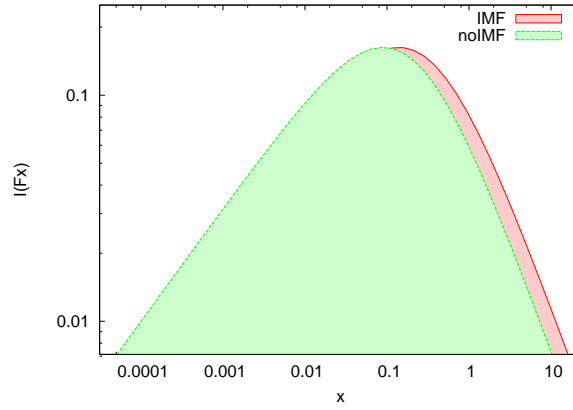


Figure 3.13: Comparison between the Spitzer condition when the IMF is considered (green region) or not (red region).

similar mean densities $x \sim 1$ or, ii) if they have similar typical radius $r_H \sim r_L$.

The condition $x \sim 1$ implies that:

$$\frac{M_H}{M_L} = \frac{\mathcal{F}_H \langle \rho_H \rangle r_H^3}{\mathcal{F}_L \langle \rho_L \rangle r_L^3} \rightarrow \frac{1}{F} \left(\frac{r_H}{r_L} \right)^3, \quad (3.30)$$

and since $M_H \ll M_L$ we obtain that the condition is satisfied when:

$$\frac{1}{F} \left(\frac{r_H}{r_L} \right)^3 \ll 1. \quad (3.31)$$

In this limit, the Spitzer condition is given by:

$$\left(\frac{m_H}{m_L} \right)^{3/2} \frac{M_H}{M_L} = \frac{F^{1/2}}{(1 + \beta_L F)^{3/2}}, \quad (3.32)$$

different from what we can obtain with a simple bimodal distribution, which give as limit $(1 + \beta_L)^{-3/2}$.

By considering as mass distribution the Salpeter function $f(m) \propto m^{-s}$, the mean mass is given by:

$$\langle m \rangle = \frac{\int_{m_L}^{m_H} m f(m) dm}{\int_{m_L}^{m_H} f(m) dm} = \begin{cases} \frac{m_H - m_L}{\ln(m_H/m_L)} & s = 1, \\ \frac{m_H m_L \ln(m_H/m_L)}{m_H - m_L} & s = 2, \\ \frac{1 - s}{2 - s} \frac{m_H^{2-s} - m_L^{2-s}}{m_H^{1-s} - m_L^{1-s}} & s \neq 2, \end{cases} \quad (3.33)$$

which corresponds to $\langle m \rangle = 0.35 M_\odot$ if $s = 2.35$. The ratio F is given by:

$$F = \frac{\langle \mathcal{F}_L \rangle}{\langle \mathcal{F}_H \rangle} = \frac{\langle m \rangle^{2-s} - m_L^{2-s}}{m_H^{2-s} - \langle m \rangle^{2-s}}, \quad (3.34)$$

for $s = 2.35$ it is possible to find that $F = 0.64$.

Then, considering $\beta_L = 5.6$, we obtain that the Spitzer condition in the case that the two components have similar densities is:

$$\left(\frac{m_H}{m_L} \right)^{3/2} \frac{M_H}{M_L} \leq 8.15 \times 10^{-2}, \quad (3.35)$$

while if $F = 1$, i.e. there is no mass distribution, the limiting value is 5.9×10^{-2} ; then in this particular case the presence of an IMF seems to favourite the equipartition.

If we consider instead the condition $r_H \sim r_L$, which implies:

$$\frac{M_L}{M_H} = Fx, \quad (3.36)$$

we obtain a condition on the ratio of the maximum and minimum of the mass spectrum:

$$\frac{m_H}{m_L} \leq (Fx)^{-3} (1 + \beta_L Fx)^{-1}, \quad (3.37)$$

and in this case doesn't exist a maximum below which the equipartition is ensured; however, since $m_H > m_L$, we can obtain a condition over the right hand term:

$$x \leq \frac{1}{F} \sqrt{\frac{-1 + \sqrt{1 + 4\beta_L}}{2\beta_L}}, \quad (3.38)$$

that comes by solving the disequation $(Fx)^3(1 + \beta_L Fx) \leq 1$. By assuming $\beta_L = 5.6$ and $F = 0.64$, the condition to reach the equipartition becomes $x \leq 0.91$.

Now let's consider the case $\beta_H \sim \beta_L$, which correspond to a non negligible mass of the heavy population with respect the lighter one.

Considering Eq. 3.28 and assuming that the two components have similar mean densities $x \sim 1$, we find that

$$\left(\frac{m_H}{m_L} \right)^{3/2} \frac{M_H}{M_L} \leq 2.48, \quad (3.39)$$

using as made previously $\beta_L = \beta_H = 5.6$ and $F = 0.64$ and considering a bimodal distribution instead of a IMF, would imply a smaller limiting value, near the unity, therefore the IMF tends to facilitate the equipartition in this case.

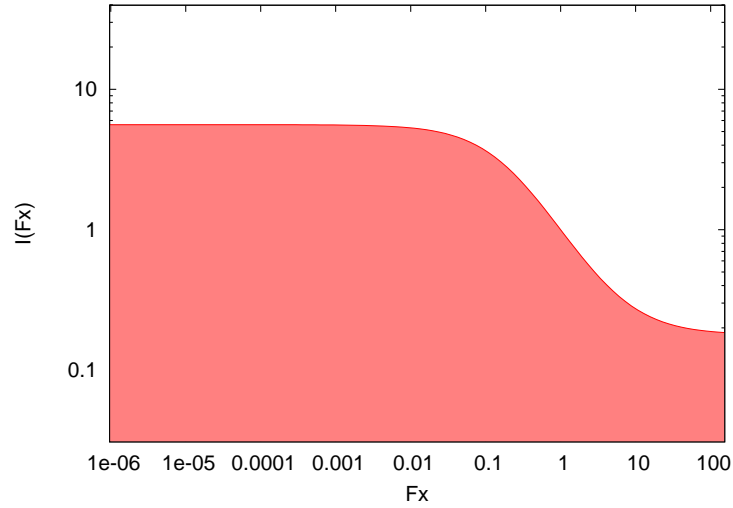


Figure 3.14: *The ratio m_H/m_L as a function of the density ratio x . The shaded region is the region in which the equipartition is verified.*

If the two components have similar length scales $r_L \sim r_H$ we obtain the analogous of Eq.3.37:

$$\frac{m_H}{m_L} \leq \frac{Fx + \beta_H}{\beta_L Fx + 1}, \quad (3.40)$$

which is a function in the range $[\beta_L, \beta_H^{-1}]$ as it is shown in Fig.3.14

Since $\beta_H = \beta_L = 5.6$, in this case the equipartition is reached simply if $m_H/m_L \leq 5.6$ and this value doesn't depend on the mass spectrum.

It is important to note that with our choice $m_H = 100M_\odot$, $m_L = 0.1M_\odot$ and $F = 0.64$, the quantity $(m_H/m_L)^{3/2} M_H/M_L$ has typical values of order 5×10^4 , which imply that in realistic situations the equipartition is almost impossible to reach.

3.1.6 Summary

What I presented in this section is a work in progress, that can be surely improved considering, as example, the effect of stellar evolution in the direct N -body simulation. Summarizing first results coming from the statistical and N -body approaches:

- gravitational encounters in a GC with a mass spectrum could lead massive stars toward the center of the system, packing a lot of mass in a relatively small volume;
- the general expression for the decay time obtained by our work on the dynamical friction process well reproduce the segregation, allowing to estimate how much mass in form of heavy stars could reach the center of the cluster in a Hubble time,

leading to the estimation of a “mass excess” which can be compared directly with observed data;

- the mass excess found in our statistical simulations, which take in account the stars mass loss due to stellar evolution, is in excellent agreement with observations; in particular, the correlation between the cluster and the central mass is really close to that argued by observed clusters;
- using direct N -body simulations, we found that the segregation leads to a packaging of mass in the very inner region of the cluster, supporting our statistical conclusion, which are that dynamical friction mechanism could be applied in dealing with this subject;
- from a theoretical point of view, it has been shown that the Spitzer instability can be extended to a system with a mass spectrum;
- clusters we simulated do not satisfy nor the Spitzer condition neither its extension, which implies that the heavy component would tend to concentrate more and more, decoupling from the system, and enhancing the mutual interactions between massive stars, which could lead over time to the formation of a IMBH.

3.2 A possible solution to the Fornax dwarf spheroidal timing problem

The Fornax galaxy is the heaviest dwarf spheroidal galaxy (dSph) satellite of the Milky Way and is the only among all of the satellite galaxies that host five globular clusters all within 1 kpc from the center of the system.

This feature represents a puzzle because of the fact that dynamical friction should strongly affect the kinematics of the globular cluster system (GCS); in fact, Fornax's GCs are very old and metal poor [71] and this places their formation to a Hubble time ago leading to the so called “timing problem”: it is really improbable that we are looking at the GCs just before they sink to the galactic center.

The case of Fornax is a perfect laboratory to study dynamical friction (hereafter *df*) mechanism in order to explain the timing problem.

Many works had been devoted to solve this puzzle, Read et al. have shown that considering a cored density profile, the Chandrasekhar formula does not provide an accurate treatment of the orbital decay [96]. In fact in this case the decaying test particle experiences an initial phase in which *df* is more than that comes from the local approximation formula, and a second phase in which *df* stalls and the test particle does not lose orbital energy anymore.

Cole et al. [30] instead considered four different models for Fornax, in order to deeply study the effect of the background distribution on the orbital decay. Their conclusions led to two possible solutions to the “timing problem”: first, the *df* has stalled long time ago or it is really slow due to the fact that Fornax has a large core in density profile; second, the system has a small core or a shallow cusp, and the GCs formed beyond the tidal radius of Fornax and then they had been caught.

Here, we would demonstrate that a careful treatment of the *df* process could solve naturally the Fornax dSph puzzle.

The procedure used in this work is the following:

- select a proper density profile to model the galaxy, in agreement as well as possible with the most modern observations;
- explore a wide range of initial conditions, integrating numerically the equation of motion of each GC by using a proper code which include the *df* term;
- check the semi analytic calculations by simulating good initial conditions using a full *N*-Body code.

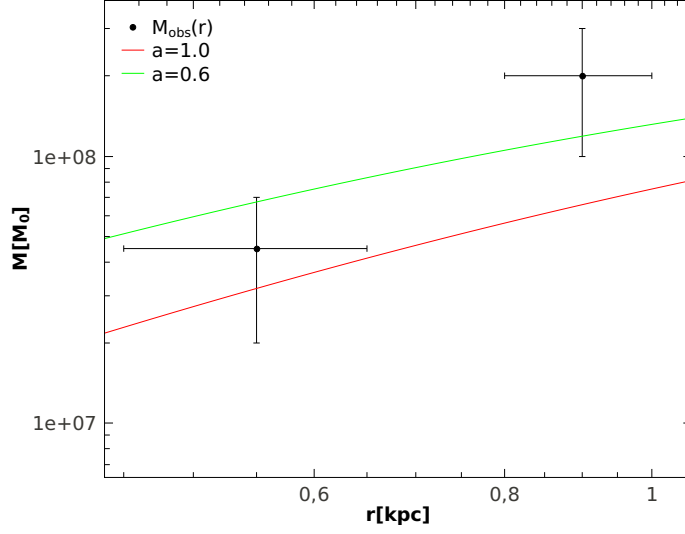


Figure 3.15: Mass profile chosen to model Fornax. The point are mass estimation given in [120].

3.2.1 The Fornax dSph model

Fornax dSph is a dark matter dominated galaxy that orbiting around the Milky Way at 140kpc . It has an estimated total mass up to $10^9 M_\odot$ [123].

Because of uncertainties in stellar kinematical data, the mass distribution agrees either with cored or cuspy density profile.

Here we would use two different γ -models, [35] in order to take in account a shallow cusp to model the galaxy; as a reminder, the density profile in this model is given by:

$$\rho(r) = \frac{(3 - \gamma_F)M_F}{4\pi a_F^3} \left(\frac{r}{a_F}\right)^{-\gamma_F} \left(\frac{r}{a_F} + 1\right)^{-4+\gamma_F}, \quad (3.41)$$

with a mass profile given by:

$$M_F(r) = M_F \left(\frac{r}{r + a_F}\right)^{3-\gamma_F}. \quad (3.42)$$

The model chosen is spherically symmetric, not so far from a realistic profile considering that Fornax has projected minor-to-major axis ratio of ~ 0.7 . In order to choose γ_F , M_F and a_F we compared density profiles with that obtained by Cole et al. [30] and mass with that estimated in Walker and Peñarrubia [120] (see Tab. 3.4).

Table 3.4

Parameters of the models considered.

<i>model</i>	γ_F	M_F	a_F
M1	0.5	$4.26 \cdot 10^8 M_\odot$	$1 kpc$
M2	0.5	$4.26 \cdot 10^8 M_\odot$	$0.6 kpc$

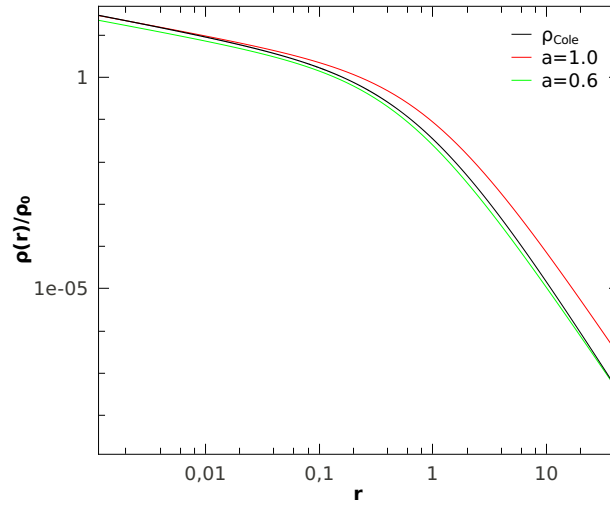


Figure 3.16: Normalized density profiles for the two models considered. As a comparison, we show the density profile given in [30]. The profiles are normalized to a density scale, which is for the Dehnen models chosen as $\rho_0 = (3 - \gamma_F)M_F / (4\pi a_F^3)$. Details about the structural parameters of the models are given in tab.(3.4).

Table 3.5

Observational data for the Fornax dSph

object	$M(10^5 M_\odot)$	$r_{obs}(kpc)$	$v_{obs}(kms^{-1})$
Fornax A	1420	—	—
GC1	0.37	1.6	—
GC2	1.82	1.05	-1.2 ± 4.6
GC3	3.63	0.43	7.1 ± 3.9
GC4	1.32	0.24	5.9 ± 3.4
GC5	1.78	1.43	8.7 ± 3.6

Column 2: mass of the objects ; column 3: projected distance from the distance of the Fornax center and column 4: observed line-of-sight velocity with respect the system itself [76].

Table 3.6

Critical initial conditions for GCs

object	M1c	M1r	M2c	M2r
GC1	0.89	2.21	1.38	3.41
GC2	1.62	4.00	2.50	6.18
GC3	2.09	5.18	3.23	8.00
GC4	1.44	3.55	2.22	5.48
GC5	1.60	3.96	2.48	6.12

Column 1-2: distance for circular and radial orbits under which the i -th GC decay within a Hubble time in the M1 model; column 3-4 refers to the model M2.

3.2.2 Initial conditions for the Fornax Globular Cluster System

To choose the initial conditions (IC) for the GCs we identify firstly the forbidden region in which, at their birth, the clusters cannot be to avoid the sink within a Hubble time.

To find this region, we consider the useful expression for df time:

$$\tau_{df} = (2 - \gamma_F)\tau_0(1 + g(e)) \left(\frac{M_{GC}}{M_F} \right)^{-0.658} \left(\frac{r_0}{a_F} \right)^{1.76}, \quad (3.43)$$

in which γ_F , M_F and a_F are the parameters concerning the galaxy model, τ_0 is a normalization parameter and $g(e)$ depends on the orbit of the cluster. M_{GC} and r_0 are respectively mass and initial position of the cluster.

By inverting this equation is possible to obtain the maximum distance, r_0^{lim} , at which τ_{df} is smaller than the Hubble time t_H :

$$r_0^{lim} = a_F \left(\left(\frac{M_{GC}}{M_F} \right)^{0.658} \frac{t_H}{(2 - \gamma_F)\tau_0(1 + \tilde{\tau})} \right)^{1/1.76}. \quad (3.44)$$

In Tab. 3.5 are listed the values estimated for r_0^{lim} for circular and radial orbits in the M1 and M2 models.

From these considerations we obtain therefore a lower limit for the initial positions of the five GCs.

The more natural way to estimate an upper limit, is to find the tidal radius of the galaxy, i.e. the radius at which a test particle can be considered still bound to the galaxy itself.

If we name R the distance between Fornax and the Milky Way, the Fornax tidal radius r_t is given solving the following equation:

$$F_{MW}(R + r_t) - F_{MW}(R - r_t) = 2F_{Frn}(r_t), \quad (3.45)$$

being $F_{MW}(\tilde{r}) = -\nabla\Phi(\tilde{r})$ the gravitational force due to the galaxy.

To model the Milky Way, following various examples in literature [2, 80, 123], we use an extended Dark Matter Halo (DMH) described by a Navarro-Frenk-White profile [85]:

$$\Phi_{DMH}(r) = -4\pi G\rho_0 r_s^3 \frac{\ln(1 + r/r_s)}{r/r_s}; \quad (3.46)$$

here $r_s = R_{vir}/c$ with $R_{vir} = 174kpc$ the virial radius and $c = 12$ the concentration; ρ_0 is obtained by the equation:

$$M_{vir} = 4\pi\rho_0 (R_{vir}/c)^3 (\ln(1 + c) - c/(1 + c)), \quad (3.47)$$

by assuming a virial mass $M_{vir} = 1.3 \times 10^{12}M_\odot$.

The galactic disk is instead modeled with a Miyamoto Nagai potential [84]:

$$\Phi_d(R, z) = -\frac{GM_d}{\sqrt{R^2 + (a + \sqrt{z^2 + b^2})^2}}, \quad (3.48)$$

with $M_d = 5 \times 10^{12}M_\odot$, $a = 3.5kpc$ and $b = 0.35kpc$, while the galactic bulge with a Plummer sphere [93]:

$$\Phi_{GB}(r) = -\frac{GM_{GB}}{\sqrt{r^2 + a_B^2}}, \quad (3.49)$$

$a_B = 0.7kpc$ and $M = 5 \times 10^{11}M_\odot$ are lenght and mass scale of the model, respectively. Moreover we include a Nuclear Bulge [72] modeled by a Dehnen profile with γ index equal to 0.5 and a central supermassive black hole which mass is $M_{BH} = 4 \times 10^6 M_\odot$:

$$\Phi_{NB}(r) = -\frac{GM_{NB}}{(2 - \gamma)a_\gamma} \left[1 - \left(\frac{r}{r + a_\gamma} \right)^{2-\gamma} \right] + \frac{GM_{BH}}{r^2}; \quad (3.50)$$

here $a_\gamma = 0.15kpc$ and $M_{NB} = 1.4 \times 10^9 M_\odot$.

With this galactic model for the Milky Way, we found for Fornax a tidal radius $r_t \simeq 5kpc$ with no sensitive changing passing by M1 to M2 model.

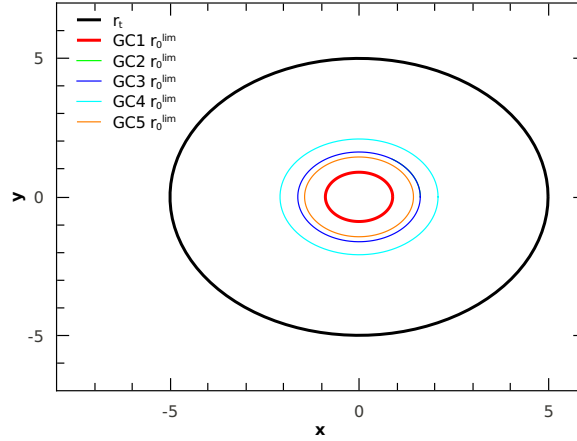


Figure 3.17: Lower and upper limit for r_0 of the five GCs in case of circular orbits for the model M1. The black circle represent the tidal radius, i.e. the outer limit.

Therefore, the initial position for the i – th GC should be kept between r_0^{lim} and r_t as it is shown in Fig.(3.17).

It is interesting to note that there are many cases in which a nearly circular orbit is most favourable, since r_0^{lim} for radial orbits lies beyond the tidal radius of Fornax (see tab.(3.6)).

Moreover, as preliminary consideration, it is evident that a set of IC which avoid the sink of the clusters within a Hubble time exists.

3.2.3 Semi analytical simulations

To explore a wide range of ICs in a relatively small time, we solved numerically the equation of motion of each cluster by developing a 6th order Runge-Kutta-Nyström with stepsize control integrator [45], which includes the friction term.

For the sake of simplicity, we assumed that the orbital plane of each cluster lies in the plane normal to our sight-of-view; this allowed us to explore the worst ICs possible, since clusters positions are not affected by perspective and their evolution is only due to the dynamical friction action.

Moreover, since this work is still in progress, here I show only results concerning circular orbits with ICs in the range r_0^{lim} and r_{tid} .

In Tab. 3.7 are shown simulations made using our semi-analytical code for the M1 model. From simulated ICs, we found a subset of simulations which could predict the real, observed positions of the clusters.

Table 3.7

Results from the analytical treatment

object	$r_{0_{sim}}$	$r_{H_{sim}}$	$r_{obs}(1kpc)$
GC1	2.0	1.8	1.6
GC1	1.85	1.63	1.6
GC1	1.7	1.45	1.6
GC2	2.3	1.6	1.05
GC2	2.15	1.047	1.05
GC3	3.0	1.84	0.43
GC3	2.5	0.427	0.43
GC4	2.0	1.16	0.24
GC4	1.8	0.62	0.24
GC4	1.7	0.38	0.24
GC4	1.6	0.148	0.24
GC5	2.5	1.76	1.43
GC5	2.4	1.58	1.43
GC5	2.3	1.39	1.43
GC5	2.0	0.81	1.43

All the initial velocity were kept as the circular velocity given in the initial position. All the results in this table refer to the model M1.

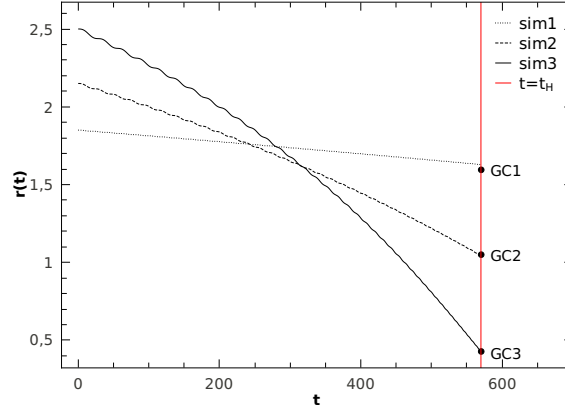


Figure 3.18: Trajectories for three different GCs that give actual position (black points) in perfect agreement with the observed distribution of clusters in Fornax. These results have been obtained through semi analytical simulations.

As example, in Fig. 3.18 are shown trajectories for clusters GC1, GC2, GC3 compared with their observed locations.

Concerning the M2 model, instead, we proceeded in a slightly different way. In this case, in fact, firstly we made a direct N -body simulation of the cluster GC3; then we used it to calibrate the semi-analytical code, as it is shown in Fig. 3.19. Then, we found the optimal ICs set for each cluster performing hundreds of semi-analytical simulations (see Fig. 3.20), and finally this subset has been used to simulate the evolution of all clusters using our N -body code, as it will discussed in following sections.

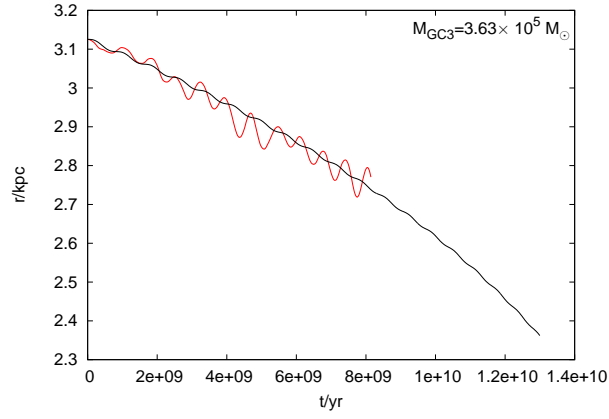


Figure 3.19: *N*-body (red line) and semi-analytical (black line) trajectories evaluated for the cluster GC3 in the M2 model.

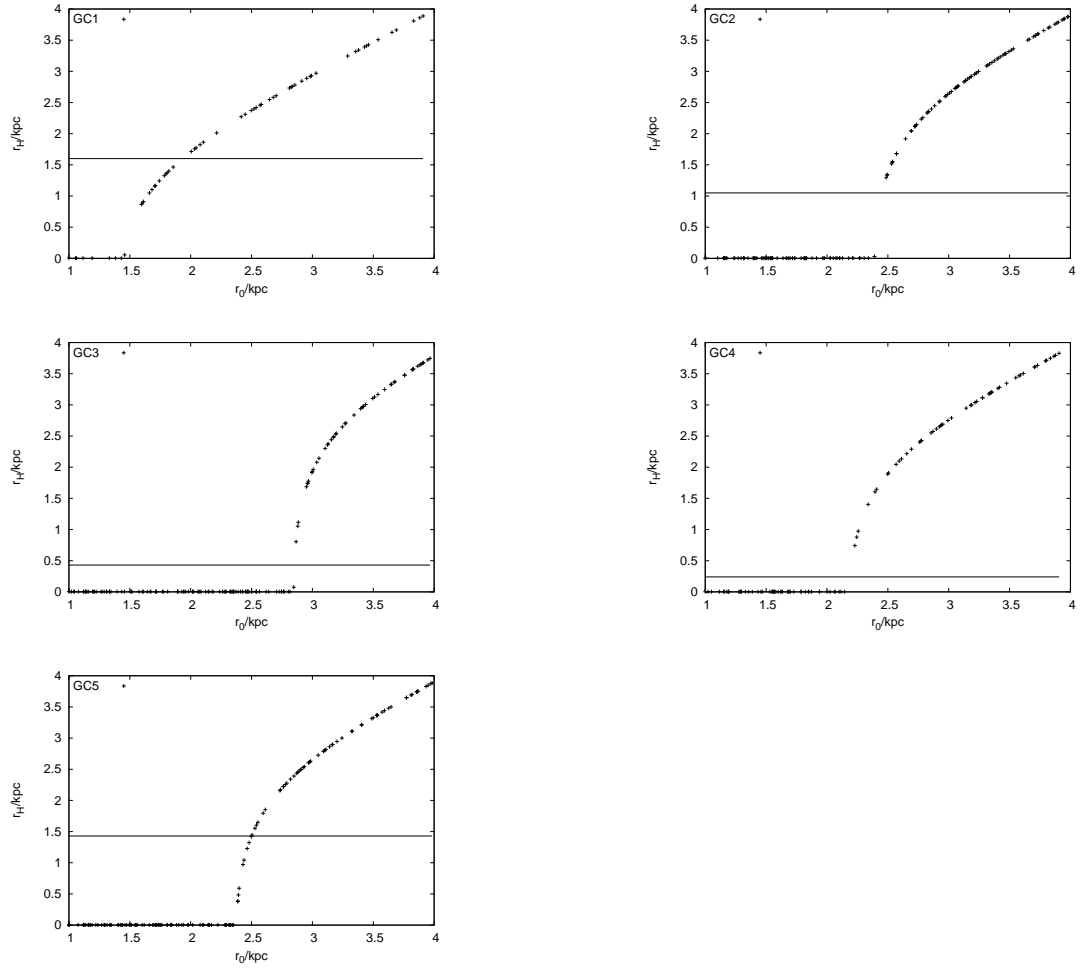


Figure 3.20: Final positions after a Hubble time of each cluster with respect its initial position in hypothesis of circular orbit. The green line represent the actual position of the cluster. Simulations have been carried out by using the semi-analycal code.

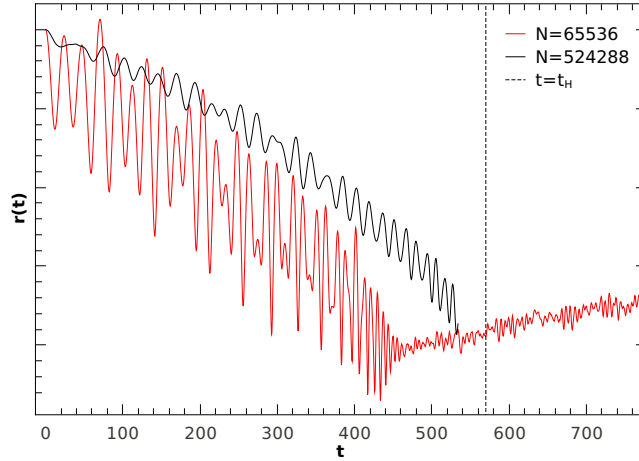


Figure 3.21: Trajectories for GC3 in two different simulations with $N = 5 \cdot 10^5$ and $6 \cdot 10^4$ particles. It is evident that in the first case, due to high number of particles the trajectory is more stable and the noise that affects the motion due to the granularity is strongly reduced.

3.2.4 Nbody simulations

To check the semi analytical calculations, as explained in Chap.2, we used direct N -Body simulations.

Fornax model M1 has been sampled by using the the widely known code NEMO [112], while to sample model M2 has been used a more accurate code we developed entirely in our group (see Appendix Chapter C).

To integrate the motion of the particles, we used the direct Nbody integrator HiG-PUs [25], a Hermite 6th order integrator that exploit completely GPUs computational power. The code is enclosed in the AMUSE project and it is freely available at - <http://amusecode.org/> .

The whole system contained $N = 524,288$ particles in order to keep reasonable computational time and minimize granularity effects that should be very important as it has been shown in Chap.2.

Just as example, we shown in Fig. 3.21 the difference in trajectory when $N \leq 10^5$ and $N \geq 10^5$.

Since a complete investigation of all the possible initial conditions for each GC would require a very huge amount of time, despite of the speed of our N -Body code and the usage of GPUs devices, we proceeded as follows to save computational and human time:

- make several semi analytical simulations to find the best initial condition for the i -th GC to reproduce its actual observed position;

Table 3.8Set of initial conditions selected for the N -body simulation.

GC NAME	r/kpc	$v/(42.8kms^{-1})$
GC1	1.93	0.582
GC2	2.43	0.549
GC3	2.85	0.525
GC4	2.10	0.570
GC5	2.50	0.545

- using this initial condition, make a N -Body simulation to check the semi analytical calculation.

In Figs. 3.22 and 3.19 are compared trajectories coming from the semi analytical calculation and the N -body simulation for the model M1 and M2, respectively. As you can see, there is a really good agreement between the two approaches, convincing us that it is possible to use the semi analytical code to identify the subset of IC required to explain the timing problem.

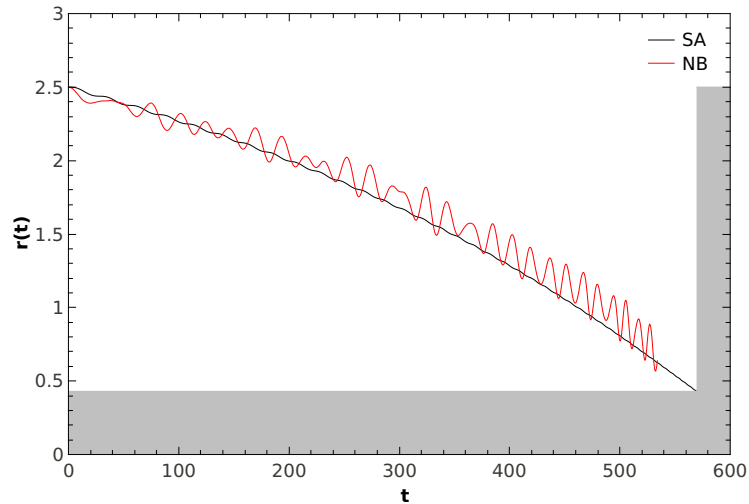


Figure 3.22: Trajectory as a function of time for GC3 starting at 2.5 kpc on a circular orbit in M1 model. As you can see, after a Hubble time, the cluster seems to be still on orbit, in a position really close to that is actually observed ($r_{now} = 0.43kpc$).

3.2.5 Self interaction effects

Concerning the model M2, we used the best ICs found with the semi-analytical integrator to perform a N -body simulation in which all the clusters evolve at the same time, together with the background galaxy. In Tab. 3.8 are shown the initial conditions used.

In Fig. 3.23 are shown the trajectories of the clusters in the space after a Hubble time.

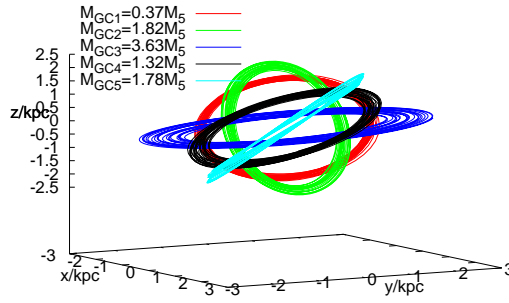


Figure 3.23: Simulated N -body trajectories of the Fornax clusters. Masses indicated in the labels are in unit of $10^5 M_\odot$.

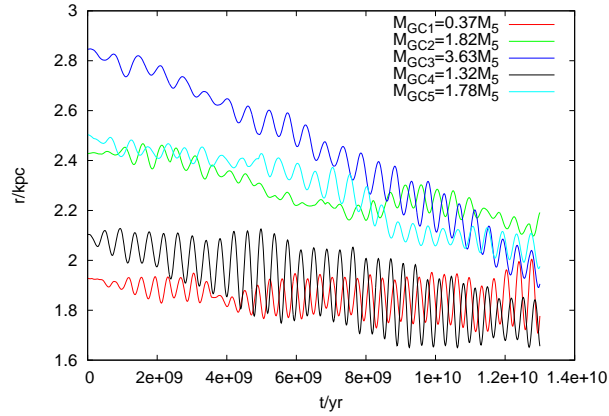


Figure 3.24: The evolution in time of the distance of each cluster from the center. As you can see, interactions between the clusters prevent their decay.

The N -body simulation reveals an interesting consequence of the fact that we are dealing with a dwarf galaxy: there is a non negligible effect of self interacting among the clusters, which suppresses in a very efficient way the decay, as it is shown in Fig. 3.24.

This effect seems to be crucial in solving the timing problem; in fact, if self-interactions between the clusters is considered, the range of optimal ICs would enlarge enough to solve the timing problem in a natural way.

3.2.6 Summary

The work I made on the timing problem in Fornax is still in a preliminary phase. Here I would summarize briefly my first results:

- we give a reliable estimation of the tidal radius of Fornax, using a composite model for the Milky Way which take in account its main components;

- concerning the M1 model, using semi-analytical simulations we showed that the sink of Fornax clusters can be avoided in a wide range of IC, without assumption about their distribution or orbital parameters;
- we simulated the decay of the cluster GC3 with a direct N -body simulation, to validate our semi-analytical treatment, founding that exist at least one set of IC which predict the observed position of the cluster;
- concerning the M2 model, we made a wide set of semi-analytical simulations of each cluster in circular orbits, selecting the initial position required to reproduce actual positions of the clusters; the calibration of these simulations has been made thanks to the N -body code used;
- we simulated the contemporary decay of all the clusters with the N -body code, finding that the self-interaction between them cannot be neglected, in fact, this interaction could avoid in a natural way the sink and solve the timing problem.

In the future, we will explore the consequences of the self-interaction between clusters by using a large set of direct simulations in order to constraint the space of IC required to obtain the actual projected positions of the Fornax clusters.

CHAPTER 4

THE FORMATION OF NUCLEAR STAR CLUSTERS

A galactic nucleus is a region in which various astrophysical phenomena interact and co-exist together. In the last few years, great interest has been refocused onto the central region of galaxies.

Thanks to the high resolution images provided by the Hubble Space Telescope, it is clear nowadays that the nuclei of the majority of elliptical and early type spiral galaxies ($M > 10^{10} M_{\odot}$) harbor supermassive black holes (SMBHs), whose mass is between $10^6 - 10^9 M_{\odot}$ up to the case of the SMBH in NGC1277 with $M_{BH} \sim 10^{10} M_{\odot}$ [117].

In many cases, the central SMBH is surrounded by a massive, very compact, star cluster commonly referred as Nuclear Star Cluster (NSC).

NSCs are observed in galaxies of every type of the Hubble sequence [19, 32] and their modes of formation and evolution are still under debate.

What we know, at present, is that NSCs are placed at the photometric and kinematic centre of the host galaxy, i.e. at the bottom of the potential well [20, 88]. This could be the reason for a peculiar formation history. In fact, if all the observed NSC have an old stellar population ($t_{age} > 1$ Gyr), most of them have also a young population of stars, with ages below 100 Myr.

NSCs are very massive objects ($10^6 - 10^7 M_{\odot}$) with a half-light radius of $2 - 5$ pc, much more luminous than ordinary globular clusters (GCs), about $4mag$ brighter.

Small sizes and high masses make the NSCs the densest stellar system in the universe [86].

The relation between NSCs and SMBHs is poorly known; they are two faces of the same coin, a “central massive object” (CMO) that depends on the host masses: galaxies with mass above $10^{10}M_{\odot}$ host a SMBH while lighter galaxies, have a well resolved NSC. Moreover, a transition region exists between $10^8 - 10^{10}M_{\odot}$ in which both the objects co-exist.

With regard to the lack of evidence of NSCs in high mass galaxies, one possible explanation is the formation of giant ellipticals through merging of smaller galaxies [81]. Quantitatively speaking, Bekki and Graham simulations showed that if the two colliding galaxies host SMBHs, a black hole binary (BHB) would form which heats the resulting stellar nucleus causing its evaporation [15]. This process shapes significantly the density profile of the merger product and can destroy the super cluster, leaving only a BHB that shrinks due to gravitational wave emission leading eventually to a SMBH.

Moreover, it is possible that in the early phase of the galaxy life, an initial NSC could be the seed for the BH birth as suggested by [87].

Recently, a number of researches had shown that scaling relations between NSC and their hosts hold; however, it is still unclear if these relations are connected to that between SMBHs and the hosts.

As example, Ferrarese et al. had shown that the NSC mass vs velocity dispersion ($M_{NSC} - \sigma_G$) relation is roughly the same observed for SMBHs ($M_{NSC} \propto \sigma_G^{-4}$) [46]. On the other hand, more recent studies ([74], [57]) claimed that the $M_{NSC} - \sigma_G$ relation is shallower than the $M_{SMBH} - \sigma_G$ ($M_{NSC} \propto \sigma_G^{1.5}$).

Moreover, it has been demonstrated that while SMBHs masses correlate with the galaxy mass, NSCs better correlate with the bulge mass.

At present, there are two debated scenarios for the NSC formation.

One scenario gives rise to the so called in-situ model: an injection of gas, i.e. for a merging event, yields to the formation of a NSC if the dynamical times of the merging galaxies are shorter than the Salpeter time $t_S \propto M_{BH}/\dot{M}_{Edd}$, with \dot{M}_{Edd} the Eddington mass rate. In this case, the central BH cannot grow quickly enough to prevent gas inflow, so it can accrete to the center until the mass reaches a saturation value and the NSC is thus formed [79].

In the second one, instead, the action of the dynamical friction process leads to the sink of globular clusters (GCs) toward the center of the host galaxy [23, 105, 114]. Their subsequent merging leads to a NSC will have a mass roughly equal to the total amount of decayed mass in form of GCs.

However, both of the two theories above encounter some troubles in explaining completely the formation process: according to some considerations, the in situ model predicts too massive NSCs, while a possible problem of the GCs infall model is that it gives lighter NSCs than observed [74].

Several authors provided detailed numerical tests for GCs merger scenario [14, 24]. Antonini et al. (hereafter AN12) simulated the decay and merge of 12 GCs in a Milky Way model including the presence of the $4 \times 10^6 M_{\odot}$ central black hole, through direct N-body simulations, obtaining a NSC that had global properties fully consistent with those observed in the nucleus of our galaxy [3].

Actually, as an improvement of the work done in AN12, we also test the dry merger scenario with a direct N-body simulation in order to improve and confirm their results.

We include in our simulation a Salpeter IMF with segregation for each decaying cluster to see whether or not a distribution of masses can modify the decay, or the final structure of the NSC.

Moreover, we modeled a greater region of the Galaxy (up to $100pc$), sampling the total system (galaxy+BH+GCS) in such a way that each star of the galaxy has a mass equal to the mean mass of the GCs stars.

The galaxy has been sampled with a total number of particles $N = 1,048,576$, 4 times about greater than that used in AN12, to investigate the effect eventually induced by the granularity of the system.

It is interesting to point out that the simulation we performed has been carried out in few days by using our own workstation. This has been possible taking advantage by the using of a fast, high parallel N-body code called HiGPUs [25]. Further information about this simulation will be provided in Appendix D.

However, such number of particles is only a tiny fraction of the real number needed to simulate a real galaxy ($N > 10^9 - 10^{11}$ particles), and modern hardware doesn't allow to simulate such a huge number.

Due to this, another approach to understand whether the dry merger scenario can explain the observed scaling laws connecting NSCs and their hosts is needed.

In this chapter I will show, by means of analytical, numerical and statistical arguments, that the dry merger model fits very well with the scaling relations holding for NSCs, resulting in a quite good agreement with observations.

4.1 NSC formation hypothesis: Globular Clusters infall scenario

The formation of a compact nucleus in the center of a galaxy through the orbital decay of globular clusters has been discussed for the first time by Tremaine et al. [114]. Working on a model of M31 galaxy, they demonstrated that the efficiency of the dynamical friction mechanism could provide an enough amount of matter to form a compact nucleus of $10^7 - 10^8 M_\odot$ in the center of the galaxy.

Capuzzo-Dolcetta has turned out the importance in considering the tidal disruption of the clusters as a competitive process that could disable the effect of dynamical friction [23].

Beside the infall scenario, another theory for NSCs formation has been developed by McLaughlin et al. [79] but it not will discussed here.

In this paper we would show how is it possible to predict NSCs mass both from an analytical and statistical point of view by using a proper treatment of the dynamical friction effect.

To do this, galaxies are modeled as Dehnen spheres which density profiles are given by:

$$\rho(r) = \frac{(3 - \gamma)M_G}{4\pi R_G^3} \left(\frac{r}{R_G} \right)^{-\gamma} \left(\frac{r}{R_G} + 1 \right)^{\gamma-4}, \quad (4.1)$$

with M_G the total mass of the galaxy, R_G its lenght scale and $\gamma > 0$ an index that gives the steepness of the profile. In astrophysical context, $\gamma < 0.3$ for giant galaxies ($M > 10^{10} M_\odot$) while $0.5 < \gamma < 1$ for smaller ones ($M < 10^{10} M_\odot$) [72, 81].

In this kind of systems, i.e. systems with a cusp in the density, it has been widely demonstrated that the classical Chandrasekhar formula fails in dealing with df mechanism (see for example [92], [66], [5]).

Arca Sedda and Capuzzo-Dolcetta [7] provided a more realistic formulation for the process giving a useful expression for the dynamical friction timescale:

$$\tau_{df} = (2 - \gamma)\tau_0(1 + g(e)) \left(\frac{M}{M_G} \right)^{-\alpha} \left(\frac{r}{R_G} \right)^\beta, \quad (4.2)$$

where γ , M_G and R_G are given above; τ_0 is a normalization factor and $g(e)$ depends on eccentricity e of the satellite orbit, being 0 for radial orbits and 3.93 for circular. Giving

explicitly the dependence from e :

$$g(e) = 3.93(1 - e),$$

α instead is approximately 0.6 while β is roughly 1.76 with a weak dependence from the mass of the cluster.

4.1.1 Data sample

As data base for the purposes of this work we considered three independent papers. The first ([42], hereafter EG12) combines data coming from different works covering Hubble types S0-Sm; on another side [74] (hereafter LKB12) provides data for 51 early type galaxies of the Advanced Camera Virgo Cluster Survey [31]; finally, we considered data given in [103] (hereafter SG13) which, again, collected data from earlier works.

The resulting total sample of 112 galaxies covers a wide range of Hubble types.

4.1.2 Modeling the host galaxy

The df timescale given in Eq.(4.2) had been developed by fitting results on the df decay times for massive satellites moving in a cuspy galactic density profile with different orbital eccentricities.

Looking at this equation, the relevant parameters determining the df efficiency are 4; 3 of them are directly related to the host galaxy (γ , M_G and R_G) while e is related to the satellite orbital initial conditions.

The mass of the host is fixed in the range $10^8 M_\odot \div 10^{12} M_\odot$ going from dwarf elliptical galaxies to giant ellipticals.

Due to the fact that, in general, galaxies fainter than $M_V \sim -20.5$ show steep luminosity profiles with slope > 0.5 (the so-called “power-law galaxies”), while brighter galaxies show less pronounced cusps (“core” galaxies) [72, 81], for each galaxy mass M_G , the γ exponent is randomly chosen in the range $0 \div 0.3$, when $M_G < 10^{10} M_\odot$, or in the range $0.5 \div 1$, when $M_G > 10^{10} M_\odot$.

A typical lenght scale observed in galaxies is the effective radius R_e , which is the radius enclosing half luminosity of the galaxy. This radius is connected to the half mass radius R_h by the relation:

$$R_e = 3/4 R_h, \tag{4.3}$$

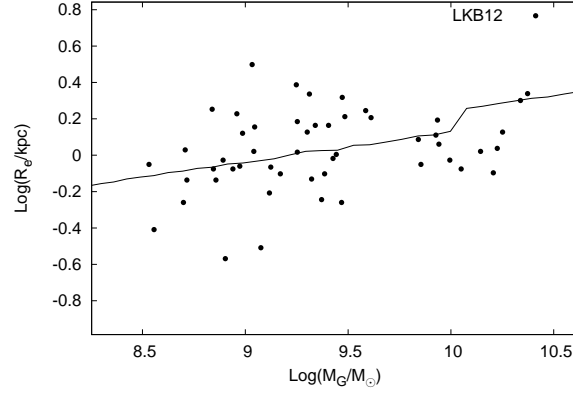


Figure 4.1: *Effective radius as a function of the galaxy mass. Black filled circles are data given in [74]*

in the hypothesis of a uniform mass-to-light ratio.

The half mass radius for Denhen models is connected to the length scale R_G :

$$R_h = \frac{R_G}{[2^{1/(3-\gamma)} - 1]}, \quad (4.4)$$

so R_G it has been chosen in order to obtain estimation for the effective radii in agreement with observations.

To obtain reasonable effective radius, we allow R_G to vary following the relation:

$$R_G = 0.3 \left(\frac{M_G}{10^8 M_\odot} \right)^{1/6} \text{ kpc}. \quad (4.5)$$

In Fig.4.1 are compared observed effective radii (the data are given in LKB12) with respect R_e evaluated by using Eq.4.3 combined with Eqs.4.4-4.5.

To give an estimation of the total radius of the galaxy we developed the following relation:

$$R = 10 R_G \left(\frac{M_G}{10^8 M_\odot} \right)^{1/6} \text{ kpc}, \quad (4.6)$$

in order to obtain total radii going from \sim kpc for dwarf galaxies to several kpc for giant ellipticals. As example, for a galaxy mass $M = 10^{12} M_\odot$ we obtain a total radius of $R \simeq 65$ kpc, that is a reasonable value for such a mass (the supergiant elliptical galaxy M87 has a radius $R \leq 100$ kpc, comparable to this value).

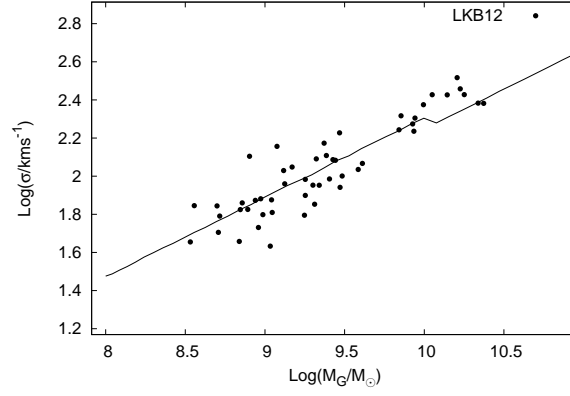


Figure 4.2: Modeled velocity dispersion compared with observations.

Another parameter that could be inferred by observations is the velocity dispersion σ_G of the galaxy. For our models, by varying the galaxy mass, we evaluate σ_G following Cappellari et al. [22]:

$$\sigma_G^2 = \frac{GM_G}{5f_\Omega R_G}, \quad (4.7)$$

where $f_\Omega = \Omega_b/\Omega_m$ is the baryonic mass fraction; we assumed $f_\Omega = 0.16$ as LKB12.

In Fig.4.2 are compared observed σ_G (LKB12) with respect values given by Eq.4.7.

Looking at both figs.4.1-4.2, the good agreement between our models and global parameters of observed galaxies convinces us that we modeled the hosts as well as possible in order to obtain reliable estimation of df times and, as consequence, reliable NSC masses.

Several authors had shown that the correlation between the bulge and the NSC mass is more dispersed than the $M_{NSC} - M_G$ relation [42].

This is related also to the fact that many galaxies are actually bulgeless systems.

Since it is difficult to define a bulge in ellipticals, we evaluate it in our models by using the correlation bulge-host given in EG12:

$$\log\left(\frac{M_B}{10^{9.7}M_\odot}\right) = (1.23 \pm 0.17) \log\left(\frac{M_G}{10^{9.7}M_\odot}\right) + (-1.21 \pm 0.13). \quad (4.8)$$

This allows us to sample bulges in good agreement with the observed values, as it is shown in Fig.4.3.

Another relevant ingredient is the globular cluster system (GCS) total mass.

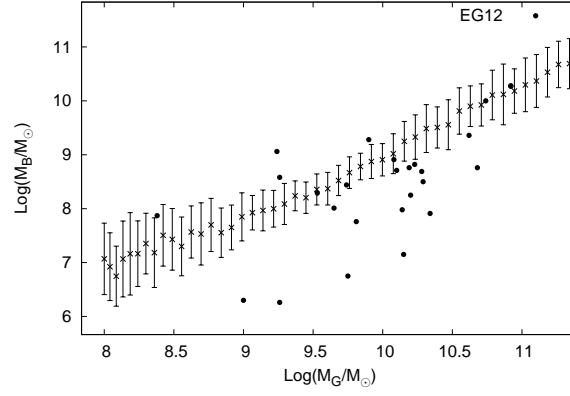


Figure 4.3: *Bulge mass in our theoretical models (crosses) compared with observed values (fill circles).*

A lower limit for the GCS mass could be obtained considering that the ratio between the NSC mass and the galaxy mass goes from $\sim 10^{-3}$ for smaller galaxies ($M_G \simeq 10^8 M_\odot$), up to 10^{-2} for the largest (M_G up to $10^{12} M_\odot$). This suggests a weak correlation between the GCS initial mass and the galaxy mass.

An expression for this correlation is

$$M_{GCS}(0) = 2 \times 10^{-3} \left(\frac{M_G}{10^8 M_\odot} \right)^{7/6}. \quad (4.9)$$

Due to that smallest galaxies host light globulars ($5 \times 10^3 \div 5 \times 10^5 M_\odot$), while in heavier galaxies the globulars masses range in the $10^5 \div 2 \times 10^6 M_\odot$ interval, we set the minimum and maximum value of the GC mass as a function of the galaxy mass:

$$M_1 = 5 \times 10^3 M_\odot \left(1 + \log \frac{M_G}{10^8 M_\odot} \right), \quad (4.10)$$

$$M_2 = 5 \times 10^5 M_\odot \left(1 + \log \frac{M_G}{10^8 M_\odot} \right). \quad (4.11)$$

As we will show in Sec. 4.2.2, this choice gives mean GC masses in good agreement with observations.

4.2 Testing the dry merger scenario

4.2.1 Analytical approach

An estimate of the NSC mass may be given by means of the following considerations: let $\Psi(M, r)dMdr$ be the number of object with masses in the $[M, M + dM]$ range in the radial interval $[r, r + dr]$. The total mass of the whole GCS is thus:

$$M_{GCS} = \int_{M_l}^{M_u} \int_V M \Psi(M, r) dM d^3r, \quad (4.12)$$

where M_l, M_u indicate, respectively, the lower and upper value for the GC mass and V is the volume enclosing all the GCs.

Keeping a sufficient level of generality, we assume $\Psi(M, r)$ as the product of two functions of M and r alone:

$$\Psi(M, r) = \xi(M)\Sigma(r), \quad (4.13)$$

A suitable expression for the mass function, $\xi(M)$, is a truncated power-law (see for example [9]):

$$\xi(M) = \xi_0 M^{-s}. \quad (4.14)$$

Eq.(4.12) becomes:

$$M_{GCS} = \int_{M_l}^{M_u} \xi_0 M^{1-s} dM \int_V \Sigma(r) d^3r. \quad (4.15)$$

On the other side, the distribution over the positions can be identified as the density profile of the GCS conveniently normalized:

$$\Sigma(r) = \rho(r)/\rho_0, \quad (4.16)$$

where ρ_0 is the normalization factor.

Due to this choice, the integration over the whole space d^3r leads to the normalized total mass of the system:

$$M_{GCS} = \int_{V(R)} \rho_{GCS}(r) d^3r, \quad (4.17)$$

being $V(R)$ the volume within R which is the radius enclosing the whole galaxy.

Combining Eq.4.11 and 4.15 yields to the determination of the normalization constant ξ_0/ρ_0 :

$$\frac{\xi_0}{\rho_0} = \begin{cases} \frac{2-s}{M_u^{2-s} - M_l^{2-s}} & s \neq 2, \\ \frac{1}{\ln\left(\frac{M_u}{M_l}\right)} & s = 2. \end{cases} \quad (4.18)$$

If the host galaxy density distribution is approximated by a Dehnen γ model, all the clusters with mass $\geq M$ and moving on orbits with eccentricity $\leq e$ enclosed in the sphere of radius r_{max} have been confined closely around the galactic center in a time $\leq t$, where:

$$r_{max} = R_G \left(\frac{t}{A_\gamma} \right)^{1/\beta} \left(\frac{M}{M_G} \right)^{\alpha/\beta}, \quad (4.19)$$

by a simple inversion of Eq.4.2 and with $A_\gamma = (2 - \gamma)\tau_0(1 + g(e))$.

For the sake of the simplicity we express Eq.4.19 as:

$$r_{max} = C(M_G, R_G, \gamma, e; t) M^{\alpha/\beta}. \quad (4.20)$$

Considering that the integration of the density profile leads to the mass profile:

$$\int_{V(r)} \rho(r_*) d^3r_* = M(r), \quad (4.21)$$

an estimation of the NSC mass can be obtained by rearranging Eq.4.15 combined with Eq.4.20:

$$M_{NSC}(t) = \int_{M_l}^{M_u} \xi_0 M^{1-s} M_{GCS}(r_{max}) dM. \quad (4.22)$$

Let's consider now a power-law distribution over the positions for the population of GCs such that:

$$M_{GCS}(r) = \begin{cases} Dr^n & r \leq R, \\ 0 & r > R. \end{cases} \quad (4.23)$$

By substituting the expression for the mass profile we obtain:

$$M_{NSC}(t) = D \frac{\xi_0}{\rho_0} C(M_G, R_G, \gamma, e; t)^n \int_{M_l}^{M_u} M^{1-s+n\alpha/\beta} dM, \quad (4.24)$$

which complete solution is given by:

$$M_{NSC}(t) = D \frac{\xi_0}{\rho_0} C(M_G, R_G, \gamma, e; t)^n \frac{M_u^{2-s+n\alpha/\beta} - M_l^{2-s+n\alpha/\beta}}{2-s+n\alpha/\beta}, \quad (4.25)$$

with $C = \left(\frac{t}{A_\gamma}\right)^{1/\beta} \left(\frac{1}{M_G}\right)^{\alpha/\beta} R_G$.

The case $n = 3$ corresponds to a flat spatial distribution, that we investigate further below.

Considering instead the γ mass profile:

$$M_{GCS}(r) = M_{GCS} \left(\frac{r}{r + R_G} \right)^{3-\gamma}, \quad (4.26)$$

the NSC mass will be given by:

$$M_{NSC}(t) = D \frac{\xi_0}{\rho_0} \int_{M_l}^{M_u} M^{1-s} \left(\frac{CM^{\alpha/\beta}}{CM^{\alpha/\beta} + R_G} \right)^{3-\gamma} dM, \quad (4.27)$$

being $C = C(M_G, R_G, \gamma, e; t)$. The complete solution in this case is given by:

$$M_{NSC} = \frac{D\xi_0\beta C^{3-\gamma}}{\rho_0} \frac{\left[-M_u^{(3-\gamma)\alpha/\beta+2-s} {}_2F_1(a, b; c; z(M_u)) + M_l^{(3-\gamma)\alpha/\beta+2-s} {}_2F_1(a, b; c; z(M_l)) \right]}{R_G^{3-\gamma}(\alpha(\gamma-3) + \beta(s-2))} \quad (4.28)$$

with ${}_2F_1(a, b; c; z)$ the Gauss's Hypergeometric Function, defined as:

$${}_2F_1(a, b; c; z) = \frac{\Gamma(c)}{\Gamma(b)\Gamma(b-c)} \int_0^1 \frac{t^{b-1}(1-t)^{c-b-1}}{(1-tz)^a} dt, \quad (4.29)$$

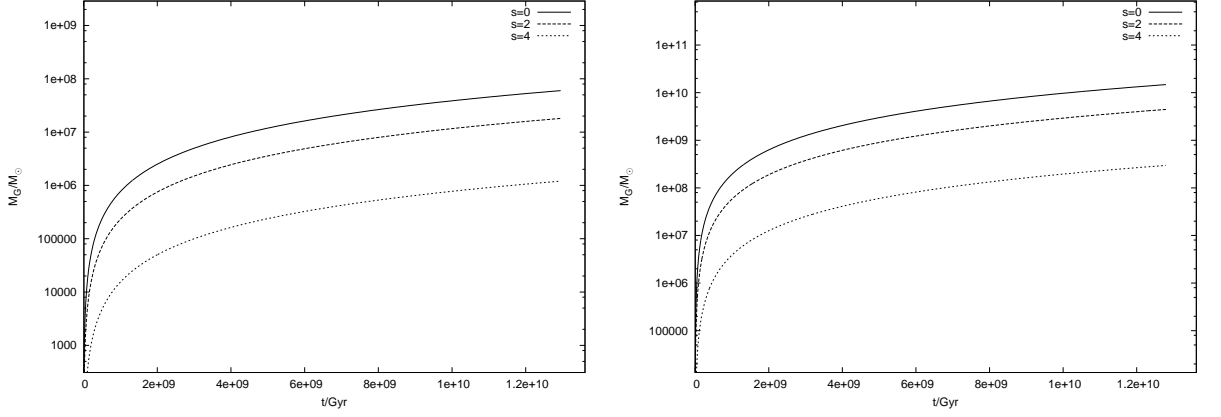


Figure 4.4: NSC mass growth for a galaxies $M_G = 10^8 M_\odot$ (left side), and $M_G = 10^{12} M_\odot$ (right side).

and the arguments in Eq.4.28 are defined:

$$\begin{aligned}
 a &= 3 - \gamma, \\
 b &= -\frac{\alpha(\gamma - 3) + \beta(s - 2)}{\alpha}, \\
 c &= -\frac{\alpha(\gamma - 4) + \beta(s - 2)}{\alpha}, \\
 z &= -\frac{CM^{\alpha/\beta}}{R_G} \\
 &.
 \end{aligned}$$

For the sake of simplicity, let's consider the simplest case of a flat spatial distribution $n = 3$; the mass of the resulting NSC as a function of the time could be estimate by selecting (M_G, γ, \bar{e}) with \bar{e} , the mean orbital eccentricity of the GCS. In the following, will be shown results obtained using this model and varying the slope of the mass distribution.

Fig.4.4 shows the NSC growth as a function of time for two extreme values of galaxy mass (10^8 and $10^{12} M_\odot$) and three different values of the s exponent of the mass function, i.e. $s = (0, 2, 4)$.

The NSC mass increases rapidly in an early phase ($t \sim 1$ Gyr) for slowing down later showing a shallow time dependence toward the Hubble time, t_H .

The predicted NSC masses are compared with observational values in Fig.(4.5). The observational data come from [42] and [74].

As it will be shown in Sec.4.3, the comparison of scaling laws between our data and observations allows to understand what is the better model.

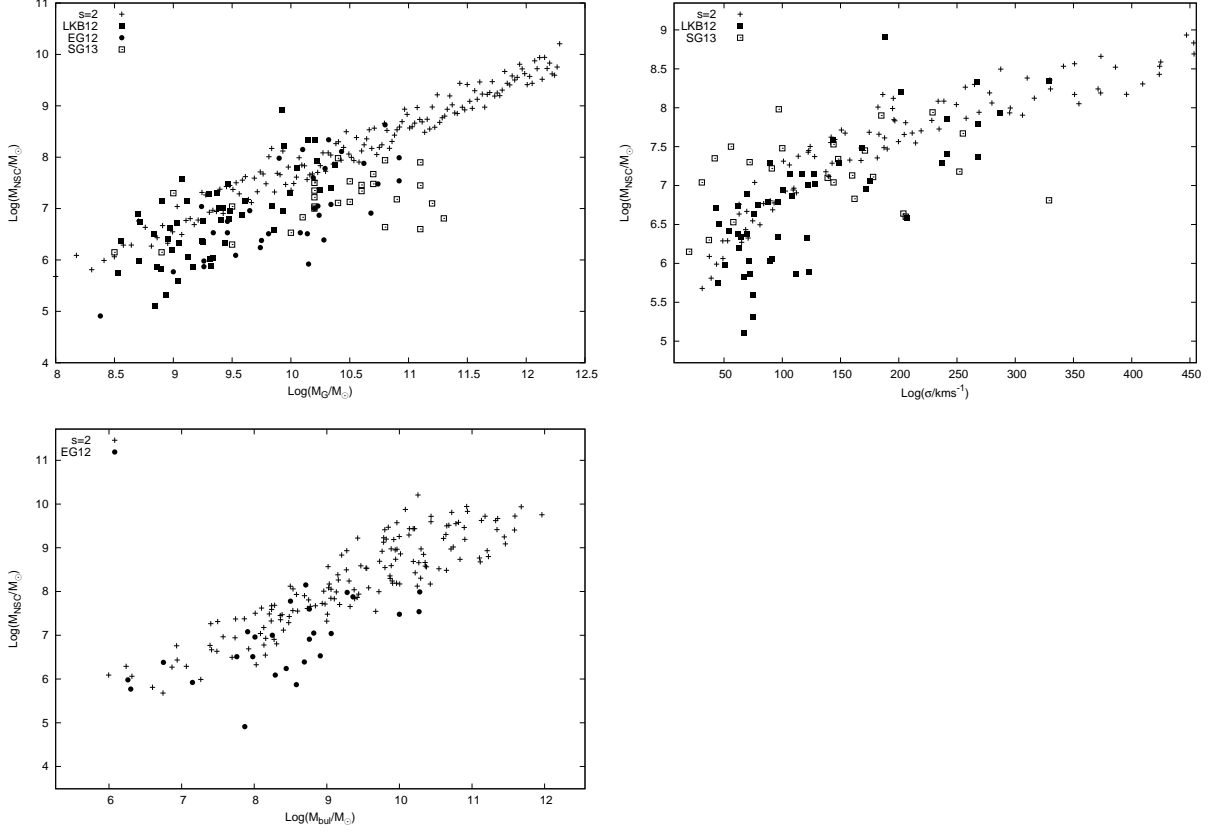


Figure 4.5: Theoretical NSCs masses with respect hosts properties (crosses), compared with data from LKB12 (filled squares), EG12 (filled circles) and SG13 (open squares). From top to the bottom, NSCs masses are compared with hosts masses, velocity dispersion and bulge mass, respectively.

In this case, the best agreement is achieved with $s = 2$, because the scaling laws discussed in Sec.4.3 agree better with observed laws.

It is relevant noting that the mass distribution of young luminous clusters (YLCs) in many galaxies is a power-law with a spectral index ranging between $s = 1.8$ and $s = 2$ [122]. Assuming such power-law as initial mass function for a GCS, Baumgardt showed that the following evolution leads toward a good agreement with up to date observations [9].

4.2.2 Statistical approach

Beside the analytical method illustrated above to estimate the NSCs masses, we investigate the infall scenario also from a statistical point of view, in order to obtain informations on the radial distribution of GCs in the host galaxy, the number of globulars centrally decayed and of those survived.

The idea behind this statistical approach is to sample the initial GCS of a given galaxy, and evaluate how many GCs are able to sink toward the galactic center within a Hubble time. To give a statistical estimate of the expected NSC mass, we sampled N_s times the GCS for each galaxy, giving also an estimation of the error. Each galaxy was modeled as explained in Sec.4.1.2, while, for each cluster, we sampled its initial position, r_0 , and orbital eccentricity, e , from a flat distribution.

From this GCS sampling it is possible to infer two interesting parameters to compare with the observations.

The first is the mean GC mass for any given host mass, that can be compared with data given in LKB12; the second parameter is the number of survived objects, which goes from few GCs (< 10) for small galaxies ($M_G \sim 10^8 M_\odot$), to few hundreds in intermediate mass galaxies and up to 10^4 in giant ellipticals.

The strong dependence of the df braking time on the individual GC mass (see Eq.4.2) deserve a careful treatment in sampling GC, as explained in detail below.

Power-law sampling (SLP)

The sampling of GC masses was made to reproduce a power-law distribution, $dN \propto M^{-s} dM$. This model is referred to as SLP-model; it is, actually, the “statistical version” of the analytical treatment (see Sec.4.2.1).

When the exponent is $s = 0$ (flat distribution) we will refer to the RND model (random sampling).

Gaussian sampling (GSS)

Another choice to sample masses is by means of a gaussian generator. The resulting distribution has a, given, mean value $M_{mean}/M_\odot = 10^5 \left[1 + \log \left(\frac{M_G}{10^8 M_\odot} \right) \right]$, a dispersion $\sigma = 0.25$.

To exclude unrealistic, too massive, globular clusters the distribution has been truncated at low masses at $M_l < 5 \times 10^3 M_\odot$ and at thigh masses $M_u = 2 \times 10^6 M_\odot$. The resulting model is referred to as GSS.

Density profile sampling (RHO).

There is no compelling evidence that GCs and stars in the galaxy followed, initially, different density profiles, so it is worth examining the case when the initial GCS density

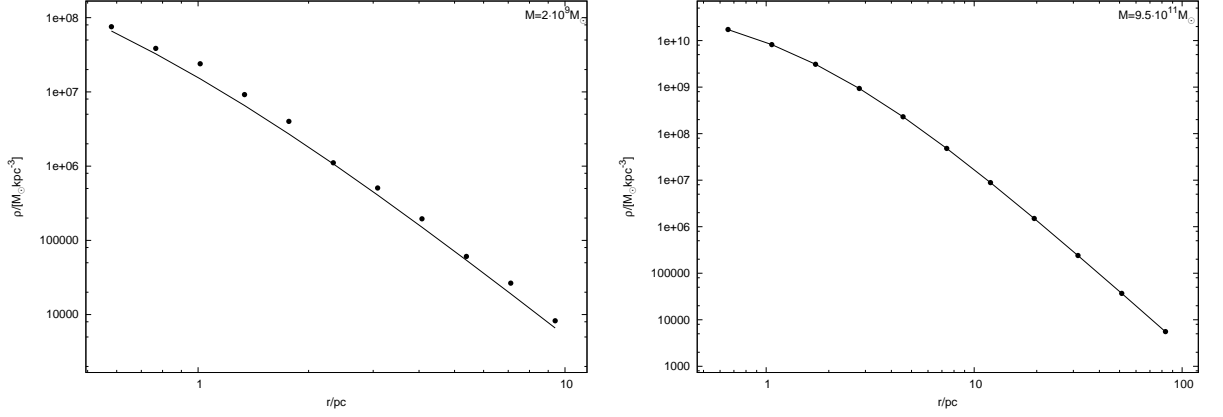


Figure 4.6: Density profile for a $M = 2 \cdot 10^9 M_\odot$ (right panel) and $M = 9.5 \cdot 10^{11} M_\odot$ galaxy (left panel). Black dots represent the sampled density while the straight line is the theoretical profile.

profile is a γ - profile with the same slope of the parent galaxy density profile (see Fig.(4.6)).

4.2.3 Results

The quality of our GC sampling can be tested, for instance, by a comparison of the GCs masses with data given in LKB12.

Looking at Fig.4.7, appears that all the models agree in general with observations.

However, the RND model seems to give an overestimation of the mean GC mass, while the SLP model gives a underestimation at high galaxy masses.

GSS and RHO models give mean masses that agree with observations both on small and high galaxy masses.

Another interesting quantity coming from this approach is the estimate of the number of “survived” clusters, which can be compared with observational data. In Fig.4.8 the number of decayed and survived clusters as a function of the hosting galaxy mass is shown.

It is not surprising to see that for massive galaxies ($M_G = 10^{10} M_\odot$) the number of survived GCs could exceed 10^4 . In fact, there are many massive galaxies hosting such a number of clusters at present. As example, we note that the giant elliptical galaxy M81 (also known as Virgo A, with a mass $\sim 2 \times 10^{12} M_\odot$ [78]) hosts 13,000 clusters around, in agreement with our prediction.

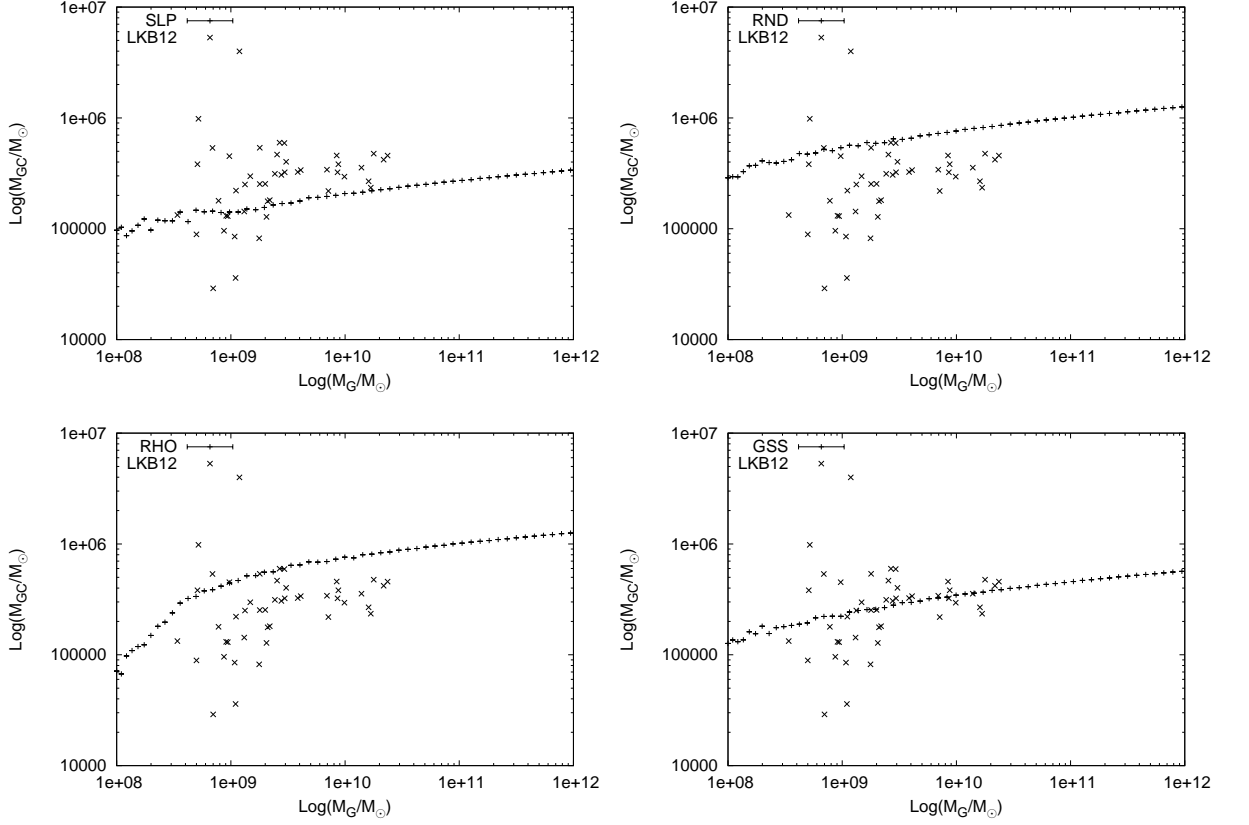


Figure 4.7: Mean mass of the sampled GCSs for each galaxy (cross) compared with data given in LKB12 (diagonal crosses). Each panel is labeled with the respective model.

In Fig.4.9 is shown the ratio between the decay time and the Hubble time t_{df}/t_H for GCs belonging to a $M_G = 10^{10}M_\odot$ sampled using SLP, RND, GSS and RHO models. All clusters with $t_{df}/t_H < 1$ are considered decayed.

It is interesting to note that only clusters lying in an innermost region could decay in a Hubble time. This region could be easily evaluated by inverting Eq.4.2 and corresponds to roughly $3kpc$ for a galaxy of such mass, assuming $R_G = 0.65kpc$, $\gamma = 0.5$, $\langle e \rangle = 0.5$ and $M \sim 10^6M_\odot$.

Therefore, the expected NSC mass is evaluated by summing all the decayed clusters. In Fig.4.10 the NSC mass vs. the host mass is reported.

Qualitatively, it seems to be again that the RHO-model fits very well observation; however only a more quantitative analysis could reveal the real agreement. For this reason could be important to draw scaling laws connecting the NSC mass with some host properties.

Fig.4.11 and Fig. 4.12 show, respectively, NSC masses as function of the host velocity dispersion and of the host galaxy bulge mass. Due to the bad definition we have about the bulge, this last relation is the worse possible.

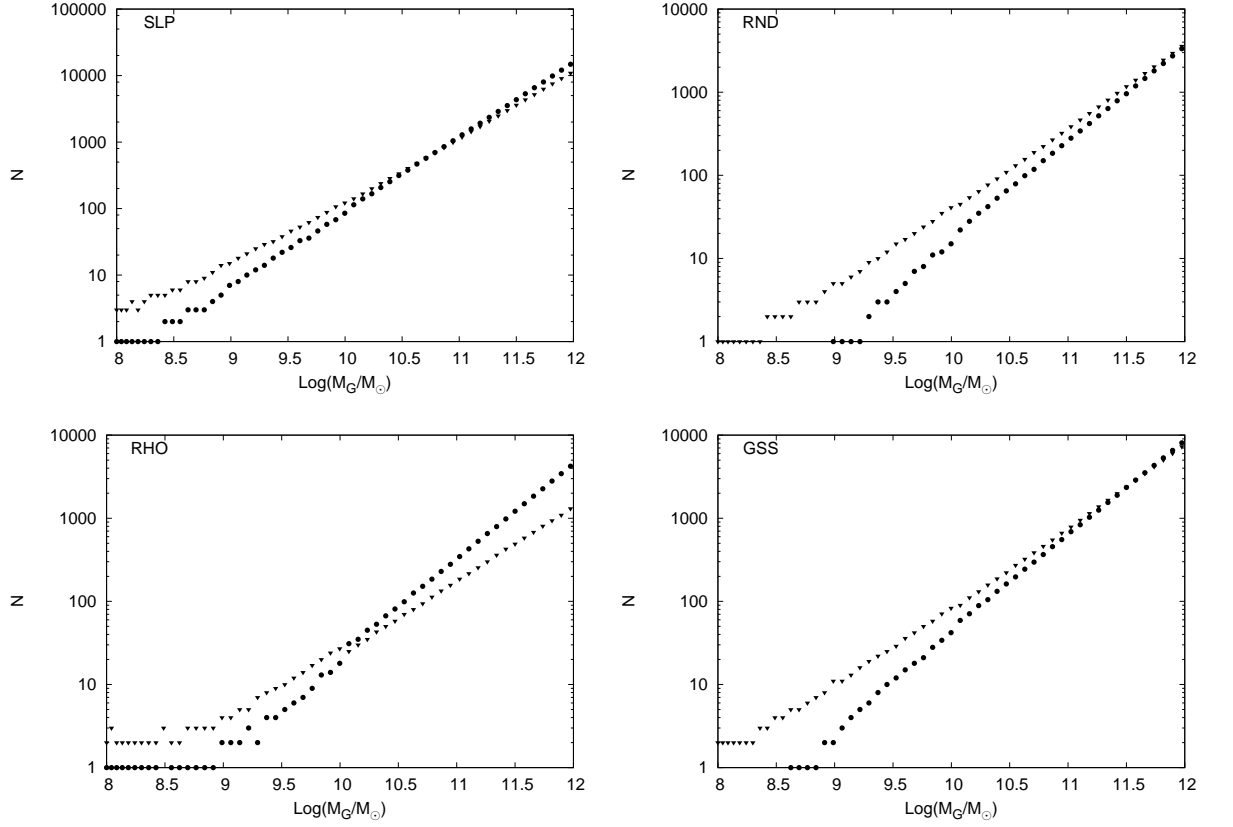


Figure 4.8: *Decayed (triangles) and survived (points) clusters within a Hubble time as a function of the host mass for each model considered.*

In the following section, scaling laws will be developed and compared with laws obtained by observations.

4.3 Scaling laws

Checking the existence of correlations and scaling relations is important to understand the actual physical mechanisms underlying the observed phenomena.

It is well known, for instance, that SMBHs correlate strongly with the host galaxy bulge velocity dispersion σ_G [46] and with the bulge mass M_B (see for example [77] and [60]), the implication is that either SMBH and galaxy growth are probably driven by similar processes. Silk and Rees suggested that a feedback mechanism exists between the early stage of life of the galaxy and the central BH [106].

In the last years, many studies were devoted to derive scaling relations among NSCs and their host galaxies, finding that they follow similar relations as SMBHs do [97]. However, it is still unclear if the two different types of CMOs really share common relations, thing that could imply an intimate link between BHs and NSCs growth and

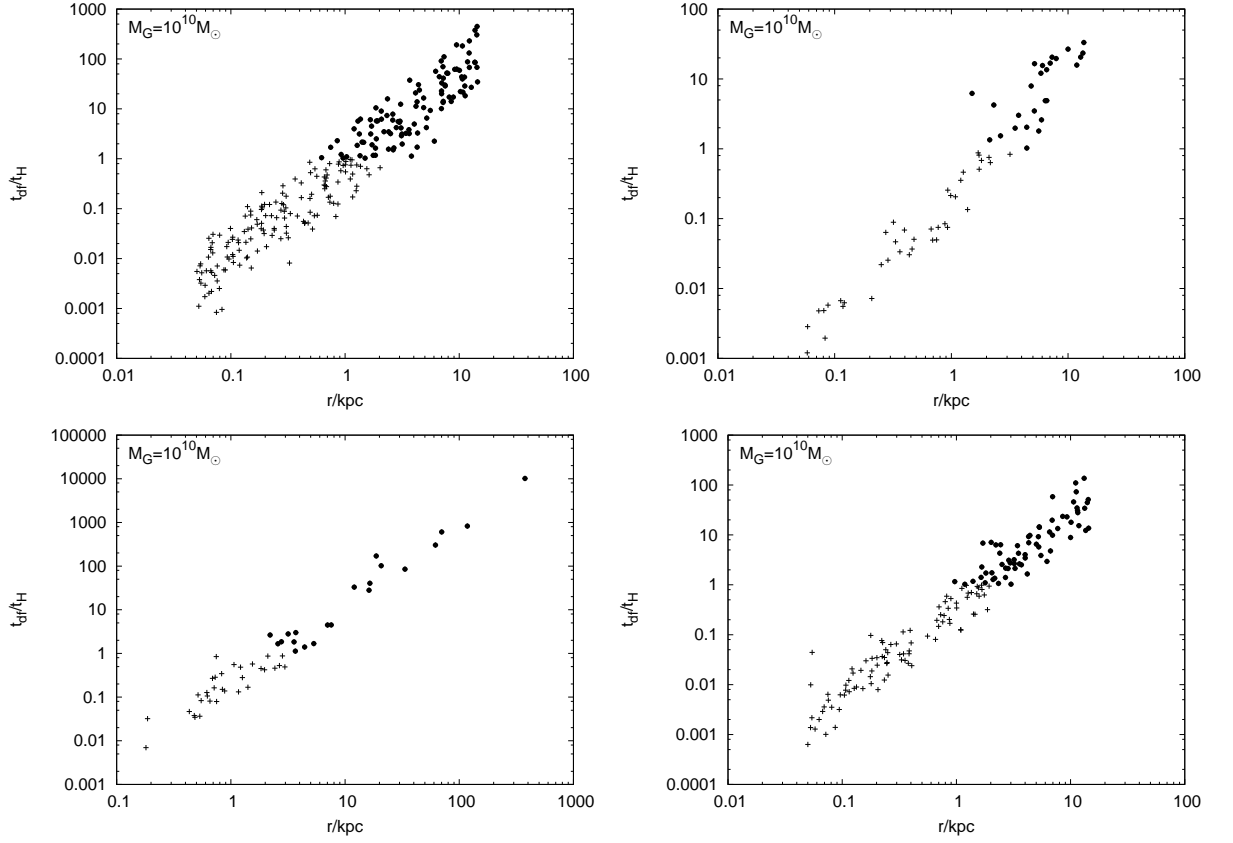


Figure 4.9: The ratio t_d/t_H is shown for a sampled galaxy $M_G = 10^{10} M_\odot$ in SLP, RND, GSS, RHO models, respectively. Decayed clusters (crosses) lie all in a region which radius is roughly $r \sim 3 \text{ kpc}$.

evolution. Actually, differences in scaling relations involving BHs or NSCs are presently debated. As an example, while Ferrarese et al. claimed that NSCs extend the $\sigma_G - M_{BH}$ relation which is a power law with an exponent between 4 and 5 [46], Graham [57] and Leigh et al. [74] finds that the exponent of the power-law differs for the two classes of objects, finding the shallower relation $M_{NSC} \propto \sigma_G^2$ for NSCs.

Moreover, while the “in situ” model is compatible with what it is found in [46], the “dry merger” scenario, instead, fits well with the conclusion drawn in [57] and [74] as we would turn out with this work.

Actually, what we know is that NSC mass seems to correlate better with the total stellar mass of the host, while the BH mass correlates better with the bulge.

Both the statistical and the analytical approaches used here allow us to draw a $M_{NSC} - M_G$ relation as well as an $M_{NSC} - M_B$ and an $M_{NSC} - \sigma_G$ relation. They can be compared with results presented in literature.

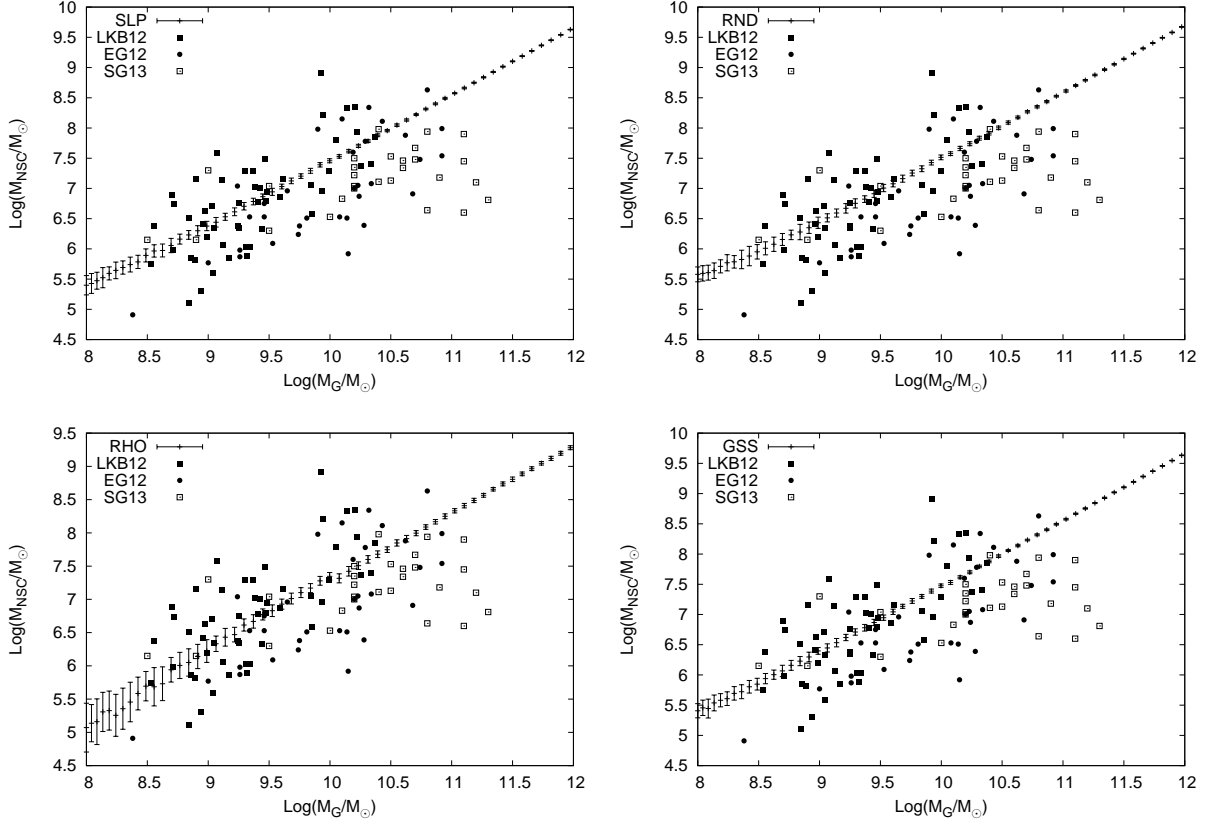


Figure 4.10: *NSCs masses with respect hosts masses. Predicted values (crosses) are compared with data given in LKB12 (filled squares), EG12 (filled circles) and SG13 (open squares).*

4.3.1 $M_{NSC} - M_G$ relation

The expected relation is a power-law whose form is:

$$\log \left(\frac{M_{NSC}}{10^{7.6} M_{\odot}} \right) = a + b \log \left(\frac{M_G}{10^{9.7} M_{\odot}} \right), \quad (4.30)$$

The best fit for the relation M_{NSC} and M_G has been obtained by using the nonlinear-regression Marquardt-Levenberg algorithm implemented in the wide known software GNUPLLOT.

Results are shown in Tab.4.1.

To compare our results with $M_{NSC} - M_G$ relation provided by analysis on observation, we consider here the slope b shown in EG12, LKB12 and SG13. Their results are shown in Tab.4.2.

To better compare different results, we plot in Fig.4.13 slope estimations for our models and literature results.

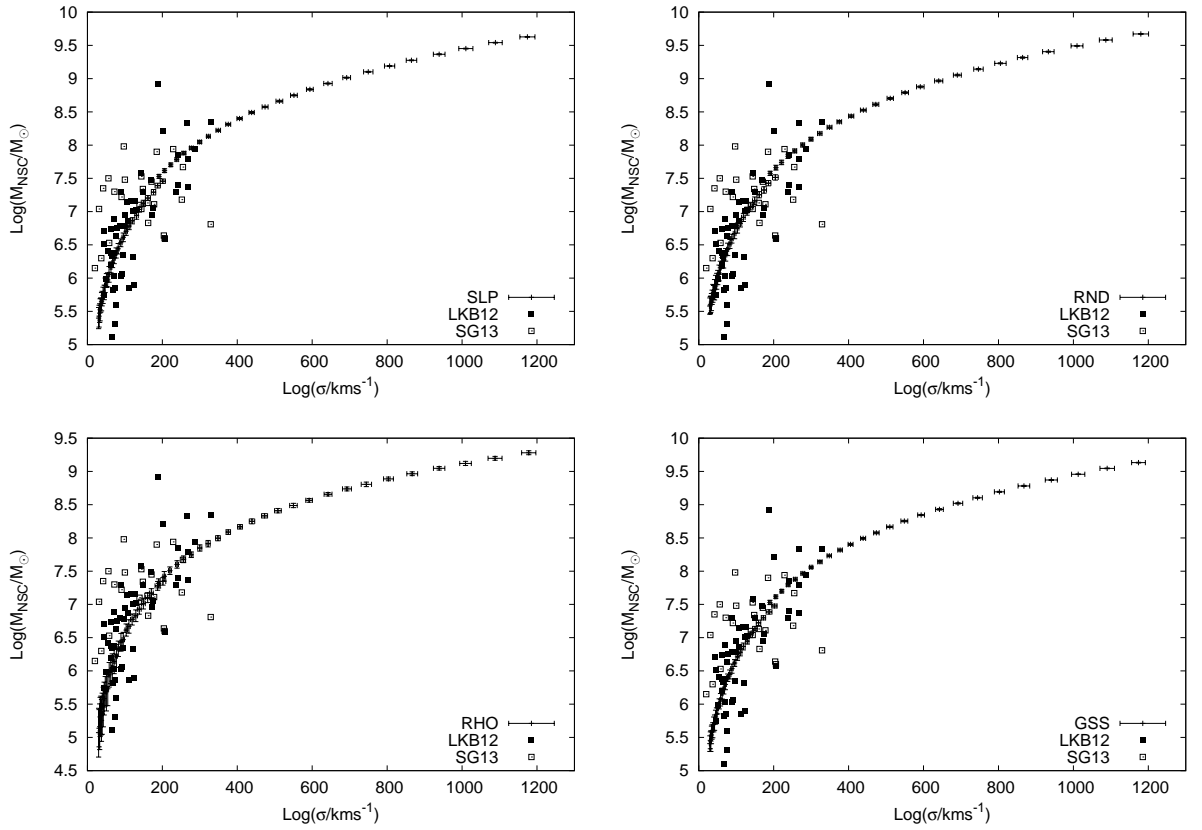


Figure 4.11: NSCs masses with respect hosts velocity dispersion. Predicted values (crosses) are compared with data given in LKB12 (filled squares) and SG13 (open squares).

Table 4.1

$M_{NSC} - M_G$ scaling relation for various model.

Model	b	err_b	a	err_a
s=2	0.955	0.015	-0.206	0.021
SLP	1.0682	0.0030	-0.4415	0.0037
RND	1.0482	0.0051	-0.3778	0.0062
GSS	1.0707	0.0028	-0.4391	0.0034
RHO	1.0488	0.0061	-0.6525	0.0075

Column 1: model name as explained in Sec.4.1.2. Column 2-5: slope b and zeropoint a and relative errors.

Table 4.2

$M_{NSC} - M_G$ scaling relation given in literature.

Model	b	err_b
LKB12	1.18	0.16
EG12	0.90	0.21
SG13	0.88	0.19

Column 1: reference paper name. Column 2-3: slope b and and relative error.

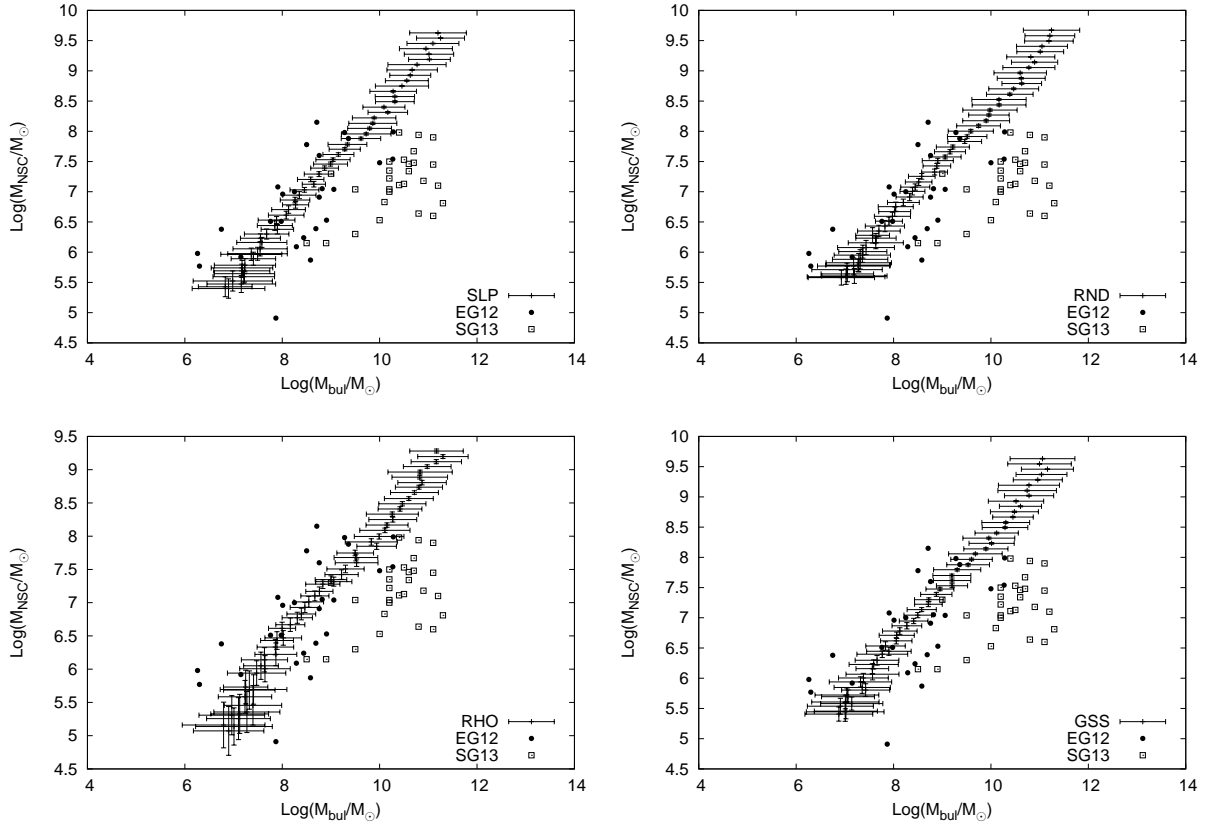


Figure 4.12: *NSCs masses with respect hosts bulge masses. Predicted values with errors (crosses) are compared with data given EG12 (filled circles).*

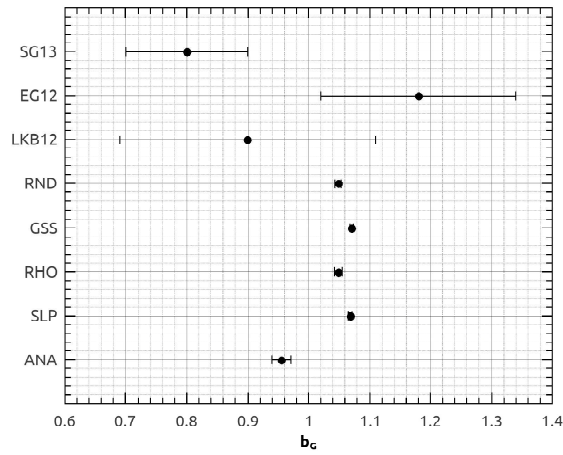


Figure 4.13: *The slope of the $M_{\text{NSC}} - M_G$ relation, b_G , with its own error is shown for each model used and compared with data. Y axis denotes the reference works and our models.*

Table 4.3 $M_{NSC} - M_B$ scaling relation for various model.

Model	b	err_b	a	err_a
s=2	0.732	0.028	1.36	0.27
SLP	0.971	0.019	-1.37	0.20
RND	0.960	0.017	-1.22	0.19
GSS	1.000	0.028	-1.61	0.30
RHO	0.840	0.012	-0.31	0.13

Column 1: model name as explained in Sec.4.1.2. Column 2-5: slope b and zeropoint a and relative errors.

The slopes of $M_{NSC} - M_G$ relation obtained with observations and with our approach are shown in Tabs.4.2, 4.1. Comparing the results, turns out that both the analytical ($s = 2$ model) and statistical approaches (SLP, GSS, RND and RHO models) give a slope in agreement with the observed relation within the errors.

The comparison is also shown in Fig.4.13, where the slope (x axis) with the associated error, is shown for each model considered (y axis).

4.3.2 $M_{NSC} - M_B$ relation

It has been shown that NSC mass correlates better with the total galaxy mass, while the correlation with the bulge is, in some cases, not statistically significant [42].

Using the bulge masses as given by Eq.4.8, the slopes of the correlation between M_{NSC} and M_B for our various models are obtained and given in Tab. 4.3.

As only term of comparison we have the slope derived in SG13:

$$b = 0.88 \pm 0.19,$$

that is in good agreement with all theoretical predictions as it is shown in Fig.4.14.

4.3.3 $M_{NSC} - \sigma_G$ relation

The correlation between NSC mass and the host galaxy velocity dispersion, σ_G , is probably the most interesting because it gives useful hints about relations between the two types of CMO objects (SMBHs and NSCs).

It is likely, indeed, that if NSCs and SMBHs follow the same correlation with σ_G , they shared the same evolutionary path.

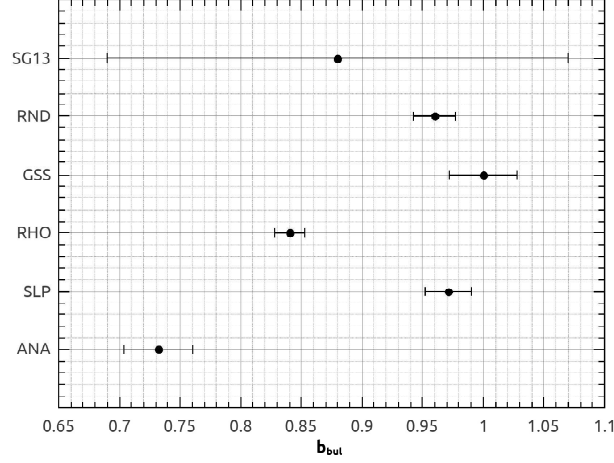


Figure 4.14: The slope of the $M_{NSC} - M_B$ relation, b_{bul} , with its own error is shown for each model used. Y axis denote models names.

Table 4.4

$M_{NSC} - \sigma_G$ scaling relation for various model.

Model	b	err_b	a	err_a
s=2	2.410	0.036	-0.336	0.021
SLP	2.699	0.015	-0.5816	0.0072
RND	2.649	0.019	-0.5139	0.0093
GSS	2.705	0.014	-0.5781	0.0067
RHO	2.651	0.012	-0.788	0.012

Column 1: model name as explained in Sec.4.1.2. Column 2-5: slope b and zeropoint a and relative errors. The relation used is: $\log(M_{NSC}/10^{7.6}M_{\odot}) \propto \log(\sigma_G/200 km s^{-1})$.

Table 4.5

$M_{NSC} - \sigma_G$ scaling relation given in literature.

Model	b	err_b
LKB12	2.73	0.29
SG13	2.11	0.31

Column 1: reference paper name. Column 2-3: slope b and relative error.

However, it is not yet clear whether this similarity does exist. Actually, while Ferrarese et al. [46] found almost the same slope (≥ 4) in the correlation of both SMBH and NSC mass with σ_G , more recent works showed that the relation is shallower for NSCs, with a slope ~ 2 (see for example [74],[42],[103]).

All our theoretical results point toward this second direction, see Tab.4.4, 4.5.

In fact, as it is shown in Fig.4.15, all the theoretical models predict a slope for the relation $2 < b_{\sigma} < 3$, in good agreement with observed values.

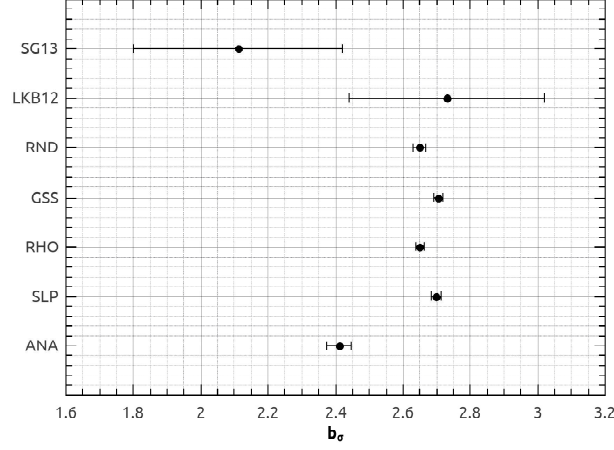


Figure 4.15: The slope of the $M_{NSC} - \sigma_G$ relation, b_σ , with its own error is shown for each model used. Y axis denote models names and results in literature.

This result would imply that NSCs and SMBHs do not share the same evolution history, or, at least, that some different kind of interaction between the two types of objects and the background occurred.

4.4 Tidal disruption effects

During their lifetime, GCs stars undergo internal evolution, experience two-body relaxation and suffer of external tidal interactions that, in some cases, can lead to their eventual complete dissolution. As it is well known, the two-body relaxation is driven by close encounters between stars bringing some of them slowly beyond the GC tidal boundary. The full dissolution is expected after few hundred times the typical two-body relaxation time [108]:

$$T_{rh} \simeq \frac{M^{1/2} r_h^{3/2}}{\langle m_* \rangle G^{1/2} \ln \Lambda N}, \quad (4.31)$$

where M is the star cluster mass, r_h its half-mass radius, $\ln \Lambda$ the Coloumb logarithm, and $\langle m_* \rangle$ is the mean mass of stars in the cluster.

Baumgardt [10], by meaning of a large set of N -body simulations, found that the dissolution time for a cluster, T_{dis} , can be connected with both the two-body relaxation time-scale in Eq. 4.31 and the crossing time of the cluster through the galaxy, T_c . The relation he found is:

$$T_{dis} = k T_{rh}^x T_c^{1-x} \quad (4.32)$$

with the exponent x depending on the initial concentration of the cluster.

This result has been generalized by Gieles et al. [52] who gave this formula for the dissolution time

$$T_{dis} = \left(\frac{M}{10^4 M_\odot} \right)^{0.62} \frac{r}{V} \frac{220 \text{ km s}^{-1}}{\text{kpc}} (1 - e) \text{ Gyr}, \quad (4.33)$$

where r is the distance from the galactic center, V the circular velocity at r , and e the eccentricity of the orbit.

A possible effect that could shorten the life-time of the cluster is the collision with giant molecular clouds. Gieles et al. [53] found that the dissolution time as a consequence of multiple collisions is given by:

$$T_{dis}^{GMC} = 2 \left(\frac{0.03 M_\odot \text{ pc}^{-3}}{\rho_n} \right) \left(\frac{M}{10^4 M_\odot} \right) \left(\frac{3.75 \text{ pc}}{r_h} \right)^3, \quad (4.34)$$

with ρ_n the molecular cloud density.

However, GMC will not be considered here, since elliptical galaxies do not contain them.

Gravitational encounters between the stellar system and a perturber, which could be a black hole, the disk, or the nucleus of the galaxy, could lead to the destruction of the system over times which are comparable with the decay time. This implies that the contribution to the destruction of clusters cannot be neglected at all.

So far, Spitzer [108], had studied this mechanism in the case in which a point mass, i.e. a black hole, M_p , perturb the orbit of a stellar system, i.e. the cluster, M_s , in the hypothesis that the duration of the encounter is short compared to the crossing time of the cluster itself. This is the so called impulse approximation, in which as a consequence of the encounter, stars in the perturbed system suffer only a change in their velocities, but not in positions. Moreover, due to the slow duration of the perturbation, the cluster motion could be approximated with a straight line.

If the perturbed system is small compared to the impact parameter, the external perturbative potential could be written as a Taylor series dropping the square terms (distant-tide approximation).

Under this hypothesis, it is possible to show that the cluster, as a consequence of the gravitational encounter, gain a total mean energy per unit mass:

$$\Delta E = \frac{4G^2 M_p^2}{3V^2 b^4} \langle r^2 \rangle, \quad (4.35)$$

where V is the relative velocity between the two systems, b is the impact parameter and $\sqrt{\langle r^2 \rangle}$ is the mean dimension of the perturbed cluster.

This equation is valid in the case in which the perturber can be approximated with a point-like object.

However, a number of studies had been done to generalize these calculations to a spherical perturber with an arbitrary mass distribution [1, 54, 55], but also in the case in which the perturber is a spherical nucleus embedded in a triaxial ellipsoid [23, 91].

Defining $U(b/r_h)$ the ratio between the impulsive energy change due to a perturber of half mass radius r_h and the change caused by a point of the same total mass, the total change in energy caused by a mass distribution is simply given by:

$$\Delta E = \frac{4G^2 M_p^2}{3V^2 b^4} \langle r^2 \rangle U(b/r_h); \quad (4.36)$$

and $U(b/r_h)$ drops rapidly to 0 when $b/r_h \leq 1$, while tend to the unity if $b/r_h > 1$.

If the energy change exceeds the internal gravitational energy of the system per unit mass:

$$E = \frac{1}{5} \frac{GM_s}{R_s}, \quad (4.37)$$

the cluster will be disrupted.

The typical decay time over which the disruption occurs can be defined roughly as the ratio between the gravitational energy of the system E and the "heating rate" due to tidal shocks:

$$\dot{E} \simeq \frac{\Delta E}{nT}, \quad (4.38)$$

where T is the orbital period of the cluster and n is the number of encounters within a period.

Therefore, the disruption time is given by:

$$t_{dis} = \frac{E}{\Delta E} nT. \quad (4.39)$$

It is possible to better quantify this typical time under the assumption that the perturber and the perturbed systems have a maxwellian distribution with velocity dispersion σ_p , σ_s , respectively.

In this case is possible to evaluate the rate of energy increase \dot{E} due to the encounters as follows.

By defining $\sigma_{rel}^2 = \sigma_s^2 + \sigma_r^2$ the relative velocity dispersion of encounters, the probability that the subject system and the perturber have relative speed in a given range is:

$$dP = \frac{4\pi V^2 dV}{(2\pi\sigma_{rel}^2)^{3/2}} \exp\left(-\frac{V^2}{2\sigma_{rel}^2}\right), \quad (4.40)$$

and the average rate at which the encounter occurs with velocity V and impact parameter b is given by:

$$\dot{C} = \frac{2\sqrt{2\pi}n_p b db}{\sigma_{rel}^3} \exp\left(-\frac{V^2}{2\sigma_{rel}^2}\right) V^3 dV. \quad (4.41)$$

It is necessary now to distinguish between two regimes: the catastrophic regime, if a single encounter could disrupt completely the system; or the diffusive regime, in which the cumulative effect of encounters leads to the disruption of the system on longer timescales.

The impact parameter which divides the two regimes b_M , is the length scale over which the energy enhancement equals the internal gravitational energy of the system $\Delta E = E$. Combining Eq.4.36 and 4.37:

$$b_M = 1.5 \left(\frac{GM_p^2 R_s^3}{M_s V^2} \right)^{1/4}, \quad (4.42)$$

where it has been used the approximation $U(b/r_h) \sim 1$ because the major contribution in energy to the impact is given when $b \simeq r_h$.

The duration of the encounter discriminate between the two regimes: hence a catastrophic collision occurs if the duration of the encounter, $t_{enc} \sim b_M/\sigma_{rel}$, is short compared to the crossing time of the cluster $t_{crs} \sim R_s/V$; on the other hand, slower encounter leads to the diffusive regime, which is a time longer than the catastrophic regime timescale.

Therefore, in the case of the catastrophic regime ($b < b_M$), the typical disruption timescale is given by integrating Eq.4.41 in the range $0 < b < b_M$ and $0 < V < \infty$:

$$t_{cat} \simeq \frac{k_{cat}}{G\rho_p} \left(\frac{GM_s}{R_s^3} \right)^{1/2}, \quad (4.43)$$

where ρ_p is the perturber density, and k_{cat} a constant.

In the diffusive regime $b > b_M$, instead, the change in energy of each particle is small compared to its velocity. In this case, it is possible to show that the disruption time is given by:

$$t_{dif} = \frac{0.043}{W} \frac{\sigma_{rel} M_s r_h^2}{GM_p \rho_p R^3}, \quad (4.44)$$

where W is defined as:

$$W = \int \frac{dx}{x^3} U(x), \quad (4.45)$$

and should be computed numerically.

We take in account tidal effects in our calculations, to investigate their effect on the NSC mass estimation. In Fig.4.16 are compared dynamical friction time t_{df} , the dissolution time t_{dis} and the tidal disruption time in the catastrophic regime t_{cat} for three different galaxy mass ($M_G = 10^8 - 10^{10} - 10^{12} M_\odot$) as a function of the radial position r . We performed the estimation setting the GC mass $M = 10^6$ and circular orbit.

The disruption time due to tidal shocks is less than the dynamical friction time only for galaxies with masses above $10^{10} M_\odot$ in a region in the range $0.1 - 100 kpc$. Hence, tidal shocks could affect significantly the mass of the decayed clusters but in a little region (10 to $100 pc$) around the center of the galaxy the decay of clusters is the dominant process depending on the mass and eccentricity of the cluster.

Due to the two competitive processes, it is clear that the number of decayed clusters depends strongly by their distribution in the space.

In the RND, SLP and GSS models, we set as minimum distance from the galaxy center for the GCs sampling $d = 50 pc$. Clusters lying in the first $50 - 100 pc$, massive enough ($M \gtrsim 10^6 M_\odot$) or with eccentric orbits are likely to decay and contribute to the final NSC mass. In Fig.4.17 is shows the number of decayed clusters to the total number for the RND model, considering or not the tidal disruption.

As you can see, while in small galaxies quite all the clusters can be considered decay, even considering the tidal disruption mechanism, in massive galaxies to consider the effects of the external field would correspond to a reduction of the estimation of the NSC mass.

However, since the percentage of decayed objects decreases by a factor $1/5$, the expected decrease in the mass of the central NSC should be roughly the same, and it is a change not very dramatic considering that NSCs for very massive galaxies ($10^{12} M_\odot$) are expected to have masses above $\sim 10^9 M_\odot$.

In the RHO model, instead, the minimum distance from the galaxy center allowed for GC formation is given by the constraint that the GCS mass profile follows a Dehnen profile, therefore it could exceed $\sim 50 pc$. In this case, as we can see in Fig.4.18, the number of decayed clusters in very massive galaxies drops to zero and NSC cannot form.

The difference between the RHO model and the others, is that here clusters are distributed in the space following the Dehnen density profile, while in the other models

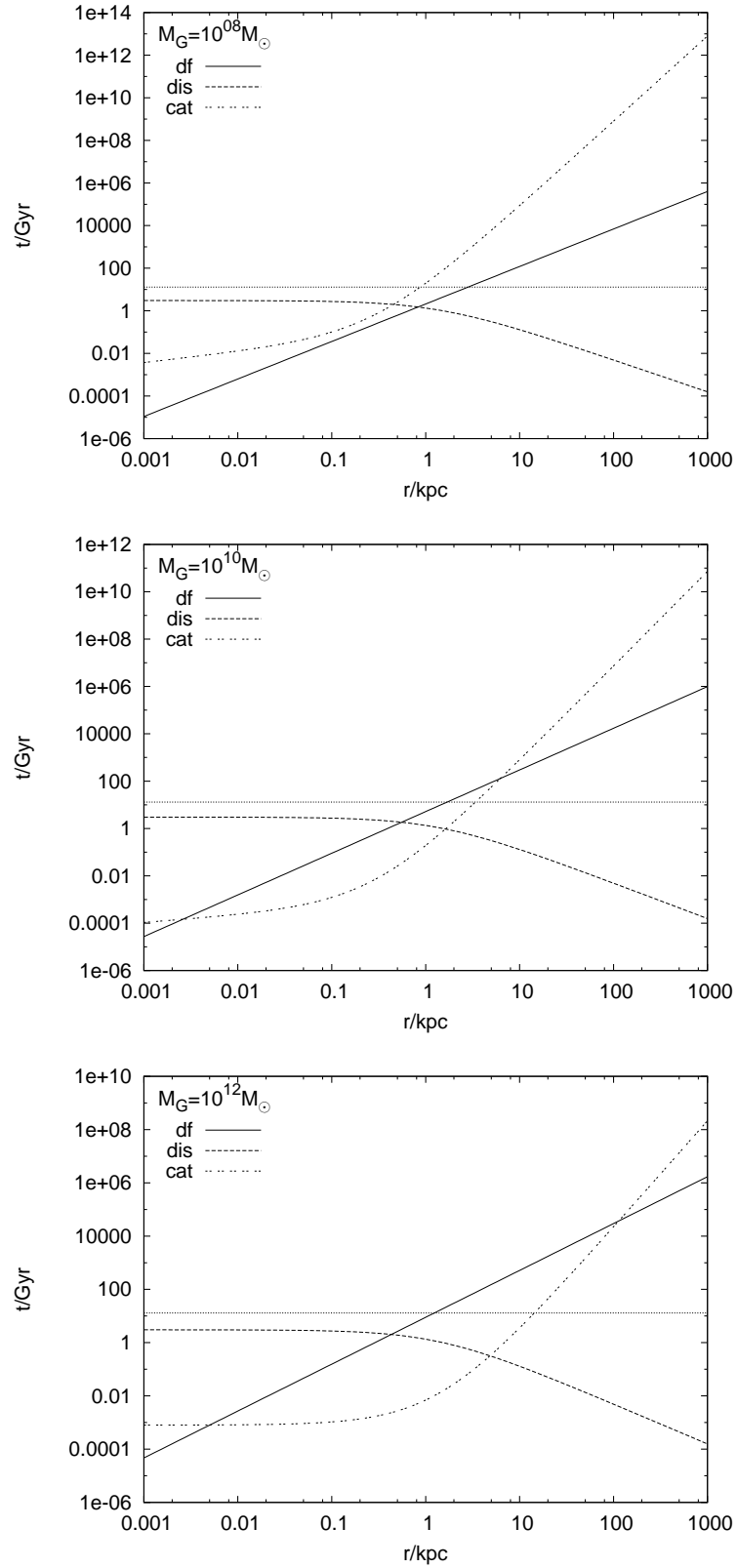


Figure 4.16: Dynamical decay and disruption times for a globular cluster on circular orbit for three different galaxy masses (from top to bottom: $10^8 - 10^{10} - 10^{12} M_\odot$). In smaller galaxies, friction process dominates on all length scales, while in heavier systems the tidal disruption is much more rapid in a region 1kpc around, suppressing the friction mechanism.

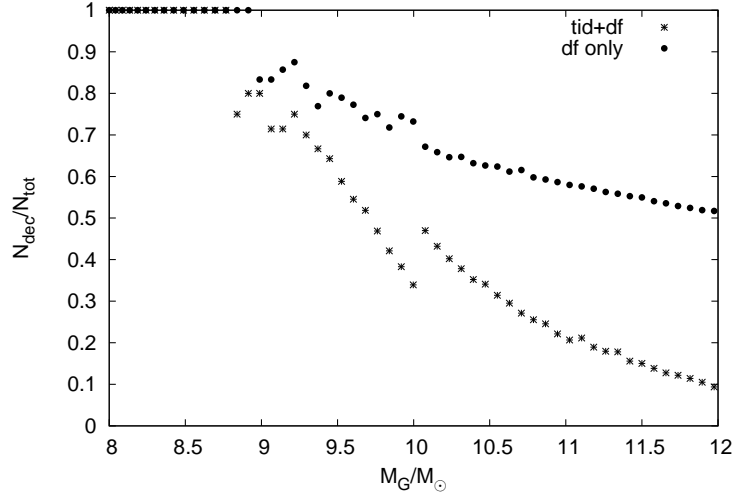


Figure 4.17: The number of decayed clusters to their total number considering only *df* (stars) or taking into account the tidal shock mechanism (black circles) in the RND model. As you can see, the number of decayed clusters in massive galaxies decrease by a factor 5 when tidal disruption is considered, changing by roughly the same factor the NSC final mass.

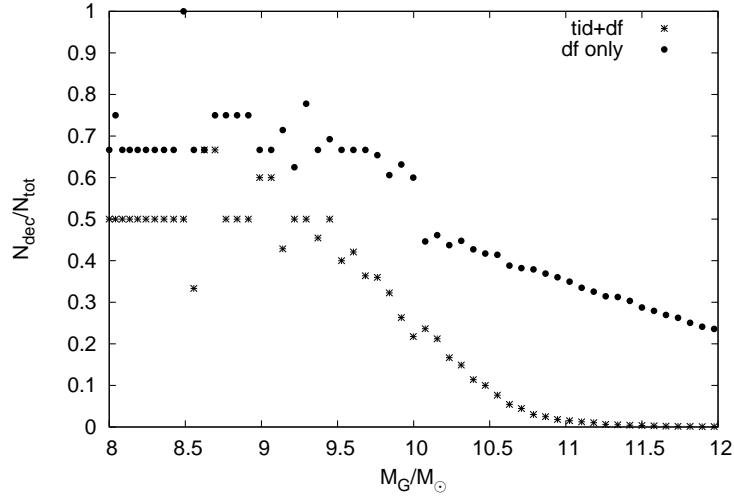


Figure 4.18: Same as in Fig.4.17, but for the RHO model. In this case, the number of decayed clusters for massive galaxies drops to 0 and there is no NSC formation.

positions are sampled randomly. This put in evidence two interesting things: the mass distribution of the clusters is not very important in deriving the NSC mass, but instead, it is very important how the clusters are distributed within the galaxies. This is due to the fact that at intermediate scales, the disruption time is smaller compared to the decay time, but it is not in the central region, within few hundred of parsecs. Hence a concentrated spatial distribution, allows the formation of the NSC because clusters in the innermost region of the galaxy decay rapidly; on the other hand, a lack of clusters in this small region, implicates that disruption process dominates over the decay process

and the NSC formation is suppressed.

In Fig.4.19 are shown NSC masses with respect to hosts masses for the RHO model taking in account the tidal disruption process. As you can see, tidal interaction suppress strongly the NSC formation for galaxies masses above $10^{10.5}M_{\odot}$, putting on evidence how much is important the spatial distribution of the clusters.

It is interesting to note that in this case, deriving the scaling relations discussed above, we found again a good agreement with the observations if we restrict the comparison in the observed range of masses ($10^8 - 10^{11}M_{\odot}$)

4.5 Summary

I found that the dry merging scenario could predict masses for NSCs and scaling laws between them and their host galaxies in excellent agreement with observations. Summarizing my results:

- reliable galaxies models have been provided, as it has been show comparing theoretical and observative global properties;
- a completely general, analytical treatment as been developed to estimate NSCs masses without assumptions about mass and spatial distribution of the cluster systems;
- assuming a power-law mass function and an uniform spatial distribution, analytical predictions fit very well observations;
- the consequences of different mass distributions on NSCs final masses has been investigated from a statistical point of view, sampling for each galaxy the whole GCS and considering how many clusters was able to sink to the galactic center within a Hubble time;
- the analysis on the statistical approach allowed to obtain some useful parameters, such as the GCs mean mass and the number of survived clusters, which resulted in good agreement with observations;
- scaling laws which connect the NSC with total mass, velocity dispersion and bulge mass of the host, have been developed; the agreement found between all the model considered and observations indicates that the GCs mass distribution should not play a crucial role in determining the final NSC mass;

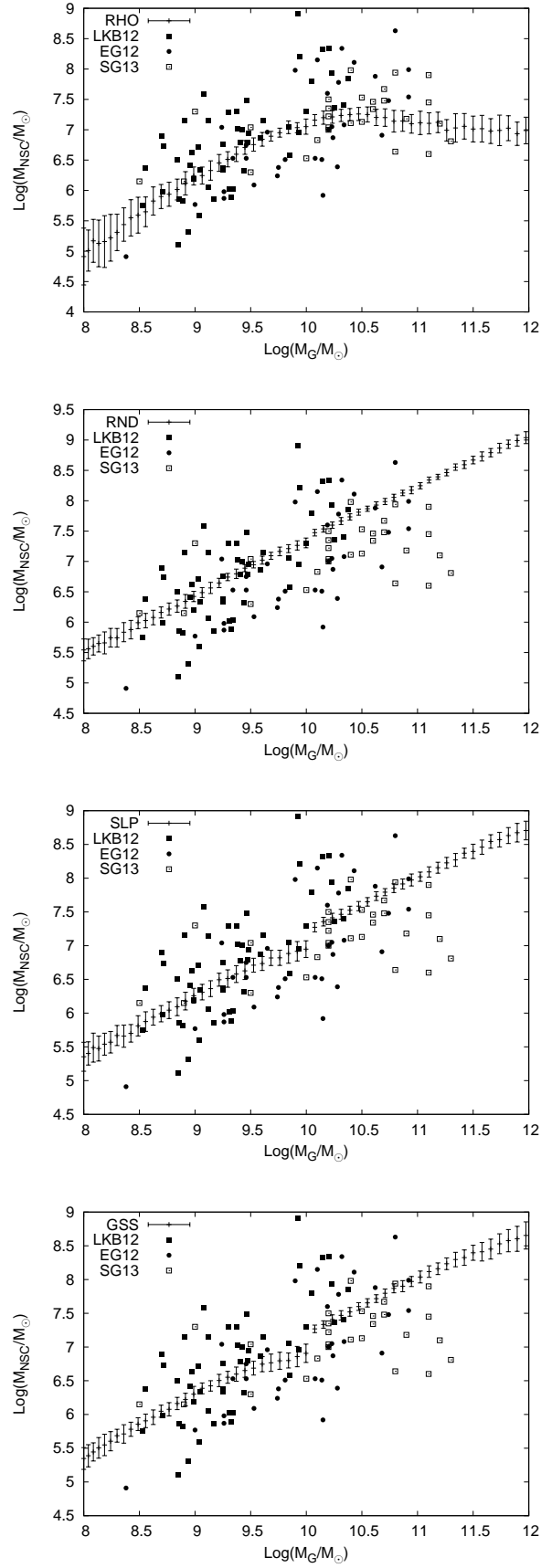


Figure 4.19: *NSC masses as a function of the galaxy mass for all the models considered taking in account the tidal disruption processes.*

- disruption mechanism have been investigated, considering both two body relaxation and tidal heating processes. In RND, SLP and GSS models tidal heating causes a decrease of predicted masses from few percent in small galaxies (down to $10^{10}M_{\odot}$) to 20% in heavier galaxies. On the other hand, tidal disruption strongly affects NSC formation in RHO model, where the predicted masses are almost constant in the range $10^{10} - 10^{11}M_{\odot}$.

The action of tidal heating gives some interesting hints about the lacking of high mass NSCs.

In the next chapter, this problem will be discussed and a possible explanation will be proposed from different points of view.

CHAPTER 5

THE LACK OF HIGH MASS NSCS

The presence of a NSC in a galactic center is, in general, argued by searching for central excesses in the luminosity profiles of galaxies (see Fig.5.1). However, it has been mentioned in Chap. 4, that is very rare to find such excesses in galaxies whose masses are above $10^{11}M_{\odot}$.

Various theories have been developed to explain this lack of nucleated region in massive galaxies; quite ever it is attributed to the dynamical effects induced by the central SMBH.

As example, giant elliptical galaxies are thought to be origin from the merging of smaller galaxies. If the colliding galaxies contain either a SMBH and a NSC, at the center of the merger product could form a black hole binary system (BHBS), which can heat the surrounding nucleus, causing its evaporation [81].

Another possibility is that the central black hole can prevent the NSC formation destroying tidally its building blocks, decaying star clusters.

Moreover, it could be possible that a NSC smaller than expected forms, as it has been shown in the last chapter, and that, due to its low mass, it cannot be recognized through the analisys of luminosity profiles.

Combining the scaling laws between the NSC, the SMBH and the host, it could be easily find that the limit over which galaxies seem to not contain NSCs correspond roughly to the limit in which the BH mass exceed the NSC mass ($M_{SMBH} > M_{NSC}$); this could connect in some way the lack of NSCs to the SMBH mass.

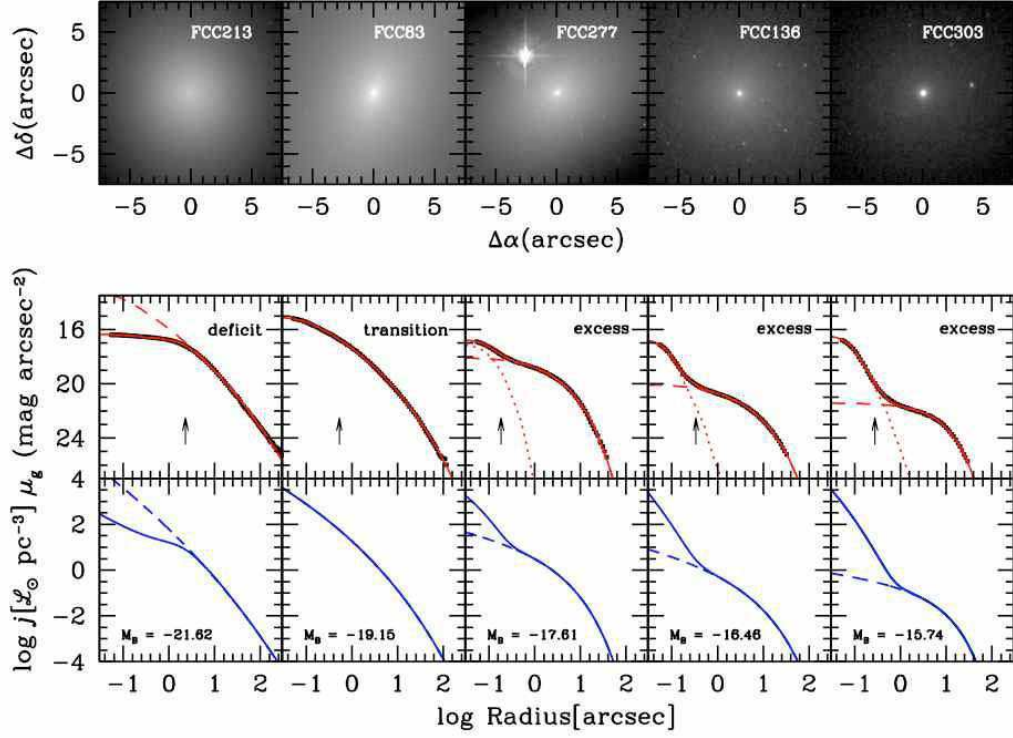


Figure 5.1: *Detection of NSCs by meaning of the surface luminosity profile [115].*

In this framework, we explored the effects of tidal forces exerted by the SMBH on the building blocks of the NSC, i.e. the decaying clusters, to check whether or not the tidal disruption process could prevent efficiently the NSC formation.

5.1 Modeling the host galaxies and the cluster

To understand if the tidal action of the central BH could prevent the formation of a NSC, we simulate the decay of a single cluster (GC) by varying the galaxy mass, i.e. the central BH mass, through N -body simulations.

The aim is to understand which effect dominates on the evolution between the dynamical friction effect, which drives the formation of the NSC in the dry merging scenario, and the tidal disruption effect, which instead suppress it.

In a direct N -body simulation, both the effects come out as a natural consequence of the mutual nature of the gravitational force.

All the simulations have been run on our workstation by using HiGPUs, the N -body code mentioned in previous sections.

The high efficiency of HiGPUs and the high quality of our hardware allowed us to use a total number of particles very high ($N = 1,048,576$) to sample both the galaxy and the cluster at a relatively small computational cost, allowing us to carry out a wide set of simulations in less than a month.

It should be noticed that the whole system has been set in such a way that stars belonging to the galaxy and the cluster have the same mass.

Host galaxies

To sample the whole system (galaxy+BH+GC), it would be required a huge number of particles.

To avoid this problem, we modeled only a small region of the galaxy in order to keep reasonable number of particles both in the galaxy and the cluster.

The sample has been made by meaning of a truncated density profile, using as truncation function the hyperbolic cosine [80]:

$$\rho_{trun}(r) = \rho(r) / \cosh(r/r_{cut}), \quad (5.1)$$

with $r_{cut} = 70pc$.

In this way, the density profile corresponds to a self-consistent and stable model.

The density profiles, $\rho(r)$, used were the Tremaine profiles [124]:

$$\rho(r) = \rho_0 \left(\frac{r}{r_s} \right)^{-\gamma} \left(\left(\frac{r}{r_s} \right)^{\alpha} + 1 \right)^{(-\beta+\gamma)/\alpha}, \quad (5.2)$$

with the choice ($\alpha = 1, \beta = 4$) corresponding to the Dehnen profiles. The length scale, r_s , depends on the galaxy model (see Tab. 5.1) while the density scale is defined $\rho_0 = (3 - \gamma)M/(4\pi r_s^3)$.

To sample the galaxy, we developed a code which takes into account the contribution to the total potential of a central point-like mass (see Appendix C).

We verified that the system (galaxy+BH) sampled this way was stable over reasonable dynamical times.

By varying the galaxy mass in the range $[10^{10} - 3.2 \cdot 10^{11} M_{\odot}]$, we followed the orbital evolution of the cluster for circular, radial and eccentric orbits starting at initial position $r_0 = 50pc$.

Table 5.1

Parameters of the simulations.

$M_{gal}(M_{\odot})$	$M_{BH}(M_{\odot})$	$r_s(pc)$	$r_{cut}(pc)$	γ	$M_{cut}(M_{\odot})$	N_{gal}	N_{clu}	$m_*(M_{\odot})$
10^{12}	1.5×10^9	3766	70	0.15	9.2×10^7	1037332	11243	89
$3.2 \cdot 10^{11}$	5×10^8	2876	70	0.2	6.8×10^7	1033332	15243	66
10^{11}	10^8	1917	70	0.2	5.9×10^7	1031338	17237	57
$3.2 \cdot 10^{10}$	2×10^7	1512	70	0.3	4.1×10^7	1024025	24550	41
10^{10}	5×10^6	995	70	0.3	3.4×10^7	1018742	29832	34

The set of simulations made is resumed in Tab. 5.1.

Globular Cluster model

The cluster has been modeled with a King profile using $W_0 = 6.5$ and $r_{core} = 0.1$, such that it is considered dynamically evolved, taking in account that we are looking at the very last stage of the cluster's trajectory. The mass of the star cluster is slightly high, $M = 10^6 M_{\odot}$, but justified by the fact that only very massive clusters can sink to the center of the host within a reasonable time, especially when the ratio between the cluster mass and the galaxy mass is small enough.

The number of particle used for the cluster goes from nearly 30,000 for the smallest galaxy considered ($M_{gal} = 10^{10} M_{\odot}$) to more than 10,000, such that there is ever a reasonable number of stars to ensure that the evolution of the cluster is driven mainly by its interaction with the environment in which it moves and not by granularity effects.

5.2 Runs analysis

Some qualitative hints about the interactions between the cluster and the SMBH can be obtained by looking at the snapshots of the simulations performed. Considering the simulation in which the galaxy has a mass $M = 10^{12} M_{\odot}$, the tidal interaction due to the SMBH is so strong that disrupts the cluster immediately, making clear that such a cluster cannot reach that region of the galaxy without a significant change in its density profile. In other words, to reach the inner region of such massive galaxy, the cluster should be more massive or concentrated.

For this reason, we can consider this simulation as an upper limit to the “resolution power” of our simulations, due to our choice about the probe used, i.e. the GC model considered.

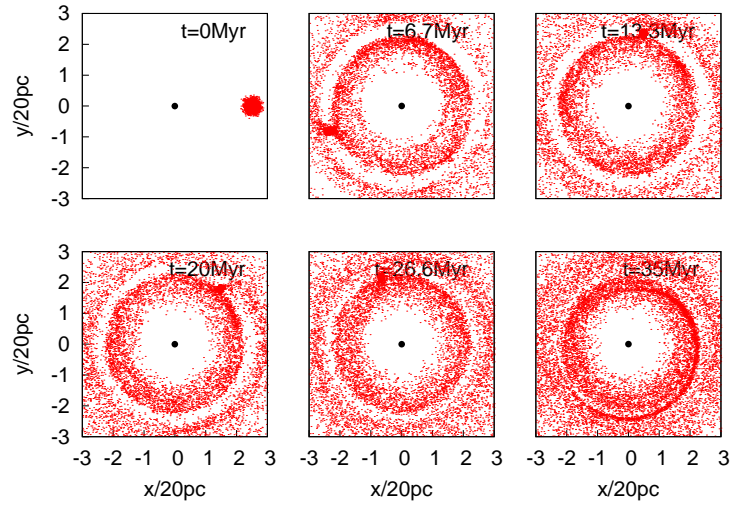


Figure 5.2: Each snapshot represents the cluster (red dots) and the BH (black point) for a circular orbit. The galaxy has a mass $M_{gal} = 3.2 \cdot 10^{11} M_{\odot}$.

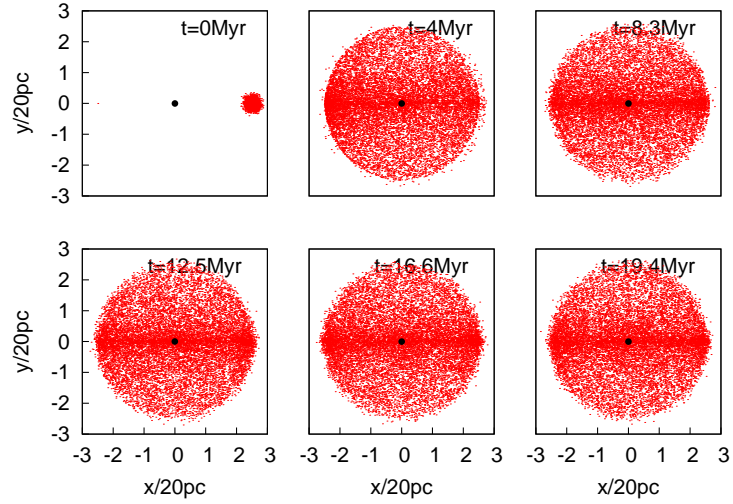


Figure 5.3: Same as in Fig. 5.2, but for a radial orbit.

In Figs. 5.2, 5.3 are shown several snapshots of the cluster trajectory for circular and radial orbits in the case $M_{gal} = 3.2 \cdot 10^{11} M_{\odot}$. As you can see, the cluster tends to disgregate completely in a few *Myr* in both cases.

However, when a smaller galaxies is considered, the cluster can reach the center without loosing its shape significantly only in the last stage of the orbital evolution (see Figs. 5.4, 5.5).

The disruption effect suffered by the cluster could be due to the evolution of the distribution of the background stars; however, it has been checked that background density profile does not evolve during the orbital evolution of the cluster. As example, in Fig.

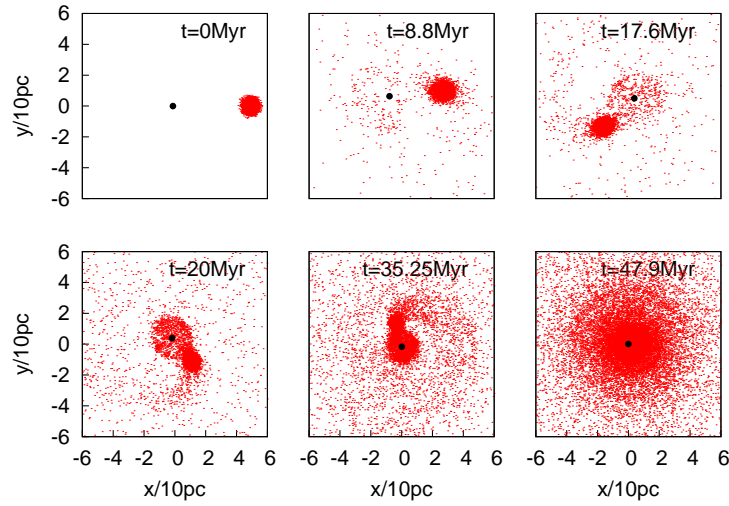


Figure 5.4: Same as in Fig.5.2, but the galaxy has a mass $M_{gal} = 10^{10} M_{\odot}$

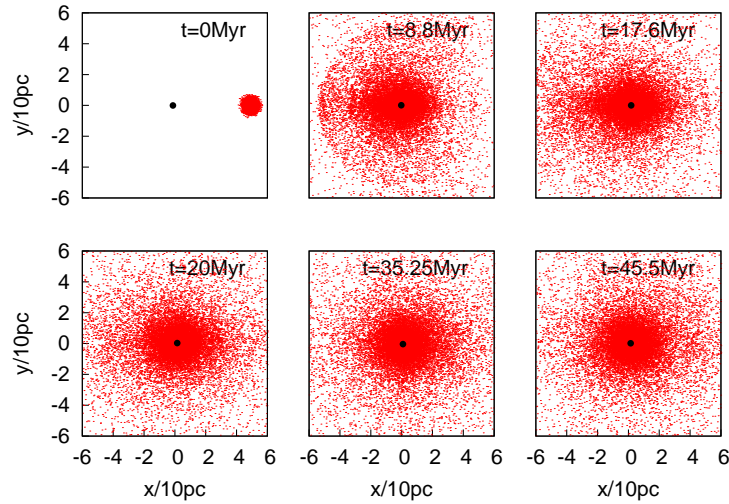


Figure 5.5: Same as in Fig.5.4, but for a radial orbit.

5.6 is shown the density profile of the galaxy at the beginning of the simulation and at the end for the galaxy whose mass was $M_{gal} = 3.2 \cdot 10^{11} M_{\odot}$.

Additional hints for the stability are the virial ratio, ω , which should be conserved, as it is shown in Fig.5.7 and the energy conservation (see Fig.5.8), since a too rapid increasing meaning an enhancement in strong gravitational encounters and in this case to follow the evolution of the system would be a very difficult task.

We checked for stability hints also in the other simulations, but we decided to restrict here the number of graphs needed to show it. In all the simulated galaxies, the density profile does not change significantly in the typical simulated time.

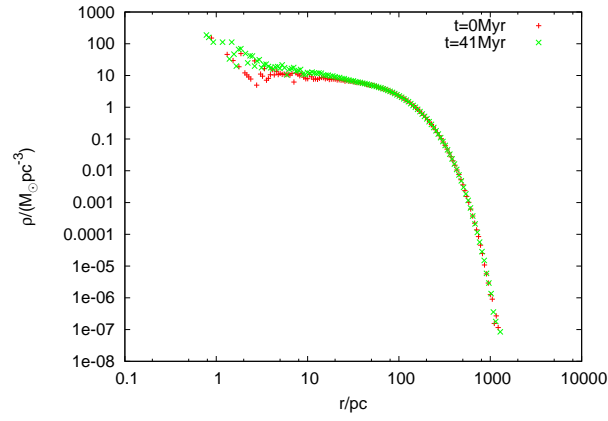


Figure 5.6: *Density profile of the galaxy at $t = 0$ and $t = 41 \text{ Myr}$.*

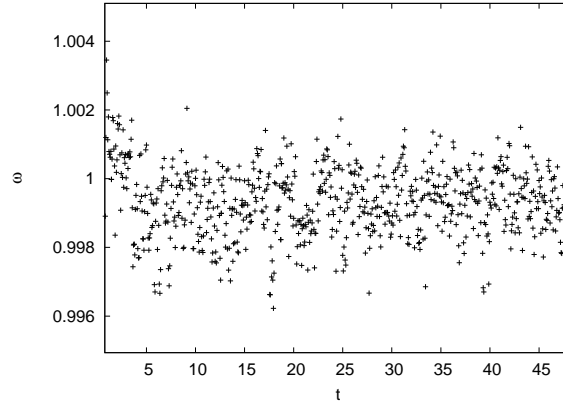


Figure 5.7: *The virial ratio ω as a function of time. The fact that it oscillates around the unity means that the galaxy nor contract neither expand in a dramatic way, since there is no evidence for a contracting “core” or an expanding “halo”.*

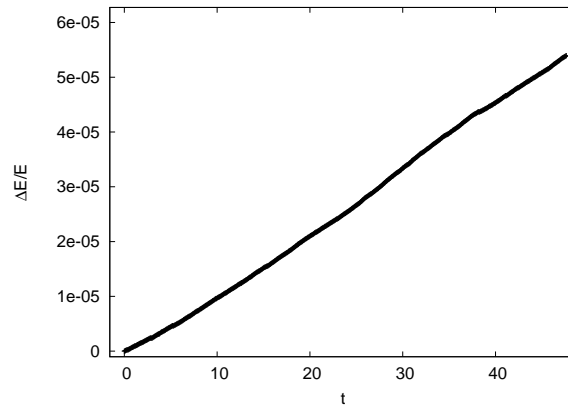


Figure 5.8: *Relative energy variation of the total system. The slow increasing in time is substantially due to the numerical method used by the N -body code, which is a 6th order Hermite integrator.*

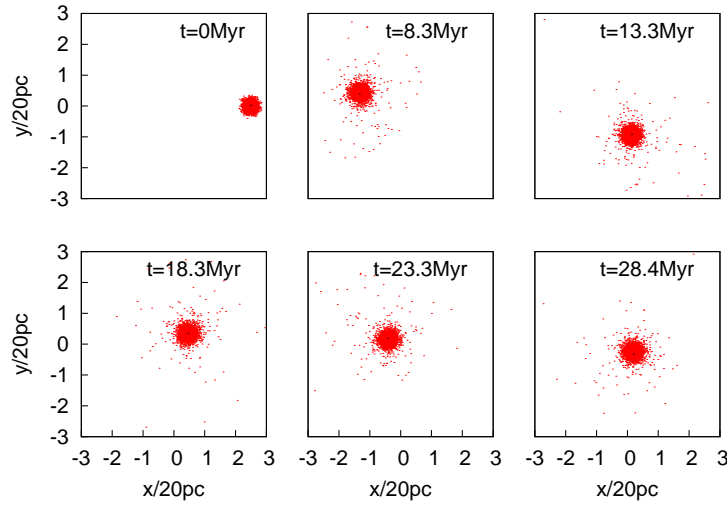


Figure 5.9: Same as in Fig. 5.2 but in this case the galaxy does not host a BH in its center.

5.2.1 Cluster analysis

As shown in Fig. 5.2, considering a quite massive system ($3.2 \cdot 10^{11} M_{\odot}$) the cluster is completely disrupted before it reaches the center of the galaxy. To find which component causes this effect (the BH or the galaxy or both of them), we performed a simulation in which the cluster moves in a galaxy with the same mass ($M_{gal} = 3.2 \cdot 10^{11} M_{\odot}$) but without the central BH, therefore the spatial distribution is the same as in the galaxy hosting a central BH, but the velocity dispersion is different. As you can see in Fig. 5.9, when the tidal effect due to the BH is removed, the cluster could reach easily the center in less than a hundred of *Myr* and its initial geometry is not altered significantly by the interaction with the background.

As a first conclusion, therefore, we can state that the major contribute to the tidal heating of the cluster comes from the central BH.

To study how the cluster structure evolves, we developed an analysis code which identify in a quite precise way the center of density of the cluster, which is crucial to obtain global properties such as density and velocity profiles, lagrangian radii, mass loss and an estimation of the radius.

The procedure we used to identify the center of the cluster can be resumed as follows: considering only the cluster's particles, overdense regions are identified in the space and their masses are used to find a center of mass; then, a number of “bubbles” are selected around the center of mass and used to correct it recursively until a convergence criteria has been reached. This allowed to follow quite well the evolution of the “core” of the cluster.

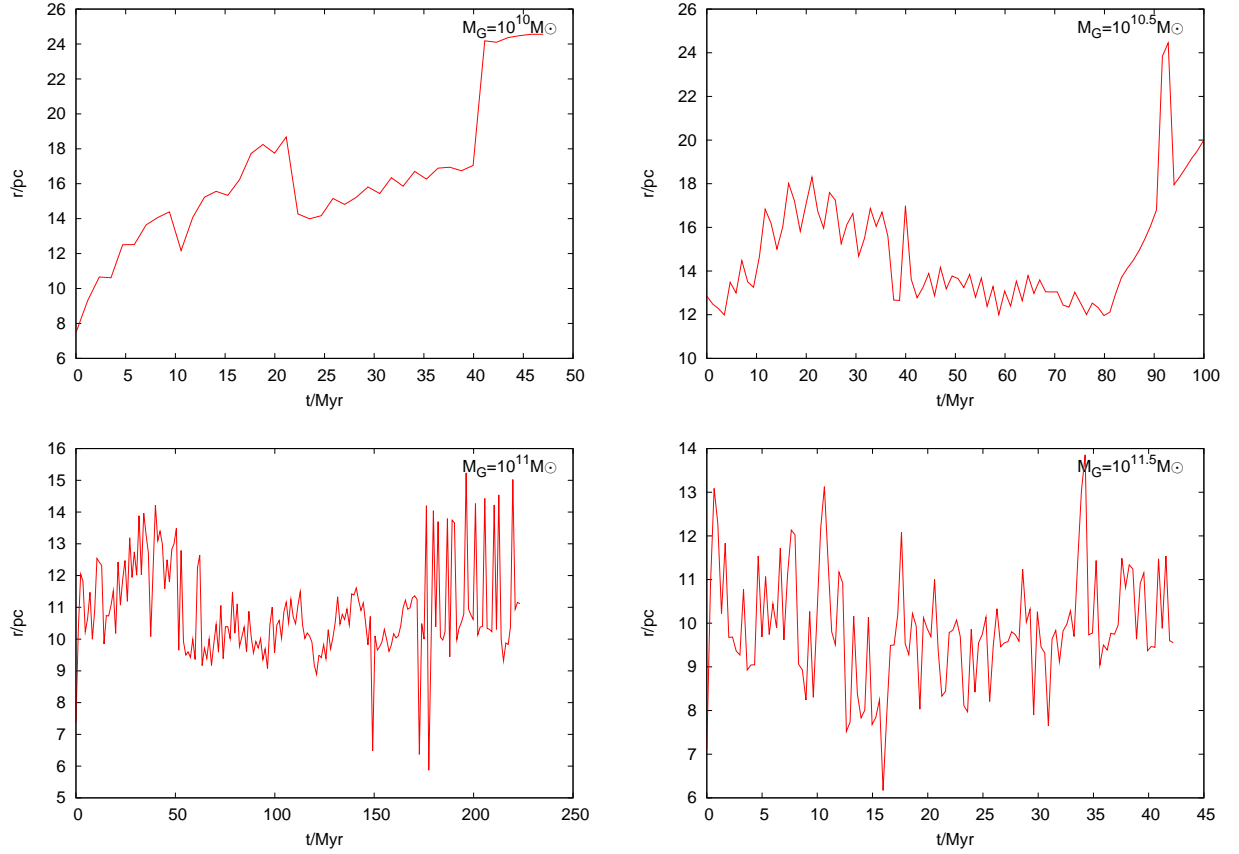


Figure 5.10: *The radius of the cluster in circular orbit as a function of time for different galaxies masses.*

The “boundary” of the cluster instead has been defined as the region over which the density of the cluster itself dominates with respect the galaxy density. In Fig. 5.10 is shown the radius of this region as a function of the time for circular orbits and different galaxy masses. As you can see, this typical lenght scale does not depend significantly on the galaxy mass, but it seems to slightly increase decreasing the galaxy mass.

Using the above definition of the cluster radius, it has been evaluated the mass lost by the cluster during its motion. The cluster mass as a function of time is shown in Fig. 5.11.

The mass loss behaviour changes singnificantly passing from galaxies below to galaxies above $3.2 \cdot 10^{10} M_{\odot}$. In fact, while for smaller galaxies the mass loss trend is quite regular, it can be divided in two main phases when greater galaxies are considered: in the first, there is a very rapid mass loss phase, and than it becomes more regular as well as small galaxies.

As it will be discussed in the next section, this is due to the fact that in galaxies above $3.2 \cdot 10^{10} M_{\odot}$ the tidal radius of the modeled cluster is smaller than its typical radius and

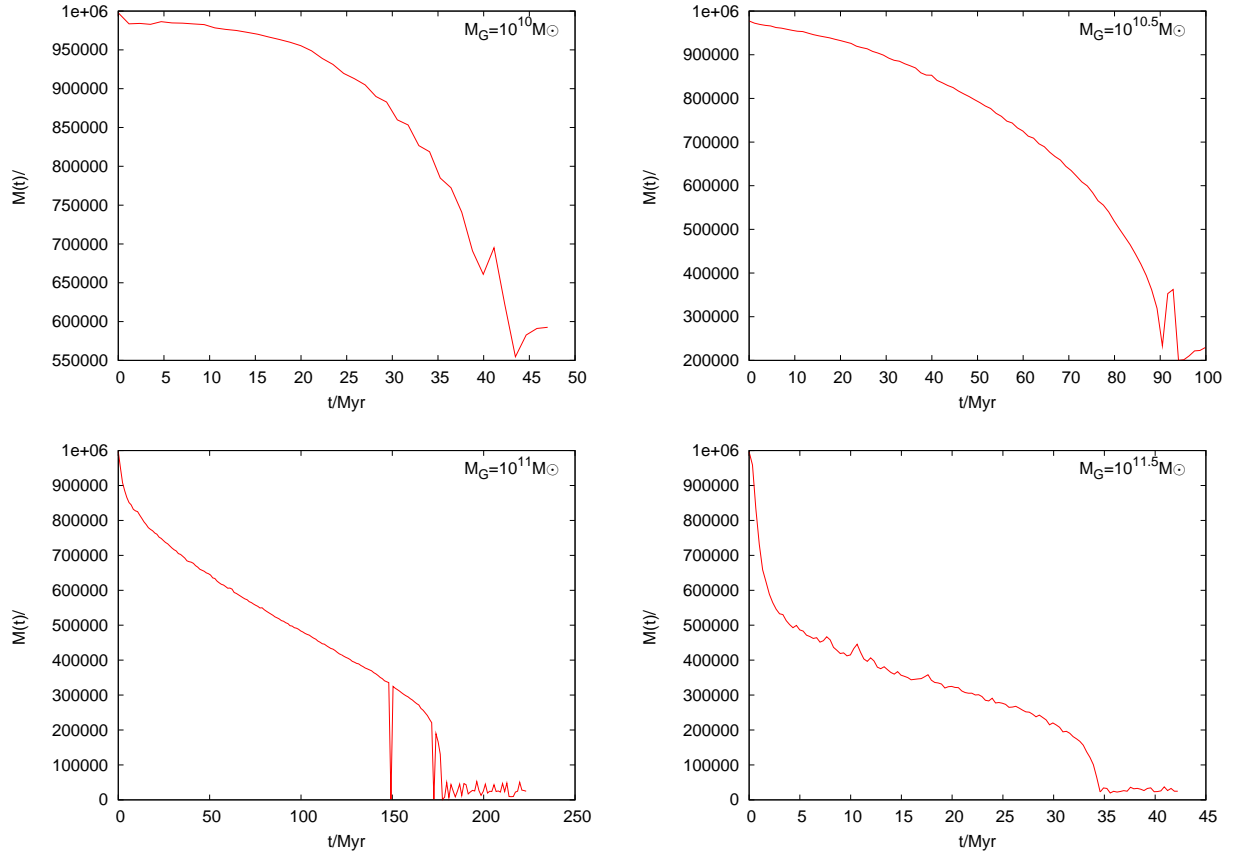


Figure 5.11: *Mass of the cluster as a function of time for different galaxies mass.*

this leads to an immediate and strong mass loss.

The continuous interaction between the cluster and the environment shapes significantly it, as it could be easily seen in the snapshot presented above. More quantitatively, the effects of the interaction could be put on evidence looking at the density profiles of the cluster, shown in Fig. 5.12.

As you can see, the cluster density slope decrease slightly in the initial phase of the evolution, and then it stabilizes until the disruption of the cluster itself.

Moreover, it is quite evident the formation of a knee which is due to escaping particles from the cluster.

Another parameter which allows to investigate the mass loss and the expansion or contraction of the system is the lagrangian radius, which is the radius enclosing a given percentage of mass.

In Fig. 5.13 are shown the lagrangian radii enclosing 25 – 50 – 75% of the total mass of the cluster, for the set of circular orbit simulations at different galaxies masses.

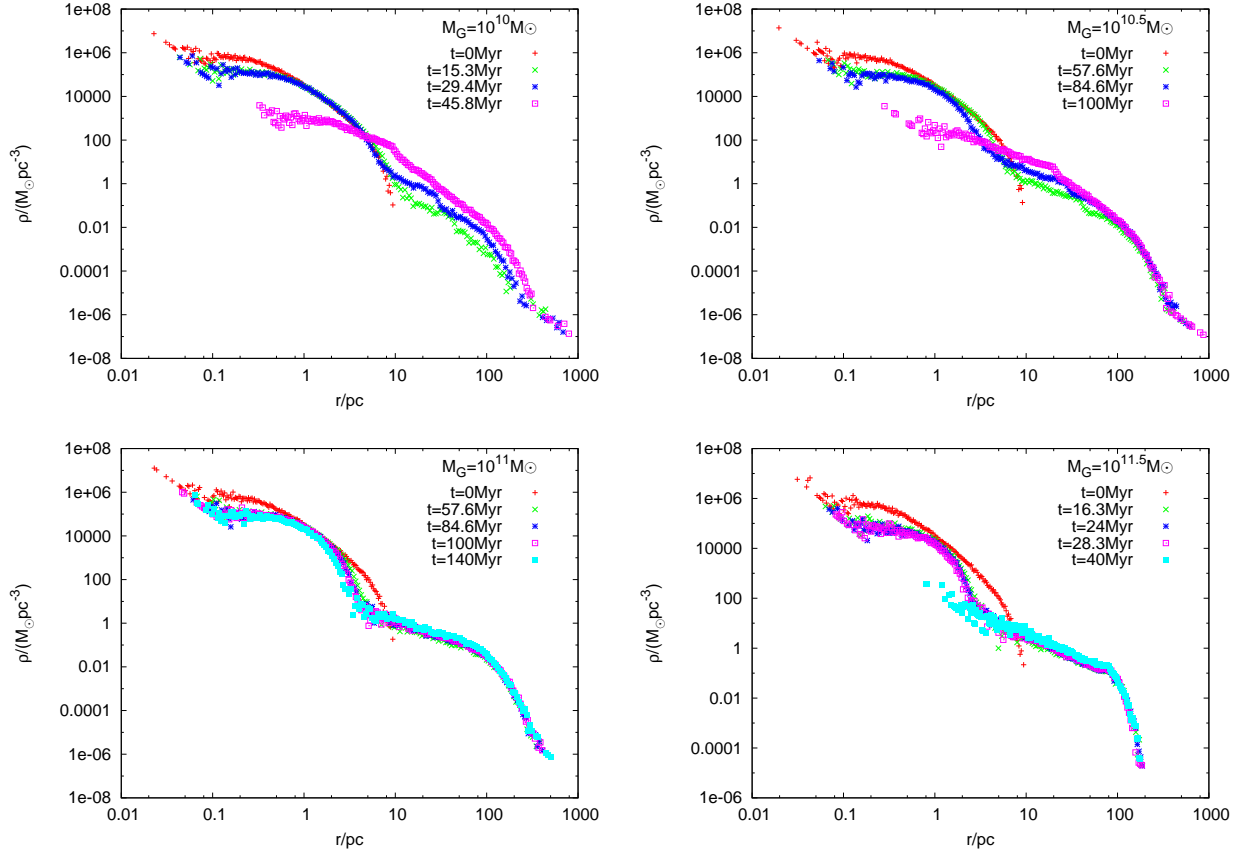


Figure 5.12: *Density profile of the cluster evaluated at different times for different galaxies masses.*

In the heaviest galaxy ($3.2 \cdot 10^{11} M_{\odot}$), there is a rapid expansion which leads to a rapid increase of the outer lagrangian radii r_{75} and r_{50} , while the inner radius r_{25} increase only in the last stage of the evolution, corresponding to the disruption of the cluster.

Instead, in the lightest simulated galaxy, ($10^{10} M_{\odot}$), the lagrangian radii r_{25} , r_{50} and r_{75} smoothly increase until the cluster reaches a very central region. It is interesting to note that seems to remain a small core containing at least 25% of mass after the decay of the cluster with a radius $\sim 6 pc$.

By comparing these two simulations, it is evident how the cluster evolves when the dominant process is the tidal heating or the dynamical friction.

High galaxies masses, which mean high BHs masses, exert on the cluster tidal forces strong enough to pull out particles from it, causing a rapid mass loss and a drop of gravitational energy which facilitates the disruption. On the other hand, if the mass of the central BH or the mass of the host galaxy is not dramatically high with respect to the mass of the cluster ($M_d/M_{BH} \geq 0.05$), dynamical friction dominates and could

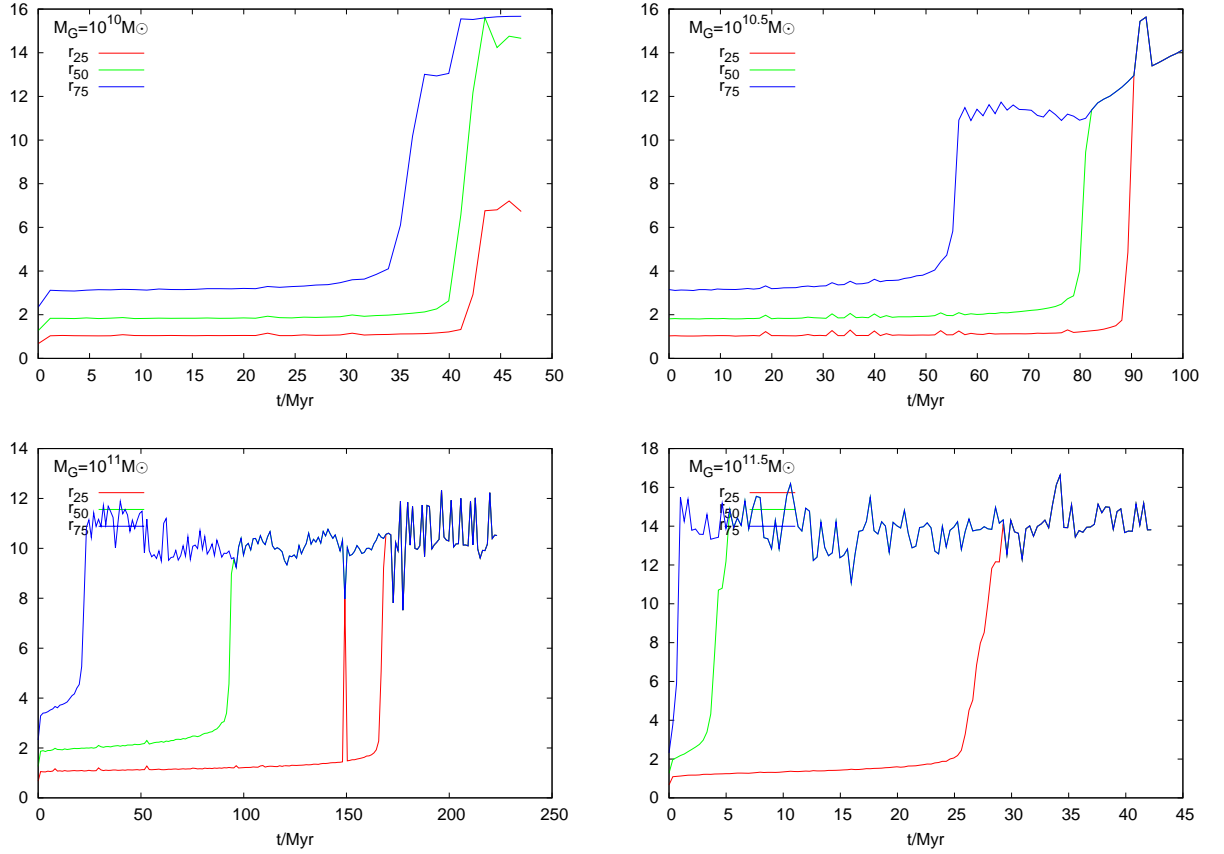


Figure 5.13: *Lagrangian radii enclosing 25 (red line), 50 (green line) and 75% (blue line) of the cluster mass for the circular orbit simulations with different galaxies masses.*

drive the cluster toward the center of the galaxy, giving a significant contribute to the NSC formation.

We performed also radial and eccentric orbits, however in this case it is very difficult to follow the evolution of the cluster from a quantitative point of view. In other words, in non circular orbits is very difficult to define a center and a radius for the cluster, since it suffers a strong deformation at every selected galaxies masses. To have an idea about the situation, in Fig. 5.14, 5.15 are shown some snapshots for two eccentric orbits in the case $M_{gal} = 3.2 \cdot 10^{11} - 10^{10} M_\odot$, respectively.

However, it is possible to infer the contribution given to a forming NSC by a cluster on eccentric orbit, by evaluating the mass lefted in a central region of the galaxy comparable with the typical NSCs dimensions (10 – 20 pc).

In Fig. 5.16, is shown the amount of mass deposited within a radius $r = 20 pc$ from the galactic center during the cluster evolution for all the simulations performed.

In smaller galaxies, $M \leq 10^{11} M_\odot$, both circular and radial orbits transport toward the galactic center up to 90% of the initial cluster mass.

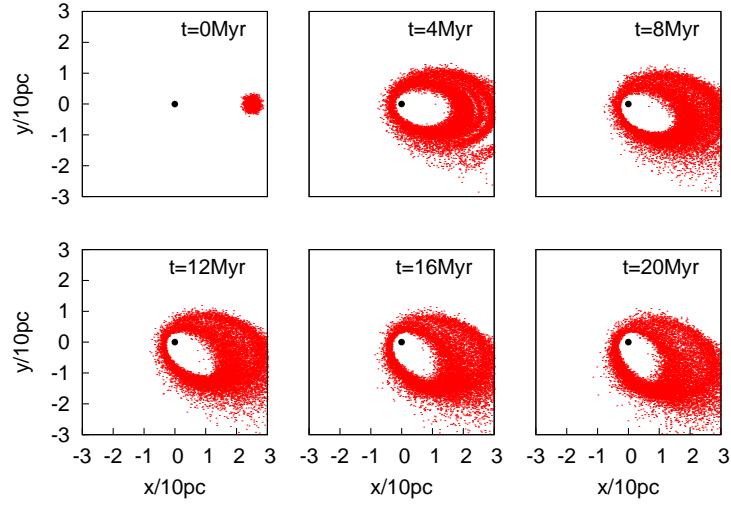


Figure 5.14: Same as in Fig. 5.2, but for eccentric orbits with eccentricity $e = 0.5$.

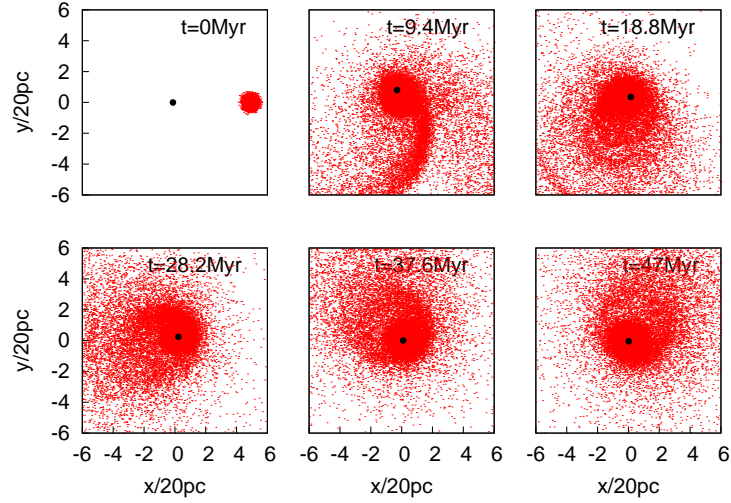


Figure 5.15: Same as in Fig. 5.2, but for eccentric orbits with eccentricity $e = 0.5$. In this case the galaxy mass is $3.2 \cdot 10^{10} M_{\odot}$.

On the other hand, in heavier galaxies, only very eccentric orbits could leave a significant amount of the cluster mass (around 20%) while circular and nearly circular orbits transport less than 1%.

Considering the highest galaxy mass simulated, $M = 3.2 \cdot 10^{11} M_{\odot}$, and using the scaling relation which connect galaxy and NSC masses, the expected NSC should have a mass $M_{NSC} \sim 10^9 M_{\odot}$ around; however, adding the fact that only 20% of the decaying cluster mass could reach the center and that only an half of the allowed orbits could deposit such a mass, we can obtain a rough estimation of the final NSC:

$$M_{NSC} \sim 10^9 \cdot 0.2 \cdot 0.5 = 10^8 M_{\odot}, \quad (5.3)$$

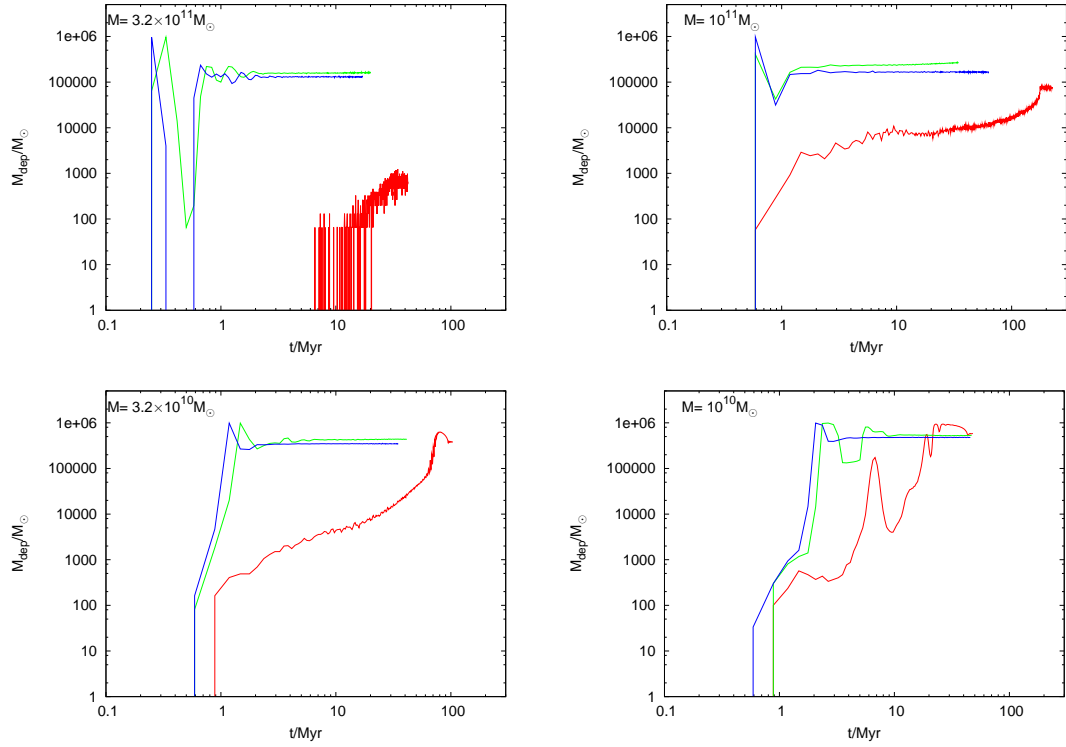


Figure 5.16: *Deposited mass to the center of the galaxy in form of cluster remnant. The region within the mass has been calculated is a sphere of radius 20pc.*

in quite good agreement with prediction obtained in Chap.4.

5.3 Caveats

Our analysis is only a first step toward a full understanding of the lack of high mass NSCs. In the near future, we improve it by enlarging the number of simulations and by changing structural properties of the cluster, and of its orbit.

In fact, in the present analysis, there are two strong simplifications:

- we use a truncated galaxy model, excluding from the N -body simulation a fraction much more massive than the simulated galaxy. The exclusion of such number of particles whose orbits could penetrate the region in which the cluster moves could affect significantly both the tidal heating and the dynamical friction processes;
- the cluster model used is equal in each simulation we made, however it can be thought that in heavier galaxies, above $10^{11}M_{\odot}$, this model is not well suited to represent the cluster since it appears strongly deformed by the external action of the BH at its start. We argued this looking to the differences between the mass

loss in the simulations. While in lighter galaxies this appears to be very regular, in heavier ones there is a rapid and strong mass loss, which could be due to a too small tidal radius for the cluster.

Actually, there are no apparent solutions for the first problem, since the number of particles required to simulate a larger fraction of the galaxy involve two additional problems: firstly, do not exist computational hardwares which could perform simulations with this high number in reasonable human time; moreover, the number of particles which can be used to simulate the cluster will be ridiculously small, due to the small ratio between the cluster and the galaxy masses.

On the other hand, we can handle the second problem performing a second set of simulations, in which the galaxy mass is kept fixed ($3.2 \cdot 10^{11} M_{\odot}$) while the cluster mass and concentration are allowed to vary. Current simulations have been carried out considering a cluster modeled with a King profile with a given potential well and core radius; however it would be interesting to investigate how simulations results change considering a more (or less) dense cluster model.

With the new set of simulations, we should be able to understand if there are possible configurations of the cluster which could reach the center and which are compatible with a realistic evolutionary history even considering a very massive galaxy.

At present, the only conclusion can be drawn from this work is that the same cluster is more efficiently disrupted at increasing galaxy masses. This point toward the original aim of this research, which was to understand wether or not the lacking of high mass NSCs could be addressed to the disruption of decaying clusters operated by the tidal action of a central BH.

5.4 Analytical considerations about the tidal radius evolution.

As mentioned before, an interesting parameter which could be monitorate to follow the interaction between the cluster and the environment in which it moves is the tidal radius, which is the radius within particles are gravitationally bounded to the cluster.

To obtain it, let be R the radius of the cluster, M its mass and \vec{r}_* the position vector of the cluster with respect the center of the galaxy. Moreover, let labels \vec{r} the position vector which separates the center of the galaxy with the nearest boundary of the cluster. Moreover, let the cluster moves on a circular orbit with angular frequency ω .

The acceleration of a particle placed at \vec{r} , will be given by:

$$a_a = r\omega^2 + \left(\frac{dU}{dr}\right)_r - \frac{GM}{|\vec{r} - \vec{r}_*|^2}, \quad (5.4)$$

while the acceleration of the center of mass:

$$a_t = r_*\omega^2 + \left(\frac{dU}{dr}\right)_{r_*}, \quad (5.5)$$

then the total acceleration exerted on the particle is given by:

$$a = (r - r_*)\omega^2 + \left(\frac{dU}{dr}\right)_r - \left(\frac{dU}{dr}\right)_{r_*} - \frac{GM(\vec{r} - \vec{r}_*)}{|\vec{r} - \vec{r}_*|^3}. \quad (5.6)$$

The particle will be in equilibrium if $a = 0$; no net forces act on it and the position of the particle can be taught as the tidal boundary of the cluster.

Since the dimension of the cluster is small compared with the distance of the cluster from the center, i.e. $R = |\vec{r} - \vec{r}_*| \ll \vec{r}_*$, the potential can be expanded:

$$\left(\frac{dU}{dr}\right)_r = \left(\frac{dU}{dr}\right)_{r_*} + \left(\frac{dU}{dr^2}\right)_{r_*} |\vec{r} - \vec{r}_*|; \quad (5.7)$$

then the equilibrium will be reached by imposing $a = 0$ and simplifying where it is possible:

$$\omega^2 + \left(\frac{dU}{dr^2}\right)_{r_*} - \frac{GM}{|\vec{r} - \vec{r}_*|_{tid}^3} = 0. \quad (5.8)$$

From the latest equation, we can obtain the tidal radius $R_t = |\vec{r} - \vec{r}_*|_{tid}$:

$$R_t^3 = \frac{GM}{\omega^2 + \left(\frac{dU}{dr^2}\right)_{R_{CM}}}, \quad (5.9)$$

where we replaced r^* with R_{CM} .

The galactic models discussed here are composed by a central BH and a truncated Dehnen density profile, therefore in this case:

$$\frac{dU}{dr^2} = \frac{2GM_{BH}}{R_{CM}^3} - \frac{GM_G}{R_{CM}^\gamma (R_{CM} + r_s)^{4-\gamma}} ((1 - \gamma)r_s - 2R_{CM}), \quad (5.10)$$

$$\omega^2 = \frac{GM_{BH}}{R_{CM}^3} + \frac{GM_G}{R_{CM}^3} \left(\frac{R_{CM}}{R_{CM} + r_s}\right)^{3-\gamma}. \quad (5.11)$$

Let's consider now the situation in which the BH potential dominates with respect the galaxy potential as happens in the simulation $M_G = 3.2 \cdot 10^{11} M_\odot$, then Eq.5.9 reduces simply to:

$$R_t^3 = \frac{1}{3} \frac{M}{M_{BH}} R_{CM}^3. \quad (5.12)$$

The cluster will lose mass if the cluster radius R exceeds the tidal radius R_t , therefore, by assuming $R > R_t$, we can find a limit over the BH mass:

$$M_{BH} > \frac{1}{3} \left(\frac{R_{CM}}{R} \right)^3 M = M_{BH,C}. \quad (5.13)$$

If the BH mass exceed $M_{BH,C}$ the cluster will lose mass. Looking at the analysis presented in previous sections, the mass loss process does not change dramatically the radius of the cluster, which is almost constant across the evolution.

Considering the case $M_G = 3.2 \cdot 10^{11} M_\odot$, the cluster radius is almost constant $R = 10 pc$, therefore initially:

$$M_{BH,C} = \frac{1}{3} \left(\frac{50 pc}{10 pc} \right)^3 10^6 M_\odot = 4.1 \times 10^7 M_\odot. \quad (5.14)$$

However, in such galaxy, the BH is expected to have a mass $M_{BH} = 5 \times 10^8 M_\odot$, greater than the critical value, and the cluster loses mass immediately.

Moreover, this process cannot be inverted; in fact, since the cluster radius and the distance from the galactic center does not change significantly, while the cluster mass decreases, the critical BH mass value decreases in time, and the condition for the mass loss is ever satisfied until the complete disruption of the cluster.

In this simple way we showed what it has been stated in the previous section, which is that the cluster we modeled in the heaviest galaxy has a tidal radius small compared to the radius and the cluster loses mass immediately.

5.5 Summary

Our investigation on the lacking of high mass NSCs can be summarized as follows:

- using HiGPUs, it has been simulated the decay of a single cluster in a galaxy containing a central SMBH in order to see the effect of tidal interaction on the cluster due to the external field in which it moves;

- it has been found that the main contribution to the “tidal heating” process is due to the central BH, since it dominates in the region in which the cluster moves;
- from runs analysis, it has been found that the greater the BH mass the smaller the disruption time and the dynamical friction effect, moreover, tidal forces suppress the dynamical braking, as it has been tested simulating the same galaxy and cluster with and without the central BH;
- by deriving analytically the tidal radius for the cluster, it has been obtained a critical mass for the central BH over which the cluster is completely disrupted;
- due to the choice of the GC model, in the cases $M_G = 10^{11}$, $3.2 \cdot 10^{11} M_\odot$ the cluster experiences two distinct mass loss phases: a very fast phase followed by a slow phase until the disruption.

In the future, it will be necessary to perform a new set of simulations in which the galaxy mass will be fixed and the GC model will be varied, in order to investigate if there are conditions under which the cluster could reach the center also in very favourable environment, it is clear that these conditions will be compared with realistic conditions.

CHAPTER 6

DISCUSSION AND CONCLUSIONS

In this thesis has been shown how dynamical friction acts on all scales and the consequences of a reliable estimation of this effect in astrophysical context.

Firstly, it has been developed a new treatment to evaluate the dynamical braking, particularly well-suited to deal with cuspy density profiles. Basically, the deceleration term has been evaluated interpolating the local and central contribution by means of a proper interpolation function.

The validity of this approach has been verified comparing the numerical solution of the equation of motion of a massive satellite suffering the dynamical friction mechanism with a wide set of N -body simulations, in which the massive satellite decays as a natural consequence of the gravitational interactions with lighter particles.

The analysis of the whole set of simulations (performed varying satellite mass, eccentricity, initial positions and background models) allowed us to find a fitting formula for the typical decay timescale, a parameter useful in drawing general scaling laws regarding astrophysical problems.

An important result coming from this treatment is that the dynamical friction time scale depends on the satellite mass in a slightly different way with respect to the classical expression developed so far by Chandrasekhar. In fact, while the classical formula predicts a time dependence inversely linear with the satellite mass, we found that the relation is shallower ($t_{df} \propto M^{-0.67}$).

The natural continuation of the work has been to apply the treatment to several astrophysical situations on very different scales, to highlight its general validity.

On “small” scales, it has been investigated the formation of Intermediate Mass Black Holes in globular clusters as consequence of stellar encounters. Assuming a Salpeter initial mass function and a cored Dehnen profile to model the cluster, it has been estimated the amount of mass deposited into the center of the cluster by varying the cluster mass in a wide range ($10^3 - 10^7 M_\odot$), taking into account stars mass loss due to stellar evolution.

On a statistical basis, but also taking advantage of N -body simulations, it has been possible to draw a scaling law connecting the deposited mass and the total mass of the cluster. The correlation found is in very good agreement with the observed one [75].

Whether or not the mass excess could lead to the formation of an IMBH has been hard to show; however, it has been put on evidence that the decayed stars are “packed” in a relatively small region (down to $0.05 pc$), where mutual interactions could become strong enough in time to lead to merging events and then to the formation of a compact object.

On a slightly larger scale, it has been studied the problem of the five clusters orbiting in the Fornax dSph. Classical estimations of the clusters decay times in this dwarf galaxy are smaller than the Hubble time, which implies that they should be decayed nowadays. However, the careful treatment of dynamical friction provided here has shown a wide range of initial conditions able to avoid the cluster sinking at all. Moreover, it has been shown through N -body simulations that self-interaction effects between the clusters cannot be neglected, since they are strong enough to prevent the decay or even suppress it at all.

Later, the work has moved toward the study of the formation of Nuclear Star Clusters in the center of galaxies in a wide range of masses (from 10^8 to $10^{12} M_\odot$). Using both analytical and statistical arguments, it has been shown that NSC formation could be ascribed to decaying globular clusters. The work gave in this scientific framework an effort to the so called dry merger scenario.

Predicted masses for NSCs have been compared with observation, showing an excellent agreement. Moreover, some scaling laws connecting the NSCs masses with the hosts global properties have been provided. A very promising agreement has been found between our and observed scaling laws, indicating that the dry merger scenario is a well suited theory to give reason for the existence of NSCs.

As an example, it is interesting to note the agreement between our theoretical results and the observations about the correlation between the NSC mass and the host velocity dispersion. This is a power-law with slope ~ 2 , very different from the corresponding correlation between the central Super Massive Black Hole and the host, whose slope is 4.

In the last part of this thesis has been investigated the lacking of NSCs in high mass galaxies.

Taking advantages of a wide set of high resolution, direct N -body simulations, it has been followed the orbital evolution of a cluster in a relatively small region of a galaxy hosting a central SMBH, whose mass with respect to the galaxy mass has been determined by using the most modern scaling laws.

To simulate the whole system, it has been possible to use a very large number of particles (over a million), thanks to the great efficiency of the N -body integrator and the high quality level of our hardware.

The runs analysis has shown that tidal forces exerted by the black hole strongly determines the fate of the cluster. In fact, in galaxies below $10^{11}M_{\odot}$, which correspond to black hole masses below 10^8M_{\odot} , the dynamical friction dominates over tidal heating process, and the cluster could better penetrate the inner region of the galaxy. On the other hand, in heavier galaxies, tidal forces heat the cluster so efficiently that it is completely disrupted well before it reaches the galactic center.

It has been also pointed out that the main contribution to the tidal forces is the one coming from the black hole; in fact, when the black hole is not considered, the cluster easily reaches the galactic center even for very massive galaxies ($\sim 10^{12}M_{\odot}$).

The consequences of strong tidal forces due to the central black hole seem to prevent the NSC formation, or at least to allow the formation of a lighter NSC than expected, as it has been shown also from a statistical point of view. However, low mass NSCs would be very difficult to observe in massive galaxies, since their luminosity profiles cannot emerge from the background luminosity.

As a general conclusion, we showed in this thesis that a careful treatment of a general process such as dynamical friction can be applied successfully to astrophysical problems on very different scales: from the accumulation of mass in star clusters to the formation of massive star clusters in galactic centers.

The work I did during my Ph.D. opened a series of question that, in my opinion, should be answered. Regarding the formation of IMBH in globular clusters, it would be interesting to improve the work in several ways: i) investigate the consequences of using a different mass spectrum (or density profile) on the accumulated central mass excess; ii) analyze better whether or not the energy equipartition could be reached, which is a crucial point to determine whether or not the heavy sub-system could leads to the formation of an Intermediate Mass Black Hole; iii) by using our very detailed N -body simulations, it would be possible to evaluate the gravitational waves emission during the phase of the

formation of the IMBH, which could be compared to the present experiments devoted to the detection of such signals. On the other hand, the formation and lacking of NSC in galaxies could be improved performing a more detailed set of N-body simulations, in which would be varied the parameters characterizing the decaying cluster, to see whether or not the tidal forces induced by the central black hole could effectively destroy the building blocks of NSC. Moreover, it would be very interesting to investigate how much mass could be transferred from the NSC to the central black hole, and whether or not this process could turn on the Active Galactic Nuclei mechanism.

APPENDIX A

DYNAMICAL FRICTION INTEGRAL CONVERGENCE

To model spherical, cuspy systems, we used the so called Dehnen (or *gamma*) models, which are self-consistent models whose density profiles follows the 3 parameter law:

$$\rho(r) = \frac{(3 - \gamma)M}{4\pi a^3} \frac{1}{(r/a)^\gamma (1 + r/a)^{4-\gamma}}, \quad (\text{A.1})$$

where $0 \leq \gamma \leq 3$ gives the slope of the centrally diverging (if $\gamma > 0$) profile, a is the length scale, and M is the total mass of the model. The case $\gamma = 0$ corresponds to a central core, where density flattens. The cases $\gamma = 1$, and $\gamma = 2$ correspond to the classic Hernquist [62] and Jaffe [65] models, respectively. The potential generated by this family of density laws is easily obtained by solving the Poisson's equation, leading to:

$$\Phi(r) = \frac{GM}{a} \times \begin{cases} \ln\left(\frac{r}{r+a}\right) & \gamma = 2, \\ \frac{1}{\gamma - 2} \left[1 - \left(\frac{r}{r+a}\right)^{2-\gamma} \right] & \gamma \neq 2. \end{cases} \quad (\text{A.2})$$

Note that $\Phi(r)$ is centrally unbound for $\gamma \geq 2$, while the force per unit mass, $\nabla\Phi$, is unbound for $\gamma \geq 1$. This was properly taken into account in the one-body orbital integrations.

Defining the adimensional potential $\Psi(r) = -\Phi(r)/(\frac{GM}{a})$ and the (adimensional) binding energy $\mathcal{E} = -E/(\frac{GM}{a})$, the density profile can be written as:

$$\rho(r) = 4\pi \int_0^\Psi f(\mathcal{E}) \sqrt{2(\Psi - \mathcal{E})} d\mathcal{E}, \quad (\text{A.3})$$

in the assumption of full isotropy for the DF, $f(\mathcal{E})$. Eqs. A.1 and A.2 allow the expression of ρ as function of Ψ , so that it is possible to apply the Eddington [38] inversion formula to obtain the unknown distribution function $f(\mathcal{E})$ as:

$$f(\mathcal{E}) = \frac{(3 - \gamma)}{2(2\pi^2 GM a)^{3/2}} \int_0^\mathcal{E} \frac{(1 - x)^2 [\gamma + 2x + (4 - \gamma)x^2]}{x^{4-\gamma} \sqrt{\mathcal{E} - \Psi}} d\Psi, \quad (\text{A.4})$$

where

$$x \equiv x(\Psi) = \begin{cases} e^{-\Psi} & \gamma = 2 \\ [1 - (2 - \gamma)\Psi]^{1/(2-\gamma)} & \gamma \neq 2. \end{cases} \quad (\text{A.5})$$

For low binding energies (outer spatial regions), the distribution function decays as $f(\mathcal{E}) \propto \mathcal{E}^{5/2}$, while for high binding energies ($\mathcal{E} \rightarrow \Psi(0)$, inner spatial regions) it behaves as:

$$f(\mathcal{E}) \propto \begin{cases} [\Psi(0) - \mathcal{E}]^{-1} & \gamma = 0, \\ [\Psi(0) - \mathcal{E}]^{-(6-\gamma)/[2(2-\gamma)]} & 0 < \gamma < 2, \\ e^{2\mathcal{E}} & \gamma = 2, \\ \mathcal{E}^{(6-\gamma)/[2(2-\gamma)]} & 2 < \gamma < 3. \end{cases} \quad (\text{A.6})$$

If $(2 - \gamma)^{-1}$ is integer or half-integer, the integral in Eq.A.4 can be calculated in terms of linear combination of hypergeometric series, easily reduced to elementary functions [56].

Due to that cusps steeper than $\gamma = 2$ are not observed in real galaxies, we limited to consider the cases $\gamma = 0, 1/2, 1, 4/3, 3/2, 7/4, 2$, which are all values leading to $(2 - \gamma)^{-1}$ integer or half-integer leading to analytic expressions for $f(\mathcal{E})$, but $\gamma = 1/2$ which deserves a numerical integration to get $f(\mathcal{E})$ which was later fitted in a way to have this general expression for the isotropic DF:

Table A.1

Values of the parameters of the DFs of Eq. A.7

γ	0	1	4/3	3/2	7/4
A_γ	$(3/2\pi^3)$	$(8\sqrt{2}\pi^3)^{-1}$	$(62208\pi^3)^{-1}$	$3(32\sqrt{2}\pi^3)^{-1}$	$(1281280\sqrt{2}\pi^3)^{-1}$
B_γ	0	1	$-2\sqrt{2}$	8	1
b_0	0	3	-54675	-9/16	-4188784600
b_1	0	2	186300	-99/16	34508145672
b_2	0	-24	-293328	405/8	-55318781804
b_3	0	16	206496	-3705/56	48778694536
b_4	0	0	-67584	561/14	-28754568388
b_5	0	0	8192	-181/14	12242267940
b_6	0	0	0	15/7	-3910165630
b_7	0	0	0	-1/7	697897200
b_8	0	0	0	0	955019800
b_9	0	0	0	0	-179608380
b_{10}	0	0	0	0	25921460
b_{11}	0	0	0	0	-2828990
b_{12}	0	0	0	0	226548
b_{13}	0	0	0	0	-12586
b_{14}	0	0	0	0	434
b_{15}	0	0	0	0	-7

$$f_\gamma(\mathcal{E}) = \frac{M}{(GMa)^{3/2}} \frac{A_\gamma}{(\Psi(0) - \mathcal{E})^{(6-\gamma)/(2(2-\gamma))}} \left[g_\gamma(\mathcal{E}) + B_\gamma \sqrt{\mathcal{E}} \sqrt{\psi(0) - \mathcal{E}} \left(\sum_{i=0}^{(2+\gamma)/(2-\gamma)} b_i \mathcal{E}^i \right) \right], \quad (\text{A.7})$$

where $g_\gamma(\mathcal{E})$ is

$$g_\gamma(\mathcal{E}) = \begin{cases} (3 - 4\mathcal{E})\sqrt{2\mathcal{E}}\sqrt{\Psi(0) - \mathcal{E}} - 3\sqrt{(\Psi(0) - \mathcal{E})^3} \log\left(\frac{1+\sqrt{2\mathcal{E}}}{\sqrt{1-2\mathcal{E}}}\right), & \gamma = 0 \\ 3 \arcsin \sqrt{\mathcal{E}}, & \gamma = 1 \\ 54675\sqrt{2} \arcsin \sqrt{\frac{2\mathcal{E}}{3}} - 450\sqrt{6}(3 - 2\mathcal{E})^{9/2} \log\left(\frac{3+2\sqrt{6\mathcal{E}}+2\mathcal{E}}{3-2\mathcal{E}}\right), & \gamma = 4/3 \\ 3(3 + 32\mathcal{E} - 8\mathcal{E}^2) \arcsin \sqrt{\frac{\mathcal{E}}{2}}, & \gamma = 3/2 \\ -33633600(83 - 512\mathcal{E} + 192\mathcal{E}^2 - 32\mathcal{E}^3 + 2\mathcal{E}^4) \arcsin \frac{\sqrt{\mathcal{E}}}{2}. & \gamma = 7/4 \end{cases} \quad (\text{A.8})$$

and the values of A_γ and of b_i are reported in Table A.1.

Finally, the $\gamma = 2$ case (Jaffe's model) has a formal expression that is not easily reduced into the form of Eq. A.7; as known [65] it is given by

$$f(\mathcal{E}) = \frac{M}{2\pi^3(GMa)^{3/2}} \left[F_- \left(\sqrt{2\mathcal{E}} \right) - \sqrt{2}F_+ \left(\sqrt{2\mathcal{E}} \right) - \sqrt{2}F_- \left(\sqrt{2\mathcal{E}} \right) + F_+ \left(\sqrt{2\mathcal{E}} \right) \right] \quad (\text{A.9})$$

where

$$F_{\pm}(\eta) = e^{\mp x^2} \int_0^x e^{\pm \eta^2} d\eta. \quad (\text{A.10})$$

The convergence of the dynamical friction integral

We study here the convergence of the dynamical friction integral in Eq. 2.4, which is an improper integral in the case of the a cuspy matter density distributions such as the case of the family of the *gamma* laws given by Eq. A.1. Only when $\gamma = 0$ (which means a central core) the df integral is not singular, while it is for any $\gamma > 0$. In these cases, the adoption of the DFs in their limit for high binding energies as expressed by Eq. A.8 leads to a df integral which in a neighbourhood of the origin of the phase-space (that is for a slow motion around the galactic center) assumes the form:

$$\frac{d\mathbf{v}_M}{dt} = -A \int_{b_{min}}^{b_{max}} \int \frac{1}{2} \left[\frac{v^2}{(GM)/a} + (r/(r+a))^2 \right] \frac{Vb}{1 + b^2 V^4 G^{-2} (m+M)^{-2}} \mathbf{V} d^3 \mathbf{v}_m db, \quad (\text{A.11})$$

for $\gamma = 0$, and

$$\begin{aligned} \frac{d\mathbf{v}_M}{dt} = -A \int_{b_{min}}^{b_{max}} \int \left[\frac{1}{2} \frac{v^2}{(GM)/a} + \frac{1}{2-\gamma} \left(\frac{r}{r+a} \right)^{2-\gamma} \right]^{- (6-\gamma)/(2(2-\gamma))} \times \\ \times \frac{Vb}{1 + b^2 V^4 G^{-2} (m+M)^{-2}} \mathbf{V} d^3 \mathbf{v}_m db, \end{aligned} \quad (\text{A.12})$$

for $0 < \gamma < 2$, and

$$\frac{d\mathbf{v}_M}{dt} = -A \int_{b_{min}}^{b_{max}} \int e^{-v^2/((GM)/a)} \left(\frac{r}{r+a} \right)^{-2} \frac{Vb}{1 + b^2 V^4 G^{-2} (m+M)^{-2}} \mathbf{V} d^3 \mathbf{v}_m db, \quad (\text{A.13})$$

for $\gamma = 2$, and

$$\begin{aligned} \frac{d\mathbf{v}_M}{dt} = & -A \int_{b_{min}}^{b_{max}} \int \left\{ \frac{1}{2-\gamma} \left[1 - \left(\frac{r}{r+a} \right)^{2-\gamma} \right] - \frac{v^2}{2b} \right\}^{[6-\gamma]/[2(2-\gamma)]} \times \\ & \times \frac{Vb}{1 + b^2 V^4 G^{-2} (m+M)^{-2}} \mathbf{V} d^3 \mathbf{v}_m db, \end{aligned} \quad (\text{A.14})$$

for $2 < \gamma < 3$.

The convergence of the above improper integrals can be studied by analysing the properties of the integrands (which we call I_1, I_2 and I_3 , respectively) for r/a and $(1/2)v^2/(GM)/a$ going contemporarily to zero (i.e. with the same order), introducing the auxiliary infinitesimal variable $x \equiv r/a = v^2/(2b)$. This way, it is easily seen that the four integrands behave, for $x \ll 1$, as:

$$I_1 \approx x \left(1 + \frac{1}{2}x \right)^{-1}, \quad \gamma = 0, \quad (\text{A.15})$$

$$I_2 \approx x^2 [x(1 + x^{1-\gamma})]^{-(6-\gamma)/(2(2-\gamma))}, \quad 0 < \gamma < 2, \quad (\text{A.16})$$

$$I_3 \approx e^{-x}, \quad \gamma = 2, \quad (\text{A.17})$$

$$I_4 \approx x^{(10-\gamma)/2}, \quad 2 < \gamma < 3 \quad (\text{A.18})$$

In the case of Eq. A.12: if $0 < \gamma \leq 1$ the behaviour is $x^{(2-3\gamma)/(2(2-\gamma))}$ whose exponent is $\geq -1/2$, implying the integral convergence; if $1 < \gamma < 2$ the behaviour is $x^{-(2-\gamma)/2}$ whose exponent is ≥ -1 , which again guarantees convergence. In the cases of Eq. A.13 and Eq. A.14 the limits are again finite, different from zero when $\gamma = 2$ and equal to zero for $2 < \gamma < 3$. Note that this latter case has not always an acceptable physical meaning because it may give negative values for the DF around the origin of the phase space.

APPENDIX B

DYNAMICAL FRICTION MASS DEPENDENCES

While the hypothesis of dynamical friction as cumulative effect of multiple hyperbolic encounters implies a growth of its effect at increasing values of M , the df integrand (Eq. 2.4) is such that the final dependence on M may be different than a simple proportionality to M , although in the limit $m \ll M$.

Actually, the expression for df given by Eq. 2.10 contains two additive terms. The local term (Eq. 2.5) has an explicit, dominant linear dependence on $m + M$ and another, weaker, dependence through the Coulomb's logarithm (essentially a $\ln(b_{max}/b_{min})$ dependence). The central term (Eq. 2.9) has an inversely linear dependence on $m + M$ in the multiplicative factor of the integral and depends on M also in the integrand and in the integration limits. Applying the Leibnitz's formula for the integral differentiation we have three terms in the derivative respect to M :

$$\begin{aligned} \frac{1}{4\pi m} \frac{d}{dM} \left(\frac{d\mathbf{v}_M}{dt} \right)_{\text{cen}} &= - \int_{b_{min}}^{b_{max}} \int f(b, \mathbf{v}_m) \frac{d}{dM} \frac{V}{(m+M) [1 + b^2 V^4 G^{-2} (m+M)^{-2}]} \mathbf{V} d^3 \mathbf{v}_m b db + \\ &- \frac{db_{max}}{dM} \int f(b_{max}, \mathbf{v}_m) \frac{V}{(m+M) [1 + b^2 V^4 G^{-2} (m+M)^{-2}]} \mathbf{V} b_{max} d^3 \mathbf{v}_m + \\ &+ \frac{db_{min}}{dM} \int f(b_{min}, \mathbf{v}_m) \frac{V}{(m+M) [1 + b^2 V^4 G^{-2} (m+M)^{-2}]} \mathbf{V} b_{min} d^3 \mathbf{v}_m. \end{aligned} \quad (\text{B.1})$$

The first term results to be

$$\frac{1}{(m+M)^2} \int_{b_{min}}^{b_{max}} \int f(b, \mathbf{v}_m) \frac{1 - b^2 V^4 G^{-2} (m+M)^{-2}}{[1 + b^2 V^4 G^{-2} (m+M)^{-2}]^2} V \mathbf{V} d^3 \mathbf{v}_m b db, \quad (\text{B.2})$$

which tends to a mass independent value (i.e. linearity of df deceleration in $m + M$) only in the weak encounter regime

$$\frac{b^2 V^4}{G^2(m + M)^2} \gg 1, \quad (\text{B.3})$$

while in the opposite (strong encounter) regime

$$\frac{b^2 V^4}{G^2(m + M)^2} \ll 1, \quad (\text{B.4})$$

it shows an inverse quadratic dependence on $m + M$ (lighter test masses would be more strongly decelerated).

Regarding the other two terms in Eq. B.1 the first is usually set to 0 by the assumption of b_{max} as the, fixed, characteristic length size of the system, while the second depends on the choice for b_{min} . For a generic dependence of b_{min} on M , the dependence on M through the explicit derivative of b_{min} respect to M is modulated by the dependence on b_{min} in the integrand. If we impose to b_{min} the logical constraint to be large enough to allow 2-body hyperbolic encounters, only, something like $b_{min} = G(m + M)/v_\infty^2$ (where v_∞ is the speed of the free test mass) is obtained, whose derivative respect to M is G/v_∞^2 . Hence, the second term has the likely dominant dependence on M in its explicit part in the integrand and, thus neglecting the dependence on M through $f(b_{min}, \mathbf{v}_m)$, we have that the regime:

$$\frac{b^2 V^4}{G^2(m + M)^2} \gg 1, \quad (\text{B.5})$$

gives a direct linear dependence on $m + M$ (i.e. quadratic in df), while in the opposite regime

$$\frac{b^2 V^4}{G^2(m + M)^2} \ll 1, \quad (\text{B.6})$$

the dependence is inversely linear in $m + M$ (i.e. a logarithmic dependence of df on $m + M$).

From what we said above, also assuming that df is mainly contributed by the cumulation of many weak encounters, the df dependence on mass is not simply linear in $m + M$ but it is altered by an additive $\ln(m + M)$ dependence whose amplitude is modulated by

the degree of spatial divergence of the DF. In any case, the expected df dependence on $m + M$ is something like $\propto (m + M)^\alpha$, with $0 < \alpha < 1$.

APPENDIX C

SAMPLING SELF CONSISTENT MODELS FOR N -BODY SIMULATIONS

C.1 Introduction

In the last decades, a great effort to the study of dynamics in a various range of astrophysical situation has been given by N -body simulations.

However, beyond the simulation a very difficult task to perform is to find an easy way to sample the initial conditions (IC) required to model the system choosen.

In fact, to determine a complete set of IC it is necessary to know the density profile and the distribution function (DF) which describes the positions and energy distribution of the particles, respectively. This quantities are often really difficult to obtain analitically and numerical techniques are required to gain a self-consistent IC ensamble.

General approaches discussed in literature take advantage from well suited statistical methods substantially based on Monte-Carlo techniques, however in general authors produce codes very focused on the matter of investigation and in most cases the code is not release to the scientific community.

There are only few codes freely available that generate IC for a limited class of models.

As example, the widely used toolbox NEMO [112] allows the sampling of many well known models such as King, Dehnen, Plummer and Toomre models giving also a various utilities to integrate, analyze and visualize SPH and N -body like systems.

Moreover, the tool McLuster [70] is another freely available code devoted either to the generation of IC for N -body simulation or to the generation of artificial evolved star

clusters modeling them with a King profile. This code gives also the possibility to take in account a mass spectrum for the stellar population.

However, the usage of this packages often could be complicated due to the fact that the output files are given in particular formats, or limitative, due to the limited number of models implemented.

As part of my Ph.D. research, I collaborated with Dr. M. Spera to develop a code completely devoted to the sampling of IC for N -body systems as general as possible.

The powerful of the code is hidden in the very precise numerical evaluation of the global properties of the system, i.e. potential profile, mass profile and distribution function of the energies.

The chapter is divided as follows: in Sec.C.2 we recall the theory about the description of self-gravitating systems, in Sec.C.3 we will explain the ideas beyond the code and the sampling strategy, in Sec.C.4 a range of well-known models implemented yet in the code are shown.

Sec.C.5 is a sort of quick guide to the code, while Sec.C.6 refers to some tests we made to check stability of the sampled systems.

C.2 N -body system: global properties

To obtain positions and velocities for each particle in the ensemble, we need the mass profile and the distribution function of energies. While the mass profile can be obtained by the density profile in a relative simple way, the distribution function is more complicated to get.

In this framework, seems to be appropriated to recall some math beyond gravitationally bounded systems.

A N -body system is an ensemble of N particles in which the i -th component interacts with each others via gravitational force:

$$\ddot{\vec{r}}_i = -G \sum_{j=0}^N \frac{m_j}{r_{ij}^2} = - \sum_{j=0}^N \nabla_{ij} \Phi, \quad (\text{C.1})$$

being r_{ij} the distance between i -th and j -th particles.

Therefore, the motion of each particle depends on the distribution of the others.

For any given density distribution, $\rho(r)$, it is possible to evaluate the gravitational potential using the Poisson equation:

$$\nabla^2 \Phi(\vec{r}) = -4\pi G \rho(\vec{r}), \quad (\text{C.2})$$

and the mass profile of the system, which is given by integrating the density profile over the whole space by definition:

$$M(\vec{r}) = \int_V \rho(\vec{r}) d^3 \vec{r}. \quad (\text{C.3})$$

These equations are simplified in the case of spherical systems, which provide a good approximation to the reality in many astrophysical systems such as globular clusters, elliptical galaxies and galaxies clusters.

Taking advantage from the spherical symmetry, equations above transform to:

$$\frac{1}{r^2} \frac{d}{dr} \left(r^2 \frac{d\Phi(r)}{dr} \right) = -4\pi G \rho(r), \quad (\text{C.4})$$

and

$$M(r) = 4\pi \int_0^R \rho(r) r^2 dr. \quad (\text{C.5})$$

It is trivial to show that mass and potential profile are connected by the relation:

$$M(r) = -\frac{r^2}{G} \frac{d\Phi(r)}{dr}. \quad (\text{C.6})$$

Defining the DF $f(r, v)$ such that $f(r, v) d^3 r d^3 v$ is the number of particle distributed in the volume $[r, r + d^3 r]$ and $[v, v + d^3 v]$, it can be connected to the density profile through the relation:

$$\rho(r) = 4\pi \int f(r, v) v^2 dv. \quad (\text{C.7})$$

As it will be shown in the next section, concerning the sampling of N -body the DF is fundamental to obtain the velocities of the particles. Unfortunately, its expression is not known in many cases or very difficult to evaluate, often numerical integration is needed.

To find a suitable expression for the df, it is convenient to define the relative potential $\Psi = \Phi - \Phi_0$ and the relative energy:

$$\mathcal{E} = \Psi - \frac{1}{2} v^2, \quad (\text{C.8})$$

where Φ_0 is automatically defined by requiring that the distribution function vanishes for $\mathcal{E} \leq 0$.

By the definition, it is possible to rewrite Eq.(C.7) as a function of the relative energy:

$$\rho(r) = 4\pi \int_0^\Psi f(\mathcal{E}) \sqrt{2(\Psi - \mathcal{E})} d\mathcal{E}, \quad (\text{C.9})$$

differentiating with respect to the relative potential leads to:

$$\frac{1}{\sqrt{8\pi}} \frac{d\rho}{d\Psi} = \int_0^\Psi d\mathcal{E} \frac{f(\mathcal{E})}{\sqrt{\Psi - \mathcal{E}}}, \quad (\text{C.10})$$

widely known as Eddington formula, that is an Abel integral whose solution is given in [38]:

$$f(\mathcal{E}) = \frac{1}{\sqrt{8\pi^2}} \frac{d}{d\mathcal{E}} \int_0^\mathcal{E} \frac{d\rho}{d\Psi} \frac{d\Psi}{\sqrt{\mathcal{E} - \Psi}}. \quad (\text{C.11})$$

The equation above allows the evaluation of an ergodic DF for any spherical systems, however, it should be positive everywhere; hence a spherical distribution can arise from an ergodic DF if and only if the term:

$$\int_0^\mathcal{E} \frac{1}{\sqrt{\mathcal{E} - \Psi}} \frac{d\rho}{d\Psi} d\Psi, \quad (\text{C.12})$$

is an increasing function of \mathcal{E} .

Whenever is possible to give analytical expressions for Eq.(C.5) and (C.11), the sampling can be made by meaning of Monte-Carlo methods.

However, since in most cases there are not known expressions for such relations, our code solve all the equations numerically, ensuring however great precision as it will be shown in the Section C.5 and C.6.

C.3 Sampling strategy

The first step in the sampling process is to solve numerically the Poisson equation in order to obtain the potential of the system on a grid of position.

The program solve Eq.(C.2) in two ways, depending on the density profile choosen: if we are handling truncated density profile, such as the King profile, the problem is solved giving central initial condition; on the other hand, if the profile is not confined in the space, the solution is obtained by integrating out to center using keplerian conditions

that are satisfied starting the integration at $R = 10^{14}r_l$, with r_l the length scale of the model considered.

Solving Eq.(C.5), the total mass is evaluated and used to obtain the keplerian potential GM/R that is the initial condition to integrate inward together with the requirement that the first derivative of the potential vanish at R .

The integration of the equations given above are made by meaning of the Burlisch-Stör algorithm [111]: an high precision, very fast integrator for ODE which combines Richardson extrapolation and the modified midpoint method.

The numerical solutions of Eqs. (C.2), (C.3) allows to draw a grid of positions, density, potential and mass. Interpolating the grid, it is possible then to evaluate the term $d\rho/d\Psi$ to solve numerically Eq. (C.11) and obtain the DF.

Extracting randomly a value M^* between the minimum M_{min} and the maximum M_{max} of the mass profile, it is possible to obtain the correspondent position $r(M^*)$ by inverting the mass profile; this process is repeated iteratively until the total mass of the system is achieved.

Regarding the velocities sampling, it is necessary to get a grid of \mathcal{E} and $f(\mathcal{E})$ by solving Eq.(C.11). However, to perform this task three steps are required:

1. to evaluate $d\rho/d\Psi$;
2. to evaluate the integral in Eq. (C.11);
3. to evaluate the derivative of the integral with respect to the relative energy.

The simplest numerical evaluation of a derivative is made computing the different quotient:

$$g'(x) = \frac{g(x+h) - g(x)}{2h}; \quad (\text{C.13})$$

however, since the grid in potential and density is not equally spaced we generalized this formula by arranging the Taylor expansion truncated to the 3rd order of the function $\rho(\Psi)$ evaluated in three different points:

$$\begin{aligned} \rho(\Psi_0 + h_1) &= \sum_{n=0}^3 \frac{1}{n!} \frac{d^n \rho(\Psi)}{d\Psi^n} \Big|_{\Psi_0} h_1^n + O(h^4), \\ \rho(\Psi_0 - h_2) &= \sum_{n=0}^3 \frac{1}{n!} \frac{d^n \rho(\Psi)}{d\Psi^n} \Big|_{\Psi_0} h_2^n + O(h^4), \\ \rho(\Psi_0 \pm 2h_3) &= \sum_{n=0}^3 \frac{1}{n!} \frac{d^n \rho(\Psi)}{d\Psi^n} \Big|_{\Psi_0 (2h_3)^n + O(h^4)}; \end{aligned} \quad (\text{C.14})$$

manipulating algebraically these equations and by using Eq. (C.13) it is possible to find $\rho'(\Psi)$. To improve the precision we evaluated the derivative once using $\rho(\Psi_0 + 2h_3)$ and once using $\rho(\Psi_0 - 2h_3)$; we obtained this way two evaluations of the derivative, let's say ρ'_+ and ρ'_- , and the final evaluation given is the arithmetic mean of these two quantites:

$$\rho'(\Psi) = \frac{\rho'_+ + \rho'_-}{2}. \quad (\text{C.15})$$

Hence, the solution of the integral:

$$I(\mathcal{E}) = \int_0^{\mathcal{E}} \frac{d\rho}{d\Psi} \frac{d\Psi}{\sqrt{\mathcal{E} - \Psi}}, \quad (\text{C.16})$$

is achieved by meaning of the Cavalieri-Simpson formula,

$$I(x) = \int_a^b f(x)dx = \frac{h}{3} \left[y_0 + y_n + 2 \sum_{i=2}^{2n-2} y_i + 4 \sum_{i=1}^{2n-1} y_i \right]. \quad (\text{C.17})$$

The derivative with respect to the energy of the integral $dI/d\mathcal{E}$ is made finally by meaning of the two-point rule:

$$I'(\mathcal{E}) = \frac{I(\mathcal{E} + h) - I(\mathcal{E} - h)}{2h}. \quad (\text{C.18})$$

Despite the numerical techniques used are not high order precision, they ensure great accuracy in distribution function evaluation, as we will show in Sec. C.6.

Recalling that the local escape velocity for a particle placed in r_i is given by:

$$v_{esc}^2 = 2\Psi(r_i), \quad (\text{C.19})$$

It is possible to define the ratio, q , between the velocity of the i -th particle and v_{esc} . This parameter is linked to the relative energy and the potential dividing Eq.(C.8) by $\Psi(r_i)$ such that:

$$q^2 = 1 - \frac{\mathcal{E}}{2\Psi(r_i)}. \quad (\text{C.20})$$

The probability to have an absolute value for the velocity v at a given position r then is given then by:

$$g(q) \propto f(q)q^2. \quad (\text{C.21})$$

For a given value q^* in the range $[q_{min}, q_{max}]$, the velocity $v^* = v_{esc}(r)q^*$ is assigned to the i -th particle if the value $g(q^*)$ evaluated by means of a linear interpolation is such that $g(q^*) < g^*$, with g^* extracted randomly between the minimum, g_{min} , and the maximum, g_{max} , of the function $g(q)$.

In the next section, a range of models widely used in theoretical astrophysics are presented. These models are implemented yet in the code and can be sampled in a very easy way as it will be shown in Sec. C.5.

C.4 Well-known density profiles

Spherical models are widely used to simulate various astrophysical situations. As an example, the King distribution has been used over many years to describe globular clusters [69], while random spheres are used often to describe the initial stages of galaxy clusters; moreover, for many galaxy models are used density profiles with a central cusp [35].

Also for dark matter haloes a cuspidal density profile is used, the most used for many years has been the Navarro, Frenk and White profile [85].

To include a large fraction of these density profiles and give a very comfortable environment to the user, the code is ready to sample a King sphere, a broken powerlaw sphere with or without taking in account a central point-like object; otherwise, the user can write down its own density profile.

In the following, we just briefly recall some important features of the King and the powerlaw density profiles.

King models are a family of lowered isothermal models in which the distribution function of the isothermal sphere is truncated to 0 when the relative energy exceed a given value such that:

$$f_K(\mathcal{E}) = \begin{cases} \rho_1 (2\pi\sigma^2)^{-3/2} \left(e^{\mathcal{E}/\sigma^2} - 1 \right) & \mathcal{E} > 0, \\ 0 & \mathcal{E} \leq 0. \end{cases} \quad (\text{C.22})$$

By using Eq.(C.7) the density profile is given in terms of the relative potential:

$$\rho(r) = \rho_1 \left[e^{\Psi/\sigma^2} \operatorname{erf} \left(\frac{\sqrt{\Psi}}{\sigma} \right) - \sqrt{\frac{4\Psi}{\pi\sigma^2}} \left(1 + \frac{2\Psi}{3\sigma^2} \right) \right]. \quad (\text{C.23})$$

Since these kind of density profiles are very useful in dealing with systems with a central relaxed core which and tidally truncated by an external field, they had been widely used to model globular clusters and in some cases elliptical galaxies.

On the other hand, broken power-law profiles were proposed firstly by Hernquist [62] and consist in density profiles depending on three free parameters (α, β, γ) :

$$\rho(r) = \rho_b \left(\frac{r}{r_b} \right)^{-\gamma} \left(1 + \left(\frac{r}{r_b} \right)^\alpha \right)^{(\gamma-\beta)/\alpha}; \quad (\text{C.24})$$

these density profiles represent a wide range of dynamical models suitable to describe reliable astrophysical situations. The choice $(2, 5, 0)$ leads to the Plummer sphere used often to model star clusters, while the choice $(1, 4, \gamma)$ leads to the Dehnen models [35] widely used to model elliptical galaxies with a core (or a cusp) in their central regions. Instead, the triplet $(1, 3, 1)$ corresponds to the Navarro, Frenk and White profile (NFW), widely used to model cold dark matter halos [85].

Moreover, the choice $(n, 3 - k/n, \gamma)$, with (n, k) natural numbers and $\gamma \in [0, 3]$, represent a subset in which could be considered a central mass allowing also an analytical evaluation of $\rho(r)$, $\phi(r)$, $M(r)$, $\sigma^2(r)$ [124].

Due to the fact that many observational features had allowed in recent times the discovery of black holes in many astrophysical systems, the code produces stable, self-consistent models with a central point-like objects for any given density profile.

To produce such samples, the code assigns the positions to the particles, by using the density profile of the background, cause it is not affected by the central point, while the velocities are obtained by evaluating the DF as discussed in Eq. (C.11) considering as total potential the sum of the background potential Φ_* , and the keplerian potential $\Phi_{BH} = Gm_{BH}/r$.

C.5 User utilities

C.5.1 Input parameters

As mentioned above, since often ellipticals and dwarf galaxies are modeled through powerlaw density profiles, and that globular clusters instead are described by the King models, these two classes of profiles are included in the code yet. User can choose which kind of model sample writing the corresponding key words in the input file “parameters.txt”. If the user would like to use a different density profile instead, he should just write the correct expression of the density in the file “rho.cpp”.

Now, let's take a close look to the input file, in the following.

```
***** PARAMETERS.TXT *****
brokenpl // model that you want to sample:
    king, brokenpl, custom
*****
***** PARAMETERS FOR KING MODEL *****
*****
1.0      // king's core radius
6.0      // king's W0
*****
** PARAMETERS FOR BROKEN POWER LAW MODEL **
*****
2.0      // alpha
5.0      // beta
0.0      // gamma
0.238732414637843 // rho_b
1.0      // r_b
*****
***** GENERAL AND COMMON PARAMETERS *****
*****
1.0      // total mass of the system
(excluding the eventual black hole)
1.0e12   // infinite distance
(the potential is become keplerian)
0.0      // mass of the central black hole
131072   // number of particles
*****
```

The first row allows the user to select a broken powerlaw profile, a King profile or a “custom” profile by writing “king”, “brokenpl”, or “custom”, respectively.

To sample a King sphere, the user has to fill the two row relative to the section - “PARAMETERS FOR KING MODEL”: the first row requires the King radius

$$r_0 \equiv \sqrt{\frac{9\sigma^2}{4\pi G\rho_0}}, \quad (\text{C.25})$$

where ρ_0 is the central density and σ the velocity dispersion of the model; the second row, instead, would require the central relative potential, W_0 , related to the potential

through the relation:

$$W_0 = \Phi(0)/\sigma^2. \quad (\text{C.26})$$

To sample a broken power law the user should fill the second section “PARAMETERS FOR BROKEN POWER LAW MODEL” selecting (α, β, γ) , the density scale (ρ_b) and the length scale (r_b) defined in Eq.(C.24).

In the third case instead, the user will write its own density profile in the file “rho.cpp”.

The last section, “GENERAL AND COMMON PARAMETERS”, contains some parameters that should be given by the user for any density profile choosen: the total mass of the system (without take in account the eventual BH mass), the distance over which the keplerian potential is a good approximation to the real potential, the mass of the central BH and the number of particle to sample.

C.5.2 Compiling and running the code

To use the code, after downloaded the package at the website and extracted the archive, it should be compiled on a UNIX system just typing on a command line:

```
> sh make.sh
```

the executable takes what it needs directly from the “parameter.txt” file, then it is not needed to recompile everytime the code is used.

The executable GSam.x can be launched typing on a command line:

```
> ./GSam.x
```

Positions, velocities and mass of the generated particles will be written then on “pos_vel_out.dat” file.

Moreover, it is possible to generate, if the user requests them, two files:

- “distribution_function.dat”;
- “quantities_info.dat”;

the first file contains relative energy (\mathcal{E}) in the first column and the distribution function $(f(\mathcal{E}))$ given in Eq.(C.7), in the second column. The second file instead has five columns

model	α	β	γ	BH(y/n)	r_{cut}
PLUM	2	5	0	n	∞
D05	1	4	0.5	n	∞
D1	1	4	1	n	∞
NFW	1	3	1	n	∞
KING	-	-	-	n	∞
D02c	1	4	0.2	y	0.070

Table C.1: *Sampled models using our code GSam, are indicated the slopes of the generalized Tremaine profiles and the radius at which the models as been truncated. $r_{cut} = \infty$ means that the profile has been cut at a radius 1000 times the scale radius of the profile, which has been set equal to the unity. Any model contains (y) or not (n) a central point-like mass.*

each one contains, respectively: the radius r , the density ρ , the potential Φ , the derivative $d\rho/d\Phi$ and the mass M of the system.

To generate these files, or one of them, the user should run in the command line:

```
> ./GSam -v=OPT
```

where OPT should be “all” to have both the files, “df” to have only the distribution function file, or “rho” to have the file with density, potential, and mass profile.

C.6 Tests and comparison

To put on evidence the quality of our sampled systems, in this section it is shown the agreement between analytical and sampled quantities such as density, mass and potential profiles and the stability over significant dynamical timescale.

In Tab. (C.1) are listed the models used, which are Dehnen models with different slopes and containing or not a central point like mass, a Plummer model, a NFW model and finally a King model.

All the models have mass and lenght scale set equal to the unity. For each model, we run a simulation with $N = 131,072$ particles to check the stability on timescales wich are roughly 40 times the dynamical time of each system.

In the following, we briefly describe the models we investigated, and the stability results obtained through direct N -body simulations.

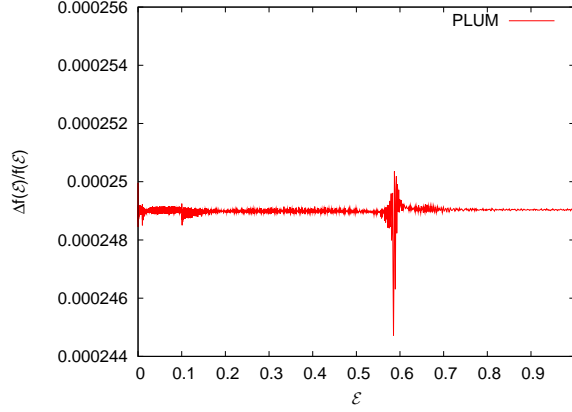


Figure C.1: *Relative error on the DF evaluation for the PLUM model.*

C.6.1 Plummer profile

The Plummer model has been widely used to model globular clusters, although it does not match real density profiles at large radii.

It is possible to provide a full analytical expression for the DF in this case:

$$f(\mathcal{E}) = \frac{24\sqrt{2}}{7\pi^3} \mathcal{E}^{7/2}, \quad (\text{C.27})$$

which can be compared with its numerical extrapolation obtained through our code. In Fig. (C.1) is shown the relative error of the numerical to the analytical evaluation of the DF.

The Plummer density profile is given by:

$$\rho(r) = \left(\frac{3M}{4\pi r_s^3} \right) \left(1 + \frac{r^2}{r_s^2} \right)^{-5/2}, \quad (\text{C.28})$$

connected to the potential profile:

$$\Phi(r) = -\frac{GM}{\sqrt{r^2 + r_s^2}}, \quad (\text{C.29})$$

and mass profile:

$$M(r) = \frac{r^3}{(r^2 + r_s^2)^{3/2}} M, \quad (\text{C.30})$$

compared with their numerical evaluations as it is shown in FigC.2 and C.3. In this case, the agreement between analytical expression and numerical evaluation is excellent.

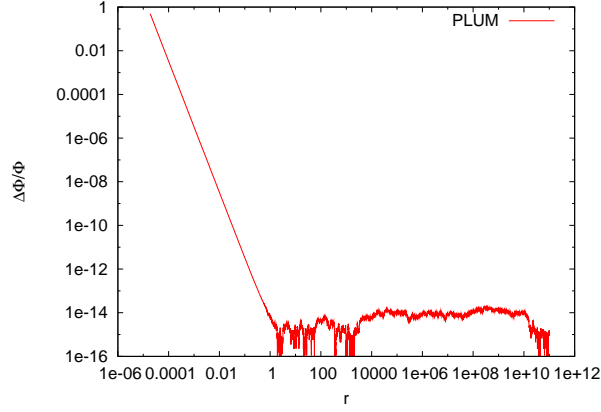


Figure C.2: *Relative error of the potential profile in the PLUM model.*

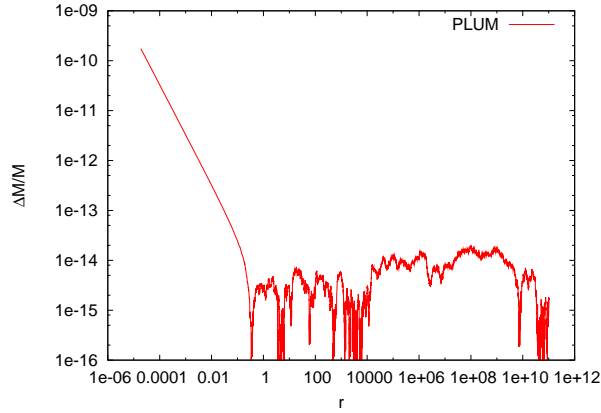


Figure C.3: *Relative error of the mass profile in the PLUM model.*

Running a sample of 10^5 particles, we found an excellent stability, as can be seen looking at the density profile in Fig. (C.4), which does not change significantly over 40 dynamical times.

C.6.2 Dehnen profiles

This family of density pairs provides analytical expressions for density, mass and potential profiles; however, the fully analytical expression for the DF can be found only if $(2 - \gamma)^{-1}$ is an integer or half-integer. In this case, we compare our results with the analytical expression for DF in the case $\gamma = 1$ and with a numerical estimation in the case $\gamma = 0.5$.

The analytical expression of the distribution function in the case $\gamma = 1$ has been presented in Eq. (A.7) and has been used to evaluate the relative error of our numerical estimation as it is shown in Fig. (C.5).

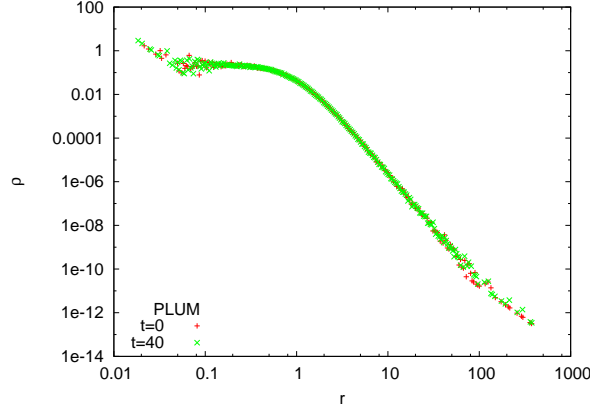


Figure C.4: Density profile evaluated at the start of the simulation and after 40 dynamical times. As you can see, there are no changes during the evolution of the system.

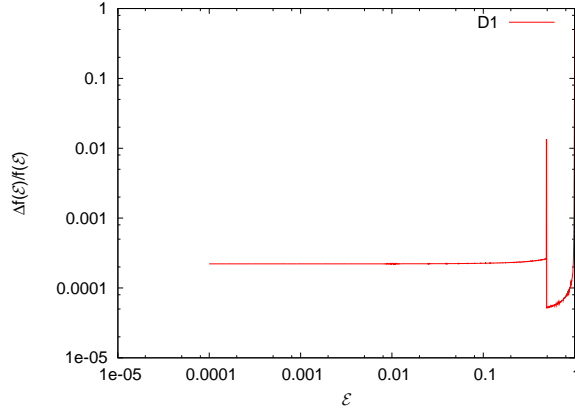


Figure C.5: Relative error of the DF for D1 model.

Moreover, we compared the potential and mass profiles, whose relative errors are shown in Fig. (C.6) and (C.7), respectively.

In the model D05, instead, the DF is not given analytically, and the relative error shown in Fig. (C.8) is made by using an alternative way to evaluate it numerically. The differences in the two methods cause the great relative error measured.

However, the excellent agreement with the potential and mass profile found also in this model ensure us that the code is able to sample quite well such a system (see Figs. (C.9), (C.10)).

In these two cases (D1 and D05), it is shown moreover the stability of the systems in Fig.C.18 together with NFW and KING models.

The model D02c instead, represent a Dehnen truncated model with a central BH. The density slope has been set $\gamma = 0.2$, and the truncation radius $r_{cut} = 0.07r_s$, with r_s the length scale of the system.

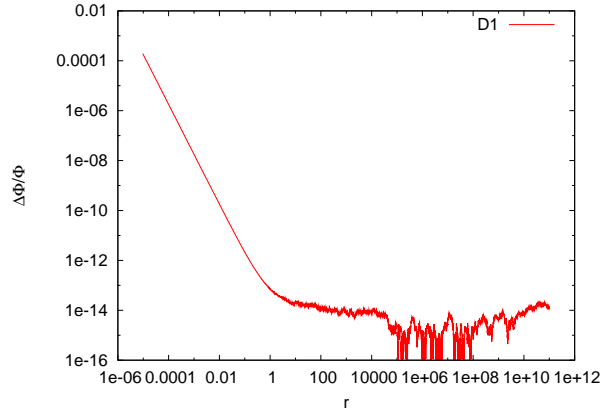


Figure C.6: Relative error of the potential profile in the D1 model.

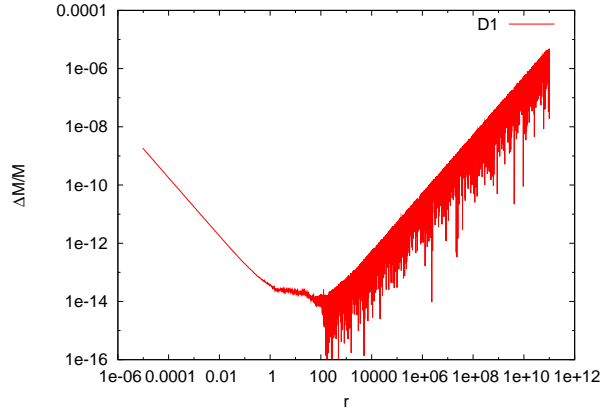


Figure C.7: Relative error of the mass profile in the D1 model.

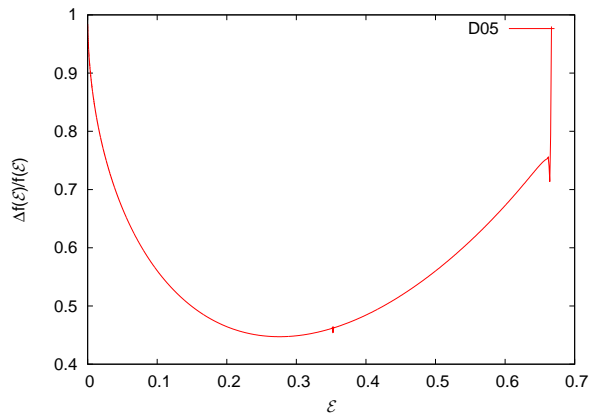


Figure C.8: Relative error of the DF in the D05 model. Since it is not possible to give an analytical expression for the DF, the error has been estimated by using as calibration a numerical expression of the DF evaluated with a different procedure.

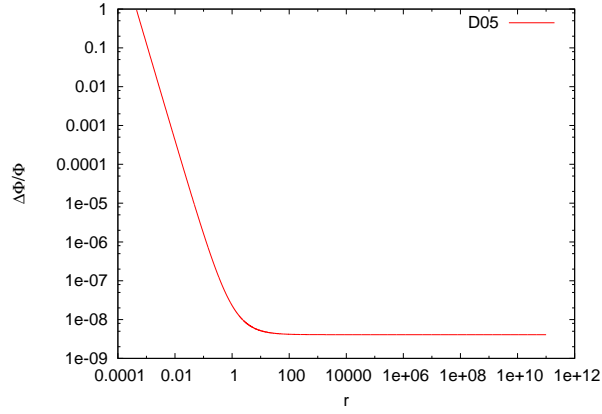


Figure C.9: *Relative error of the potential profile in the D05 model.*

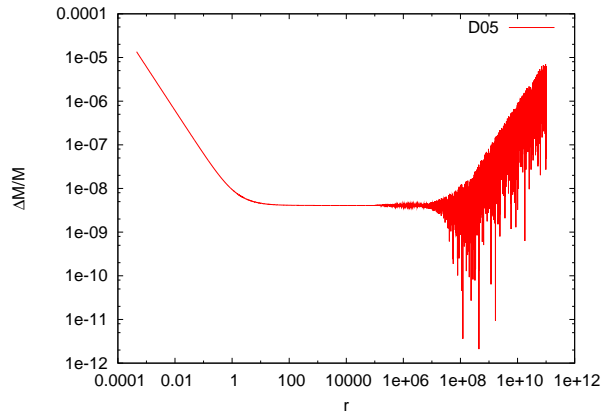


Figure C.10: *Relative error of the mass profile in the D05 model.*

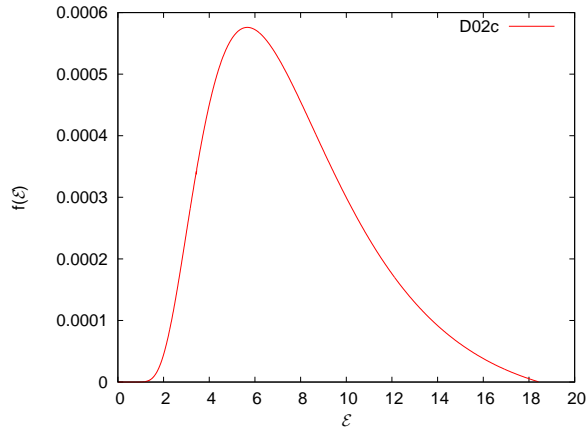


Figure C.11: *Distribution function in the D02c model.*

Unfortunately, in this case is not possible to give an analytical expression nor for the DF neither for the potential and mass profiles, and we limit to show here the numerical evaluation of these quantities (Figs. (C.11), (C.12) and (C.13), respectively) and the stability check (Fig. (C.14)).

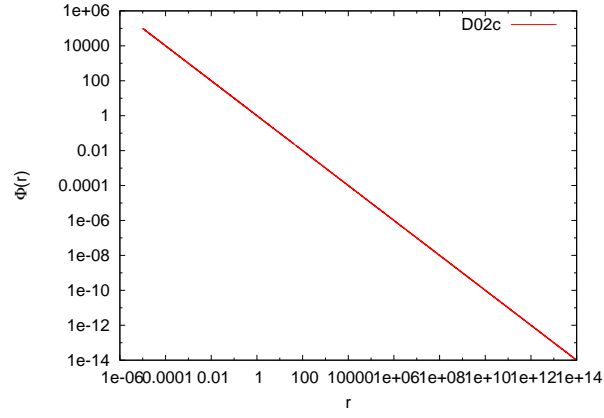


Figure C.12: *Potential profile in the D02c model.*

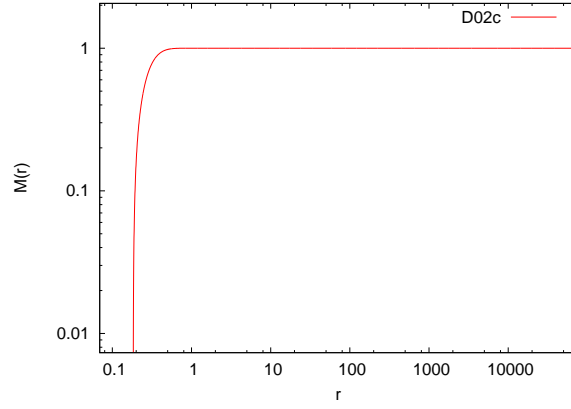


Figure C.13: *Mass profile in the D02c model.*

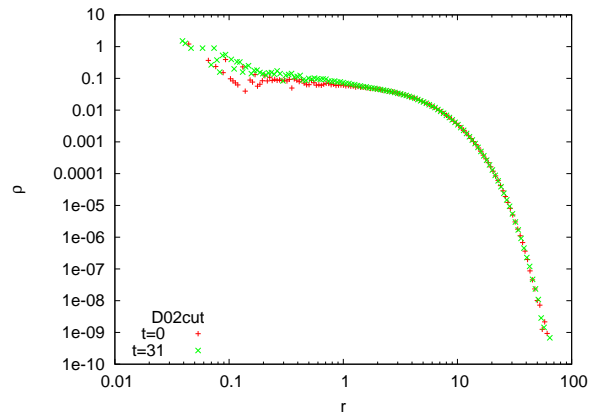


Figure C.14: *Density profiles evaluated in two different times for D02c model. Since there are no significant changes we can conclude that the sampled system is quite stable over significant dynamical timescales.*

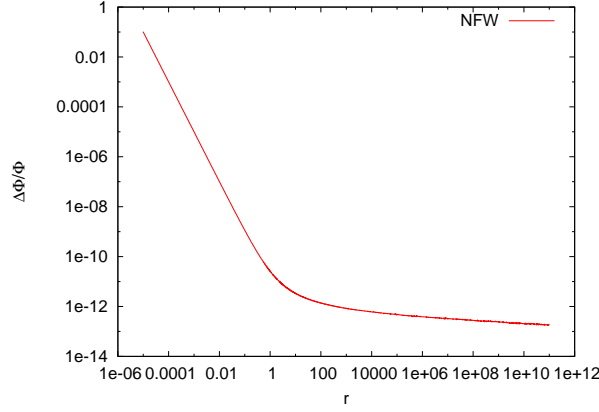


Figure C.15: *Relative error for the potential profile in the NFW model.*

C.6.3 NFW profile

This profile has been used to model dark matter halos (DMH) surrounding galaxies and galaxy clusters, although there is growing evidence for alternative distribution for this component of the Universe.

Concerning the DF, there exist in literature only numerical estimations for this model, then we decided to not compare them with our evaluation.

Instead, it is possible to evaluate analytically the density profile, which is given by:

$$\Phi(r) = \Phi_0 \frac{\ln(1 + r/r_s)}{r/r_s}, \quad (\text{C.31})$$

and the mass profiles, instead, given by:

$$M(r) = 4\pi\rho_0 r_s^3 \left[\ln\left(\frac{r_s + r}{r_s}\right) - \frac{r}{r + r_s} \right]. \quad (\text{C.32})$$

The comparison between analytical and numerical evaluation of these profiles are shown in Fig. (C.15) and (C.16).

The agreement with analytical expressions also in this case is good, and the sampled system is stable as it is shown in Fig. (C.18).

C.6.4 King profile

The King profile has been widely used over years to model globular clusters but also galaxies clusters. Here we model a King profile with a core radius $r_{core} = 1$ and adimensional potential well $W_0 = 6$.

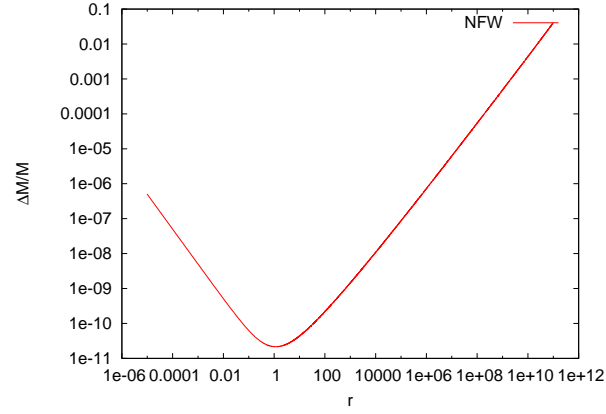


Figure C.16: *Relative error for the mass profile in the NFW model.*

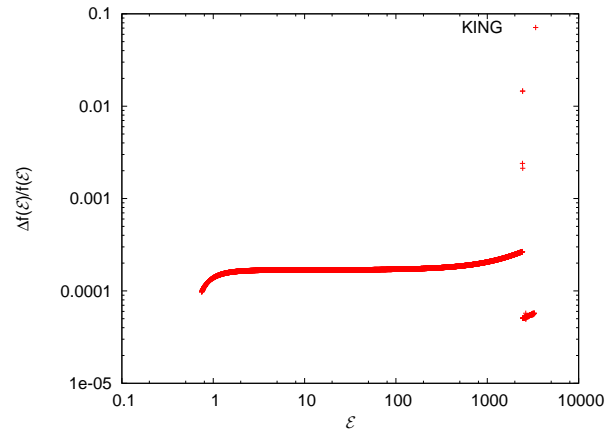


Figure C.17: *Relative error for the DF in the KING model.*

Since the Poisson equation in this case is an integro-differential equation of the potential, it is not possible to give an analytical expression of $\Phi(r)$ which instead exists for the DF.

The comparison between $f(\mathcal{E})$ described in Eq.C.22 and the numerical evaluation is shown in Fig.C.17.

The stability of such system is shown in Fig.C.18 together with the stability check made for others models.

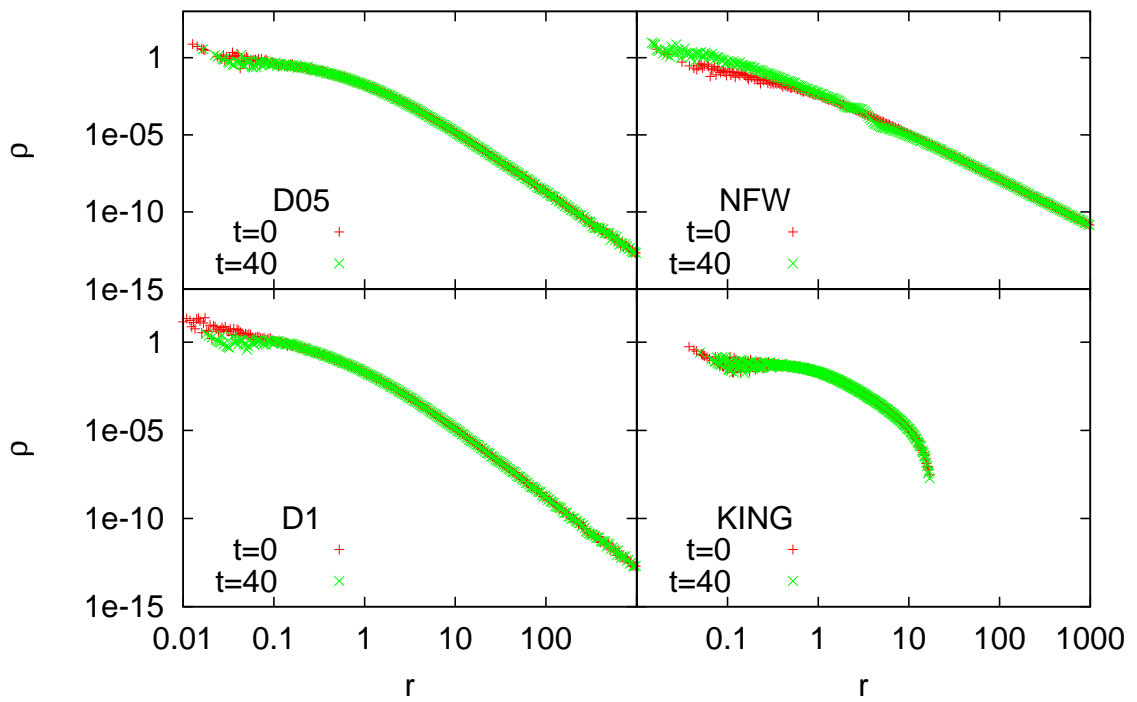


Figure C.18: *Density profiles evaluated at two different times, in four different systems. As you can see, there are no significant changes during the evolution which imply a quite good stability of each system.*

APPENDIX D

THE FORMATION OF THE MILKY WAY NUCLEAR STAR CLUSTER

D.1 The Milky Way galaxy

Our known galaxy, the Milky Way, is a barred spiral galaxy (Sb type in the Hubble classification) belonging to a small cluster of galaxies (around 70 objects) called Local Group.

The Local Group is a small part of a larger cluster called Virgo Supercluster which contains at least 100 group and cluster of galaxies, with a total mass of more than $10^{15}M_{\odot}$ [40].

Due to our position in the Galaxy, it is quite complex to draw its structure. What we know at present, thanks to various experiment during the last 20 years, is that the Milky Way can be modeled as a sum of different components [2, 80].

Consider as first the external part, the whole galaxy is embedded in a dark matter halo (DMH) which mass is roughly $M_{DMH} \sim 9 \times 10^{11}M_{\odot}$ and extends beyond $100kpc$; this component contributes significantly to the total mass of the system, giving an explanation for the far end of the rotation curve.

Going inside the galaxy, there is a galactic disk (GD), extended up to $10kpc$ from the center, rich in gas and stars. Our solar system is located at the periphery of the disk, at nearly $8.5kpc$ from the galactic center. The galactic disk consists in two major components: a thick disk, with a height scale $z = 900pc$, and a thin disk ($z = 300pc$). The total contribution in mass from the disk is $M_{GD} \sim 8.6 \times 10^{10}M_{\odot}$.

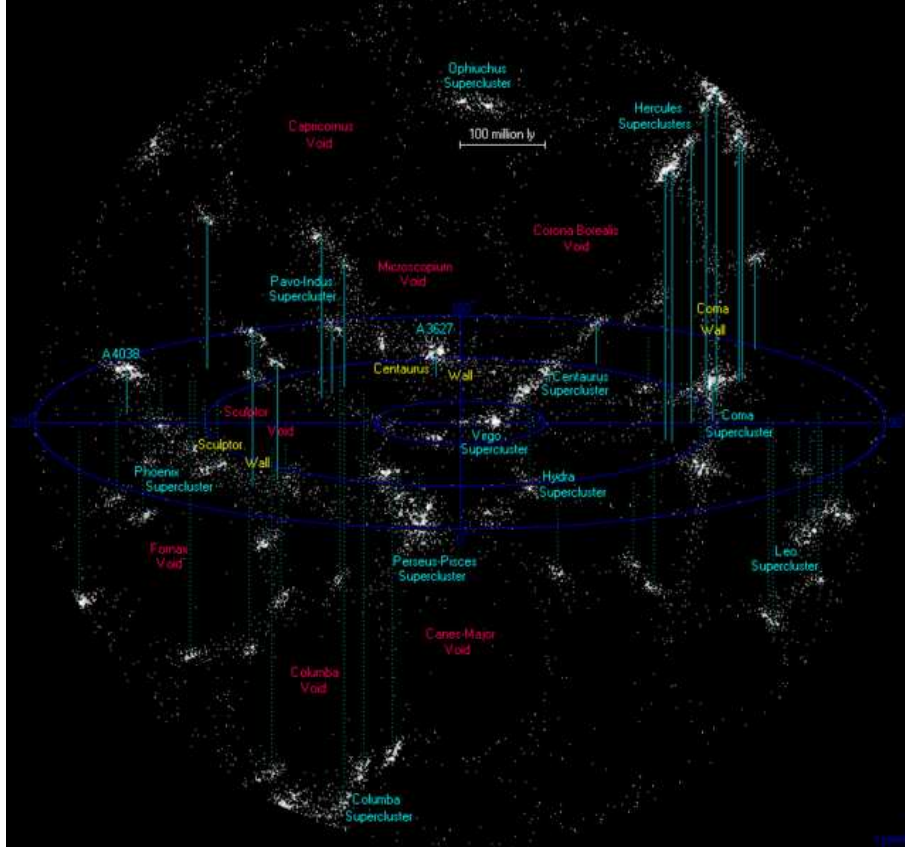


Figure D.1: *The Virgo supercluster.*

The central part is dominated by the galactic bulge (GB), a nearly prolate region extended up to $2kpc$, which contains the heart of the galaxy. This region gives a mass contribution of $M_{GB} \simeq 9 \times 10^9 M_{\odot}$.

Taking a closer look to the galactic center (GC), it is possible to distinguish a small substructured region enclosed within roughly $300pc$ [73].

This region can be subdivided in two main components: the Central Molecular Zone (CMZ) which is the component related to the Inter Stellar Medium (ISM) and the Nuclear Bulge (NB), related instead to the stellar component.

The CMZ contains all molecular gas in the central kpc of the Galaxy including cold molecular gas outside the NB in the GB. An internal substructure is the Nuclear Molecular Disk (NMD) that is the gas heated by the stars belonging to the NB.

The NMD can be divided in an inner warm disk, a small disk composed by warm dust and molecular gas in a small region of $\sim 120pc$; and an outer cold torus with colder dust and molecular gas.

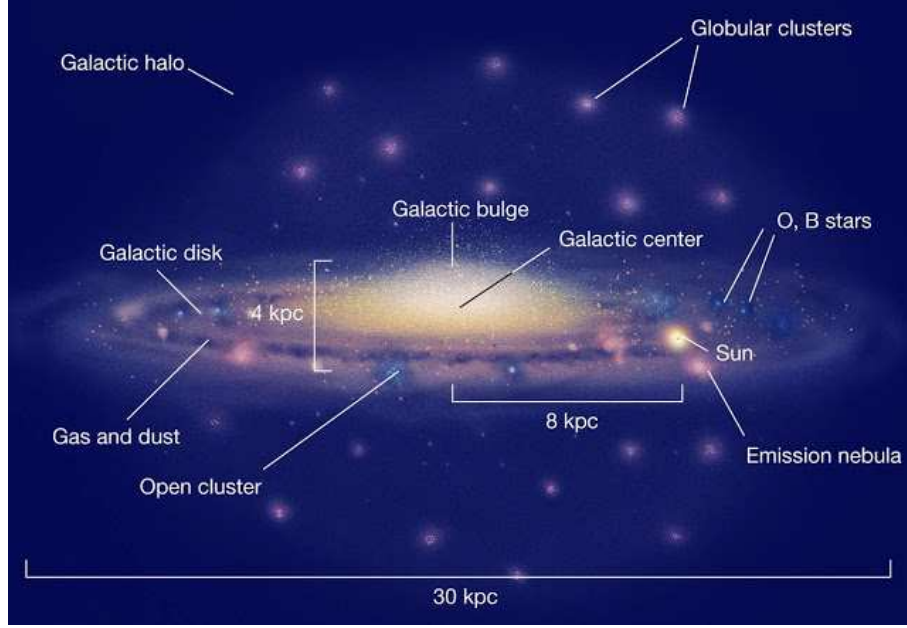


Figure D.2: *Structure of the Milky Way.*

The NB is a region extended within $120 - 200 pc$ that can be divided in two main components: the Nuclear Stellar Disk (NSD), which is a large scale disk of mainly cool stars, and the Nuclear Star Cluster (NSC) which extends few pc from the center.

Firstly observed by Becklin and Neugebauer [12], the Milky Way NSC seems to be very similar to its extragalactic cousins and, being the closest NSC with respect to us, it is a valid location to understand them.

Our NSC has a total mass $M_{NSC} \geq 10^7 M_{\odot}$, a radius $r = 3 - 5 pc$ and seems to have a quite complex star formation history. It cannot be thought as an old dynamically relaxed system, due to the fact that it shows clearly signature for repeated star formation bursts [100].

Recent studies had shown that there is a core of red giant stars within $\sim 0.5 pc$, while early type stars had a steeper surface density profile within $\leq 0.04 pc$ from the center [36, 73].

Placed at the center of this quite complicated system, there is a massive black hole whose mass is $M \sim 4 \times 10^6 M_{\odot}$ [49, 51], which strongly interacts with the stars of the NSC, dominating the mass distribution within $1.25 pc$ from the center [73].

D.2 The formation of the Milky Way Nuclear Star Cluster

The formation of a NSC in our galaxy is still under debate, as well as the formation of compact nuclei in other galaxies (see Chap.4).

The more straightforward way in attempting to explain its formation through the merger scenario, is to use direct N -body simulations, as we explained before.

However, there are at least two main problems in dealing with N -body simulations reproducing such a system:

- first, the quite complicate geometry of the Galaxy requires a very refined sampling method, in order to take in account the presence of the disk, the spiral arms, the different density profiles related to each component of the system itself;
- second, the ratio between the NSC building blocks (GCs) and the whole galaxy is very low $M_{GC}/M_{MW} \sim 10^5$. This means that if we would simulate the galaxy with, let's say, 10^6 particles, we will use for each cluster only 10 particles, each one representing a star of $\sim 10^5 M_\odot$.

To solve the second problem, the better solution is to use $N \simeq 10^{12}$ particles in the simulation. Unfortunately, this is quite impossible at the present, due to the fact that such a simulation will require more than a Hubble time to give some results.

Due to this, it is quite useless to solve the first problem, thus in general what it can be done is to simulate only a small fraction of the galaxy, let's say hundreds of parsecs.

D.3 Previous works

On this topic, an interesting work has been done by Antonini et al. [3]. They simulated the decay of 12 globular clusters limiting their Milky Way model to a small region, in order to follow their latest evolution toward the merging phase and beyond.

To model the galaxy up to $R = 50pc$, they used a truncated power-law profile:

$$\rho(r) = \tilde{\rho} \left(\frac{r}{\tilde{r}} \right)^{-\gamma} \text{sech} \left(\frac{r}{r_{cut}} \right), \quad (\text{D.1})$$

with $\tilde{\rho} = 400 M_\odot pc^{-3}$, $\tilde{r} = 10pc$ and $r_{cut} = 22pc$. This choice led to a mass density at $10pc$ similar to those observed in the Milky Way ($\sim 400 M_\odot pc^{-3}$). The total mass of the truncated model was $M = 9.1 \times 10^7 M_\odot$.

The number of particles to model the galaxy was $N = 240,000$ corresponding to a mass for each particle of the system $m_* = 380M_\odot$.

On the other side, each GC has been sampled following a King model with $W_0 = 6.5$ and tidal radius $r_T = 8pc$, total mass $M_{GC} = 10^6 M_\odot$ and each one was represented with $N = 5715$ particle, corresponding to a single particle mass $m_* = 200M_\odot$.

Star clusters started in circular and radial orbits at $r_0 = 20pc$, while the gravitational interaction was smoothed with a softening parameter $\epsilon = 0.01pc$.

The main results of this work are summarized in the following:

- after the merging, the resulting star cluster had a density profile cored within $1pc$, that fell off outside as $\sim r^{-2}$;
- the final NSC evolved toward an oblate/axysimmetric shape, with a slow rotation and a mild tangential anisotropy within $30pc$;
- the evolution post-NSC formation led the system toward the spherical symmetry in position and velocity phase space, the initial core tends shrink due to the action of the SMBH, leading after $10Gyr$ to a small cored region ($\sim 10pc$) and a steep density profile outward ($\sim r^{-2}$) compatible with a Bachall-Wolf cusp [8];

D.4 A new, improved simulation of the Milky Way NSC

As a part of this Ph.D. research, we made a new simulation changing the initial set-up of the Globular Cluster System (GCS) to investigate whether or not there are significant changes in the formation and evolution of the Milky Way NSC.

The galaxy has been modeled by using the same density profile used in [3], but sampling a larger number of particles, $N_{GAL} = 911,370$, which allowed us to increase the stars in the GCS ($N_{GCS} = 137,206$) reaching for each cluster a considerable number of objects ($N_{GC} = 11,433$).

Each cluster has been sampled considering a Salpeter initial mass function $\xi(M) \propto M^{-s}$ with $s = 2.35$ [98] with initial mass segregation in order to take in account the previous evolution of the clusters before they reached the inner $100pc$.

This choices would imply that the mean mass of stars belonging to the cluster and the mass of galactic stars is reasonable ($m_* \simeq 22M_\odot$).

We simulated the same circular orbits with the same smoothing lenght as it has been done in [3].

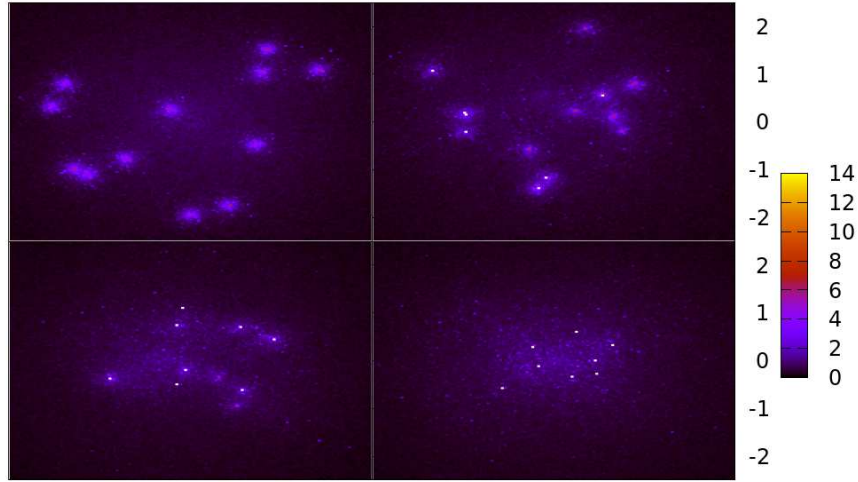


Figure D.3: *Contour plot showing the evolution of the GCS. From left to right, the snapshot are taken at $t = 0, 5, 10, 20T_u$, where $T_u = 2.35 \times 10^5 \text{yr}$.*

In Fig. (D.3) are shown different phases of the globular clusters evolution. The merging phase leads to the total disruption of the clusters in less than a *Myr* ($t_{\text{merge}} \simeq 5.8 \times 10^5 \text{yr}$).

In Fig. (D.4) is shown the density profile of the whole system at the beginning of the simulation and after the merging.

It is interesting to note that the density profile of the system after the merging is substantially unchanged, there is only a small lowering in the slope.

During the GCs decay, the galaxy suffers a small expansion as it can be argued looking at the lagrangian radii (see Fig. (D.5)).

The kinematical evolution of the whole system is well evident in Fig.D.6, in which is shown the velocity profile. After the merge, there is a sort of valley in a small region between 1 and $10pc$, that correspond to an increase of high velocity particles in the far end of the distribution, roughly at $r > 500 - 1000pc$, hence, the interaction between single stars, clusters and the central BH leads to an energization of a small fraction of particles that run away from the system at high velocity, with respect to the mean local velocity. In the following, we will try to understand to what part of the system do the particles belong.

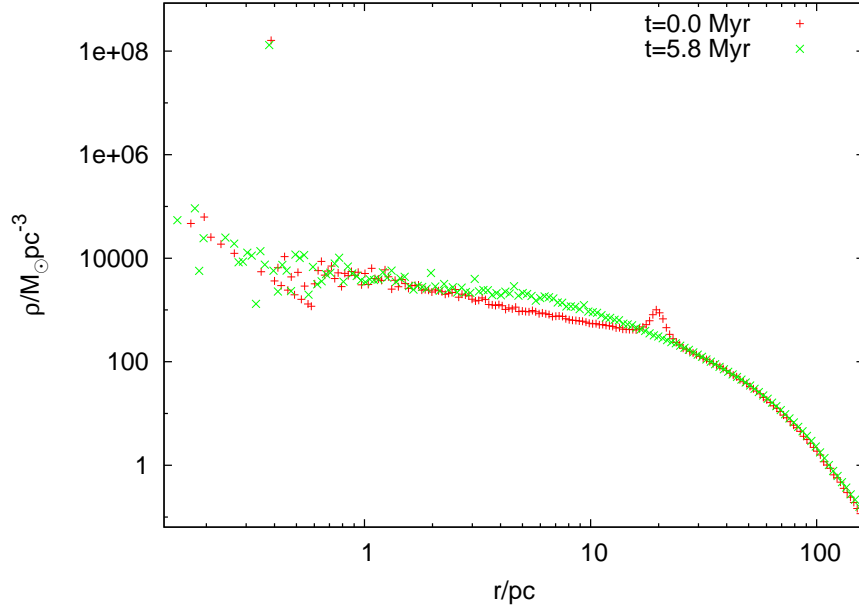


Figure D.4: *The density profile of the whole system seen at $t = 0$ and $t = 5.8 \text{ Myr}$. The small red peak identifies the GCS. In the green profile, the peak had disappeared because of the destruction of all the clusters. The overdensity at $r \simeq 0.2 \text{ pc}$ is due to the BH.*

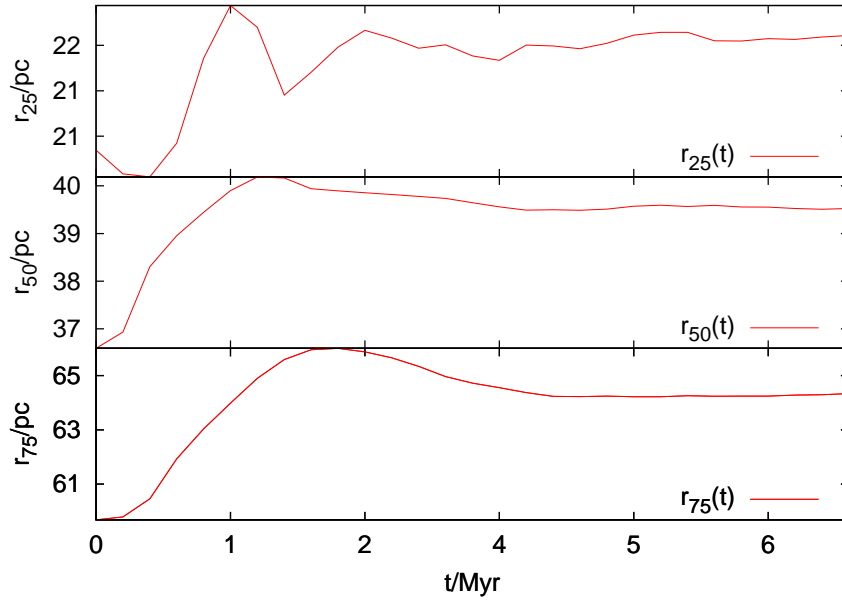


Figure D.5: *Lagrangian radii as a function of the time. From top to bottom are shown the 25%, 50%, 75% mass lagrangian radius, respectively.*

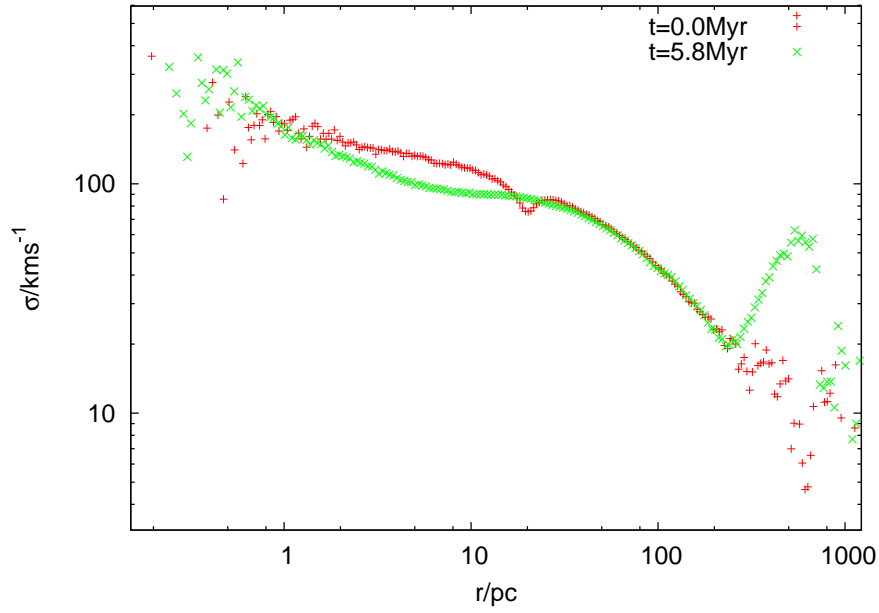


Figure D.6: *The velocity dispersion of the whole system (galaxy+BH+GCs) at the beginning of the simulation and after the merging of the 12 clusters.*

After the merging, which occurs in $t \sim 6 Myr$, we evolve the system up to $t = 68 Myr$ in order to investigate both the stability of the NSC formed and dynamical effects on the distribution of particles.

Fig. (D.7) shows the time evolution of the NSC lagrangian radii containing 25–50–75% of the total mass. There is a sort of stabilization after roughly $40 Myr$ and then a slow increase.

Instead, Fig. (D.8) shows the evolution of the lagragian radii which contain 25–50–75% in mass of massive stars with masses above $2000 M_{\odot}$ (red line in the graph) and the contribution of lighter mass whit masses below $40 M_{\odot}$. It should keep in mind that each cluster has been sampled with only 11,433 particles to simulate a total mass of $10^6 M_{\odot}$, that imply a mean mass of $m \sim 22 M_{\odot}$, so it is not surprising to have such high masses for each star in the cluster. It is evident the segregation in mass, with heavier stars that concentrates more in the core of the NSC and the lighter stars in the outer zone. The radius of the NSC can be argued from these three figures, which is $R_{NSC} \in [9 - 20] pc$.

Despite the mass segregation, the resulting NSC shows a density profile substantially stable over all the simulated time, as it is shown in Fig.D.9.

The NSC contribution to the whole density profile of the system is shown in Fig.D.10.

Information about the kinematics of the NSC can be obtained by comparing the velocity dispersion components radial and tangential. Looking at Fig.D.12, the radial velocity dispersion is sistematically lower than the tangential component, indicating that our

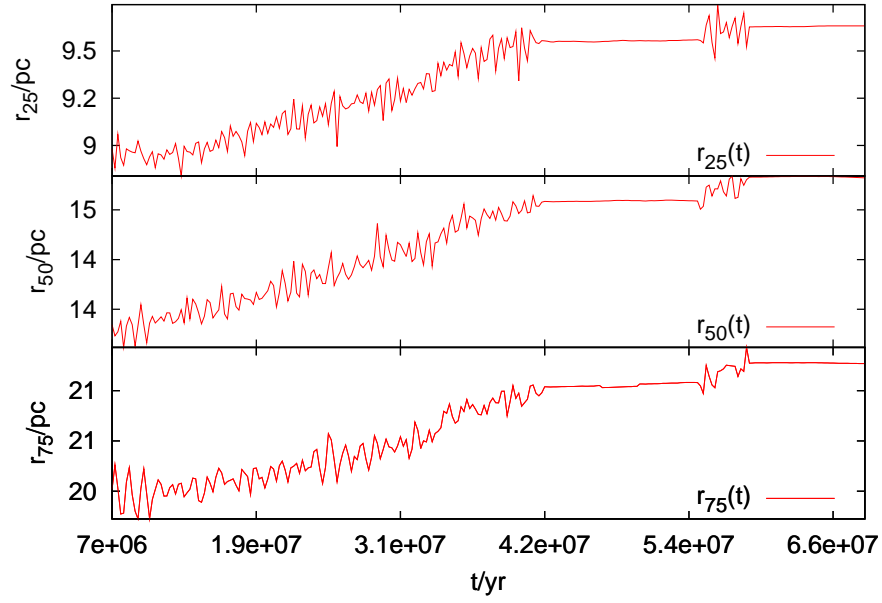


Figure D.7: *Lagrangian radii as a function of the time for the NSC. From top to bottom are shown the 25%, 50%, 75% mass lagrangian radius, respectively.*

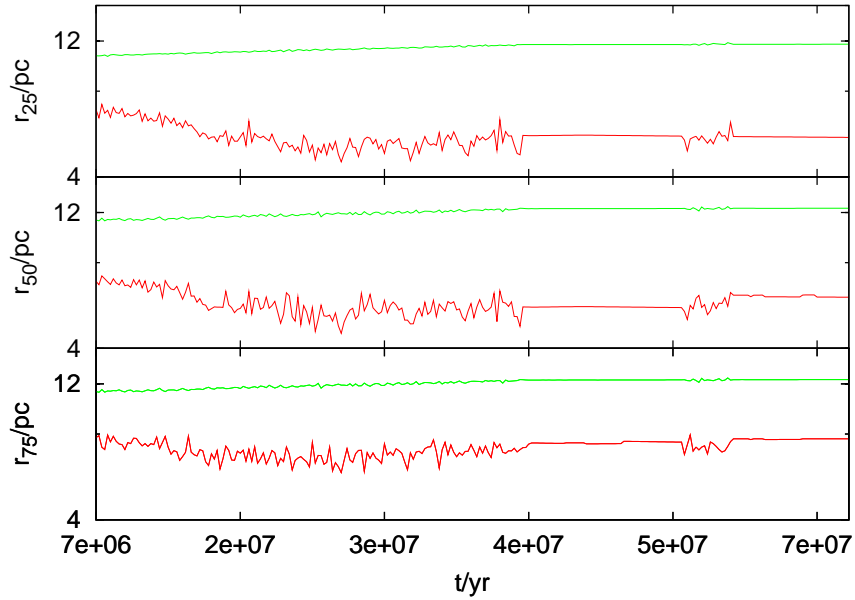


Figure D.8: *Lagrangian radii as a function of the time for more massive stars (red line) and lighter stars (green line). It is evident the segregation. From top to bottom are shown the 25%, 50%, 75% mass lagrangian radius, respectively.*

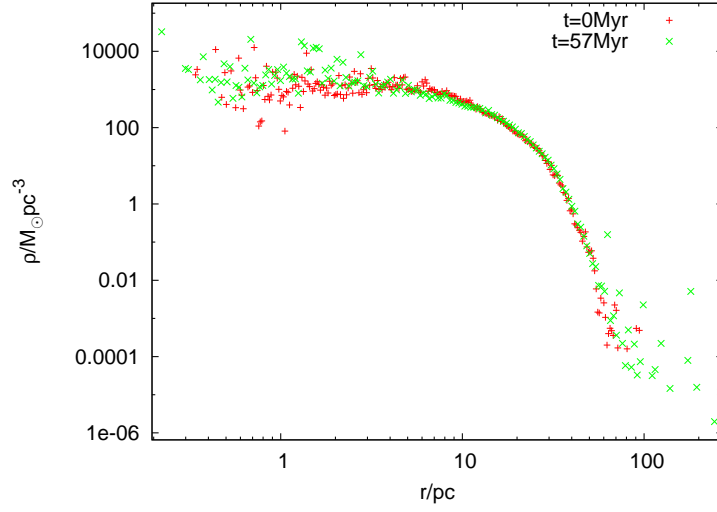


Figure D.9: Density profile for the NSC at two different times. There is not a significant evolution over 60 Myr.

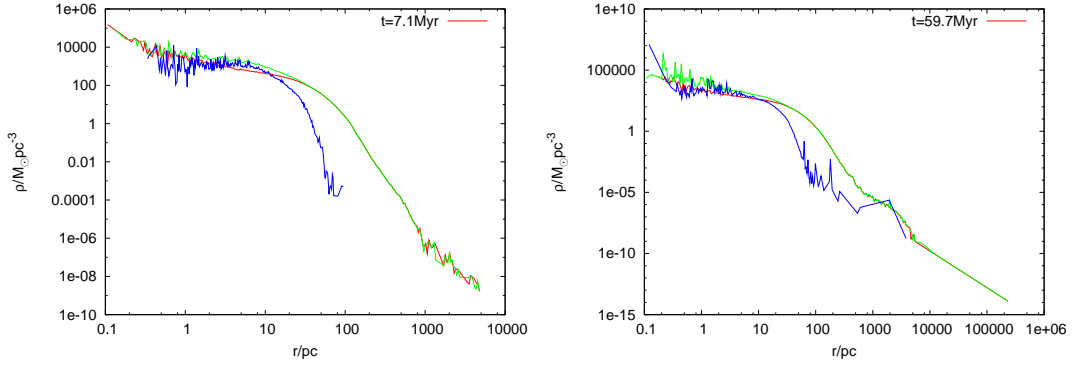


Figure D.10: The whole system (green line), galaxy (red line) and NSC density profile (blue line) at two different times (left panel $t = 0$ and right panel $t = 57\text{Myr}$, respectively). As you can see, NSC give only a small contribution in overdensity at $r \simeq 7\text{pc}$ at $t = 0$, and later at $r \simeq 2\text{pc}$ at $t = 57\text{Myr}$.

NSC has not an isotropic velocity dispersion. This is clear also looking at the β parameter, defined as:

$$\beta = 1 - \frac{\sigma_\phi^2 + \sigma_\theta^2}{2\sigma_r^2}, \quad (\text{D.2})$$

which gives the degree of anisotropy of the system and it is shown in Fig. (D.11).

Looking at Fig. (D.13), which shows the angular momentum of the NSC after its formation, it is evident that the system is initially rotating, but the rotation slows down during the evolution. Moreover, NSC rotates in a plane quite parallel to the plane $y = 0$, as it can be argued looking at the evolution of the angular momentum components in Fig. (D.14).

Concerning the central black hole, we found that it gains an initial energy that launches it until 0.4pc from the center of mass of the galaxy at $t \sim 10^6\text{yr}$, which corresponds to the

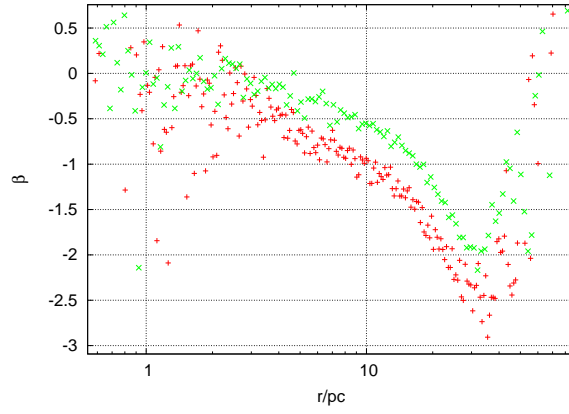


Figure D.11: *Beta parameter in two different times.*

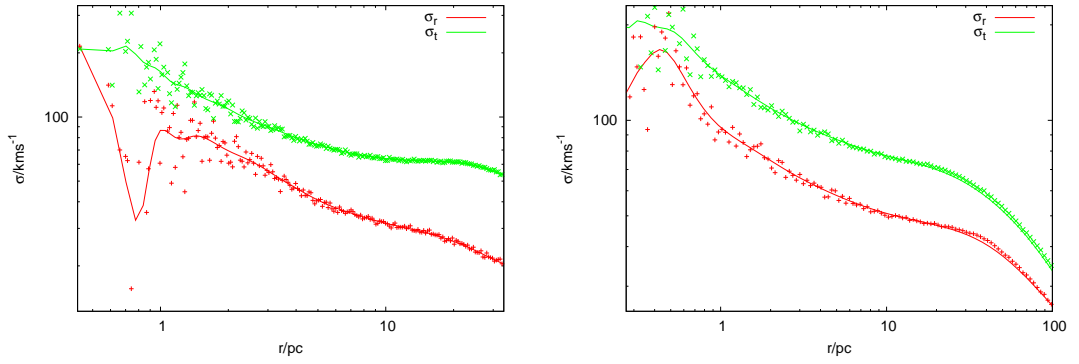


Figure D.12: *Left panel: radial (red line) and tangential (green line) velocity dispersion for the NSC at its formation. Right panel: as in the left panel, but at time $t = 61 \text{ Myr}$.*

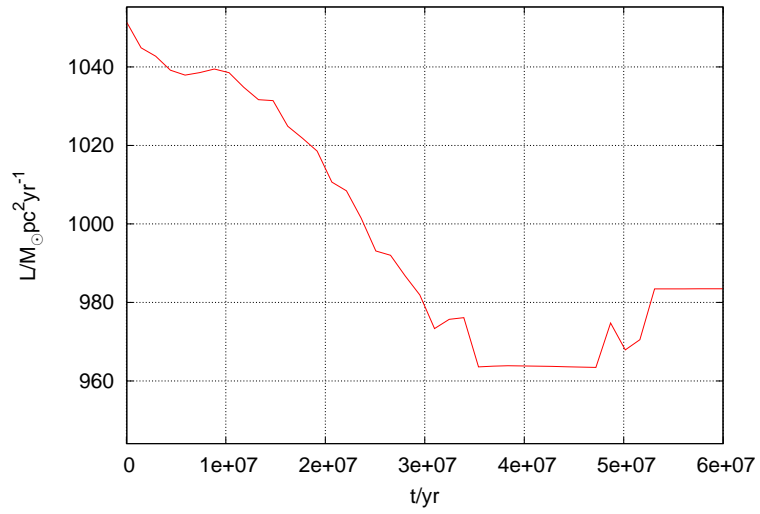


Figure D.13: *Angular momentum of the NSC as a function of time.*

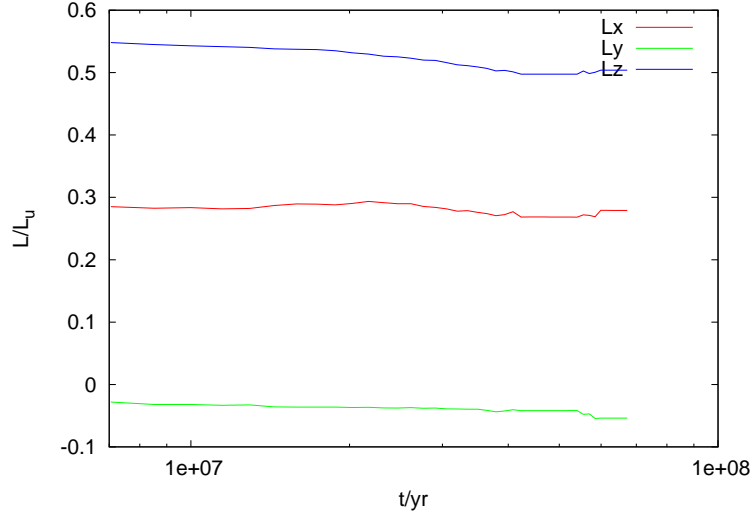


Figure D.14: *Angular momentum components for the NSC.*

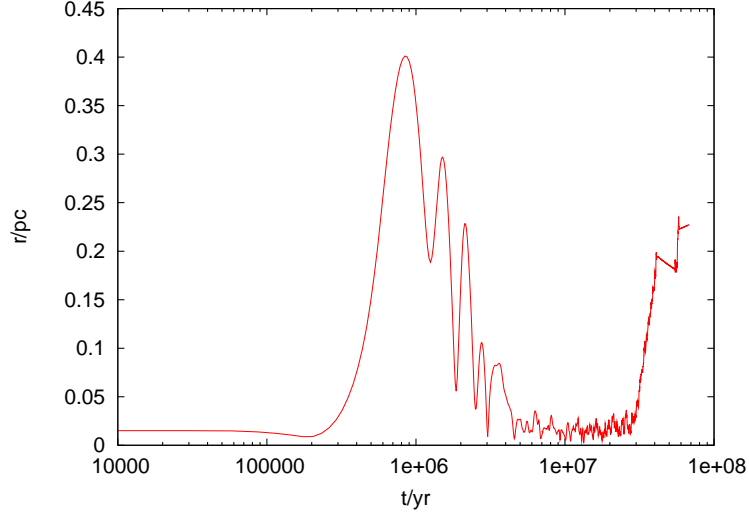


Figure D.15: *BH trajectory as a function of the time.*

time needed to the clusters to reach the center (see Fig. (D.15)). This is due to the fact that clusters and the BH have similar masses, therefore the interaction between them forces the BH to move, reaching this apocenter. Later, due to the dynamical friction process, it comes back to the center.

It is intriguing to see that at $t \sim 20 Myr$ the BH gains another kick, because at this time does not relevant happens apparently to justify this injection of energy in the BH.

To better understand the role played by the BH in the evolution of the NSC, it can be used the so-called influence radius R_{BH} , that it the radius within the dynamical influence of the BH is significant. It it generally defined as follows:

$$R_{BH} = \frac{GM_{BH}}{\sigma_{NSC}^2}, \quad (D.3)$$

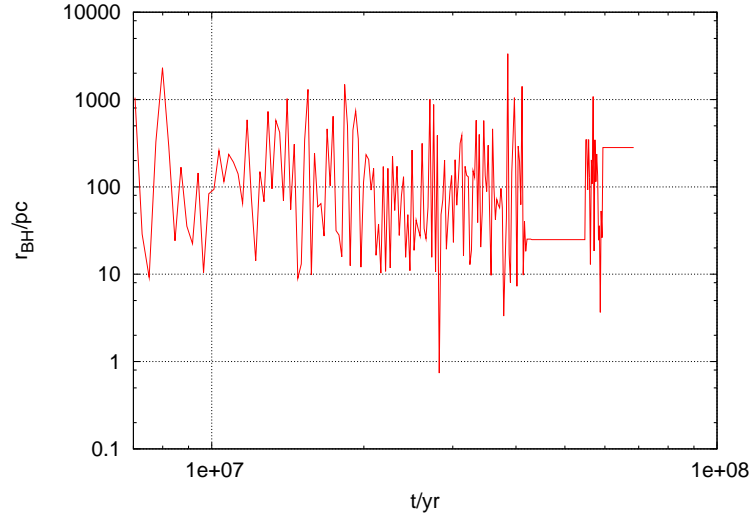


Figure D.16: *Influence radius of the central BH.*

and depends on the velocity dispersion of the galaxy, which is a function of the position and hence may vary significantly. However, it can be shown that for an isothermal sphere R_{BH} is the radius which encloses twice the mass of the BH. In Fig.(D.16) is shown the evolution of this radius evaluated this way: the average measured value, $\sim 13pc$, is greater than the observed values ($3pc$), but this is due to the fact that the galaxy models is not an isothermal sphere; in fact, taking the central velocity dispersion $\sigma = 100km.s^{-1}$ (see Fig. (D.12)), the influence radius evaluated through Eq. D.3 becomes $R_{BH} \simeq 1.3pc$, in better agreement with observations.

D.5 Summary

To summarize our work, we would point out that:

- the dynamical friction mechanism is very efficient, leading to the total merging of the 12 clusters within $7Myr$, a time compatible with the fitting formula in Eq. 2.15, which gives for a cluster $M = 10^6 M_\odot$ moving at $r = 20pc$, a decay time of $t_{df} = 6Myr$;
- in the pre and post-merging phases, the structural properties of the galaxy are substantially unchanged in terms of density profile and velocity dispersion, putting on evidence that the GCs interactions are not relevant in the evolution of the galactic center;
- as a consequence of the fact that the BH has a mass quite close to the cluster mass, it moves from its initial position, coming back toward the center of the system due

to dynamical friction process; moreover, after a dozen of Myr, a kick displaced it again from its central position, but causes are not clear;

- the influence radius of the BH depends on its own definition, to evaluate it we used Eq.D.3, finding a value in good agreement with observations ($1.3pc$);
- after the merging, NSC tends to reach an equilibrium status, as it can be seen by the density profile, which is stable over the whole simulation and put on evidence that the NSC is confined in a region which extends roughly up to $R_{NSC} \simeq 30pc$;
- due to the initial conditions describing the GCS, the NSC at its birth has an angular momentum that tends to decrease within the simulated time, leaving at the end of the simulation the NSC still in rotation. The dominant components of the angular momentum is the \hat{z} component, however there are also non null components on \hat{x} and \hat{y} axis;
- the NSC shows also a weakly anisotropy in the velocity dispersion, since it has the tangential component of the velocity greater than the radial at $\sim 30pc$, this difference between the components seems to decrease in time by a factor ~ 1.2 , in agreement with conclusions drawn from Antonini et al.;
- the lagrangian radii of the NSC gives us an upper limit of the extension of the system, which is $24pc$ at the end of the simulation;
- after the merging, the massive stars population segregates in the NSC, being enclosed within $r_{75} = 7.8pc$ from the center, while lighter stars are distributed beyond $20pc$ from the galactic center;

What it has presented here is only a preliminary analysis, in future we would try to simulate again the system, by using a different mass spectrum in the GCS and by varying initial orbits in order to study the emerging NSC in terms of shape and kinematics, to understand wether or not the IC of the decaying clusters play a crucial role.

RINGRAZIAMENTI

“Il raggiungimento di un grande obiettivo non può essere mai addebitato al singolo...” così iniziavano i ringraziamenti della mia tesi di laurea specialistica tre anni fa, e così voglio iniziarli anche stavolta. Non perché non voglia impegnarmi per trovare un modo più originale di aprire questi ringraziamenti, ma perché credo che sia così, quando si agguanta un grande risultato non conta tanto chi lo afferra, bensì contano tutte le persone che ti spingono ad afferrare quel risultato.

Io mi sento molto fortunato, perché tante persone hanno contribuito per permettermi di mettere le mani su questo grande risultato, e qui voglio ringraziarle.

Sono passati parecchi anni da quando è iniziato questo percorso universitario, un percorso lungo, difficile, a tratti avvilente, ma che alla lunga ha dato belle soddisfazioni, prima fra tutte quella di accedere al dottorato di ricerca. Avere la fortuna di fare un lavoro che adori (e in cui addirittura ti pagano!), anche se solo per tre anni, non è da tutti ed io sono molto orgoglioso e felice di aver avuto questa possibilità.

Ora, dopo tre anni di intenso lavoro, eccomi qua a passare in rassegna quanto ho fatto, a concludere questo percorso in attesa di intraprenderne uno nuovo, speriamo più lungo stavolta, e ringraziare quanti mi hanno aiutato ad arrivare fin qui.

Il primo grazie è istituzionale, al dipartimento di Fisica dell'Università “La Sapienza”, che mi ha messo a disposizione una squadra di docenti affidabile, esperta, preparata. Non tutte le facoltà dispongono di docenti che ascoltano i propri studenti, non mancano a lezione, non mandano assistenti inesperti a fare le lezioni al loro posto, non cambiano date degli appelli il giorno stesso degli appelli, fingono di non avere ricevuto mai nessuna mail anche se tu sai che l'ha letta perchè, ebbene sì, gmail può dirti anche questo. Beh, noi, a differenza di tanti nostri colleghi, non abbiamo mai avuto questi problemi, tutti

si sono sempre dimostrati gentili e disponibili per ogni evenienza. Certo, il classico “professore stronzo” ce l’abbiamo pure noi, la perfezione in fondo non è di questo mondo, dicono.

Fra tutti i docenti, voglio ringraziare in particolare il mio relatore, **Roberto Capuzzo-Dolcetta**, che in questi tre anni di dottorato mi ha permesso di lavorare al meglio, dando ampio spazio alla mia immaginazione, permettendomi di lavorare su cose che mi appassionano e che ritengo molto interessanti. Poter lavorare in un clima in cui non si ha paura di proporre le proprie idee è fondamentale per crescere insieme, sia come persone che come gruppo, e in questo il professore è stato bravissimo, dandomi la possibilità di proporre temi di ricerca, ideare, fare cose anche in autonomia ma sempre accompagnandomi con esperienza per evitare inutili buchi nell’acqua, guidandomi attraverso le mie, tanto minime quanto soddisfacenti, piccole scoperte da “giovane scienziato” (ve lo concedo, giovane scienziato è un po’ pomposo ma non mi veniva in mente altro).

Grazie prof., spero di poter continuare a collaborare con lei.

Il dottorato richiede sacrifici, giornate intere passate davanti al pc per capire perché quella o questa simulazione non vanno, i calcoli non tornano, i grafici non hanno senso, i computer non funzionano. Tutto questo è stressante, perché fare il dottorato di ricerca significa dimostrare che lo stipendio che ti danno è ben speso, dimostrare che i cinque anni di università non sono stati buttati, dimostrare che hai del talento e che quel talento va tenuto in considerazione, va spronato, va coltivato, per dimostrare a se stessi che sì, ce la si può fare, e per dimostrare che è vero che nella società non servono troppi scienziati, ma tu sì, tu servi perché sei bravo.

Queste pressioni, che in larga parte nascono nella nostra mente, possono essere alleggerite solo con una cosa: una cura di allegria, basata principalmente sull’amicizia.

L’amicizia di persone che in questi anni sono cresciuti con te e hanno vissuto come te l’esperienza degli esami ostici, delle nottate sui libri, dell’ansia di dire una cazzata all’orale, di partecipare al concorso di dottorato.

Grazie amici miei, per aver alleggerito questi lunghi otto anni di università. Grazie a tutti per aver reso le feste a casa di Grazia fantastiche (abbiamo addirittura giocato a strega di mezzanotte una volta, vi rendete conto??), con Sandro e Rosalba, sempre gentilissimi, che ci rifocillano sempre ogni volta che andiamo e giocano pure con noi, e Frida, che ogni volta che ci vede dimostra che la mole non ci dice nulla sul carattere, almeno se si considera un cane da mezza tonnellata. Grazie per le giornate a Palestrina da Jacopo, con Carla che ci vuole bene come fossimo suoi figli e ci fa sentire a casa.

Grazie **Gracie**, una delle prime persone che ho conosciuto tra i banchi dell'aula Amaldi quel lontano ottobre di otto anni fa, negli anni sei diventata un'amica insostituibile, alla quale voglio un bene sincero. Le nostre (poche) scornate che si concludono in un abbraccio e una risata sono la dimostrazione che l'amore non è bello se non è fricciarellò.

Grazie **Silvietta**, la mia extracomunitaria preferita, la tua solarità perenne è confortante, grazie a te tante mattinate iniziate buie si sono illuminate subito. Certo, sei una fan sfegatata di Robbie Williams, ma in fondo, chi è senza peccato scagli la prima pietra, no?!

Grazie a entrambe, fidanzate segrete, perchè senza il vostro tocco femminile, che va dalle serate truzzissime all'albero di natale in stanza dottorandi tutto questo non sarebbe stato ugualmente bello.

Grazie **Pippo**, le serate a casa, le chiacchiere all'università, le nerdosità che ci piacciono tanto a noi, le chiacchiere scientifiche. Per rendere perfetto il nostro rapporto servirebbe solo una collaborazione scientifica... DATTE NA MOSSA CO STO PROGRAMMA!! daje che faremo un bellissimo lavoro di evoluzione stellare, e poi per festeggiare ci vediamo tutta la serie dei film di star wars o tutto il signore degli anelli in soluzione unica e ci sfondiamo al mc. Spero che il tuo cammino in Inghilterra ti dia tutte le soddisfazioni che meriti.

Grazie **Poppo**, che nei primi due anni di dottorato sei stato un compagno di lavoro fantastico, il nostro viaggio a Bologna sarà ricordato nei secoli (tu sai a cosa mi riferisco), e le serate a Cefalù pure.

Alessandra, la nostra mentore nelle prime fasi del dottorato, il tuo aiuto, la tua disponibilità sono state più che preziose, anche se adesso sei dall'altra parte del mediterraneo, spero di vederti presto. Il nostro viaggio a Cefalù è stato troppo divertente, e ne sei uscita alla grande nonostante fossi una povera piccola donna contro tre bestie come me, Mario e Davide. Certo, alla fine quella famosa pizza non ce l'hai mai fatta...

Grazie **Zdnecek**, il ceco più italiano che io abbia mai conosciuto, è stato bello condividere con te questi tre anni di dottorato, sono contento di averti conosciuto e spero di rivederti presto. Good luck my friend and remember: "Don't listen to Mario, NEVER". Hoping to see you soon!!.

Grazie **Maurè**, per le uscite e le risate fatte insieme, le pause caffè e le partite a pes o risiko, dove tu non rosichi mai (ti dico solo gol al 90th di un ragazzino semi-sconosciuto). Le nostre discussioni di arti marziali sono sempre un ottimo spunto per apprendere insieme, peccato che non siamo mai riusciti a farci un allenamento insieme...magari quando te rimetti a posto la mano te sconocchio l'altra.

Grazie **Sofia**, grande acquisto della nostra stanza dottorandi, sono stra-felice di averti conosciuto! e poi, qualcuno con l'accento toscano nella mia vita doveva esserci per forza.

L'ambiente di lavoro è fondamentale per poter lavorare in santa pace e fare in modo che 10 ore davanti al computer passino abbastanza velocemente. Avere dei colleghi musoni, antipatici o rompiscatole avrebbe reso tutto molto difficile, e avrebbe reso il mio orario di lavoro decisamente più corto di quello che poi è effettivamente stato. Quindi grazie a **Carlo**, a **Matteo**, a **Leo**, a **Francesco** e **Corrado**, grazie per non avermi mai rotto le scatole, nemmeno quando ascolto la musica (discutibile, a dire di qualcuno) senza cuffie.

Grazie anche a due persone che ho conosciuto da poco ma che sono già riuscite a entrare nel mio cuore, **Ale** e **Laura**, avete deciso di mischiarvi con noi vecchietti, ma credo non siate rimasti delusi. Grazie della vostra simpatia e compagnia, ci sono tutti i presupposti per una bella e solida amicizia.

E come non ringraziare l'**Euculpi**, per la sua innata e spiccatissima simpatia e sense of humour.. no davvero, grazie Vale, mi hai dimostrato che non è necessario conoscersi da una vita nè sentirsi ogni giorno per dimostrare di essere amici, so che di te mi posso fidare.

Il nostro ambiente universitario a favorito la nascita di una specie di famiglia, di cui tutti voi che ho appena ringraziato fate parte, grazie ancora ragazzi.

E in una famiglia ovviamente si instaurano legami più o meno solidi, più o meno duraturi... per quanto mi riguarda in questi 8 anni ho costruito due legami molto forti.

J, il mio amico sin dalle prime due settimane di Università, quando ancora non capivamo na mazza di fisica, quando momenti manco sapevi fare gli integrali. In questi anni sono successe tante cose, e la nostra amicizia è andata rafforzandosi di giorno in giorno, e oggi so che se ho un problema posso bussare alla tua porta senza pensarci troppo. Le chiacchierate, le pause caffè, Game of thrones, i pokemon, i conti che non tornano e i consigli che non guastano mai.. le correzioni della tesi e del draft dell'articolo... senza questo il mio dottorato sarebbe stato diverso, meno colorato. Grazie amico mio, non mollare, mi raccomando.

E poi c'è **Fennel**, si potrebbe quasi dire che eravamo destinati a stare insieme. Fine laurea insieme, inizio dottorato insieme, esami insieme, era quasi naturale che andassimo pure a convivere. Per chi non avesse capito, non parlo di Martina, parlo di Mariolino, col quale ho stretto un bellissimo rapporto di amicizia, che si è stretto ancora di più da quando condividiamo la stessa casa. Le serate a PES, le risate, le discussioni di "alto profilo scientifico" sono insostituibili. Le idee geniali che abbiamo avuto, e che inevitabilmente ci porteranno a un prematuro Nobel. Tutto questo rende il mio dottorato migliore, quasi

perfetto; spero continueremo a lavorare insieme in qualche modo, anche se rischiamo di essere spediti in due parti del mondo diverse. Grazie caro, grazie di tutto.

All'università si passa la maggior parte della giornata, della settimana, dell'anno, devo dire che per me non è stato difficile, non è mai stato un peso venire la mattina presto e andare via la sera tardi. Perché? beh, prima di tutto perchè adoro quello che faccio, in più l'alzataccia e il duro lavoro sono sempre stati stemperati da buone compagnie serali, da scampagnate in compagnia, da risate senza sosta.

E chi sono gli artefici di tutto questo divertimento? altri amici, tanti amici.

Grazie **Chicca** e **Gio'**, per le serate passate insieme in compagnia di buon vino o birra a suon di risate e caciara.. a proposito devo assaggiare assolutamente la birra che fa Giovanni... (promemoria).

Grazie **Gian** e **Giuls**, siete semplicemente fantastici, dobbiamo fare quella famosa cenetta...magari con il nuovo anno riusciremo a vederci più spesso!!

Grazie per la loro spontaneità, la loro disponibilità, simpatia e bellezza (ammazza quanto miele...) alle fantastiche donnine: **Fede**, **Marti** e **Tata**. Vi voglio bene ragazze, grazie per il supporto quando è stato necessario. Grazie delle scampagnate, delle serate al Gianicolo, degli aperitivi a Trastevere e delle mega risate che ci facciamo insieme. Grazie di giornate fantastiche come quelle di Santa Marinella, delle Marmore, della Feniglia-Giannella. Grazie del compleanno fantastico che avete organizzato per me, facendo spesa e cucinando pure, e grazie per avermi fatto ascoltare tutte quelle belle canzoni (questa era sarcastica...). Grazie, perchè anche se siete le amiche di sempre della mia fidanzata, so di poter contare su di voi. Sappiate che per qualsiasi problema potete contare sul papi.

Grazie **Simo**, uno dei pochi maschi del nostro "gruppo", siamo proprio beati tra le donne, che gioia... grazie per il rapporto che va consolidandosi di giorno in giorno, le discussioni ingegneri-fisici sono spesso oggetto di barzellette, ma noi dimostriamo che si può essere grandi amici pur appartenendo a due "classi rivali". Le cazzate che diciamo e le risate che ci facciamo insieme completano e colorano al meglio le nostre serate.

Grazie alla new entry **Fabrizio**, sono molto contento di averti conosciuto, a me e Simone serviva proprio un alleato in più. Adesso possiamo batterci quasi alla pari con le donnine (e ovviamente vincere, ma quello non è mai stato in dubbio).

Il tempo passa, le cose cambiano, qualcuno si allontana dal gruppo per lavoro o per altri motivi, qualcuno non lascia il segno, qualcun altro invece lascia una traccia indelebile.

Vale, amico mio, anche se è un po' di tempo che non ci vediamo la nostra amicizia, nata nel corso degli ultimi anni, non passa, sei una persona sincera e leale, e le nostre WhatsApp dimostrano che l'amicizia vera non dipende dalle relazioni con gli altri, grazie della tua simpatia e amicizia, che dimostri continuamente.

Ci si allontana dicevo, qualcuno rimane in territorio italico, qualcun altro emigra.

Etta, devo dirtelo, mi manchi.. ormai sei una parigina a tutti gli effetti, sono contento che tu sia tornata quella di un tempo, ti voglio bene e spero di sentirti prestissimo. Ti auguro il meglio in quel di Paris e conto di venirti a trovare al più presto. Le serate e le vacanze insieme sono state fondamentali in questi anni, ricordi che porto sempre con me.

Le cose cambiano, gli amici restano. **Gian**, tu sei per me quasi come un fratello, e sebbene tu sia ormai lassù (NO, non è morto...lavora a Treviso), ti sento più vicino che mai. La prossima volta che passi sulla Tiburtina però ricordati che io abito la!!! Sono contento di averti incontrato sulla mia strada, sono felice di poter contare su uno come te sempre. Una delle mie due spalle più grosse.

Il tempo passa, e quando si arriva ad un qualche traguardo si tende a volgere lo sguardo indietro, per dare un'occhiata a come è stata la strada che ci ha portati fino a qua. Guardando indietro vedo tante cose: la pallavolo, il teatro.. amici che non sento da tanto, che sono stati fondamentali per la mia crescita, dalle cui strade mi sono allontanato, per un motivo o per l'altro.

Grazie alla squadra di pallavolo storica con la quale sono cresciuto e ai suoi componenti: **Luca, Sandrone, Simone, Andrea, Umberto, Mattia, Lucio** e tutti gli altri. Grazie ragazzi, non sono diventato un fenomeno della pallavolo (e voi lo sapete bene), ma mi sono divertito na cifra.

Grazie a tutta la compagnia dei **celebri ignoti**, che mi ha permesso di "fare l'attore"... le commedie che abbiamo portato in scena mi hanno aiutato a crescere, tanto. Mi manca un po' il palco, tutta quell'adrenalina che scorre poco prima di andare in scena. Grazie al team di regia più pazzo, scatenato e divertente che abbia mai conosciuto: **Elena, Claudia, Simona** e **Sonia**. Sono passati parecchi anni da famiglia tromboni, ma vi porto sempre con me e vi penso spesso, sappiatelo!

Che altro vedo? Il liceo. Scientifico Statale Taletè, "Maxi Sperimentazione Brocca" indirizzo Scientifico. Sbem!! Grazie alla mia classe, grazie a chi vedo ancora e a chi non sento da tanto. I cinque anni passati con voi non si possono dimenticare, e non si può dire che non abbiano influito sulla mia crescita, sul mio IO di oggi. Grazie ragazzi. E

grazie ai docenti, grazie alla **Bevilacqua**, alla **Mastrantonio**, alla **Danusso**, alla **Pinelli** e a tutti gli altri, che ci hanno aiutato a diventare quello che siamo oggi. Grazie a tutti.

Frequento ancora qualche amico del liceo, magari un pò di rado, dati i tanti impegni che ognuno di noi ha. Grazie allora a **Matteo** e **Domenico**, che mi dimostrano sempre che anche se non ci vediamo per un anno, la nostra amicizia non è cambiata di una virgola.

E grazie a **Marta**, che vedo molto più di frequente, anche se i recenti cambiamenti ci hanno allontanato un pò, sicuramente riusciremo a rifarci sotto le vacanze di Natale.

Tutti noi abbiamo un “migliore amico”: un orso di pezza, un amico immaginario, la statuetta di sirio il dragone... i casi più fortunati hanno un migliore amico vero, in carne e ossa. La classica persona che puoi chiamare sempre, per qualsiasi cosa, per parlare di politica, di ragazze, di lavoro, del fatto che la benzina sale sale e non fa male, del fatto che è inconcepibile che io debba emigrare mentre Barbara D’Urso fa un programma tutto suo a Canale 5, o che il premier di una nazione confonda una prostituta con la nipote di un altro premier...ma vabbè, non divaghiamo... dicevo, il migliore amico... nel mio caso, io ho **Dario**, che sebbene stia ormai da un anno lavorando a Pavia, si dimostra sempre vicino a me. Pensate che subito dopo aver discusso la tesi di dottorato con il nostro collegio docenti mi ha chiamato, anche se non gli avevo mai detto che la discussione era quel giorno..se non è empatia questa. Grazie fratellino per esserci sempre.

Per chiunque sia arrivato fin qui nella lettura dei ringraziamenti, sappiate che non è finita, voglio ancora ripercorrere un pò questo strano percorso e ringraziare chi ho incontrato lungo la strada. Vi consiglio comunque di arrivare fino alla fine, ci sarà una bella sorpresa e.. NO! non vale andare direttamente all’ultima pagina.

Ci si guarda indietro, dicevo. Guardando a una decina di anni fa vedo una grossa svolta nella mia vita (NO, a quella parte non ci siamo ancora arrivati..portate pazienza per favore): il ritorno alle arti marziali. Quasi dieci anni in cui ho avuto l’onore di vedere crescere una grande scuola, la **IMAA**, sorretta dai fantastici maestri **Luigi** e **Monica**, che si sono dimostrati di una apertura mentale rara. Complimenti maestri, siete fantastici. Sono orgoglioso di fare parte della vostra scuola e di poter dire di averla vista crescere ed esplodere nella meravigliosa realtà che è adesso. Voglio raccontare a tutti un aneddoto, per fare capire quanto le arti marziali non siano solo un modo come un altro per fare a pugni. Nella nostra scuola si pratica anche la meditazione. Bene, da quando ho iniziato a fare meditazione il giorno prima di un esame, accompagnato da una bella sessione di allenamento, la mia media non è più scesa sotto al 28, e io non credo alle coincidenze.

Grazie ai maestri, che mi hanno insegnato tanto e mi hanno permesso di conoscere personaggi illustri delle arti marziali, i quali si sono dimostrati gentili e pronti a insegnarmi pur non essendo loro allievo. Grazie ai maestri **Yoshioka**, **Gutierrez**, **Yee Seil**, **Spina**,

Diotallevi, Basile, Tabili, Mazzola, Taramanni, Di Mauro, Bramante, Alessi, Cortese; grazie al maestro Gentili, che ha curato il mio povero naso gonfio dopo i regionali di combat. Grazie a tutti, dimostrate di incarnare l'essenza dell'arte.

Grazie a tutti i ragazzi che hanno incrociato i pugni con me in questi anni, primi fra tutti Andrea, che conosco da ben 15 anni o giù di lì, e Marisa, che conosco addirittura da 23 anni (è stata la mia maestra d'asilo). Grazie delle mazzolate che mi date ogni volta che vengo ad allenarmi.

Il carico di lavoro degli ultimi tempi non mi ha consentito di allenarmi con tutti voi di recente, e pochi sanno quanto questo mi manchi... ma conto di tornare presto, anche perchè prendere a pugni e calci un muro non è il massimo...per il muro, ovviamente.

Con tutto il miele che sto sversando in queste pagine mi ritroverò senza denti prima dei 30 anni mi sa...vabbè, ci si penserà più in là.. un problema alla volta!

Allora, fatemi pensare, chi mi sto dimenticando?? Cari lettori, mi sa che ci stiamo avvicinando al termine di questa lunga carrellata sulla mia vita e sulle persone che la stanno rendendo fantastica.

In questi tre anni ho potuto dare un'occhiata più da vicino al mondo, sono stato in Svezia, Finlandia e Colorado e ho avuto l'opportunità di conoscere persone fantastiche e interessanti, che mi hanno dato prova del fatto che le barriere culturali non esistono. Thanks to Sylvana, Tuan, Ann-Marie, Tobias, Sambaran, Anson and all the guys which were with me at Aspen, Stockholm or Turku; thanks to all of you, it was a wonderful experience. Hoping to see you soon.

Stavo raccontando dei viaggi fatti durante gli ultimi tre anni, anche se devo dire che non c'è niente di meglio che tornare a casetta propria, tra le braccia di coloro che ami.

E siamo quindi di nuovo nella nostra bella Italia, che tanta fatica fa a trattenere i propri figli, che amarezza...

Dunque.. torniamo alle cose importanti. L'evento più importante degli ultimi otto anni è stato un appuntamento, un film di Leonardo Pieraccioni e poi uno di Woody Allen, che però non hanno dato i frutti sperati. C'è voluto quasi un anno perchè quell'appuntamento diventasse l'inizio della storia più importante della mia vita. La storia inizia, conosci meglio la ragazza, conosci la sua famiglia, e ad un certo punto, la sua famiglia è entrata nel tuo cuore, ed è diventata parte di te. E di questo sono felicissimo. Grazie Alberto e Rina, mi fate sentire a casa. Grazie a Nonno Giuseppe e Nonna Ave, due nonni acquisiti e fantastici. Grazie a Nonna Clelia..

Grazie a **Dario** e **Ludo**, testimoni del primo e (spero) ultimo svenimento della mia vita. Spero che presto potremo farci un altro viaggetto e passare un pò di tempo insieme. E quando vogliamo farci un altro week-end a Montegiorgio (anche solo maschioni, come l'ultima volta), io sono sempre pronto!!

Quell'appuntamento di otto anni fa, ma soprattutto quella partita di calcetto di sette anni fa (in cui, peraltro, segnai su rigore), hanno segnato in maniera indelebile la mia vita, che da allora può considerare come uno di due fili intrecciati, l'altro filo appartiene a te **amore**, che in questi anni mi hai sorretto con la tua determinazione, il tuo amore. Grazie di tutto tesoro mio, sono orgoglioso che tu sia riuscita a raggiungere il tuo sogno, vincendo il dottorato con borsa (tra l'altro così almeno uno dei due porta a casa qualche soldo).

Voglio raccontarvi una storia. Tanto, tantissimo tempo fa, quando ancora si credeva negli dei, gli esseri umani non erano suddivisi per genere, e ciascuno di essi aveva quattro braccia, quattro gambe e due teste. Per gelosia nei confronti della perfezione umana, gli dei li separarono in due parti con un fulmine, e da allora ogni uomo sulla faccia della terra è alla ricerca della sua anima gemella (grazie Aldo, Giovanni e Giacomo). Beh, io sono sicuro che la mia metà esatta non esista, ma sono anche convinto che la metà che ho trovato aderisca perfettamente, perché gli ultimi sette anni ci sono serviti per limare e modellare le nostre due metà, fino a farle quasi combaciare (violino in sottofondo...).

E adesso che le due metà sono ricongiunte, anche se grazie all'espedito del vivere giorno per giorno, adattandosi alle esigenze dell'altro e evolvendo assieme, non vedo nuvole o fulmini all'orizzonte che possano dividerle. Grazie amore mio.

Mi piace molto guardarmi indietro, perchè pur essendo ancora giovane vedo tante cose: luoghi, colori, eventi, persone che mi vogliono e alle quali voglio bene.

Ma la cosa che più mi piace e mi rassicura è non importa in che direzione io guardi, riesco sempre a scorgerla lì, sempre pronta a difendermi e sorreggermi: è la mia famiglia.

Se oggi sono una persona che non vede differenze tra bianchi o neri, etero o gay, poveri o ricchi, lo devo alla mia famiglia. Se oggi sono una persona alla quale piace studiare, capire, imparare, confrontarsi, lo devo alla mia famiglia. Se in questi anni ho seguito le mie passioni e sono riuscito a raggiungere questo obiettivo, lo devo alla mia famiglia.

Lo devo al piccolo grande **Spank**, che mi ha fatto capire che l'amore di, e verso, un cane può essere tanto intenso quanto quello che si ha verso i propri familiari. Buon viaggio, amico mio.. che la tua vacanza possa durare per l'eternità.

Lo devo alla mia bisnonna **Gilda**, che mi ha insegnato a non essere fregnone, e che attraverso le sue storie mi ha insegnato quanto sia importante guardarsi indietro per

ricordarsi da dove si viene, e meglio capire dove si va. Lo devo a nonna **Salvatorica** e nonno **Gianuario**, che mi hanno insegnato quanto sia importante vivere a contatto con la natura, e mi hanno dimostrato come un amore possa andare avanti per sempre anche quando uno dei due ci lascia. Lo devo a nonna **Anna**, che mi ha sempre accudito e coccolato, che mi ha mostrato l'importanza del risparmio, e che mi dimostra ogni giorno una forza incrollabile, che permette di andare avanti anche nei momenti più duri e bui. Grazie nonni, vi voglio bene. Grazie per tutti i vostri insegnamenti.

Se oggi sono così, lo devo a zia **Francesca**, che mi accompagnava all'asilo da piccolino, non vedo l'ora di rivederti zia, meno male che c'è skype! E lo devo a zio **Mario**, una delle persone più simpatiche che esistano, sempre con la battuta pronta, anche nei momenti peggiori. Mi hai insegnato a non prendermi troppo sul serio, grazie.

Se oggi sono così, lo devo a zio **Peppe**, per avermi insegnato l'importanza dell'umiltà, per avermi mostrato l'importanza di avere il cuore più grande delle braccia, l'importanza della generosità. Te ne sei andato via troppo presto, non avresti dovuto.. ma grazie per averci aspettato.

Se oggi sono così è anche grazie alle mie cuginette **Ilenia** e **Marina**, e a **Sonia**, ormai già grandetta; e alla piccola **Elisa** (piccola mia, zio è un Astrofisico..yuppidu!!). E al cugino acquisito **Tore**, che sono certo saprà proteggere mia cugina e darle il meglio.

Ed è anche grazie a **Jennifer**, **Jessica** e **Michele**, che non vedo da tanto, troppo tempo. Mi mancate, spero di vedervi presto. Speriamo almeno prima che io mi sposi!

Ma soprattutto, se oggi sono così, è grazie a **mamma** e **papà**, i miei più grandi sostenitori, le persone che so di avere sempre al mio fianco, anche ora che li vedo solo una volta la settimana. Le persone che più mi hanno insegnato l'importanza di capire le cose, l'importanza di vedere tutti allo stesso livello, di andare oltre i colori, le bandiere, le preferenze. Grazie, sono orgoglioso di essere vostro figlio; questo, e gli altri obiettivi che ho raggiunto nel corso degli anni, lo devo a voi, al vostro amore incondizionato. Lo devo a quello sguardo che dice: "bravo, sono fiero di te". Ora che vivo da solo mi rendo conto di quanto siate fondamentali nella mia vita, di quanto sia importante sentirvi almeno una volta al giorno, per raccontarvi come va, per sapere che fate. Grazie per tutti i sacrifici che avete fatto, per avermi spronato nelle mie scelte, senza obiettare troppo, assecondandomi il giusto, e cercando di farmi vedere dove facevo i miei sbagli. Grazie per avermi sempre fatto sentire all'altezza della situazione, anche quando da piccolino mi mettevo a disquisire con gli adulti come fossi uno di loro. Grazie per avermi trasmesso l'amore per la lettura, e per avermi spiegato l'importanza dell'onesta. Grazie per avermi mostrato come si comporta una vera famiglia. E grazie per quel pizzone, dato al momento giusto, nel posto giusto. Grazie di tutto.

Sembra che io abbia finito. Manca ancora un piccola, ma più che fondamentale, parte.

È la parte in cui ringrazio le due persone più importanti della mia vita, quelle che veramente capiscono cosa penso, come lo penso e perché lo penso solo sentendo la mia voce al telefono, guardandomi negli occhi o leggendo quello che gli scrivo su facebook (ah.. potere della tecnologia, quarant'anni fa avrei dovuto scrivere qualcosa del tipo: "leggendo ciò che scrivo nelle lettere che spedisco regolarmente loro" .. decisamente troppo formale per i miei gusti). Mi sembra ovvio di chi sto parlando no?! Sto parlando dei miei fratelli, **Mike** e **Chris**. Negli ultimi tempi siamo diventati un vero "branco" (voi capite a cosa mi riferisco...). Il cinema, il bowling, la pasta a mezzanotte, tutti momenti unici e irripetibili che solo chi ha un fratello può capire. Sembrano banalità, ma vi assicuro che sapere esattamente cosa sta passando per la testa di una persona, anticiparlo, ridere delle sue battute come se venissero dal proprio cervello è qualcosa di inebriante, di calmante, di rassicurante, è una specie di droga, la miglior droga del mondo.

Gli interessi comuni poi, facilitano tutto. La nostra passione per le arti marziali è quasi leggenda, le mazzolate che ci diamo sul cemento nelle mattine d'estate sono qualcosa a cui difficilmente potrò rinunciare. Già mi immagino alla soglia dei 60 che combattiamo davanti al palazzetto dello sport, uno con calci devastanti, l'altro con leve terrificanti... gli "Arca Bros." ..indivisibili.

Grazie fratellini, in voi mi rivedo costantemente, siamo diversi ovviamente, ma proveniamo dalla stessa matrice. Sono orgoglioso di voi, spero che nella vita possiate essere soddisfatti di quello che fate tanto quanto lo sono io.

Ok, come si dice al giorno d'oggi, mi sono un pò accollato. Comunque cari lettori forza e coraggio (che dopo aprile viene maggio... questa era pessima), siamo quasi arrivati alla fine, e poi arriva la sorpresa.

Dunque chi mi manca? Ah già...l'ultimo grazie va a te! te che stai leggendo sti ringraziamenti da venti minuti e magari ancora non hai visto il tuo nome, grazie per averli letti fino in fondo, grazie perché se stai leggendo sicuramente sei entrato nella mia vita e hai lasciato un segno, anche se per esigenze di spazio non ho potuto citarti. **GRAZIE MILLE.**

È l'ultimissimo grazie lo tengo per me, perché credo fermamente in quello che faccio, perché in questi tre anni mi sono alzato tutte le mattine alle 6:30 e sono stato qui in dipartimento fino a sera, non per vantarmi, ma perché amo questo lavoro e sono convinto di poterlo fare bene; perché in questi tre anni non mi sono accontentato di fare il minimo sindacale e ho voluto continuare a cercare, a fare, come tutti gli altri ragazzi che mi sono stati vicini, che ogni giorno hanno dimostrato di tenere a quello che fanno, di non buttare via la propria vita, di sacrificarsi per raggiungere i propri obiettivi, senza se

e senza ma, senza compromessi. Senza credere a false parole, senza ricorrere a mezzucci o scorciatoie. Superando sempre ogni ostacolo che la vita gli ha messo davanti. Sono orgoglioso di quello che ho fatto, sono orgoglioso delle persone che ho conosciuto, sono contento del lavoro prodotto in questi anni, sono convinto che un giorno potrò tornare qui e dire, di nuovo, finalmente ce l'ho fatta.

P.S.: Io sono Iron Man (no, scusate, questa era una cazzata per gli intenditori!!)

Grazie ancora a tutti, e spero non vi si siano cariati i denti, anche perché attualmente sono a tutti gli effetti disoccupato e quindi se mi denunciate mi mandate sul lastrico.

Con amore,

Manuel

- [1] Aguilar L. A., White S. D. M., 1985, ApJ, 295, 374
- [2] Allen C., Santillan A., 1991, Rev. Mex. A. A., 22, 255
- [3] Antonini F., Capuzzo-Dolcetta R., Mastrobuono-Battisti A., Merritt D., 2012, ApJ, 750, 111
- [4] Antonini F., Merritt D., 2012, ApJ, 745, 83
- [5] Antonini, F. and Merritt, D. 2012, ApJ., 745
- [6] Antonucci R., 1993, ARAA, 31, 473
- [7] Arca-Sedda M., Capuzzo-Dolcetta R., 2013, ArXiv e-prints
- [8] Bahcall J. N., Wolf R. A., 1976, ApJ, 209, 214
- [9] Baumgardt H., 1998, AAP, 330, 480
- [10] Baumgardt H., 2001, MNRAS, 325, 1323
- [11] Baumgardt H., Hut P., Makino J., McMillan S., Portegies Zwart S., 2003, ApJL, 582, L21
- [12] Becklin E. E., Neugebauer G., 1968, ApJ, 151, 145
- [13] Bekenstein J. D., 1973, ApJ, 183, 657
- [14] Bekki K., 2010, MNRAS, 401, 2753
- [15] Bekki K., Graham A. W., 2010, ApJL, 714, L313
- [16] Binney J., 1977, MNRAS, 181, 735

- [17] Binney J., Tremaine S., 2008, Galactic dynamics. Princeton university press
- [18] Blumenthal G. R., Faber S. M., Flores R., Primack J. R., 1986, ApJ, 301, 27
- [19] Boeker T., 2012, ArXiv e-prints
- [20] Böker T., Laine S., van der Marel R. P., Sarzi M., Rix H.-W., Ho L. C., Shields J. C., 2002, AJ, 123, 1389
- [21] Campanelli M., Lousto C., Zlochower Y., Merritt D., 2007, ApJl, 659, L5
- [22] Cappellari M., Bacon R., Bureau M., Damen M. C., Davies R. L., de Zeeuw P. T., Emsellem E., Falcón-Barroso J., Krajnović D., Kuntschner H., McDermid R. M., Peletier R. F., Sarzi M., van den Bosch R. C. E., van de Ven G., 2006, MNRAS, 366, 1126
- [23] Capuzzo-Dolcetta R., 1993, ApJ, 415, 616
- [24] Capuzzo-Dolcetta R., Miocchi P., 2008, MNRAS, 388, L69
- [25] Capuzzo-Dolcetta R., Spera M., Punzo D., 2013, Journal of Computational Physics, 236, 580
- [26] Chandrasekhar S., 1943, ApJ, 97, 255
- [27] Chandrasekhar S., von Neumann J., 1942, ApJ, 95, 489
- [28] Chandrasekhar S., von Neumann J., 1943, ApJ, 97, 1
- [29] Chieffi A., Limongi M., 2013, ApJ, 764, 21
- [30] Cole D. R., Dehnen W., Read J. I., Wilkinson M. I., 2012, MNRAS, 426, 601
- [31] Côté P., Blakeslee J. P., Ferrarese L., Jordán A., Mei S., Merritt D., Milosavljević M., Peng E. W., Tonry J. L., West M. J., 2004, ApJS, 153, 223
- [32] Côté P., Piatek S., Ferrarese L., Jordán A., Merritt D., Peng E. W., Hasegan M., Blakeslee J. P., Mei S., West M. J., Milosavljević M., Tonry J. L., 2006, ApJS, 165, 57
- [33] de Jager C., Nieuwenhuijzen H., van der Hucht K. A., 1988, AAPs, 72, 259
- [34] de Vaucouleurs G., 1948, Annales d'Astrophysique, 11, 247
- [35] Dehnen W., 1993, MNRAS, 265, 250
- [36] Do T., Lu J. R., Ghez A. M., Morris M. R., Yelda S., Martinez G. D., Wright S. A., Matthews K., 2013, ApJ, 764, 154

- [37] Dubinski J., 1994, *ApJ*, 431, 617
- [38] Eddington A. S., 1915, *MNRAS*, 75, 366
- [39] Einasto J., 1965, *Trudy Astrofizicheskogo Instituta Alma-Ata*, 5, 87
- [40] Einasto M., Saar E., Liivamägi L. J., Einasto J., Tago E., Martínez V. J., Starck J.-L., Müller V., Heinämäki P., Nurmi P., Gramann M., Hütsi G., 2007, *AAP*, 476, 697
- [41] Eke V. R., Navarro J. F., Steinmetz M., 2001, *ApJ*, 554, 114
- [42] Erwin P., Gadotti D. A., 2012, *Advances in Astronomy*, 2012
- [43] Espelid T., Genz A., 1994, *Numerical Algorithms*, 8, 201
- [44] Fehlberg E., 1972, *NASA Technical Report*, 381, 1
- [45] Fehlberg E., 1975, *NASA-TR-R*, 432, 546
- [46] Ferrarese L., Côté P., Dalla Bontà E., Peng E. W., Merritt D., Jordán A., Blakeslee J. P., Hasegan M., Mei S., Piatek S., Tonry J. L., West M. J., 2006, *ApJL*, 644, L21
- [47] Gebhardt K., Rich R. M., Ho L. C., 2002, *ApJl*, 578, L41
- [48] Gebhardt K., Rich R. M., Ho L. C., 2005, *ApJ*, 634, 1093
- [49] Genzel R., Eisenhauer F., Gillessen S., 2010, *Reviews of Modern Physics*, 82, 3121
- [50] Gerssen J., van der Marel R. P., Gebhardt K., Guhathakurta P., Peterson R. C., Pryor C., 2002, *AJ*, 124, 3270
- [51] Ghez A. M., Morris M., Becklin E. E., Tanner A., Kremenek T., 2000, *NAT*, 407, 349
- [52] Gieles M., Lamers H. J. G. L. M., Baumgardt H., 2008, in Vesperini E., Giersz M., Sills A., eds, *IAU Symposium Vol. 246 of IAU Symposium, Star Cluster Life-times: Dependence on Mass, Radius and Environment*. pp 171–175
- [53] Gieles M., Portegies Zwart S. F., Baumgardt H., Athanassoula E., Lamers H. J. G. L. M., Sipior M., Leenaarts J., 2006, *MNRAS*, 371, 793
- [54] Gnedin O. Y., Hernquist L., Ostriker J. P., 1999, *ApJ*, 514, 109
- [55] Gnedin O. Y., Ostriker J. P., 1997, *ApJ*, 474, 223
- [56] Gradshteyn I., Ryzhik I., 2007, *Table of Integrals, Series and Products* (seventh edition). Elsevier Academic Press

- [57] Graham A. W., 2012, MNRAS, 422, 1586
- [58] Gualandris A., Merritt D., 2008, ApJ, 678, 780
- [59] Gürkan M. A., Freitag M., Rasio F. A., 2004, ApJ, 604, 632
- [60] Häring N., Rix H.-W., 2004, ApJL, 604, L89
- [61] Hénon M., 1960, Annales d'Astrophysique, 23, 668
- [62] Hernquist L., 1990, ApJ, 356, 359
- [63] Huss A., Jain B., Steinmetz M., 1999a, ApJ, 517, 64
- [64] Huss A., Jain B., Steinmetz M., 1999b, MNRAS, 308, 1011
- [65] Jaffe W., 1983, MNRAS, 202, 995
- [66] Just A., Khan F. M., Berczik P., Ernst A., Spurzem R., 2011, MNRAS, 411, 653
- [67] Just A., Peñarrubia J., 2005, AAP, 431, 861
- [68] Kalnajs A. J., 1972, in Lecar M., ed., IAU Colloq. 10: Gravitational N-Body Problem Vol. 31 of Astrophysics and Space Science Library, Polarization Clouds and Dynamical Friction. p. 13
- [69] King I. R., 1966, AJ, 71, 64
- [70] Küpper A. H. W., Maschberger T., Kroupa P., Baumgardt H., 2011, MNRAS, 417, 2300
- [71] Larsen S. S., Strader J., Brodie J. P., 2012, AAP, 544, L14
- [72] Lauer T., et al. 2007, ApJ, 664, 226
- [73] Launhardt R., Zylka R., Mezger P. G., 2002, AAP, 384, 112
- [74] Leigh N., Böker T., Knigge C., 2012, MNRAS, 424, 2130
- [75] Lützgendorf N., Kissler-Patig M., Neumayer N., Baumgardt H., Noyola E., de Zeeuw P. T., Gebhardt K., Jalali B., Feldmeier A., 2013, AAP, 555, A26
- [76] Mackey A. D., Gilmore G. F., 2003, in Piotto G., Meylan G., Djorgovski S. G., Riello M., eds, New Horizons in Globular Cluster Astronomy Vol. 296 of Astronomical Society of the Pacific Conference Series, Dynamical Evolution of Globular Clusters in the Magellanic Clouds and Other Local Systems. p. 497
- [77] Marconi A., Hunt L. K., 2003, ApJL, 589, L21
- [78] McLaughlin D. E., Harris W. E., Hanes D. A., 1994, ApJ, 422, 486

-
- [79] McLaughlin D. E., King A. R., Nayakshin S., 2006, *ApJL*, 650, L37
 - [80] McMillan P. J., 2011, *MNRAS*, 414, 2446
 - [81] Merritt D., 2006, *Rep. Prog. Phys.*, p. 2513
 - [82] Miller M. C., Hamilton D. P., 2002, *MNRAS*, 330, 232
 - [83] Milosavljević M., Merritt D., 2001, *ApJ*, 563, 34
 - [84] Miyamoto M., Nagai R., 1975, *PASJ*, 27, 533
 - [85] Navarro J. F., Frenk C. S., White S. D. M., 1996, *ApJ*, 462, 563
 - [86] Neumayer N., 2012, *ArXiv e-prints*
 - [87] Neumayer N., Walcher C. J., 2012, *Advances in Astronomy*, 2012
 - [88] Neumayer N., Walcher C. J., Andersen D., Sánchez S. F., Böker T., Rix H.-W., 2011, *MNRAS*, 413, 1875
 - [89] Noyola E., Gebhardt K., Bergmann M., 2008, *ApJ*, 676, 1008
 - [90] Nugis T., Lamers H. J. G. L. M., 2000, *AAP*, 360, 227
 - [91] Ostriker J. P., Binney J., Saha P., 1989, *MNRAS*, 241, 849
 - [92] Pesce E., Capuzzo-Dolcetta R., Vietri M., 1992, *MNRAS*, 254, 466
 - [93] Plummer H. C., 1911, *MNRAS*, 71, 460
 - [94] Portegies Zwart S. F., Makino J., McMillan S. L. W., Hut P., 1999, *AAP*, 348, 117
 - [95] Read J. I., Goerdt T., Moore B., Pontzen A. P., Stadel J., Lake G., 2006a, *MNRAS*, 373, 1451
 - [96] Read J. I., Goerdt T., Moore B., Pontzen A. P., Stadel J., Lake G., 2006b, *MNRAS*, 373, 1451
 - [97] Rossa J., van der Marel R. P., Böker T., Gerssen J., Ho L. C., Rix H.-W., Shields J. C., Walcher C.-J., 2006, *AJ*, 132, 1074
 - [98] Salpeter E. E., 1955, *ApJ*, 121, 161
 - [99] Saslaw W. C., De Young D. S., 1971, *ApJ*, 170, 423
 - [100] Schödel R., 2011, in Morris M. R., Wang Q. D., Yuan F., eds, *The Galactic Center: a Window to the Nuclear Environment of Disk Galaxies* Vol. 439 of *Astronomical Society of the Pacific Conference Series*, *The Milky Way Nuclear Star Cluster in Context*. p. 222

- [101] Schröder K.-P., Cuntz M., 2005, *ApJl*, 630, L73
- [102] Schutz B. F., 1999, *Classical and Quantum Gravity*, 16, A131
- [103] Scott N., Graham A. W., 2013, *ApJ*, 763, 76
- [104] Sérsic J. L., 1963, *Boletin de la Asociacion Argentina de Astronomia La Plata Argentina*, 6, 41
- [105] Shapiro S. L., 1977, *ApJ*, 217, 281
- [106] Silk J., Rees M. J., 1998, *AAP*, 331, L1
- [107] Silvestri F., Ventura P., D'Antona F., Mazzitelli I., 1998, *ApJ*, 509, 192
- [108] Spitzer L., 1987, *Dynamical evolution of globular clusters*
- [109] Spitzer Jr. L., 1940, *MNRAS*, 100, 396
- [110] Spitzer Jr. L., 1969, *ApJl*, 158, L139
- [111] Stöer J., Burlish R., 2008, *Introduction to numerical analysis third edition*. Springer
- [112] Teuben P., 1995, *PASP Conf Series*, p. 398
- [113] Tremaine S. D., 1976, *ApJ*, 203, 72
- [114] Tremaine S. D., Ostriker J. P., Spitzer Jr. L., 1975, *ApJ*, 196, 407
- [115] Turner M. L., Côté P., Ferrarese L., Jordán A., Blakeslee J. P., Mei S., Peng E. W., West M. J., 2012, *ApJS*, 203, 5
- [116] Urry C. M., Padovani P., 1995, *PASP*, 107, 803
- [117] van den Bosch R. C. E., Gebhardt K., Gültekin K., van de Ven G., van der Wel A., Walsh J. L., 2012, *NAT*, 491, 729
- [118] Vicari A., Capuzzo-Dolcetta R., Merritt D., 2007, *ApJ*, 662, 797
- [119] Vishniac E. T., 1978, *ApJ*, 223, 986
- [120] Walker M. G., Peñarrubia J., 2011, *ApJ*, 742, 20
- [121] Wang Q. D., 1995, *AJ*, 110, 2622
- [122] Whitmore B. C., Chandar R., Schweizer F., Rothberg B., Leitherer C., Rieke M., Rieke G., Blair W. P., Mangel S., Alonso-Herrero A., 2010, *AJ*, 140, 75
- [123] Yozin C., Bekki K., 2012, *ApJL*, 756, L18
- [124] Zhao H., 1996, *MNRAS*, 278, 488